Cosmology beyond the standard model with precise measurements of the cosmic microwave background polarisation

Adrien La Posta

université PARIS-SACLAY

Cosmology beyond the standard model with precise measurements of the cosmic microwave background polarisation

Cosmologie au-delà du modèle standard avec les mesures précises de la polarisation du fond diffus cosmologique

Thèse de doctorat de l'université Paris-Saclay

École doctorale n° 576, Particules, hadrons, énergie et noyau : instrumentation, imagerie, cosmos et simulation (PHENIICS)
Spécialité de doctorat: Science des Astroparticules & Cosmologie
Graduate School : Physique. Référent : Faculté des sciences d'Orsay

Thèse préparée dans l'unité de recherche **IJCLab (Université Paris-Saclay, CNRS)**, sous la direction de **Matthieu TRISTRAM**, Directeur de Recherche, le co-encadrement de **Thibaut LOUIS**, Chargé de Recherche

Thèse soutenue à Paris-Saclay, le 28 septembre 2023, par

Adrien LA POSTA

Composition du jury

Membres du jury avec voix délibérative

Achille STOCCHI Professeur des Universités, Université Paris-Saclay	Président
Karim BENABED Directeur de recherche, Sorbonne Université	Rapporteur & Examinateur
Juan-Francisco MACIAS-PÉREZ Directeur de recherche, Université Grenoble-Alpes	Rapporteur & Examinateur
Joanna DUNKLEY Professeur, Princeton University	Examinatrice
Stéphanie ESCOFFIER Directrice de recherche, Université Aix-Marseille	Examinatrice
Mickael RIGAULT Chargé de recherche, Université Claude Bernard Lyon I	Examinateur

THESE DE DOCTORAT
NNT : 2023UPASP109

université PARIS-SACLAY

ÉCOLE DOCTORALE
Particules, hadrons, énergie et noyau : instrumentation, imagerie, cosmos et simulation (PHENIICS)

Titre: Cosmologie au-delà du modèle standard avec les mesures précises de la polarisation du fond diffus cosmologique
Mots clés: Fond diffus cosmologique, Cosmologie, Tension de Hubble, Modèle Lambda-CDM

Résumé: La cosmologie a connu des progrès remarquables grâce aux mesures de plus en plus précises de différentes sondes cosmologiques telles que les relevés de galaxies, ou le fond diffus cosmologique, permettant l'émergence du modèle standard ΛCDM. Ce modèle fournit une description précise de la structure à grande échelle de l'Univers et de son évolution. Cependant, les mesures locales de la constante de Hubble, qui quantifie le taux d'expansion de l'Univers aujourd'hui, viennent le remettre en cause. La valeur de la constante de Hubble dérivée de l'observation des supernovae de type IA est en désaccord avec la mesure la plus précise de la constante de Hubble obtenue via le fond diffus cosmologique. Cette thèse explore différentes hypothèses qui ont été proposée pour expliquer la tension. Tout d'abord, la différence pourrait provenir d'effets instrumentaux non modélisés dans l'analyse du CMB. Je présente des méthodes pour quantifier les effets systématiques instrumentaux en étudiant la consistance entre les mesures de température et de polarisation du CMB. La tension de Hubble pourrait également être une indication en faveur de la nécessité d'aller au-delà du modèle standard. J'aborde également cette hypothèse en discutant des contraintes obtenues sur un modèle d'énergie noire primordiale, qui induirait une phase d'expansion accélérée dans l'Univers primordial. Je présente également un statut de l'analyse des spectres en puissance pour la future analyse cosmologique des données provenant du télescope ACT (Atacama Cosmology Telescope) qui devrait fournir des contraintes sur la cosmologie indépendantes de Planck avec une précision similaire.

Title: Cosmology beyond the standard model with precise measurements of the cosmic microwave background polarisation
Keywords: Cosmic microwave background, Cosmology, Hubble tension, Lambda-CDM model

Abstract: Cosmology has witnessed remarkable progress in recent years with more and more precise observations of different probes, including galaxy surveys and observations of cosmic microwave background, consistently supporting the standard model of cosmology. The ΛCDM model provides an accurate description of the large-scale structure and evolution of the Universe. However, a growing challenge to the ΛCDM model arises from local measurements of the Hubble constant, which quantifies the expansion rate of the Universe at present time. The value of the Hubble constant inferred from type IA supernovae is 5σ discrepant with the most precise determination of the Hubble constant from the CMB. This thesis explores different hypothesis that were proposed to alleviate the tension. First, this difference may have arised from unmodelled instrumental effects in the CMB datasets. I present methods to quantify instrumental systematic effects by studying the consistency of CMB temperature and polarisation. The Hubble tension may also be a hint in favor of physics beyond the standard model. I discuss the constraints obtained from various CMB datasets on the Early Dark Energy scenario, a promising solution that induces a phase of accelerated expansion at early time. Lastly, I present the analysis status of the future data release from the Atacama Cosmology Telescope which will provide constraints on cosmology independent from Planck with a similar precision.

Remerciements

Je vais commencer par un énorme merci pour mon directeur de thèse Thibaut pour sa bonne humeur et sa bienveillance. J'ai beaucoup appris grâce à toi durant ces dernières années, bien entendu sur la cosmologie mais également à faire preuve de rigueur dans mon travail scientifique.

J'aimerais également remercier les membres de mon jury. Tout d'abord un grand merci à mes rapporteurs Juan-Francisco Macias-Pérez et Karim Benabed. Je remercie également Stéphanie Escoffier et Mickael Rigault d'avoir accepté de participer à mon jury. I would like to thank Jo Dunkley for participating in my jury and for your constant enthusiasm. Merci également à Achille Stocchi de m'avoir fait l'honneur de présider mon jury.

Un grand merci également au groupe CMB d'IJCLab, Matthieu, Sophie, Xavier, Gilles et Stéphane. Merci de m'avoir accompagné pendant cette thèse et d'avoir toujours eu des commentaires nombreux et pertinents sur mon travail. J'ai le sentiment d'avoir beaucoup progressé à vos côtés. Un merci tout particulier à Gilles avec qui j'ai partagé un bureau dans la bonne humeur pendant presque 2 ans. Merci beaucoup à Xavier de m'avoir accepté comme collègue d'enseignement et de m'avoir appris tant de choses en python.

I would like to thank the whole ACT collaboration, and in particular the PS working group for being so welcoming.

Je remercie également Emmanuel Schaan. Merci beaucoup pour nos discussions quasi hebdomadaires qui m'ont permis d'élargir mes horizons au-delà du fond diffus cosmologique.

Un grand merci à tous mes amis du lycée, Lise, Coralie, Alexis (ouais je t'ai mis là !), Jade, Ludivine, Kaina, Laura, Clément, Clément (devinez lequel), Arthur, Paulin, Robin, Martin. Même si on s'est dispersé partout en France, c'est toujours avec grand plaisir qu'on se retrouve !

J'ai aussi une pensée pour mes amis Baptiste, Robin, Léo et Bastien que j'ai rencontré pendant mon master de Physique à Grenoble. J'ai passé de très belles années à vos côtés.

Merci à mes colocataires, Baptiste et Delphine. C'était un plaisir de s'installer ensemble au bord de l'Yvette. Ça égaie un peu le quotidien souvent grisâtre de la vallée de Chevreuse de vous avoir chaque jour.

J'aimerais remercier ma belle famille, Jocelyn, Françoise, Arthur et Emma de m'avoir toujours accueilli chaleureusement.

J'ai une pensée émue pour toute ma famille, en particulier envers mes parents et mon frère

qui m'ont toujours encouragé et soutenu dans les différents projets que j'ai entrepris.

Pour terminer j'aimerais te remercier toi, Juliette, avec qui je partage ma vie depuis presque 10 ans. Merci pour ton soutien permanent et ta joie de vivre au quotidien. Merci pour tout ce que tu m'as apporté pendant ces 10 ans. Merci d'être toi.

Summary

This manuscript presents the work I have conducted over the past three years as part of the CMB team at the Laboratoire de Physique des 2 Infinis Irène Joliot Curie. My research focuses on the analysis of anisotropies in the cosmic microwave background (CMB), specifically in search of potential systematic effects and/or deviations from the standard model that could explain the Hubble tension. During my doctoral studies, I had the opportunity to publish several articles in peer-reviewed journals, from which the chapters 2, 3, and 4 are adapted.

First, I obtained the first cosmological constraints using a combination of power spectra: the correlation coefficient between the T and E modes, based on data from the Planck satellite (*La Posta et al. Phys. Rev. D 104, 023527 (2021)* [1]). This quantity, which is independent of multiplicative effects, allows for the detection of such systematic effects in CMB datasets. I estimated the correlation coefficient of Planck NPIPE data and adapted the public HiLLiPoP likelihood to $\mathcal{R}_\ell^{TE}$. This study is presented in Chapter 2.

I conducted another study aiming to detect potential systematic effects through an inconsistency between temperature and polarisation anisotropies (*La Posta et al. Phys. Rev. D 107, 023510 (2023)* [2]). My contributions to this article are highlighted in Chapter 3. I used additional parameters to describe the T-E inconsistencies at the likelihood level. I applied this method on publicly available data from the Planck satellite, the Atacama Cosmology Telescope, and the South Pole Telescope to identify possible deviations from the model in the best available datasets.

I also investigated a possible solution to the Hubble tension, which proposes to introduce a new component in the Universe that allow for an accelerated expansion phase around matter-radiation equality. I analysed the constraints on this model using polarisation data from the South Pole Telescope, as well as combinations with other CMB experiments or large-scale structure probes (*La Posta et al. Phys. Rev. D 105, 083519 (2022)* [3]). The results are discussed in Chapter 4.

Finally, my supervisor (Thibaut Louis) and I are involved in the Atacama Cosmology Telescope collaboration and are leading the future data release of the power spectrum analysis of ACT. The analysis is still ongoing, so Chapter 5 presents the current status of the power spectrum analysis. I contributed to the characterisation of the maps from the sixth data release of

ACT. Specifically, I contributed to the characterisation of the maps (calibrations, polarisation efficiency, transfer functions) of DR6, which were used in the CMB lensing analysis [4], [5]. I also contributed to the development of the power spectrum analysis pipeline (PSpipe), in particular by developing routines to perform a calibration against Planck, tools to assess for the internal consistency of the data and by implementing a bandpass integration procedure to account for the passband differences between detector arrays.

Table of contents

CHAPTER 1

The standard cosmological model

Summary

In this first chapter, I will summarise the key concepts of Physical cosmology, in order to give a description of the homogeneous Universe and the evolution of perturbations from the early Universe to the one we are observing today with a focus on the Cosmic Microwave Background. I will also present a brief review of state-of-the-art cosmological results from various instruments and collaborations. This introduction heavily relies on Ref. [6] and Ref. [7].

1.1. Describing the expanding Universe

1.1.1. General Relativity and the Friedmann equations

The standard model of Cosmology is based on General Relativity with the assumption that the Universe is homogeneous and isotropic. This assumption is good enough to describe the Universe at large scales (i.e. scales larger than a few hundred megaparsecs). We describe the Universe as a mathematical four-dimensional manifold with the Friedmann-Lemaître-Robertson-Walker (FLRW) metric expressed in polar coordinates,

$$ds^2 = -dt^2 + a^2(t)\left[\frac{dr^2}{1-Kr^2} + r^2 d\Omega^2\right], \tag{1.1}$$

where a is the scale factor representing the evolution of the Universe size as a function of time, and K describe its geometry. Historically, we use the convention $a(t = t_0) = 1$ where t_0 is the cosmic time today (around 14 billion years) and K has three different values $K = -1, 0, 1$ for an open, flat and closed Universe respectively. We also use a unit system in which $c = \hbar = 1$. The so-called FLRW metric is a solution of the Einstein equations which relates the geometry of space-time — contained in the tensor $G_{\mu\nu}$ — and the energy content of the Universe — described by the energy-momentum tensor $T_{\mu\nu}$

$$G_{\mu\nu} + \Lambda g_{\mu\nu} = R_{\mu\nu} - \frac{1}{2} g_{\mu\nu}\mathcal{R} + \Lambda g_{\mu\nu} = 8\pi G T_{\mu\nu}. \tag{1.2}$$

where we introduced the Ricci tensor $R_{\mu\nu}$ and its contraction the Ricci scalar $\mathcal{R}$.

Introducing χ as the comoving distance, the FLRW metric can be expressed as

$$ds^2 = -dt^2 + a^2(t)\left[d\chi^2 + S_K(\chi)^2 d\Omega^2\right], \tag{1.3}$$

where S_K depends on the geometry

$$S_K(\chi) = \begin{cases} \sin(\chi) & \text{if } K = 1 \text{ (spherical)} \\ \chi & \text{if } K = 0 \text{ (flat)} \\ \sinh(\chi) & \text{if } K = -1 \text{ (hyperbolic)} \end{cases} \tag{1.4}$$

Now, in order to describe the expanding Universe, one needs to find an expression for the energy-momentum tensor $T_{\mu\nu}$. The energy content of the Universe is assumed to be a perfect fluid with an energy density ρ and a pressure p measured in the rest frame of the fluid. Since the metric in Eq. (1.2) is diagonal, one needs to focus only on the diagonal elements of the Ricci tensor $R_{\mu\nu}$. The equation from the time component of this tensor is known as the Friedmann equation and is expressed as

$$\left(\frac{\dot{a}}{a}\right)^2 + \frac{K}{a^2} - \frac{\Lambda}{3} = \frac{8\pi G}{3}\rho. \tag{1.5}$$

Similarly, the spatial component of the Einstein equation gives us the following relation, also known as the Friedmann acceleration equation,

$$\left(\frac{\ddot{a}}{a}\right) = -\frac{4\pi G}{3}(3p + \rho) + \frac{\Lambda}{3}. \tag{1.6}$$

Equation (1.5) is useful to define fundamental quantities in cosmology; in particular one can define the expansion rate as $H(a) := \dot{a}/a$. It is convenient to express the curvature term (i.e. K/a^2) and the cosmological constant (i.e. $-\Lambda/3$) as energy densities on the right hand side of Eq. (1.5). We define $\rho_\Lambda = \Lambda/(8\pi G)$ and $\rho_K = -3K/(8\pi G)$ such that

$$H^2(a) = \left(\frac{\dot{a}}{a}\right)^2 = \frac{8\pi G}{3}\left[\rho + \rho_K a^{-2} + \rho_\Lambda\right]. \tag{1.7}$$

1.1.2. Densities as cosmological parameters

The purpose of this section is to define some important quantities in cosmology that will be used in the different analyses performed throughout this manuscript. We define the critical density as $\rho_c = 3H_0^2/(8\pi G)$, where H_0 is Hubble expansion rate evaluated at present time t_0 known as the ***Hubble constant***. The critical density represents the total energy density today required for the Universe to be flat. This allows us to rewrite the Friedmann equation as

$$H^2(a) = H_0^2\left[\Omega_{\rm tot}(a) + \Omega_K a^{-2}\right], \tag{1.8}$$

where $\Omega_{\rm tot} = \sum_i \Omega_i + \Omega_\Lambda$ and $\Omega_i = \rho_i/\rho_c$. Note that it implies that the sum of normalised density parameters is equal to 1 at $t = t_0$ for a flat Universe : $\Omega_{\rm tot}(t = t_0) = 1 - \Omega_K$.

At this stage, we need to develop the expression of ρ in order to correctly describe the energy content of the Universe. Assuming that the different fluids contributing to the energy density of

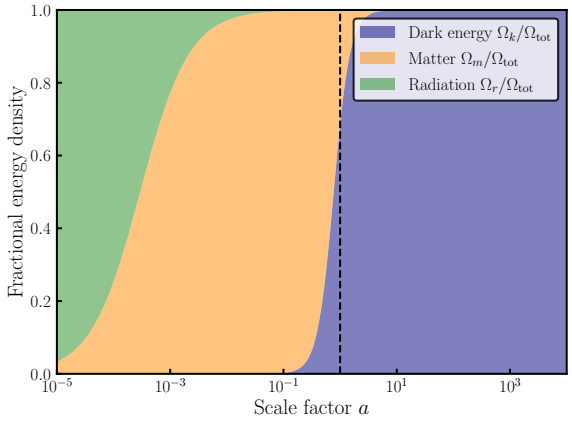

(a) Evolution of the fractional energy densities for the different species that contribute to the energy budget of the Universe as described by the ΛCDM model. The Universe was initially dominated by radiation (green), then by matter (orange). The dark energy (or cosmological constant Λ) is dominant at late times (blue) due to the dilution of the other densities. The dotted line corresponds to today (i.e. $t = t_0$). Relative densities of each species at a scale factor a can be read on vertical slices.

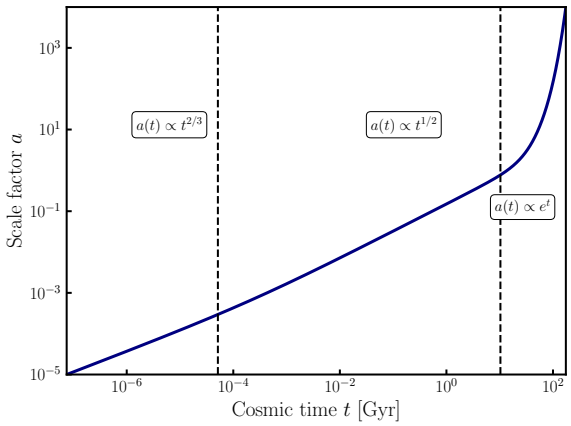

(b) Evolution of the scale factor a (that encodes the expansion of the Universe) as a function of cosmic time in billion years. The scale factor behaves differently in the radiation-dominated era (with $a(t) \propto t^{1/2}$), in the matter-dominated era ($a(t) \propto t^{2/3}$) and in the dark energy-dominated era (with an exponentially increasing scale factor $a(t) \propto e^t$).

Figure 1.1: Evolution of the energy densities of the different species that comprise the Universe (left) and evolution of the scale factor (right) according to the Friedmann equation for the flat ΛCDM model with $H_0 = 67$ km/s/Mpc, $\Omega_b = 0.0498$, $\Omega_c = 0.2673$ and $\Omega_r = 8.2 \times 10^{-4}$.

the Universe follow the equation of state $P_i = w_i \rho_i$ where i stands for either baryonic matter, dark matter, photons or neutrinos, one can derive from the continuity equation (1.9) the following relation : $\rho_i = \rho_i(t = t_0) a^{-3(1+w_i)}$.

$$\frac{d\rho}{dt} + 3H\left[\rho + P\right] = 0 \tag{1.9}$$

In order to explain what we observe (e.g. the rotation curves of galaxies, the Coma cluster, or the Cosmic Microwave Background signal), the standard model of cosmology assumes that the Universe is filled with ordinary matter (baryonic matter) and dark matter which interacts only gravitationally with the other species. We can express the total matter density as a sum of these two contributions $\rho_m(a) = \rho_b(a) + \rho_{\rm CDM}(a)$. Matter is assumed to be composed of non-relativistic species and to be pressureless. Hence, it means that $w_m = 0$ and therefore that the energy density $\rho_m(a) = \rho_m^0 a^{-3}$ scales as the number density — which is inversely proportional to the volume that goes like a^3. The relativistic species — or radiation — follow the equation of state $w_r = 1/3$, which means that $\rho_r(a) = \rho_r^0 a^{-4}$. We can note that the cosmological constant energy density that we have defined earlier is constant during the evolution of the Universe. As a consequence, the corresponding equation of state is $w_\Lambda = -1$ and is the simplest description of dark energy that is responsible for the accelerated expansion of the Universe. With this in mind, we can rewrite Eq. (1.8) as

$$H^2(a) = H_0^2 \left[\Omega_b a^{-3} + \Omega_c a^{-3} + \Omega_r a^{-4} + \Omega_K a^{-2} + \Omega_\Lambda\right]. \tag{1.10}$$

Note that the normalised densities defined this way are not independent of the value of the Hubble constant H_0 — i.e. $\Omega_i = \rho_i/\rho_c = 8\pi G\rho_i/(3H_0^2)$. When we want to jointly constrain the densities and H_0, we often use the quantities $\Omega_i h^2$, where the dimensionless reduced Hubble constant h is defined as $H_0 = 100h$ km/s/Mpc. Since we know the dependence of the different energy densities with the scale factor (displayed in Fig. (1.1(a))), we are able to solve the differential equation Eq. (1.8) and compute the evolution of the scale factor as a function of time (displayed in Fig. (1.1(b))). We are able to define three different epochs in the evolution of the Universe : the ***radiation-dominated*** era that occurs during the first 50000 years after the Big Bang, the ***matter-dominated*** era, and the ***dark energy-dominated*** era that has started in the recent Universe around 10 Gyr after the Big Bang. It is straightforward to get the evolution of the scale factor as a function of time in these different regimes.

Radiation-dominated Universe :

$$\frac{da}{dt} = \left(H_0\sqrt{\Omega_r}\right) a^{-1} \quad \Longrightarrow \quad a(t) \propto t^{1/2}. \tag{1.11}$$

Matter-dominated Universe :

$$\frac{da}{dt} = \left(H_0\sqrt{\Omega_m}\right) a^{-1/2} \quad \Longrightarrow \quad a(t) \propto t^{2/3} \tag{1.12}$$

Dark energy-dominated Universe :

$$\frac{da}{dt} = aH_0\sqrt{\Omega_\Lambda} \quad \Longrightarrow \quad a(t) \propto e^{H_0\sqrt{\Omega_\Lambda}t} \tag{1.13}$$

It is often convenient to use conformal time η instead of cosmic time t. The ***particle horizon*** — the maximum distance a particle could have travelled since the Big Bang — is given by $c\eta$,

$$\eta(t) = \int_0^t \frac{d\tilde{t}}{a(\tilde{t})} = \int_0^a \frac{d\tilde{a}}{\tilde{a}^2 H(\tilde{a})} = \int_0^z \frac{d\tilde{z}}{H(\tilde{z})}. \tag{1.14}$$

where we have introduced the ***redshift*** z defined as

$$z = \frac{\lambda_{\text{obs}}}{\lambda_{\text{emitted}}} - 1 = \frac{a_0}{a} - 1. \tag{1.15}$$

Photons emitted from a distant astrophysical source with a wavelength λ_{emitted} are observed with a wavelength λ_{obs} at $t = t_0$.

1.1.3. Cosmological distances

From the FLRW metric (Eq. (1.1)), one can define the radial comoving distance with

$$\chi = \int_{t_e}^{t_{\text{obs}}} \frac{cdt}{a(t)}, \tag{1.16}$$

The proper distance d — defined as the actual distance between the object and the observer — is then computed from $d(t) = a(t)\chi$. Note that the normlisation of the scale factor implies that the comoving distance corresponds to the proper distance at $t = t_0$. Distance measurements rely

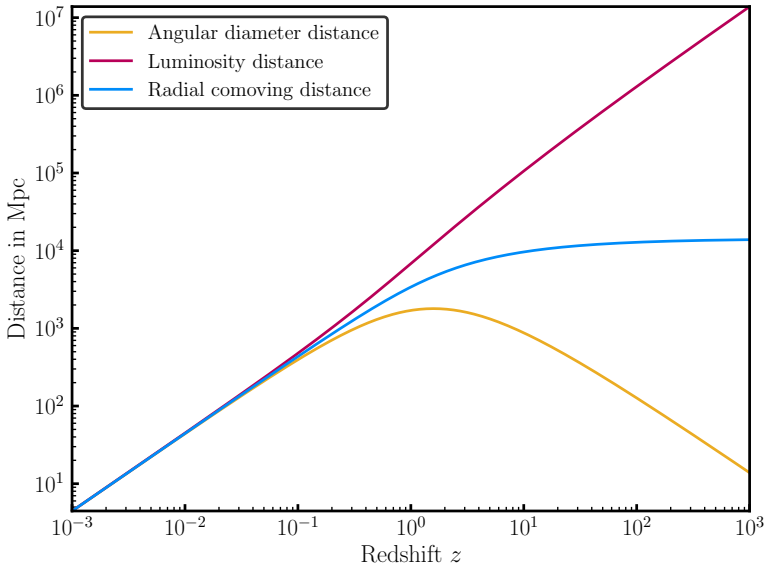

Figure 1.2: Three main distances between an observer at $z = 0$ and an astrophysical object at redshift z in the case of a flat ΛCDM model.

on two fundamental distances definitions widely used in cosmology namely the angular diameter distance and the luminosity distance respectively.

Angular diameter distance : The comoving angular diameter distance is defined such that the comoving size of the object dl_c we are looking at is $d\theta d_M$, where $d_M = S_K(\chi)$. Now suppose that we are observing an astrophysical object at an unknown comoving distance χ that has a known physical size dl (***standard ruler***) and an observed angular size $d\theta$. Using trigonometry we get $d\theta = dl/(a(t_e)\chi)$. We can measure the proper distance between the observer and the object by computing the ratio between its angular size and its physical size at the time the light was emitted, such that

$$d_A(t) = \frac{d\theta}{dl} = a(t)S_K(\chi) = a(t)d_M \tag{1.17}$$

Luminosity distance : Now, we suppose that the astrophysical object has a known intrinsic luminosity L (***standard candle***), and that we measure a flux F at $t = t_0$. The observed flux can be written as a function of the luminosity at $t = t_0$ as $F = L_0/(4\pi d^2(t = t_0))$. The luminosity corresponds to an energy per unit of time. The photon wavelength will evolve as $\lambda_{\text{emitted}} = (a/a_0)\lambda_0$ and the time interval will also be dilated such that $\delta t_{\text{emitted}} = (a_0/a)\delta t_0$. As a consequence $L_0 = (a/a_0)^2 L$. Then, the flux is

$$F = \frac{(a/a_0)^2 L}{4\pi a_0^2 \chi^2} = \frac{L}{4\pi \left[a_0^2 \chi^2 (1+z)^2\right]} = \frac{L}{4\pi d_L^2}, \tag{1.18}$$

where we introduce the luminosity distance d_L.

1.2. The perturbed Universe

This section summarises the standard approach to describe the perturbed Universe. A common assumption in Cosmology is that deviations from a homogeneous FLRW Universe are small enough to be approached using perturbative methods. This analytical derivation will prove helpful in providing a comprehensive understanding of the cosmic microwave background signal that we observe in the present day.

1.2.1. Perturbation of the energy content of the Universe

The energy content of the Universe (matter and radiation) can be described from a statistical point of view. To this aim, we will use the ***distribution function***, which represents the phase-space probability density function of a system. It means that the distribution function f follows the relation

$$dN(\vec{x},\vec{p},t) = f(\vec{x},\vec{p},t)\frac{d^3\vec{x}d^3\vec{p}}{(2\pi)^3}, \tag{1.19}$$

where $\vec{x}$ and $\vec{p}$ stand for the position and momentum of the particles respectively. This function will be very useful for the following analytical derivation in particular to get the macroscopic energy density from its second moment (i.e. by integrating $\vec{p}^2 f(\vec{x},\vec{p},t)$ over the momentum). The evolution of the distribution function is ruled by a relation that will be used to establish the equations that govern the evolution of the different species also known as the ***Boltzmann equation***,

$$\frac{df}{dt} = C[f], \tag{1.20}$$

which tells us that the distribution function can change with time only if there are interactions between the particles. These interactions are encoded in the functional $C[f]$ also called the ***collision term***. The total-derivative with respect to time can be expanded as

$$\frac{df}{dt} = \frac{\partial f}{\partial t} + \frac{\partial f}{\partial x^i}\frac{dx^i}{dt} + \frac{\partial f}{\partial p}\frac{dp}{dt} + \frac{\partial f}{\partial \hat{p}^i}\frac{d\hat{p}^i}{dt}, \tag{1.21}$$

where we split the dependence on the momentum amplitude p and the dependence on the momentum direction $\hat{p}$. At this stage, one needs to introduce the four-momentum $P^\mu = \frac{dx^\mu}{d\lambda}$ where λ is a variable defined along the geodesic followed by the particle. The time component can be identified with the energy $P^0 = \frac{dt}{d\lambda} = E$ such that we can write $P^\mu = (E, \vec{p}/a)$. The scale factor a appears here because $\vec{p}$ is defined as the physical momentum. In the following, we will consider that $\vec{p}$ is proportional to the momentum direction with $p^i = \hat{p}^i p$. First, the term dx^i/dt can be expressed as

$$\frac{dx^i}{dt} = \frac{dx^i}{d\lambda}\frac{d\lambda}{dt} = P^i \times \frac{1}{P^0} = \frac{p\hat{p}^i}{aE}. \tag{1.22}$$

Then, using the time component of the geodesic equation $\frac{dP^\alpha}{d\lambda} = -\Gamma^\alpha_{\mu\nu}P^\mu P^\nu$ one can demonstrate that the term dp/dt simplifies to $-Hp$.

In order to handle perturbations, we introduce two function Ψ and Φ — that will depend both on space and time — such that the metric of the perturbed Universe can be written

$$ds^2 = -\left(1+2\Psi(\vec{x},t)\right)dt^2 + a^2(t)\delta_{ij}\left(1+2\Phi(\vec{x},t)\right)dx^i dx^j, \tag{1.23}$$

where Ψ is the Newtonian gravitational potential and Φ is the spatial curvature perturbation that acts as a position-dependent perturbation to the scale factor. One should note that the way of writing Eq. (1.23) depends on the gauge we chose, here the metric is expressed in the Newtonian gauge. Recalling that the energy is defined as $E^2 = p^2 + m^2$, the four momentum can be expressed as $P^\mu = \left(E/\sqrt{1+2\Psi}, p^i/a\sqrt{1+2\Phi}\right) \simeq \left(E(1-\Psi), p^i(1-\Phi)/a\right)$ at first order. The perturbed Boltzmann equation can be obtained from Eq. (1.21), accounting for the first order perturbations to the metric in Ψ and Φ. This results in the following expression

$$\begin{aligned}\frac{df}{dt} = &\frac{\partial f}{\partial t} + \frac{\partial f}{\partial x^i}\frac{p\hat{p}^i}{aE}(1-\Phi+\Psi) - \frac{\partial f}{\partial p}\left((H+\frac{\partial\Phi}{\partial t})p + \frac{E}{a}\hat{p}^i\frac{\partial\Psi}{\partial x^i}\right)\\ &+ \frac{\partial f}{\partial \hat{p}^i}\frac{E}{ap}\left(\frac{\partial}{\partial x^i}(\frac{p^2}{E^2}\Phi - \Psi) - \hat{p}^i\hat{p}^k\frac{\partial}{\partial x^k}(\frac{p^2}{E^2}\Phi - \Psi)\right),\end{aligned} \tag{1.24}$$

where we recover the Boltzmann equation in an homogeneous Universe if we ignore the first order corrections. It is interesting to note that the time dependence of the momentum direction depends only on first-order quantities since we have assumed that $d\hat{p}^i/dt = 0$ for the homogeneous Universe. To simplify further, one needs to assume that the distribution function depends only on the momentum modulus p at the zeroth order (i.e. in the homogeneous Universe). As a consequence, $\frac{\partial f}{\partial x^i}$ and $\frac{\partial f}{\partial \hat{p}^i}$ are first-order quantities. Equation (1.24) becomes

$$\frac{df}{dt} = \frac{\partial f}{\partial t} + \frac{\partial f}{\partial x^i}\frac{p\hat{p}^i}{aE} - \frac{\partial f}{\partial p}\left((H+\frac{\partial\Phi}{\partial t})p + \frac{E}{a}\hat{p}^i\frac{\partial\Psi}{\partial x^i}\right). \tag{1.25}$$

For massless or ultra-relativistic particles, we can use the fact that $p/E = 1$ to simplify again this equation. In the following, we will write down the equations governing the evolution of perturbations for the different species that compose the Universe according to the ΛCDM model: cold dark matter, photons, baryons and neutrinos.

Dark matter perturbations : According to the ΛCDM model, dark matter is considered non-relativistic (cold) such that $p/m \ll 1$. Dark matter is also non-interacting so that there is no collision term in the Boltzmann equation describing the evolution of cold dark matter perturbations. Recalling that we can define number density and fluid velocity as

$$n_c(\vec{x},t) = \int \frac{d^3\vec{p}}{(2\pi)^3} f(\vec{x},\vec{p},t) \quad \text{and} \quad v_c(\vec{x},t) = \frac{1}{n_c}\int \frac{d^3\vec{p}}{(2\pi)^3}\frac{p\hat{p}^i}{E} f(\vec{x},\vec{p},t), \tag{1.26}$$

we get a first differential equation by integrating Eq (1.25) over the momentum :

$$\frac{\partial n_c}{\partial t} + \frac{1}{a}\frac{\partial n_c v_c^i}{\partial x^i} + 3(H + \frac{\partial\Phi}{\partial t})n_c = 0. \tag{1.27}$$

At zeroth order, this equation leads to the continuity equation for cold dark matter $\partial_t n_c + 3Hn_c = 0$ which implies that cold dark matter density dilutes as a^{-3}. If we define the density perturbation δ_c such that $n_c(\vec{x},t) = \bar{n}_c\left(1+\delta_c(\vec{x},t)\right)$ — where $\bar{n}_c$ is the zeroth order number density — we obtain the first order equation

$$\frac{\partial \delta_c}{\partial t} + \frac{1}{a}\frac{\partial v_c^i}{\partial x^i} + 3\frac{\partial \Phi}{\partial t} = 0. \tag{1.28}$$

The second equation is obtained by taking the first moment of Eq (1.25), assuming that terms proportional to $(p/E)^2$ can be neglected (as well as higher orders),

$$\frac{\partial v_c^i}{\partial t} + H(t)v_c^i + \frac{1}{a}\frac{\partial \Psi}{\partial x^i}. \tag{1.29}$$

If we use the conformal time η instead of cosmic time t as well as the Fourier transform of equations (1.28) & (1.29), we get

$$\partial_\eta \delta_c + ikv_c + 3\partial_\eta \Phi = 0 \tag{1.30}$$

$$\partial_\eta v_c + \frac{\partial_\eta a}{a} v_c + ik\Psi = 0 \tag{1.31}$$

Photon perturbations : Since photons are massless particles, we have $p = E$ and then the left-hand side of the Boltzmann equation becomes

$$\frac{df_\gamma}{dt} = \frac{\partial f_\gamma}{\partial t} + \frac{\partial f_\gamma}{\partial x^i}\frac{\hat{p}^i}{a} - \frac{\partial f_\gamma}{\partial p} p \left[(H + \partial_t \Phi) + \frac{1}{a}\hat{p}^i \frac{\partial \Psi}{\partial x^i} \right]. \tag{1.32}$$

Additionally, we know that photons are bosons and thus have a Bose-Einstein distribution function. In this derivation, we are interested in a small perturbation around the homogeneous photon distribution such that

$$f_\gamma(\vec{x}, \vec{p}, t) = \frac{1}{\exp\left[\frac{p}{T(t)(1+\Theta(\vec{x},\hat{p},t))}\right] - 1}, \tag{1.33}$$

where $\Theta = \delta T/T$ and $\Theta(\vec{x}_{\rm obs}, \hat{p}, t_{\rm obs})$ corresponds to the temperature anisotropies that we observe at a position $\vec{x}$ and time t. We can expand this expression at first order,

$$f_\gamma(\vec{x}, \vec{p}, t) = \bar{f}_\gamma(p, t) + T(t)\Theta(\vec{x}, \hat{p}, t)\partial_T \bar{f}_\gamma(p, t) = \bar{f}_\gamma(p, t) - p\frac{\partial \bar{f}_\gamma}{\partial p}\Theta(\vec{x}, \vec{p}, t), \tag{1.34}$$

using the fact that $\bar{f}_\gamma(p, t) = (\exp(p/T) - 1)^{-1}$ is the homogeneous distribution function. The partial derivatives of the distribution function are given by

$$\frac{\partial f}{\partial t} = \frac{\partial \bar{f}_\gamma}{\partial t} - p\frac{\partial}{\partial t}\left[\frac{\partial \bar{f}_\gamma}{\partial p}\Theta\right], \tag{1.35}$$

$$\frac{\partial f}{\partial x^i} = -p\frac{\partial \bar{f}_\gamma}{\partial p}\frac{\partial \Theta}{\partial x^i}, \tag{1.36}$$

$$\frac{\partial f}{\partial p} = \frac{\partial \bar{f}_\gamma}{\partial p} - \frac{\partial \bar{f}_\gamma}{\partial p}\Theta - p\frac{\partial^2 \bar{f}_\gamma}{\partial p^2}\Theta, \tag{1.37}$$

from which we can extract the zeroth and first order equations. As for dark matter, the zeroth order equation constrains the dependence of the homogeneous temperature T as a function of the scale factor

$$\left(-\frac{\partial_t T}{T} - \frac{\partial_t a}{a}\right) = 0 \quad \Longrightarrow \quad T \propto \frac{1}{a}. \tag{1.38}$$

The first order equation governing the evolution of the photon perturbations is

$$-p\frac{\partial \bar{f}_\gamma}{\partial p}\left(\partial_t \Theta + \frac{\hat{p}^i}{a}\frac{\partial \Theta}{\partial x^i} + \partial_t \Phi + \frac{\hat{p}^i}{a}\frac{\partial \Psi}{\partial x^i}\right) = C[f]. \tag{1.39}$$

Photons interact via Compton scattering with electrons $e^- + \gamma \leftrightarrow e^- + \gamma$; therefore we need to include the collision term $C[f]$ in this equation.

$$C[f] = -p\frac{\partial \bar{f}_\gamma}{\partial p} n_e \sigma_T \left(\Theta_0 - \Theta + \hat{p} \cdot v_b\right) \tag{1.40}$$

This term is expressed as a function of the monopole of the photon perturbation which corresponds to the angular integral of the perturbation Θ such that $\Theta_0(\vec{x}, t) = \int \frac{d\Omega}{4\pi}\Theta(\hat{p}, \vec{x}, t)$. v_b is the baryon fluid velocity — assumed to be equal to the electron fluid velocity due to tight coupling, σ_T is the cross-section of the interaction and n_e the electron number density. Defining $\mu = \vec{k} \cdot \hat{p}/k$ and the optical depth τ as

$$\tau(\eta) = \int_\eta^{\eta_0} d\tilde{\eta}\; n_e \sigma_T a, \tag{1.41}$$

we are able to get the Boltzmann equation for photon perturbations in Fourier space

$$\partial_\eta \Theta + ik\mu\Theta + \partial_\eta \Phi + ik\mu\Psi = -\partial_\eta \tau \left(\Theta_0 - \Theta + \mu v_b\right) \tag{1.42}$$

Baryon perturbations : At early times, protons and electrons were tightly coupled due to Coulomb interactions and therefore we use the b subscript (*baryons*) to describe the density perturbations and bulk velocities either for the electrons or protons such that $\delta_b = \delta\rho_e/\rho_e = \delta\rho_p/\rho_p$. Since this proton-electron fluid is considered to be non-relativistic, we can follow the same procedure as for deriving the cold dark matter equations. The continuity equation is unchanged, even if we have some interactions between the baryon and the photon fluids. Indeed this equation was derived from the zeroth moment of Eq. (1.25), and since the number density is constant, the collision term can be ignored. Contributions from the collision term are no longer vanishing in the Euler equation for baryons since it derives from the first moment of the Boltzmann equation. However, the collision term is computed by extracting the first moment of Eq. (1.42) since it corresponds to the momentum transfer between the baryon and photon fluids. This derivation leads to the Boltzmann equations for baryons

$$\partial_\eta \delta_b + ikv_b + 3\partial_\eta \Phi = 0 \tag{1.43}$$

$$\partial_\eta v_b + \frac{\partial_\eta a}{a} v_b + ik\Psi = \partial_\eta \tau \frac{4\rho_\gamma}{3\rho_b}\left(3i\Theta_1 + v_b\right) \tag{1.44}$$

This equation involves the dipole of the photon pertubation Θ_1 defined as $\Theta_1(k, \eta) = i\int \frac{d\mu}{2}\mu\Theta(\mu, k, \eta)$, that will drag baryons along the direction of the dipole.

Neutrino perturbations : Neutrinos are described as fermions and are distributed according to the Fermi-Dirac distribution. Similarly to what we did for the photons, we introduce the neutrino perturbation $\mathcal{N}$ such that

$$f_\nu(\vec{x},\vec{p},t) = \frac{1}{\exp\left[\frac{p}{T_\nu(t)(1+\mathcal{N}(\vec{x},\vec{p},t))}\right]+1}. \tag{1.45}$$

Neutrinos are considered relativistic prior to recombination (i.e. $p/E \simeq 1$), but this is not the case at late time. Then, to get a general equation describing the evolution of neutrino perturbations, one needs to use the non-relativistic Boltzmann equation (Eq. (1.25)). The first order equation is therefore very similar to Eq. (1.42),

$$\partial_\eta \mathcal{N} + ik\mu\frac{p}{E}\mathcal{N} + \partial_\eta\Phi + ik\mu\frac{E}{p}\Psi - Hp\frac{\partial\mathcal{N}}{\partial p} = 0, \tag{1.46}$$

where we can assume that $\mathcal{N}$ is independent of the momentum p to recover the collisionless Boltzmann equation for photons.

1.2.2. Gravitational perturbations

The previous section was focused on deriving equations governing the evolution of the perturbations for the different species in the Universe. However, we have introduced two functions Ψ and Φ to describe the perturbed FLRW metric in Eq. (1.23). In order to solve this set of differential equations, two equations are missing and we can derive them from the Einstein equations. Defining the perturbed Einstein tensor as $G^\mu_\nu = \bar{G}^\mu_\nu + \delta G^\mu_\nu$, and the first order contribution to the energy momentum tensor δT^μ_ν, it is possible to get two independent equations from the time and spatial components of $\delta G^\mu_\nu = 8\pi G \delta T^\mu_\nu$,

$$k^2\Phi + 3\frac{\partial_\eta a}{a}\left(\partial_\eta\Phi - \frac{\partial_\eta a}{a}\Psi\right) = 4\pi G a^2\left(\rho_c\delta_c + \rho_b\delta_b + 4\rho_\gamma\Theta_0 + 4\rho_\nu\mathcal{N}_0\right), \tag{1.47}$$

$$k^2\left(\Phi+\Psi\right) = -32\pi G a^2\left(\rho_\gamma\Theta_2 + \rho_\nu\mathcal{N}_2\right), \tag{1.48}$$

where $\mathcal{N}_0$ and $\mathcal{N}_2$ are the monopole and quadrupole of the neutrino distribution perturbation. Equation (1.47) is a generalisation of the Poisson equation in an expanding Universe. Note that these two equations describe only the evolution of scalar perturbations since they are the one we are interested in for now.

1.2.3. Primordial fluctuations

The Universe as described in the previous sections faces two major issues : the ***horizon problem*** and the ***flatness problem***. To begin with, observables such as the Cosmic Microwave Background suggest that the Universe is quasi-homogeneous with very tiny anisotropies $\delta T/T \sim 10^{-5}$. However, there are regions of the sky which have the same mean temperature but which should not have been in causal contact in the past. Therefore, thermalisation is not sufficient to explain the apparent homogeneity of the Universe. Secondly, the spatial curvature of the Universe has been well constrained in Ref. [8] from a combination of CMB anisotropies and Baryonic Acoustic Oscillations (BAO) to a value of $\Omega_k = 0.0007 \pm 0.0037$, consistent with a flat Universe. In order to highlight the issue here, one can rewrite the Friedmann equation (1.5) as

$$\left(\frac{\rho(a)-\rho_c(a)}{\rho(a)}\right) = \frac{K}{a^2H^2(a)} \tag{1.49}$$

where $\rho_c(a)$ is the critical density evaluated at a scale factor a and ρ is the total energy density of the Universe (matter, radiation and dark energy). Since $a^2H^2(a)$ grows with time and the spatial curvature density is very small at time $t = t_0$, the term on the left has to go to 0 as the scale factor a tends to 0. It means that the density ρ have to be arbitrarly close to ρ_c as t is close to 0.

The paradigm that have been introduced to solve both of these issues is called ***inflation***. It consists in a phase of accelerated expansion in the early Universe. If the expansion rate is constant with time, the scale factor a is proportional to e^{Ht}. As a consequence, the Hubble radius $1/(aH)$ decreases with time, allowing ρ to be different from the critical density at early times. It also allows to solve the horizon problem by increasing the proper distance travelled by the photons due to the early time contribution of $1/(a^2H)$.

The most simple way to describe a component that will induce an accelerated expansion phase is to use a scalar field ϕ that evolves in a potential V according to the Klein-Gordon equation in an expanding Universe

$$\ddot{\phi} + 3H\dot{\phi} + \frac{dV}{d\phi}. \tag{1.50}$$

The energy density and pressure associated to the scalar field are $\rho_\phi = \dot{\phi}^2/2 + V$ and $P_\phi = \dot{\phi}^2/2 - V$ such that the equation of state is

$$w_\phi = \frac{\dot{\phi}^2/2 - V}{\dot{\phi}^2/2 + V}. \tag{1.51}$$

When the kinetic energy of the field is negligible with respect to its potential energy $\dot{\phi} \ll V(\phi)$, the field acts as a cosmological constant with $w = -1$. This condition is usually called a ***slow-roll*** condition. An interesting consequence of inflation is that the field will decay into particles at the end of the inflationary epoch (through a process called reheating) and will also produce primordial fluctuations that will evolve according to what we described in the previous section. Inflation produces both tensor and scalar perturbations : the former should have left an imprint in the cosmic microwave background anisotropies as B-modes polarisation, and the latter have been the source of primordial fluctuations in the gravitational potential Ψ. The primordial scalar perturbations are described using the power spectrum of the curvature perturbation $\mathcal{R}$,

$$P_{\mathcal{R}}(k) = \frac{2\pi^2}{k^3} A_s \left(\frac{k}{k_p}\right)^{n_s - 1}, \tag{1.52}$$

where A_s is the amplitude of the power spectrum at the pivot scale k_p and n_s is the scalar spectral index that describes the shape of the initial power spectrum. In the following, we define A_s and n_s at a pivot scale $k_p = 0.05$ Mpc^{-1}. The same parametrisation holds for the tensor perturbation, introducing n_T as the tensor spectral index

$$P_T(k) = \frac{2\pi^2}{k^3} A_T \left(\frac{k}{k_p}\right)^{n_T}, \tag{1.53}$$

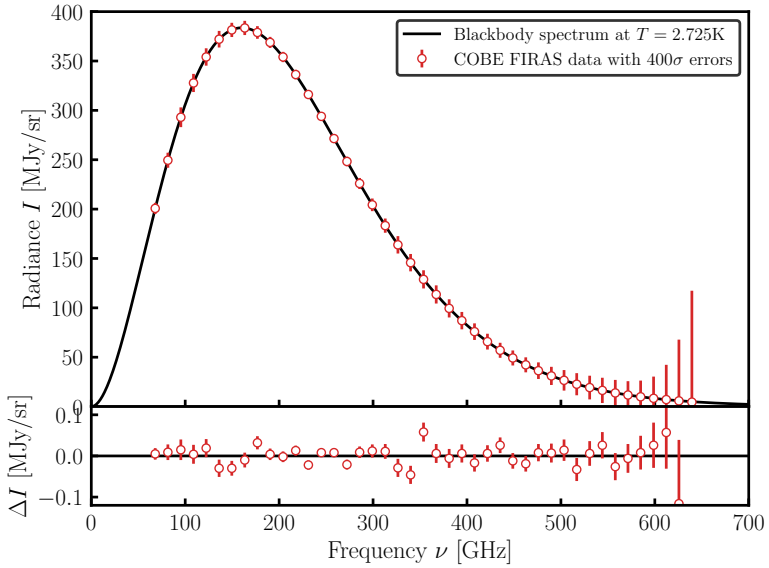

Figure 1.3: Cosmic microwave background spectrum as measured by the FIRAS instrument embarked on the COBE satellite [9] (red data point). The black line is a theory curve corresponding to a blackbody radiation with a temperature of $T = 2.725$ K. The errorbars have been inflated by a factor 400 to make them visible. Data used in the figure have been downloaded from https://lambda.gsfc.nasa.gov/product/cobe/firas_monopole_get.html.

such that the tensor to scalar ratio r is defined as the ratio of the primordial power spectra at the pivot scale $r(k_p) = A_T(k_p)/A_s(k_p)$.

1.3. The cosmic microwave background

As we have seen before, matter and radiation in the very early Universe were tightly coupled in the primordial plasma due to to Compton scattering $e^- + \gamma \leftrightarrow e^- + \gamma$. Since the unperturbed photon temperature evolves as $T(t) = T_0/a(t)$ due to the expansion, approximately 300 000 years after the Big Bang protons and electrons recombined to form neutral hydrogen. Then, the Compton interaction rate dropped below the Hubble expansion rate and photons decoupled from the plasma. The photon bath emitted around $z = 1100$ is what we call the cosmic microwave background. This radiation is nearly isotropic on the sky and well described by a blackbody spectrum

$$B_\nu(\nu, T_0) = \frac{2h\nu^3}{c^2} \frac{1}{\exp\left(\frac{h\nu}{k_B T_0}\right) - 1}, \tag{1.54}$$

with a temperature $T_0 = 2.7255$ K and where we used standard SI units. The CMB blackbody spectrum has been measured by the FIRAS instrument in the COBE satellite with an exquisite precision [9] as shown in Fig. (1.3). The observed isotropy of this radiation is a strong evidence in favor of the large scale homogeneity assumed by the cosmological principle. However, primordial fluctuations gave birth to tiny anisotropies in the photon perturbation Θ such that the observed temperature anisotropies today are of order $\delta T(t_0)/T(t_0) \sim 10^{-5}$. This section will discuss the

evolution of the photon perturbation from the hot Big Bang to today, starting from the tight coupling era.

1.3.1. Tight coupling era

At very early times, with $z \gg z_{\rm rec}$ photons and baryons were tightly coupled. In other words, the interaction rate τ' was much larger than the expansion rate a'/a. We check for the validity of this assumption by computing the ratio

$$r_{\rm TC} = \frac{|\tau'|}{a'/a} = \frac{n_e \sigma_T a}{H_0 E(a)} \sim \frac{\rho_b^0 \sigma_T}{m_b H_0 f(a) a^2}, \tag{1.55}$$

where $E(a) = \sqrt{\Omega(a)}$ and where $f(a)$ is $\sqrt{\Omega_r} a^{-1}$ during radiation domination and $\sqrt{\Omega_m} a^{-1/2}$ during matter domination. m_b stands for the typical mass of a baryonic matter particle. For simplicity we set this mass to the proton mass (1 GeV). During radiation domination or matter domination, $r_{\rm TC}$ evolves with a^{-1} and $a^{-3/2}$ respectively, and therefore goes to infinity as a approaches 0.

According to this tight coupling hypothesis, the photon and baryon fluids are supposed to be fully correlated. Then, the photon fluid behaves like a perfect fluid described only with two quantities : the monopole and the dipole of $\Theta(\vec{x}, \hat{p}, t)$. Recalling the definition of the monopole $\Theta_0(k,\eta) = \frac{1}{2}\int d\mu \Theta(k,\eta,\mu)$ and the dipole $\Theta_1(k,\eta) = \frac{i}{2}\int d\mu \mu \Theta(k,\eta,\mu)$ — where $\mu = \vec{k}\cdot\hat{p}/k$ — we can integrate over μ the Boltzmann equation for photons (1.42) to get

$$\Theta_0' + k\Theta_1 = -\Phi' \tag{1.56}$$

$$\Theta_1' - \frac{k\Theta_0}{3} = \frac{k\Psi}{3} + \tau'\left(\Theta_1 - \frac{i v_b}{3}\right) \tag{1.57}$$

To get rid of the baryon velocity in Eq. (1.57), one needs to use the baryon velocity equation (1.44)

$$v_b = -3i\Theta_1 + \frac{R}{\tau'}\left(v_b' + \frac{a'}{a}v_b + ik\Psi\right) \simeq -3i\Theta_1 + \frac{R}{\tau'}\left(-3i\Theta_1' - 3i\frac{a'}{a}\Theta_1 + ik\Psi\right), \tag{1.58}$$

where we have introduced the baryon to photon ratio $R = 3\rho_b/4\rho_\gamma$. The second equality holds because we are working at first order in $1/\tau'$ with at zeroth order $v_b = -3i\Theta_1$. This differential system can be combined in one second order equation on the monopole Θ_0

$$\Theta_0'' + \frac{a'}{a}\frac{R}{1+R}\Theta_0' + \frac{k^2}{3(1+R)}\Theta_0 = -\Phi'' - \frac{a'}{a}\frac{R}{1+R}\Phi' - k^2\frac{\Psi}{3}. \tag{1.59}$$

This equation describes a damped harmonic oscillator with a source term of the form : $\ddot{X} + 2\zeta k c_s \dot{X} + k^2 c_s^2 X = F$, where the second term is a friction term with ζ the damping ratio and c_s is the sound speed. Therefore we can identify some useful quantities such as

$$c_s(\eta) = \frac{1}{\sqrt{3(1+R(\eta))}} \quad \text{and} \quad \zeta = \frac{a'}{a}\frac{\sqrt{3}R(\eta)}{2k\sqrt{1+R(\eta)}}, \tag{1.60}$$

where $R(\eta) = \frac{3\rho_b^0}{4\rho_\gamma^0}a$. The speed of the sound waves propagating in the primordial plasma is close to the limit of $1/\sqrt{3}$ when baryon density is negligible at early times. One can note that the damping ratio ζ is proportional to $1/\sqrt{1+R(\eta_0)a}$ in a radiation dominated Universe : in other words, the damping of the oscillations decreases with time.

We can define a fundamental quantity from the sound speed in the primordial plasma : the sound-horizon $r_s(\eta)$. It is defined as the maximum distance travelled by a sound wave from $\eta = 0$ up to conformal time η

$$r_s(\eta) = \int_0^\eta d\tilde{\eta} c_s(\tilde{\eta}) = \int_0^a d\tilde{a} \frac{c_s(\tilde{a})}{\tilde{a}^2 H(\tilde{a})} = \int_z^\infty d\tilde{z} \frac{c_s(\tilde{z})}{H(\tilde{z})}. \tag{1.61}$$

At recombination, sound waves stop propagating due to the expansion and therefore the distribution of photons and matter will contain a standard ruler corresponding to the comoving size of the sound horizon at recombination $r_s(\eta_*) \simeq 150\,\mathrm{Mpc}$. The sound horizon scale corresponds to a physical distance of 13 kpc at the time of recombination.

1.3.2. Damping of the small scales

The high interaction rate between photons and baryons at early times implies that the mean free path of photons will be small. Since interactions tends to make the plasma more homogeneous, we expect the temperature perturbations to be washed out at small scales. The mean comoving distance travelled by the photons Λ_D is proportional to $l\sqrt{N_{\mathrm{scatter}}}$ where l is the mean free path and N_{scatter} is the number of interactions. The mean distance between two interactions is given by the inverse of the scattering rate $l = 1/(n_e \sigma_T a)$ and the number of interactions is $N_{\mathrm{scatter}} = n_e \sigma_T / H$. Therefore the mean comoving distance travelled by the photons is

$$\lambda_D \simeq \frac{1}{\sqrt{n_e \sigma_T H a}}. \tag{1.62}$$

In a radiation dominated Universe, $\lambda_D \propto a^{3/2}$ and we recover the fact that there is less interactions as the Universe evolves. This means that there are different regions of the sky with a characteristic size of λ_D that are homogeneised by Compton scattering; and that therefore we won't be able to see fluctuations smaller than $1/\lambda_D$ in the photon perturbation.

1.3.3. Free streaming after recombination

Now that we have equations that govern the evolution of perturbations before the emission of the cosmic microwave background, we need to establish an equation that relates the photon perturbation at the time of last scattering $\Theta(\vec{k}, \eta = \eta_*)$ to the photon temperature anisotropies measured by an observer at $\eta = \eta_{\mathrm{obs}}$.

The Boltzmann equation for photons (1.42) can be rewritten as

$$\Theta' + (ik\mu - \tau')\Theta = \hat{S}, \tag{1.63}$$

where $\hat{S} = -\Phi' - ik\mu\Psi - \tau'(\Theta_0 + \mu v_b)$ in absence of polarisation. The left hand side of Eq. (1.63) can be equivalently expressed as

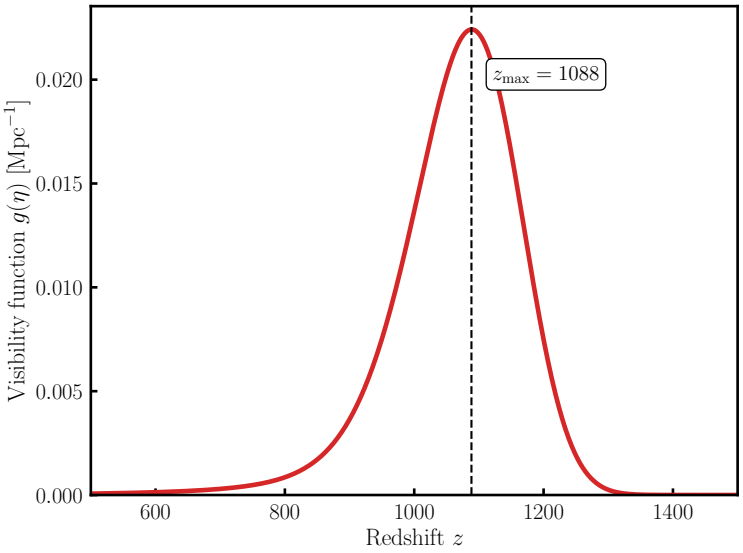

Figure 1.4: Visibility function of the cosmic microwave background photons. It represents the probability density that a photon we observed was last scattered at a redshift z. The distribution peaks around a $z = 1088$ which is often defined as the last scattering surface redshift.

$$\Theta' + (ik\mu - \tau')\Theta = e^{-ik\mu\eta+\tau}\frac{d}{d\eta}\left(\Theta e^{ik\mu\eta-\tau}\right) = \hat{S}. \tag{1.64}$$

The integral over conformal times from $\eta = 0$ and $\eta = \eta_{\rm obs}$ of this equation results in a solution for the temperature anisotropies for the observer.

$$\Theta(k, \eta_{\rm obs}, \mu) = \int_0^{\eta_{\rm obs}} d\eta \hat{S}(k, \eta, \mu) e^{ik\mu(\eta-\eta_{\rm obs})-\tau(\eta)}. \tag{1.65}$$

At this stage, it is convenient to do a multipolar expansion of Θ that helps to handle the μ-dependence in the free-streaming equation. This expansion involves the spherical Bessel functions j_l. The observed multipole Θ_l is therefore

$$\Theta_l(k, \eta_{\rm obs}) = \int_0^{\eta_{\rm obs}} d\eta S(k, \eta) j_l\left(k(\eta_{\rm obs} - \eta)\right). \tag{1.66}$$

The source term is now defined as

$$S(k, \eta) = g(\eta)\left(\Theta_0(k, \eta) + \Psi(k, \eta)\right) + \frac{i}{k}\frac{d}{d\eta}\left(v_b(k, \eta)g(\eta)\right) + e^{-\tau}\left(\Psi'(k, \eta) - \Phi'(k, \eta)\right), \tag{1.67}$$

where g is called the visibility function and corresponds to the probability density that a photon observed today has last scattered in the time interval between η and $\eta + d\eta$, such that $dP = g(\eta)d\eta$. The visibility function g is expressed as

$$g(\eta) = -\tau'(\eta)e^{-\tau(\eta)}. \tag{1.68}$$

Figure (1.4) displays the visibility function with respect to redshift z. The visibility function computed from Planck 2018 best-fit cosmology [8] peaks around a redshift $z_* \simeq 1088$. It means

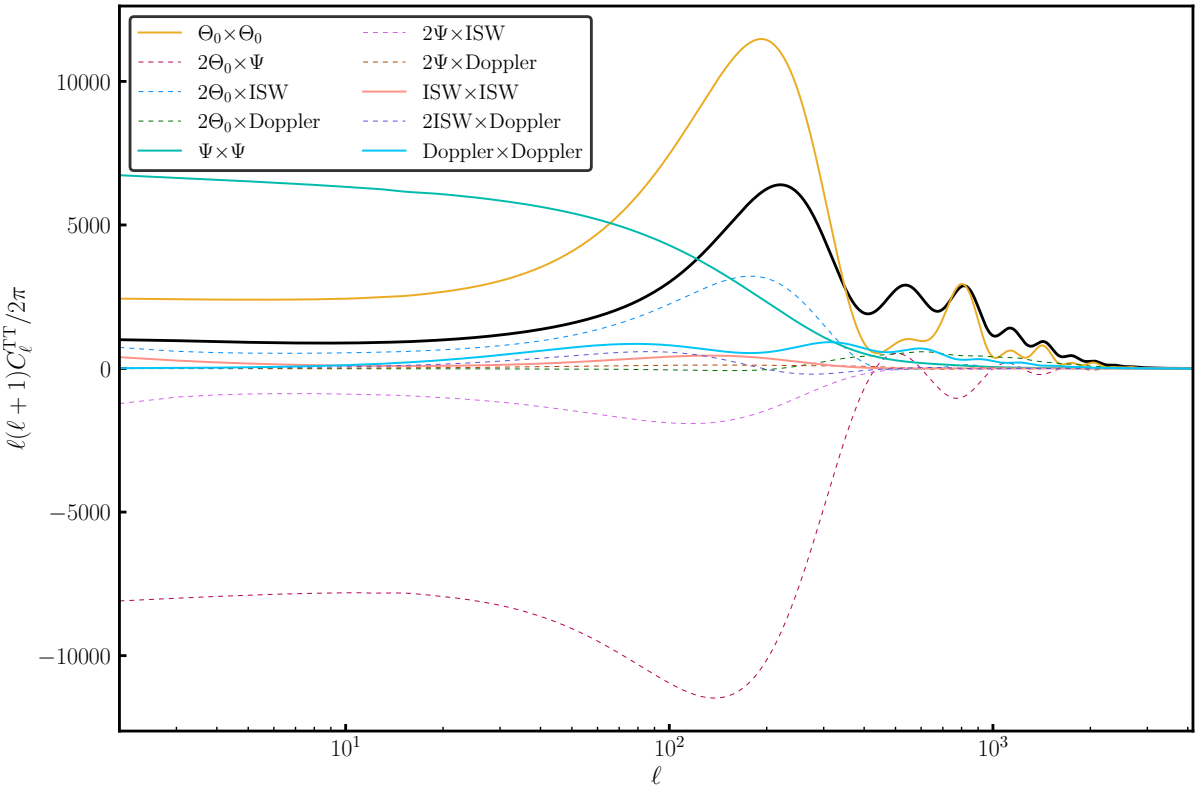

Figure 1.5: The figure shows the CMB temperature power spectrum decomposed according to the different terms of Eq. (1.69). Correlations are shown as dashed lines and have a non-negligible contribution to the total TT power spectrum (solid black line).

that most of the photons that we observe today in the CMB radiation originated from a last scattering surface located around z_*.

The fundamental equation of CMB anisotropies can then be obtained by expanding the integral (1.66)

$$\begin{aligned}\Theta_l(k,\eta_{\rm obs}) = &\int_0^{\eta_{\rm obs}} d\eta\, g(\eta)\left[\Theta_0(k,\eta)+\Psi(k,\eta)\right] j_l\left[k(\eta_{\rm obs}-\eta)\right] \\ &-\frac{i}{k}\int_0^{\eta_{\rm obs}} d\eta\, g(\eta) v_b(k,\eta)\frac{d}{d\eta} j_l\left[k(\eta_{\rm obs}-\eta)\right] \\ &+\int_0^{\eta_{\rm obs}} d\eta\, e^{-\tau}\left[\Psi'(k,\eta)-\Phi'(k,\eta)\right] j_l\left[k(\eta_{\rm obs}-\eta)\right].\end{aligned} \tag{1.69}$$

The first term is the contribution of the monopole and the gravitational Doppler shift to the observed anisotropy. We can note that since g is peaked around $z = z_*$, this first term is well approximated by $\left[\Theta_0(k,\eta_*)+\Psi(k,\eta_*)\right] j_l\left(k(\eta_{\rm obs}-\eta_*)\right)$. Thus, the monopole and gravitational Doppler shift evaluated at last scattering contribute directly to the observed anisotropy once free streamed. The second line can be seen as a Doppler effect due to the baryon fluid velocity. Once again, if we assume the visibility function to be a delta function, this term shows that the baryon

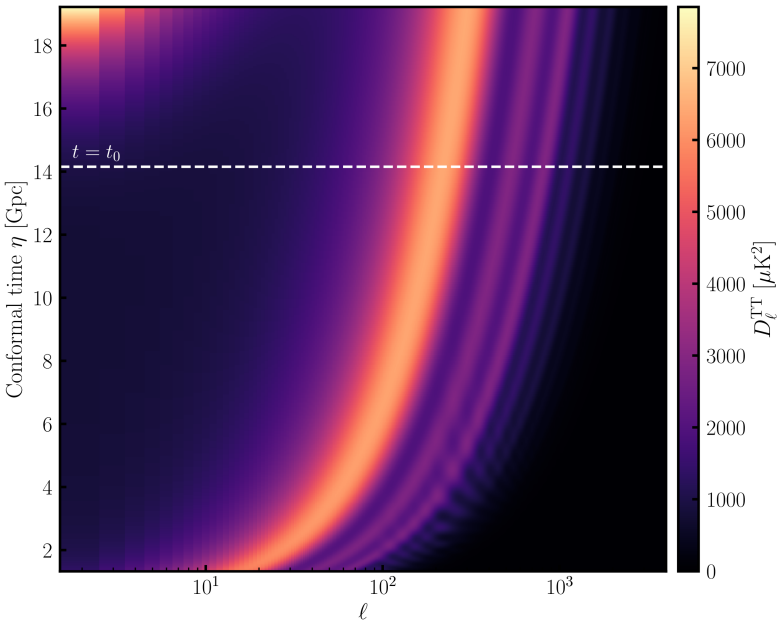

Figure 1.6: Evolution of the CMB temperature power spectrum as a function of the conformal time η (y-axis). The x-axis represents the multipole ℓ which encodes the angular scale. The peaks progressively shift towards smaller scales due to free-streaming. We also observe an increase of the ISW effect in the top left corner (in the future).

velocity at last scattering — which is proportional to the dipole at zeroth order — contributes directly to the observed anisotropy. The last line encodes the Integrated Sachs-Wolfe effect that takes into account the time variation of the gravitational potentials in which the photons are travelling. Figure (1.5) displays the different contributions to the temperature power spectrum as expressed in Eq. (1.69).

Figure (1.6) shows the evolution of the CMB temperature power spectra D_ℓ as a function of the observer conformal time η (y-axis). First, at large scales (low multipoles ℓ) we see an increase in the power spectrum with conformal time due to the ISW effect. The other particular feature that we see is the shift of the acoustic peaks towards smaller scales. This can easily be seen by looking at the first acoustic peak (the brightest in the figure).

The photon temperature perturbation $\Theta(\vec{k}, \hat{p}, \eta_0)$ can be expressed as a function of the primordial curvature perturbations via the transfer function $\mathcal{T}(\vec{k}, \hat{p}, \eta_0) = \Theta(\vec{k}, \hat{p}, \eta_0)/\mathcal{R}(\vec{k})$. Boltzmann codes such as CAMB [10], [11] or CLASS [12] usually solve for the transfer function of the different species to get the associated power spectra. As an example, the predicted temperature power spectrum as observed at time t_0 can be written as

$$C_\ell^{TT} = \frac{2}{\pi} \int_0^\infty dk\, k^2 P_{\mathcal{R}}(k) |\mathcal{T}_\ell^T(k)|^2, \tag{1.70}$$

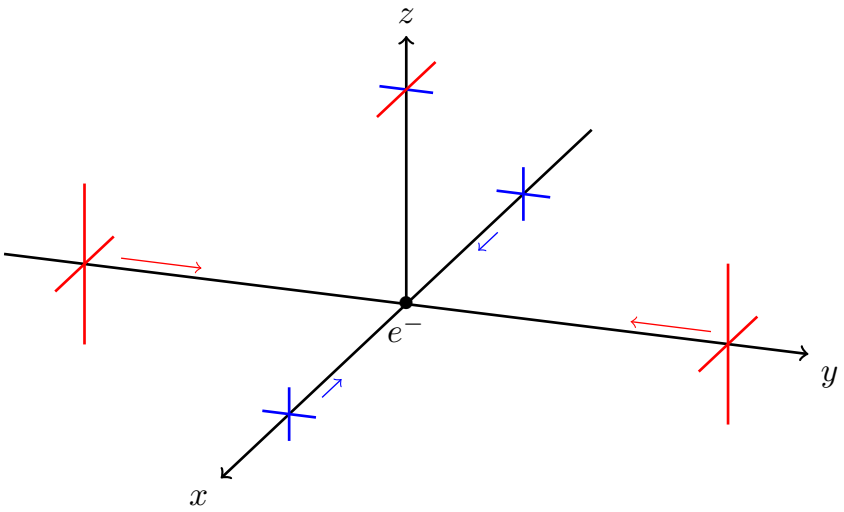

Figure 1.7: Schematic view of the mechanism that produces polarisation from Compton scattering in the primordial Universe. The electron at the center of the frame sees a quadrupolar photon temperature distribution around him (a hot direction along the y-axis and a cold one along the x-axis). The outgoing photon (along the z-axis) is polarised even if incoming light is not.

where $\mathcal{T}_\ell$ are the coefficients in the Legendre polynomials expansion of the transfer function.

1.3.4. Polarisation

For simplicity, the previous derivation ignores polarisation anisotropies but the cosmic microwave background is a polarised radiation, whose polarisation is sourced by temperature anisotropies in the primordial plasma. The main interaction occurring at early times is the Thomson scattering photons on free electrons and is expected to produce polarisation in the presence of temperature anisotropies.

Figure (1.7) explains a possible mechanism to produce polarisation. An electron, here at the center of the frame, sees photon temperature anisotropies around him. Two photons coming from the x and y directions will scatter on this free electron and transmit a polarisation perpendicularly to the z-axis. The observer will see photons travelling along the z-axis. For the monopole temperature Θ_0, the photons from every directions have a similar temperature, and therefore the outgoing photon will not be polarised. The same applies for the dipole anisotropy Θ_1 : photons coming from two opposite directions (e.g. x and $-x$) will have different temperatures but these differences will average and the outgoing photon will be unpolarised. What is sketched in Fig. (1.7) is that the quadrupole temperature anisotropy Θ_2 can produce a polarised signal. It has been shown in the litterature (in particular in Ref. [13]) that the Boltzmann equation for polarisation anisotropies is

$$\partial_\eta \Theta_P + ik\mu\Theta_P = -\partial_\eta \left(-\Theta_P + \frac{1}{2}\left[1 - \mathcal{P}_2(\mu)\right]\left[\Theta_2 + \Theta_{P0} + \Theta_{P2}\right] \right), \tag{1.71}$$

where $\mathcal{P}_2(\mu) = (3\mu^2 - 1)/2$ is the second order Legendre polynomial. This equation shows that

polarisation is sourced by the temperature quadrupole but also by the polarisation of incident light (our simplistic scheme depicted in Fig. (1.7) does not take into account this source of polarisation). A consequence of including polarisation is that the equation of scalar temperature perturbations (1.42) is modified as follows

$$\partial_\eta \Theta + ik\mu\Theta + \partial_\eta \Phi + ik\mu\Psi = -\partial_\eta \tau \left(\Theta_0 - \Theta + \mu v_b - \frac{1}{2}\mathcal{P}_2(\mu) \left[\Theta_2 + \Theta_{P0} + \Theta_{P2} \right] \right). \tag{1.72}$$

The mechanism described above is sourced by scalar perturbations in the photon distribution and induces polarisation patterns imprinted in the CMB radiation called ***E-modes***. Perturbations to the metric — or tensor perturbations — are also able to generate a polarised signal, the primordial ***B-modes*** that have not been detected yet. These tensor perturbations, or primordial gravitational waves, may be produced by inflation. Detecting B-modes would be highly constraining on the different inflation models and is a main science goal for future CMB surveys such as Simons Observatory [14], CMB-S4 [15], [16] and LiteBIRD [17].

1.3.5. Secondary anisotropies

Anisotropies observed today $\theta(\vec{x}_0, \hat{n}, t_0)$ are not exactly given by the free streaming of temperature perturbations from the last scattering surface to us. On their path to us, photons may interact with some particles or be deflected due to gravitational lensing. These are often called ***secondary anisotropies***, in the sense that they are not directly sourced by physics at the epoch of last scattering.

Integrated Sachs-Wolfe effect

A first example of secondary anisotropy is the ISW effect (last term of Eq. (1.69)). This represents the energy loss/gain of a photon travelling in a time-varying potential well. This term is often split into two part ***early*** and ***late*** ISW. The early part is due to the variation of gravitational potentials close to recombination when radiation was not negligible and peaks around $\ell \simeq 100$ (Fig. (1.5)). The late-time part is mainly due to the dark energy component, and enhances the largest scales of the temperature power spectrum. Figure (1.6) illustrates that the late-ISW effect will be higher as dark energy will dominate the energy content of the Universe.

Epoch of reionisation

An important step in the evolution of the Universe is the ***reionisation*** epoch. After recombination, the Universe was filled with neutral hydrogen. When the first generation of stars was formed, they started to ionise the surrounding gas. This phenomenon was not instantaneous, it occurs from $z \simeq 20$ to $z \simeq 6$ such that the Universe today can be considered as fully ionised. Photons from the last scattering surface travelled through this ionised medium and interact with free electrons. One can define the optical depth of reionisation $\tau_{\rm reio}$ such that the observed anisotropies in the photon distribution will be damped and $\tilde{\Theta} \to e^{-\tau_{\rm reio}}\Theta$. In addition to that, reionisation leaves a much more singular imprint on the polarisation anisotropies. A free electron at the epoch of reionisation sees a quadrupolar temperature anisotropy. In the same manner as the primordial polarisation was generated from Thomson scattering, reionisation does contribute to the observed polarisation.

Lensing of CMB photons

Photons from the last scattering surface will also be deflected by the large scale structures along their path towards us. This effect consists in a remapping of the observed anisotropy

$$\tilde{\Theta} = \Theta(\hat{n} + \vec{\nabla}\psi(\hat{n})), \tag{1.73}$$

where ψ is the lensing potential. As shown in Ref. [18], [19] for the flat-sky approximation, an analytical expression for the lensed temperature power spectrum is

$$C_l^{\tilde{\Theta}} \simeq \left(1 - \frac{l^2}{4\pi}\int \frac{dl}{l} l^4 C_l^{\psi}\right) C_l^{\Theta} + \int \frac{d^2\vec{l'}}{(2\pi)^2}(\vec{l'}\cdot(\vec{l}-\vec{l'}))^2 C_{|\vec{l}-\vec{l'}|} C_{l'}^{\Theta}. \tag{1.74}$$

The first term on the right hand side corresponds to a scale dependent amplitude shift with respect to the unlensed power spectrum, while the last term mixes different modes that are otherwise independent. The lensing potential can be reconstructed from the four-point function of the observed temperature fluctuations to get the mass integrated along the line of sight for each direction. This provides a unbiased probe of the underlying matter density field particularly interesting for cross-correlations with large-scale structure studies.

Sunyaev-Zel'dovich effects from galaxy clusters

Galaxy clusters are among the largest gravitationally bound structures known in the Universe, mainly composed of dark matter and hot electron gas ($T \sim 10$ keV $\sim 10^8$ K) that fill the Intra-Cluster Medium (ICM). CMB photons will interact with the electrons of the ICM through inverse Compton scattering : photons passing through the ICM will gain energy. This effect will distort the CMB blackbody spectrum : it will decrease the observed intensity below $\nu_0 \simeq 217$ GHz and increase it above ν_0 [20]. This corresponds to the thermal Sunyaev Zel'dovich (tSZ) effect. An additional effect — the kinetic Sunyaev Zel'dovich (kSZ) — comes from the peculiar velocities of electrons interacting with CMB photons and is not significantly detected yet from CMB primary anisotropies.

1.3.6. Astrophysical foreground signals

In addition to the CMB spectral and spatial distortions discussed in Section (1.3.5), the CMB signal coming from the last scattering surface is contaminated by foreground emissions which are either extra-galactic or originate from our galaxy.

Extra-galactic foregrounds

The main contributions to extra-galactic foregrounds are radio sources and the Cosmic Infrared Background (CIB) [21], [22]. The radio sources contribution arises from the synchrotron radiation emitted from compact regions at the center of galaxies, also known as Active Galactic Nuclei. Dusty star forming galaxies contributes to the CIB by emitting far-infrared radiations that are redshifted along their path to the observer. The radiation emitted from dusty galaxies is weakly polarised compared to the polarisation of radio sources that are the main contamination in the small scale polarisation signal.

Galactic foregrounds

Galactic foreground emission is dominated by the synchrotron radiation at low frequency ($\nu \leq 30GHz$) and by thermal dust emission at high frequency ($\nu \geq 50GHz$). The synchrotron emission comes from the motion of charged particles in the galaxy magnetic field and also produces a polarised signal [23]. Hot diffuse dust in the galaxy emits a gray-body radiation which is also polarised due to the non-spherical shape of dust grains [24], [25]. The cleaning of the galactic dust in CMB maps is one of the main challenges for the detection of polarisation B-modes. The mm-wavelength sky is also contaminated by the interaction of free electrons with free ions (free-free emission) [26] and by molecular emission lines such as transitions of carbon monoxyde CO that was first mapped in Ref. [27].

In order to extract cosmological information from the observed cosmic microwave background, we need to remove these foreground signals or at least account for them in the cosmological parameter estimation process. One can apply component separation methods to extract the CMB signal from the observed sky [25] or model the foregrounds at the power spectra level to perform a joint-fit with cosmological parameters and marginalise over the parameters used to model the foregrounds. In both cases, CMB experiments benefit from having a wide range of frequency bands to break degeneracies between the different components that do not have the same Spectral Energy Distribution (SED).

1.3.7. Mathematical description of the observed signal

At this stage we have studied the behavior of the plasma in the early Universe, prior to recombination. Then we've seen the free streaming process that propagates the photon perturbations from the last scattering surface to the observer. This section will introduce the statistical observables that can be built from observations of the cosmic microwave background anisotropies.

The cosmic microwave background anisotropies are related to the primordial fluctuations — generated by stochastic quantum fluctuations during inflation — via the transfer function. We are not able to predict what our sky will look like but rather we can predict the statistical properties of this radiation as discussed in Section (1.3.3) and compare them with the statistical properties of the observed anisotropies. Let $\Delta T(\vec{x}_0, \hat{n}, t_0)$ be the observed temperature anisotropy today on Earth such that $\Delta T(\vec{x}_0, \hat{n}, t_0) = T(\vec{x}_0, \hat{n}, t_0) - T_0$ where T_0 is the observed monopole. ΔT is a random field on a two dimensional sphere. To characterise a random field, we need to compute its N-point correlators expressed as

$$C_N(\hat{n}_1, ..., \hat{n}_N) = \langle \Delta T(\hat{n}_1) ... \Delta T(\hat{n}_N) \rangle \tag{1.75}$$

where $\langle . \rangle$ stands for the ensemble average, i.e. the average of multiple realisations of the random field. In the particular case of a Gaussian random field, the mean and the two-point correlator are sufficient to fully describe it. For the CMB radiation, we will consider $\Delta T(\hat{n})$ to be a Gaussian random field with zero mean

$$C_1(\hat{n}) = \langle \Delta T(\hat{n}) \rangle = 0 \tag{1.76}$$

$$C_2(\hat{n}_1, \hat{n}_2) = \langle \Delta T(\hat{n}_1) \Delta T(\hat{n}_2) \rangle. \tag{1.77}$$

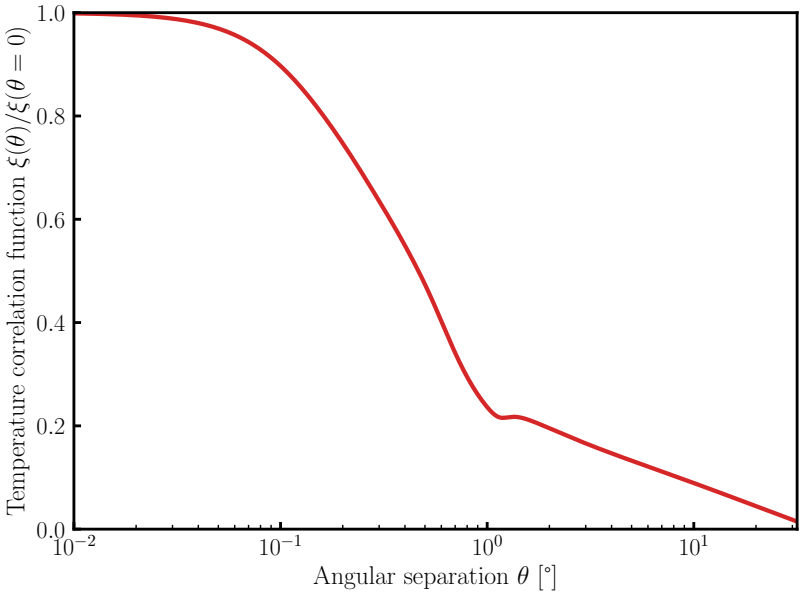

Figure 1.8: Real-space two-point correlation function of CMB temperature anisotropies. Anisotropies are highly correlated at very small scales. Around a typical angular size of around 1 degree, the correlation function shows a bump which corresponds to the size of the sound horizon imprinted in the CMB radiation.

Even though we are looking at anisotropies, the next assumption about the random field will be ***statistical isotropy***. It implies that the two-point correlation function defined in Eq. (1.77) depends only on the angle between the two directions $\hat{n}_1$ and $\hat{n}_2$ such that

$$C_2(\hat{n}_1, \hat{n}_2) = \tilde{C}_2(\theta) \quad \text{where} \quad \cos(\theta) = \hat{n}_1 \cdot \hat{n}_2. \tag{1.78}$$

The angular two-point correlation function of temperature anisotropies is displayed in Fig. (1.8) on which we see a bump around 1 degree corresponding to the sound horizon in the primordial plasma. We rarely use the real space correlation for CMB analysis. In practice we use a more convenient way of describing ΔT by expanding it on a spherical harmonics basis.

$$\Delta T(\hat{n}) = \sum_{\ell=1}^{\infty} \sum_{m=-\ell}^{m=\ell} a^T_{\ell m} Y_{\ell m}(\hat{n}), \tag{1.79}$$

where ℓ is the angular multipole (corresponding roughly to an angular scale $\theta = \pi/\ell$, and the $Y_{\ell m}$ functions are the spherical harmonics. It is straightforward that the coefficient of the spherical harmonics decomposition $a^T_{\ell m}$ have zero-mean such as the temperature anisotropy. The two-point correlation function in harmonic space, or ***power spectrum*** can be written as

$$C_2(\ell, \ell', m, m') = \langle a^T_{\ell m} a^{T*}_{\ell' m'} \rangle = \delta_{\ell\ell'} \delta_{mm'} C^{TT}_{\ell}. \tag{1.80}$$

The statistical isotropy translates into a diagonal covariance in harmonic space which is the main advantage of using this representation. The two-point correlation function defined in Eq. (1.78) may be expressed as a function of the angular power spectrum as

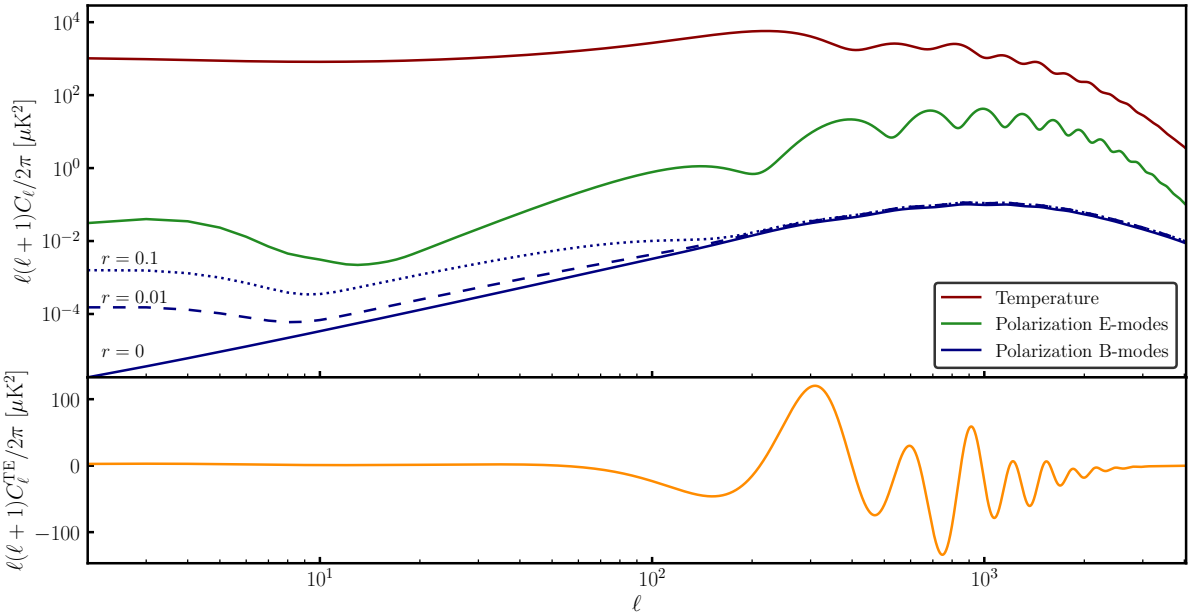

Figure 1.9: CMB temperature and polarisation power spectra for different values of the tensor to scalar ratio r (top panel). The bottom panel displays the TE power spectrum. All other spectra vanish in the ΛCDM model.

$$\tilde{C}_2(\theta) = \sum_\ell \frac{2\ell+1}{4\pi} C_\ell^{TT} \mathcal{P}_\ell(\cos\theta). \tag{1.81}$$

The linear polarisation is described using the two Stokes parameters Q and U that can be combined to get the polarisation E-modes (curl-free) and B-modes (divergence free)

$$Q(\hat{n}) \pm iU(\hat{n}) = \sum_{\ell m} (a_{\ell m}^E \pm i a_{\ell m}^B)_{\pm 2} Y_{\ell m}(\hat{n}). \tag{1.82}$$

Thus, we define the polarisation and temperature-polarisation power spectra as

$$\langle a_{\ell m}^E a_{\ell' m'}^{E*} \rangle = \delta_{\ell\ell'}\delta_{mm'} C_\ell^{EE}, \qquad \langle a_{\ell m}^B a_{\ell' m'}^{B*} \rangle = \delta_{\ell\ell'}\delta_{mm'} C_\ell^{BB}, \tag{1.83}$$

$$\langle a_{\ell m}^T a_{\ell' m'}^{E*} \rangle = \delta_{\ell\ell'}\delta_{mm'} C_\ell^{TE}, \qquad \langle a_{\ell m}^T a_{\ell' m'}^{B*} \rangle = \delta_{\ell\ell'}\delta_{mm'} C_\ell^{TB}, \tag{1.84}$$

$$\langle a_{\ell m}^E a_{\ell' m'}^{B*} \rangle = \delta_{\ell\ell'}\delta_{mm'} C_\ell^{EB}. \tag{1.85}$$

Practically, we have access to only one realisation of the CMB signal and are not able to compute an ensemble average $\langle\cdot\rangle$. In order to estimate power spectra with only one realisation of the sky, we use angular averages such that

$$\hat{C}_\ell^X = \frac{1}{2\ell+1} \sum_m a_{\ell m}^X a_{\ell m}^{X*} \tag{1.86}$$

is a unbiased estimator for the true power spectrum C_ℓ^X. The covariance of this estimator is then

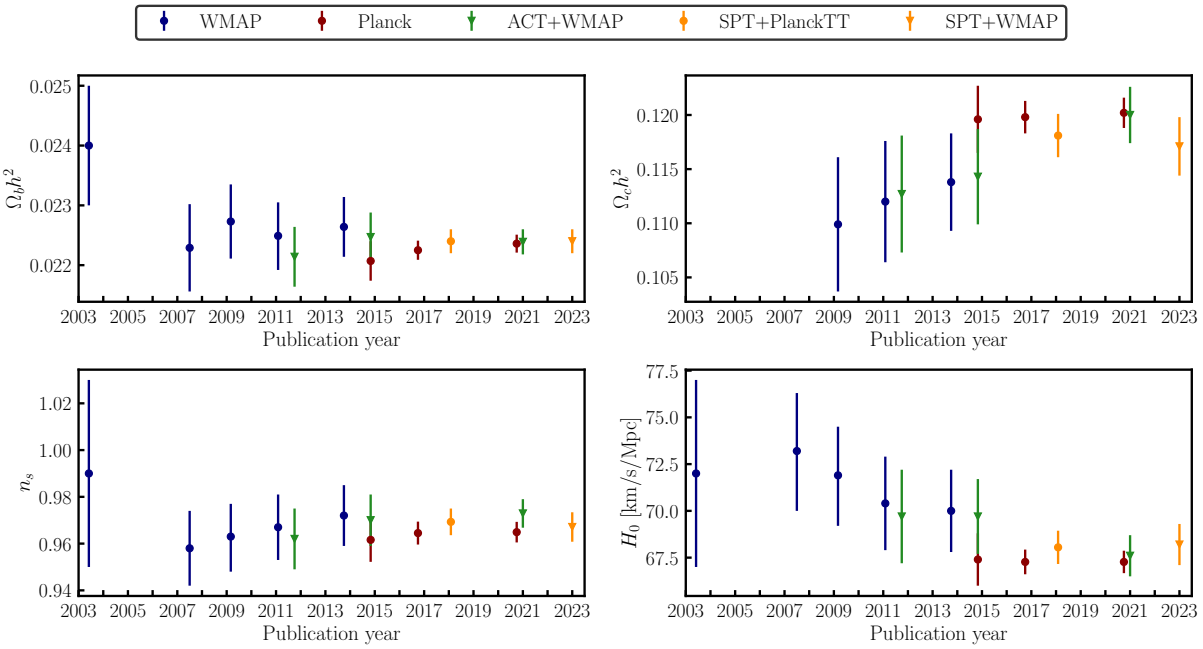

Figure 1.10: Evolution of cosmological parameter constraints derived from the main CMB experiments during the last two decades. This figure compiles results from WMAP ([28]–[32]), Planck ([8], [33], [34]), ACT ([35]–[37]) and SPT ([38], [39]). Constraints derived from ground-based telescopes are shown for a combination of WMAP or Planck temperature in the case of SPTPol and are therefore not fully independent.

$$\mathrm{cov}(\hat{C}_\ell^X) = \langle (\hat{C}_\ell^X)^2 \rangle - (C_\ell^X)^2 = \frac{2}{2\ell+1}(C_\ell^X)^2. \tag{1.87}$$

Note that we have considered a noise-free estimation of the power spectrum here and we got a non-zero covariance term well known as the ***cosmic variance***.

Figure (1.9) displays the lensed power spectra that are relevant in the context of ΛCDM that predicts vanishing TB and EB spectra. Note that polarisation — and in particular B-modes polarisation — is several order of magnitudes lower than temperature, which constitutes an observational challenge for future experiments to get a statistically significant detection of this spectra.

1.4. Observational constraints

1.4.1. Cosmological constraints from the CMB

The ΛCDM model can be described using a minimal set of parameters : the baryon density $\Omega_b h^2$, the cold dark matter density $\Omega_c h^2$, the expansion rate at present time H_0 as well as parameters describing the amplitude and shape of the primordial power spectrum A_s and n_s. In the case of the CMB, we have seen that the observed photons were re-scattered during reionisation, we then need to use the reionisation optical depth τ_{reio} to account for this effect.

At first order, $\tau_{\rm reio}$ and A_s will modulate the amplitude of CMB power spectra by a factor of $A_s e^{-2\tau_{\rm reio}}$. Reionisation is also probed from a feature that affects the largest scales of the EE power spectrum — the reionisation bump — that is visible at $\ell < 10$ on Fig. (1.9). The baryon density $\Omega_b h^2$ has three main effects on the power spectra. First, increasing the baryon density implies that the mean free path of photons in the primordial plasma is reduced. Therefore, there will be less damping of the power spectra at small scales. The second effect concerns the sound speed in the primordial plasma that depends directly on the baryon-to-photon ratio $R(\eta)$. Increasing the baryon density gives intertia to the plasma and reduces the sound speed as well as the sound horizon at recombination resulting in a shift of the acoustic peaks. Finally, the baryon density also rules the relative amplitude of odd and even acoustic peaks due to the fact that the plasma is heavier when there are more baryons. Dark matter interacts only gravitationally with the baryon-photon fluid. The main effect of increasing the dark matter density $\Omega_c h^2$ is to reach matter-radiation equality earlier in the evolution of the Universe which reduces the early-ISW effect (gravitational potentials are constant during matter domination). Figure (1.10) displays the constraints obtained from CMB anisotropies as a function of time for different experiments.

The Wilkinson Microwave Anisotropy Probe (WMAP) satellite launched in 2001 has provided a measurement of the TT power spectrum from the largest scales to the third acoustic peak as well as a measurement of the TE power spectrum [40]. The five data releases [28]–[32] have provided strong constraints on the cosmological parameters as shown in Fig. (1.10). In particular, WMAP has measured the reionisation optical depth with an increasing sensitivity, from $\tau_{\rm reio} = 0.17^{+0.08}_{-0.07}$ for WMAP-Y1 [28] to $\tau_{\rm reio} = 0.089 \pm 0.014$ for WMAP-Y9 [32].

The measurement of CMB anisotropies has been be further improved by the Planck satellite that has measured the full-sky CMB anisotropies in 9 frequency bands from 30 GHz to 857 GHz. The wide frequency range allows to map the galactic dust for astrophysical purposes [24], and provide a good way to apply component separation techniques to extract the different components that compose the observed CMB anisotropies [25], [41]–[43] taking advantage of their different scaling with frequency. The Planck satellite has performed a cosmic variance limited measurement of the temperature power spectrum up to $\ell \sim 1600$ [44] revealing the rich structure of the acoustic peaks with an exquisite precision. The measurement of the TT, TE and EE power spectra from Planck have led to extremely precise constraints on the cosmological parameters [8], [33], [34] that are shown in Fig. (1.10). The latest data release of Planck using the TT,TE and EE power spectra has provided a strong constraint on the reionisation optical depth from primary CMB $\tau_{\rm reio} = 0.0544^{+0.0070}_{-0.0081}$ that has been further improved to $\tau_{\rm reio} = 0.057 \pm 0.007$ in Ref [45]. CMB primary temperature and polarisaztion anisotropies measurements from Planck have provided a detailed view of the matter-energy content of the Universe with $\Omega_\Lambda = 0.6834 \pm 0.0084$ and $\Omega_m = 0.3166 \pm 0.0084$. The Planck collaboration has also reconstructed a full-sky map of the CMB lensing that measures the deflection of CMB photons due to the integrated mass on the line of sight [46]–[48], that has been first measured in Ref. [49] using data from the Atacama Cosmology Telescope with a significance of 4σ.

During the last decade, observations of the CMB from space instruments were completed with measurements from the ground. In particular, two instruments are mentioned in Fig. (1.10)

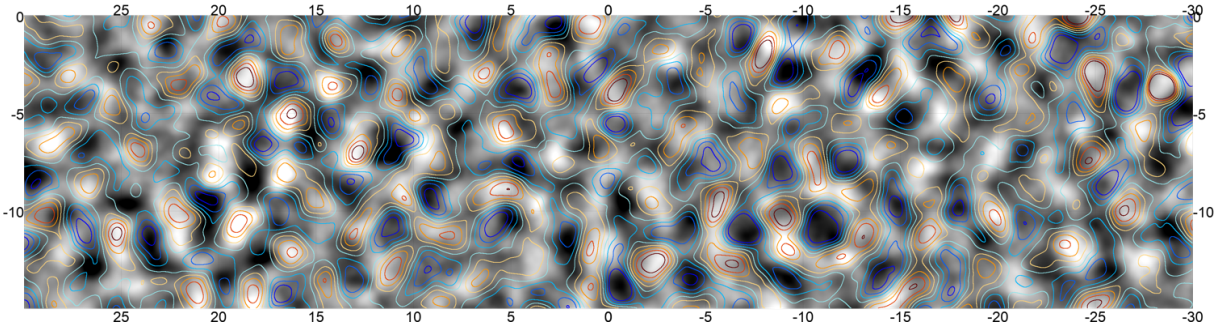

Figure 1.11: 900 deg^2 region of the Wiener filtered gravitational potential map from the ACT DR6 lensing analysis [5]. The distribution of dusty galaxies traced by the cosmic infrared background measured by the Planck satellite is overlaid as contours. Overdensities are displayed in red, while underdensities are in blue. Taken from [5].

the Atacama Cosmology Telescope (ACT) and the South Pole Telescope (SPT). These high-resolution telescopes aim at measuring the polarisation of the CMB at very small scales without being perturbed by the atmosphere that is weakly polarised. These ground-based measurements have allowed for interesting cross-checks with satellite measurements in particular combining with the large scale TT power spectrum from WMAP that is not measurable from the ground due to atmospheric contamination. This dataset combination provides constraints that are competitive and compatible with the Planck ones as shown in Fig. (1.10) for ACT and SPT. A recent analysis on the ACT data collected from 2017 to 2021 (corresponding to the Data Release 6) has produced a high signal to noise reconstruction of the CMB lensing field [5] illustrated in Fig. (1.11) for a 900 deg^2 region of the sky, as well as a 43σ measurement of the lensing power spectrum [4]. Cosmological constraints will be further improved by the upcoming CMB measurements from the Simons Observatory which will operate for a decade in the Atacama desert, followed by the CMB-S4 instruments [15], [16]. These ground-based observatories, as well as the space telescope LiteBIRD [17] are also designed to put strong constraints on the tensor-to-scalar ratio r and potentially detect the imprint of primordial gravitational waves in the CMB.

1.4.2. Constraints from the large-scale structures

Baryonic acoustic oscillations

As illustrated in Fig. (1.12) — which shows the rescaled matter correlation functions $r^2\xi(r)$ as a function of the distance r at different times — in the very early Universe (first two panels) baryons and photons were tightly coupled. At decoupling (the two middle panels) photons decouple from the plasma and baryons start to evolve in gravitational potential wells sourced by dark matter. Therefore, astrophysical objects made of baryonic matter such as galaxies may be used to trace the matter density field. Since dark matter is observable only through its gravitational effect, the distribution of galaxies is a biased tracer of the matter density field such that

$$\delta_{\rm gal}(k,z) = b(k,z)\delta_{\rm matter}(k,z), \tag{1.88}$$

where the bias b may be redshift and scale dependent. The last two panels of Fig. (1.12) highlight a particular feature in the correlation function of the matter density field at late times, which

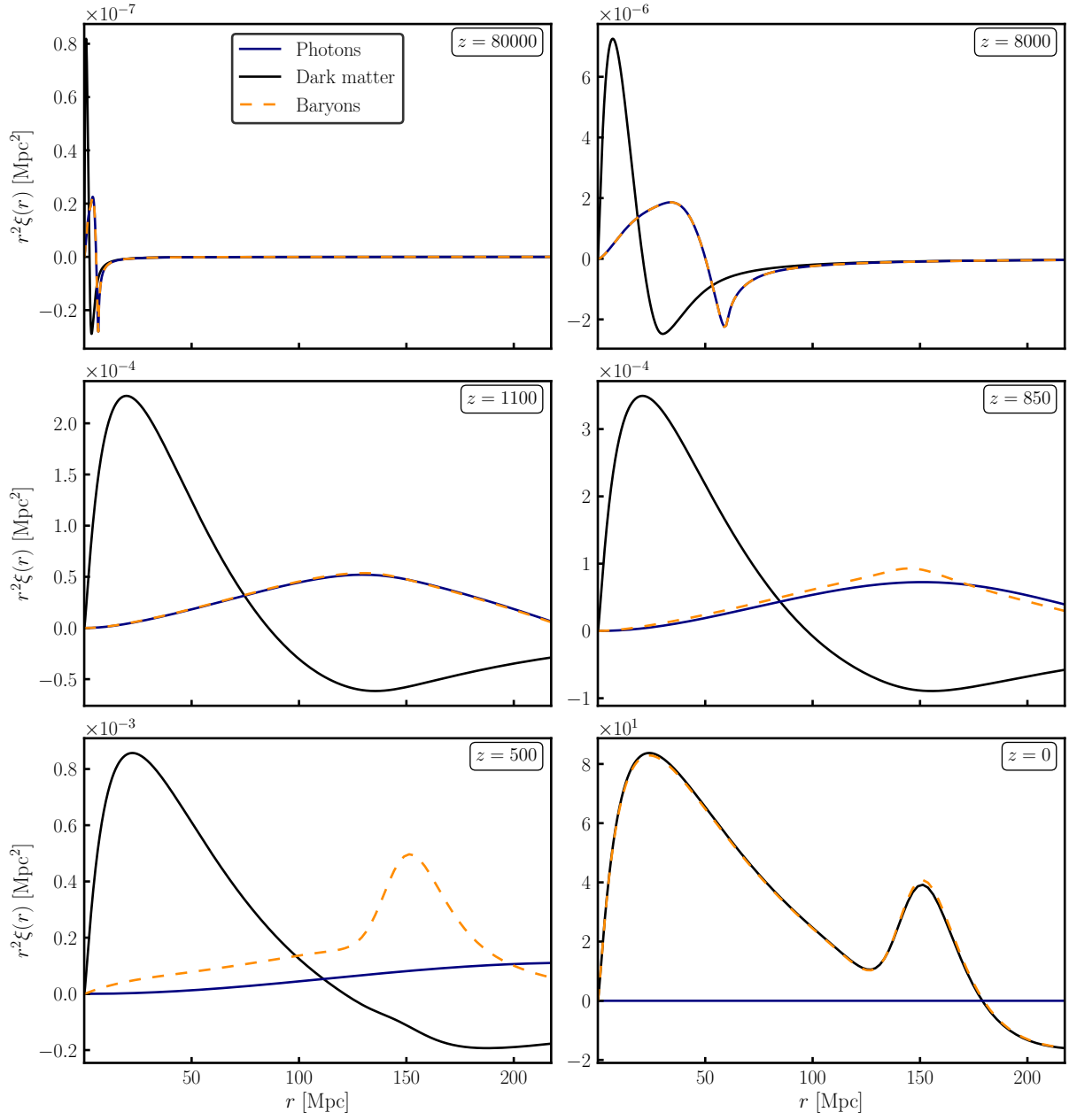

Figure 1.12: This figure displays the 2-point correlation function of different species at different redshift. The two middle panels show the correlation function around decoupling, i.e. the time at which photons and baryons decouple and baryons start to fall into dark matter gravitational potential wells. The last panel (lower right) shows the well-known feature in the distribution of matter : the sound horizon imprinted in the matter distribution with a comoving size of ~ 150 Mpc.

arises from the propagation of sound waves in the primordial plasma and called the Baryonic Acoustic Oscillations (BAO) peak. As a consequence, galaxies may be used to measure the position of this peak in their correlation function (or equivalently in the power spectrum) around $r \simeq 150$ Mpc: this is the aim of BAO studies. Spectroscopic surveys have provided catalogs

containing positions of millions of galaxies from which one can extract a transverse scale $\Delta\theta$ and a radial scale Δz corresponding to the comoving size of the sound horizon at recombination. These two scales are related to the cosmology by the two following relations

$$\Delta z = \frac{r^*}{d_H} \quad \text{and} \quad \Delta\theta = \frac{r^*}{d_M}, \tag{1.89}$$

where d_M is the transverse comoving distance and d_H is defined as the Hubble distance $d_H(z) = c/H(z)$. Measuring the evolution of these two scales as a function of redshift probes the late-time expansion of the Universe. Galaxy surveys are also affected by Redshift Space Distortions (RSD [50]) that arise from the fact that we are measuring distance through redshift measurements that are sensitive to peculiar velocities. The RSD effect depends on the growth rate and thus may be used to probe the growth of structures. The BOSS (Baryon Oscillation Spectroscopic Survey [51]) and eBOSS (extended-BOSS [52]) surveys from the Sloan Digital Sky Survey (SDSS) have mapped the low redshift Universe by providing accurate redshift measurements to extract the BAO scale from the distribution of galaxies. Latest BAO measurements from eBOSS [53] have been shown to be very efficient to constrain one-parameter extensions to ΛCDM. In particular, eBOSS BAO measurements alone constrain the spatial curvature to $\Omega_k = 0.078^{+0.086}_{0.099}$, and the combination with Planck temperature and polarisation leads to $\Omega_k = -0.0001 \pm 0.0018$, in excellent agreement with a flat Universe. The combination of CMB anisotropies with BAO measurements is also powerful to measure the dark energy equation of state. Ref. [53] quotes $w = -0.69 \pm 0.15$ for BAO alone. For comparison, Planck 2018 CMB temperature and polarisation measurements yield to $w = -1.58^{+0.16}_{-0.35}$ [8]. The combination of the two datasets tighten the constraint on w and is compatible with the description of dark energy as a cosmological constant $w = -1.034^{+0.061}_{-0.053}$.

The Lyman-α forest

Quasars, or quasi-stellar objects are bright sources whose luminosity is considered to be sourced by the accretion of matter around massive black holes at the center of distant galaxies. They emit a continuous spectrum that will be redshifted to an observer at $t = t_0$. The intergalactic medium contains neutral hydrogen that absorbs photons from a background quasar and creates an absorption line in the quasar spectrum. The set of absorption lines formed from HI Lyman-α absorption ($\lambda_{\mathrm{Ly}\alpha} = 1215.67$ Å in the rest frame of the hydrogen atom) at different redshifts is called the Lyman-α forest. The Lyman-α forest is then a powerful probe of matter density along the line-of-sight. From large surveys such as SDSS and DESI [54], one can reconstruct the 3D correlation function using the Lyα forests to constrain the BAO scales discussed above [55]. One can also take advantage of the high resolution along the line-of-sight to measure the one-dimension lyman alpha power spectrum [56], [57], highly sensitive to cosmological parameters such as the sum of the neutrino masses which damp the small scale Ly-α power spectrum. Spectroscopic surveys also allows to do tomography by reconstructing the 3D matter density field from the Lyman-α forests [58].

Galaxy weak lensing measurements

Additionally, photometric surveys such as the Kilo-Degree Survey (KiDS [59]), the Dark Energy Survey (DES [60]) and the Hyper Suprime-Cam (HSC [61]) have used the weak lensing of background galaxies from foreground structures to constrain cosmology. The idea is that although

individual galaxies are not spherical, the average intrinsic shape that we see should be circular. Therefore, correlation in the alignments of local galaxies should be attributed to the deviation of light due to the structures between the observer and the observed galaxy. The weak lensing observable is called the cosmic shear γ. From a set of galaxy positions and a measurements of their ellipticity, one can define three different quantities : the shear correlation function $\langle\gamma\gamma^*\rangle$, the galaxy clustering correlation function $\langle\delta_g\delta_g\rangle$ and the cross-correlation between galaxy positions and shear measurements $\langle\gamma\delta_g\rangle$. Cosmological constraints derived from a combination of these three probes are called 3×2pt analyses. These analyses are able to constrain the matter density Ω_m as well as the late-time evolution of the Universe (through the dark energy equation of state). It also allows to constrain the normalisation of the matter power spectrum described by the parameter σ_8 which corresponds to the amplitude of linear matter fluctuations in a sphere of radius $8h^{-1}$Mpc such that

$$\sigma_8(z) = \frac{1}{2\pi^2}\int dk\; k^2 P_{\rm lin}(k,z)|W_{8h^{-1}{\rm Mpc}}(k)|^2, \tag{1.90}$$

where $W_{8h^{-1}{\rm Mpc}}$ is the Fourier transform on a spherical top hat function [62]. A recent analysis from the KiDS collaboration [63] have constrained $\Omega_m = 0.305^{+0.010}_{-0.015}$ and $\sigma_8 = 0.76^{+0.025}_{-0.020}$ from a combination of KiDS cosmic shear and BOSS galaxy clustering measurements. Additional constraints from the three years data releases of DES [64] and HSC [65], [66] have yielded similar results from the 3×2pt analysis : $\Omega_m = 0.339^{+0.032}_{-0.031}$ and $\sigma_8 = 0.733^{+0.039}_{-0.049}$ for DES-Y3 and $\Omega_m = 0.401^{+0.056}_{-0.064}$ and $\sigma_8 = 0.666^{+0.069}_{-0.051}$. The values of σ_8 derived from weak lensing observations are consistently lower than the one derived from the best-fit cosmology from Planck [8] $\sigma_8 = 0.8120 \pm 0.0073$. DES-Y1 and KiDS analyses have quantified the significance of this difference on the combination $S_8 = \sigma_8\,(\Omega_m/0.3)^{-0.5}$ and found a 2.2σ and 3.1σ respectively. DES-Y3 and HSC-Y3 constraints have been shown to be more consistent with Planck with a difference of 1.5σ amd 1.4σ respectively.

Type IA supernovae

Type IA supernovae constitute an historically important probe in cosmology since it was used in the discovery of the accelerated expansion of the Universe in Ref. [67]. Type IA supernovae can be considered as standard candles : the physical processes involved leads to a constant peak luminosity. Therefore they can be used to estimate distances. However, type IA supernovae provide only relative distance measurements and need to be calibrated to get their absolute distances. The Hubble diagram constructed from a supernovae sample is sensitive to the matter density Ω_m and Ω_Λ that rule the evolution of the late-time Universe. The Pantheon [68] and Pantheon+ [69] samples have compiled supernovae from different surveys in line with what was done in the Joint Light-Curve Analysis (JLA) in Ref. [70]. Latest results from the Pantheon+ analysis are consistent with a flat Universe with $\Omega_m = 0.306 \pm 0.057$ and $\Omega_\Lambda = 0.625 \pm 0.084$. They also constrained the dark energy equation of state $w = -0.90 \pm 0.14$, which is compatible with a cosmological constant.

1.4.3. Measurements of the Hubble constant

In the previous section, we mostly discussed the constraints on dark energy and matter density from different cosmological probes. Another important cosmological parameter is the expansion rate of the Universe at present time H_0. The Hubble constant may be measured in

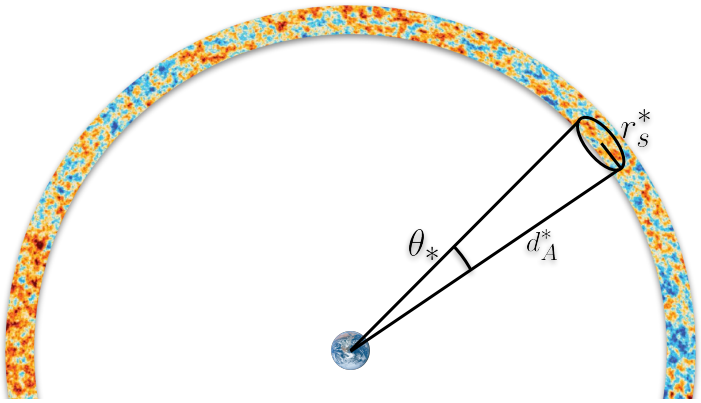

Figure 1.13: Simplistic grahpic representation of an observation of the cosmic microwave background on Earth at the center of the figure. The CMB radiation exhibits a particular angular scale θ_* that corresponds to the physical size of the sound horizon r_s^* at last scattering. d_A^* corresponds to the angular diameter distance between the observer and the last scattering surface, i.e. the proper distance when the photons were emitted.

different ways : using the cosmic microwave background anisotropies, building a cosmic distance ladder with type IA supernovae to be able to measure distances precisely, using the BAO scale as a standard ruler or even using gravitational waves signals detected by laser intereferometers such as LIGO [71] and VIRGO [72]. This section will summarize — in a non-exhaustive way — the different Hubble constant measurements as of 2023. Figure (1.14) displays the H_0 measurements discussed in this section.

Constraining H_0 from the CMB

A measurement of the CMB anisotropies does not constrain directly the Hubble expansion rate and we have to assume a model to get H_0 — which is then a derived quantity. However, we can use the particular angular size imprinted in the CMB radiation — the angular size of the sound horizon — that can be related to the physical size of the sound horizon at last scattering which is a standard ruler that is also used in BAO studies. As illustrated in Fig. (1.13), we can write the angular size of the sound horizon as the ratio of its physical size to the angular diameter distance between us and the last scattering surface at $\eta = \eta_* : \theta_* = r_s(\eta_*)/d_A^{\rm LSS}(\eta_*)$. As a consequence, θ_* can also be expressed as the ratio of the two corresponding comoving distances

$$\theta_* = \frac{r_s(\eta_*)}{d_A^{\rm LSS}(\eta_*)} = \frac{\int_0^{t_*} dt\ c_s(t)/a(t)}{\int_{t_*}^{t_0} dt\ 1/a(t)} = \frac{\int_{z_*}^{\infty} dz\ c_s(z)/H_{\rm early}(z)}{\int_{z_*}^{0} dz\ 1/H_{\rm late}(z)}. \tag{1.91}$$

Now to go further we need to assume a model. With the ΛCDM description of the Universe, the general expression for $H(z)$ is

$$H(z) = \left(\frac{8\pi G}{3}\right)^{1/2} \sqrt{\rho_m^0(1+z)^3 + \rho_r^0(1+z)^4 + \rho_\Lambda}. \tag{1.92}$$

The integral to get the sound horizon depends on Hubble expansion rate in the early Universe — where radiation and matter dominate over the dark energy component such that

$$H_{\rm early}(z) = \left(\frac{8\pi G}{3}\right)^{1/2} \sqrt{\rho_m^0 (1+z)^3 + \rho_r^0 (1+z)^4}. \tag{1.93}$$

As we have seen before, the matter density at present times is well measured from the CMB temperature and polarisation power spectra. The radiation density is measured from the mean temperature of the CMB radiation — with the additional assumption that there are three neutrino species. The size of the sound horizon at last scattering depends also on the sound speed, which is sensitive to the baryon-to-photon energy density ratio (see Eq. (1.60)).

The integral to get the comoving distance to the last scattering surface depends on the Hubble expansion rate at late times, where radiation energy density become negligible,

$$H_{\rm late}(z) = \left(\frac{8\pi G}{3}\right)^{1/2} \sqrt{\rho_m^0 (1+z)^3 + \rho_\Lambda}. \tag{1.94}$$

Given the fact that we are now able to compute r_s and that we have a measurement of θ_*, Eq. (1.91) allows us to solve for ρ_Λ. We can then use this measurement to extrapolate the value of H at redshift $z = 0$.

The tightest constraint on H_0 to date derived from CMB anisotropies was provided by Planck latest data release with $H_0 = 67.36 \pm 0.54$ km/s/Mpc. Independent measurements of the Hubble constant have been performed using data from ground-based telescopes such as the Atacama Cosmology Telescope with $H_0 = 67.9 \pm 1.5$ km/s/Mpc and the South Pole Telescope with $H_0 = 68.3 \pm 1.5$ km/s/Mpc. These constraints are further improved by combining ACT and SPT data with large-scale temperature data from WMAP-Y9. These combinations yield $H_0 = 67.6 \pm 1.1$ km/s/Mpc and $H_0 = 68.2 \pm 1.1$ km/s/Mpc for ACT+WMAP-Y9 and SPT+WMAP-Y9 respectively. Future data releases from ground-based experiments are expected to constrain the Hubble constant with a precision similar to Planck as shown at the end of Chapter 5.

Inverse distance ladder

As discussed before, the BAO scale imprinted in the galaxy distribution is related to the size of the sound horizon at recombination. However, BAO scales constrain the ratios r^*/d_H and r^*/d_M which allows to probe only the late time evolution of the Universe (Ω_m,Ω_Λ). Since r^* is related to the sound horizon, we have seen that it depends only on the baryon density (c.f. Eq. (1.60)). To build a measurement of the Hubble constant from BAO that is independent from the CMB, one can use the baryon density predicted from Big Bang Nucleosynthesis (BBN) calculations along with a measurement of the deuterium-to-hydrogen abundance D/H [73]. The latest BAO measurements from the eBOSS survey combined with the deuterium abundance measured in Ref. [73] yield to $H_0 = 67.35 \pm 0.97$ km/s/Mpc [53], a constraint that is independent from the CMB anisotropies.

Constraints on H_0 based on the matter-radiation equality scale

In addition to the sound horizon, another particular scale is imprinted in the matter power spectrum : the matter-radiation equality scale $k_{\rm eq}$ that define the position of the peak of the matter power spectrum. Ref. [74] has proposed to constrain the Hubble expansion rate from

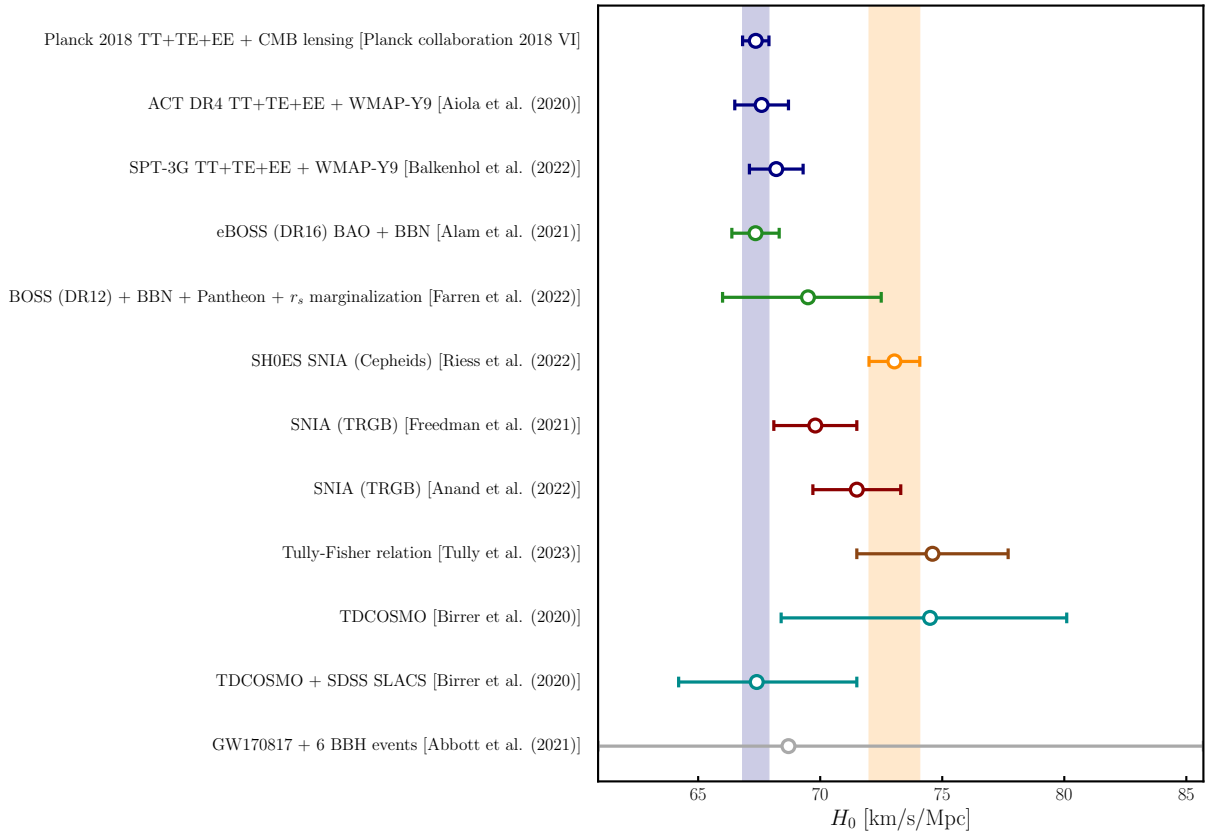

Figure 1.14: Measurements of the Hubble constant H_0 inferred from different probes. Note that these measurements are not all independent. The blue and orange bands correspond to the 1σ error on H_0 derived from Planck PR3 and the SH0ES Cepheids calibrated type IA supernovae respectively.

large-scale structure tracers in a sound-horizon independent way. The easiest way to get r_s-independent constraints is to not calibrate the standard ruler (e.g. BAO constraints without a prior on baryon density from BBN). This independence from r_s comes at a cost : a reduced constraining power. In Ref. [75], the authors have proposed a marginalisation procedure on the sound horizon to reduce the impact of r_s on the measurement while including priors on the baryon density. Using the full-shape BOSS DR12 data [76] with a prior on Ω_b from BBN and marginalising over the sound horizon results in $H_0 = 69.8^{+3.9}_{-4.9}$ km/s/Mpc. This constraint is further improved with the inclusion of a prior on Ω_m from the Pantheon supernovae analysis $H_0 = 69.5^{+3.0}_{-3.5}$ km/s/Mpc.

Type IA supernovae cosmic distance ladder

As described in the previous section, type IA supernovae can be used as distance indicators. Following Ref. [69], the distance modulus is expressed as

$$\mu = m_B + \alpha x_1 - \beta c - M - \delta_{\text{bias}} + \delta_{\text{host}}, \tag{1.95}$$

where m_B and x_1 describe the amplitude and width of the light curve, c is the light curve color,

α and β are stretch and color nuisance parameters and $\delta_{\rm bias}$ and $\delta_{\rm host}$ are corrections terms to account for selection bias and correlation with the host galaxy mass. M is the fiducial magnitude of the supernovae that need to be calibrated to measure absolute distances. Standard calibrators used in the SH0ES analyses [77], [78] are Cepheids. The stars have a variable luminosity with a period T that can be related to their intrinsic luminosity L. The first step is to calibrate this period-luminosity relation using Cepheids in host galaxies that are sufficiently close to us to measure distances using parallax. The second step consists in a calibration of the type IA supernovae fiducial magnitude M in Cepheids host galaxies. In their latest analysis the SH0ES collaboration have measured $H_0 = 73.04 \pm 1.04$ km/s/Mpc that is 4.8σ discrepant with the best estimate of H_0 from the CMB anisotropies measured by the Planck satellite. The absolute magnitude of type IA supernovae may also be calibrated using stars at the Tip of the Red Giant Branch (TRGB). Refs. [79]–[81] have performed the TRGB calibration of the cosmic distance ladder using the Carnegie Supernova Project (CSP [82]) sample resulting in $H_0 = 69.8 \pm 1.7$ km/s/Mpc. An independent TRGB calibration has been done in Ref. [83] for both the CSP and Pantheon samples resulting in $H_0 = 71.5 \pm 1.8$ km/s/Mpc.

Tully-Fisher relation

The Tully-Fisher relation [84] relates the width of the neutral hydrogen HI line observed in a spiral galaxy spectrum with the intrinsic luminosity of the galaxy. This relation can be used to get the relative distance to a galaxy and, as the type IA supernovae, need to be calibrated using TRGB and Cepheids. The *Cosmicflows*-4 program [85] compiles ~ 50000 galaxy distances and constrained $H_0 = 74.6 \pm 0.8$ (stat) ± 3.0 syst. km/s/Mpc with a large systematic uncertainty.

Time delay of lensed quasars

Time-delay cosmography exploits the time delay between images of the same background galaxy around a lens galaxy in the foreground. One can define the time delay distance $D_{\Delta t} = c\Delta t/\Delta\phi$ where ϕ is defined in Ref. [86] and depends on the lensing potential and Δt is the delay measured between the emergence of two images of the background galaxy. The time-delay distance is inversely proportional to the value of H_0 allowing for a direct constraint. Note that this measurement is dependent on the modelling of the lens galaxy. The H0LICOW collaboration have constrained the expansion rate from six gravitationally lensed quasars resulting in $H_0 = 73.3^{+1.7}_{-1.8}$ km/s/Mpc [87]. This measurement have been further refined in Ref. [86], accounting for the uncertainty associated to the lens model and using 7 lensed quasar images among which the six lensed quasars used in the H0LICOW analysis. The TDCOSMO measurement is $H_0 = 74.5^{+5.6}_{-6.1}$ km/s/Mpc. The combination of this set of lensed quasar images with spectroscopic data on a sample of lensed galaxies from SDSS helps to tighten the constraints on the deflector properties and leads to $H_0 = 67.4^{+4.1}_{-3.2}$ km/s/Mpc.

Constraints on H_0 from gravitational waves

The first direct detection of gravitational waves [88] from laser interferometers have opened new prospects for astrophysics and cosmology among which the ability to measure the expansion rate of the Universe [89]. As detailled in Ref. [90], the luminosity distance to the merger system that sourced the gravitational waves is $d_L = (1+z)\chi$ where χ is the comoving distance. This relation is well approximated by $d_L \simeq cz/H_0$ at low redshift $z \ll 1$, and therefore requires

the knowledge of the source luminosity distance and the source redshift to extract H_0. During the first two observation runs of the LIGO and VIRGO instruments, only one binary black hole (BBH) event with an electromagnetic counterpart has been observed (GW170817) resulting in $H_0 = 68.7^{+17.5}_{-8.3}$ km/s/Mpc. [91] Combining this event with six other BBH events results in $H_0 = 68.7^{+17.0}_{-7.8}$ km/s/Mpc, largely dominated by the BBH event with an electromagnetic counterpart.

As of 2023, there is no consensual solution to the $\sim 5\sigma$ tension between the Planck measurement $H_0 = 67.36 \pm 0.54$ km/s/Mpc [8] and the SH0ES measurement $H_0 = 73.04 \pm 1.04$ km/s/Mpc [78]. Different options may be explored to investigate this discrepancy : either these measurements are affected by systematic effects or the tension is a hint in favor of beyond ΛCDM physics.

In this manuscript, we will first address first the hypothesis of systematic effects affecting the value of H_0 inferred from CMB data. Chapter 2 presents the first cosmological constraints obtained from the correlation of T and E modes which is robust against a class of instrumental effects. Then, in Chapter 3, we present a method to spot inconsistencies between temperature and polarisation applied to the latest CMB data. Many theoretical attempts have been performed to solve the Hubble tension (see e.g. Refs. [92], [93] for a more in-depth review). Among the wide range of models available, models that allows to lower the size of the horizon at recombination are promising [93], [94]. Chapter 4 discusses the constraints obtained on the Early Dark Energy model [95], [96] from ground-based CMB telescopes such as ACT and SPT. Finally, Chapter 5 will give an overview of the current status of the ACT sixth data release that will provide new cosmological parameter constraints independent from Planck from small scale CMB anisotropies.

CHAPTER 2

Cosmological constraints from the T-E correlation coefficient

Summary

This chapter is focused on the impact of systematic effects on the inferred cosmological parameters, and in particular on the expansion rate H_0 measured from CMB anisotropies. We have developed an estimator for a quantity that is robust against multiplicative effects : the correlation coefficient of T and E modes. We have built a likelihood based on the correlation coefficient to derive a set of unbiased cosmological parameters. This chapter is adapted from *La Posta et al. Phys. Rev. D 104, 023527 (2021)* [1].

2.1. Impact of systematics on CMB data

In Section (1.4.3), we discussed the current state-of-the art measurements of the local expansion rate of the Universe. In particular, we have highlighted that the measurement of the Hubble constant from CMB anisotropies is $\sim 5\sigma$ away from the local (and model independent) measurement from the SH0ES collaboration [78]. This tension motivates to increase our scrutiny regarding potential instrumental systematic effects that bias our estimation of cosmological parameters. The presence of bias in the cosmic distance ladder data analysis is actively studied, in particular biases coming from supernovae light curves standardisation [97], [98]. Alternative calibrators are also used such as the TRGB calibration method as discussed in Section (1.4.3). In the following, we focus on systematic effects that could affect cosmological parameter estimations from CMB observations with a particular focus on H_0.

2.1.1. Dataset and likelihood

We use the latest Planck data release (PR4) [99]. The maps were produced using the NPIPE processing pipeline that jointly analyses data from Planck High Frequency Instrument (HFI) and Planck Low Frequency Instrument (LFI). Cosmological parameters are estimated using the Planck HiLLiPoP (High-L Likelihood Polarised for Planck) likelihood.[1]. This is a multifre-

[1]made available at https://github.com/planck-npipe

quency likelihood for the Planck cosmology channels : 100, 143 and 217 GHz. The dataset consists of two split maps for each frequency. From these maps, we obtain 15 cross power spectra from which we compute the six cross-frequency spectra used in the likelihood. The foreground model includes galactic dust, CIB, tSZ & kSZ contributions, tSZ-CIB correlation and Poisson-like distributed point source foregrounds. A more detailed description is given in [100]. The likelihood assumes that the TT, TE and EE CMB power spectra follow a Gaussian distribution, which is a good assumption at high multipoles ($\ell > 30$). The likelihood has been tested extensively against the Plik likelihood [101]. This analysis does not use low-ℓ data and use a Gaussian prior on the reionisation optical depth instead $\tau = 0.054 \pm 0.007$ [8].

2.1.2. Bias at the cosmological parameter level

As an illustration, we start by studying the impact of unmodelled systematic effects for a Planck PR4-like dataset using the TT, EE and TE high-ℓ power spectra. We generate a set of biased simulations and fit for the cosmological parameters. The simulations are generated at the power spectra level from the best fit HiLLiPoP cosmology and foreground model, we then use the Planck PR4 covariance matrix to add scatter to the spectra. Fiducial cosmology has been set to $100\theta_{\rm MC} = 1.04065$, $\Omega_b h^2 = 0.02231$, $\Omega_c h^2 = 0.1193$, $\ln(10^{10} A_{\rm s}) = 3.045$, $n_{\rm s} = 0.9619$ and $\tau = 0.0566$.

We include systematics into our simulated dataset such that the observed temperature $\tilde{a}^{\rm T}_{\ell m}$ and polarisation E-modes $\tilde{a}^{\rm E}_{\ell m}$ are given by $\tilde{a}^{\rm T}_{\ell m} = \epsilon^{\rm T}_\ell a^{\rm T}_{\ell m}$ and $\tilde{a}^{\rm E}_{\ell m} = \epsilon^{\rm P}_\ell a^{\rm E}_{\ell m}$. The measured power spectra are

$$\begin{aligned} \tilde{C}^{TT}_\ell &= (\epsilon^{\rm T}_\ell)^2 C^{TT}_\ell \\ \tilde{C}^{TE}_\ell &= \epsilon^{\rm T}_\ell \epsilon^{\rm P}_\ell C^{TE}_\ell \\ \tilde{C}^{EE}_\ell &= (\epsilon^{\rm P}_\ell)^2 C^{EE}_\ell \end{aligned} \tag{2.1}$$

These systematic effects can be constant over multipoles (e.g. polarisation efficiency) or scale-dependant (e.g. transfer functions) and we choose to focus on multiplicative effects in harmonic space which are common for CMB telescopes.

We obtain the posterior distributions of cosmological parameters using the Markov Chain Monte Carlo (MCMC) algorithm implemented in cobaya [102] with the C_ℓ-based HiLLiPoP likelihood. Figure (2.1) displays the distributions of the six standard ΛCDM parameters for a set of different transfer functions. We consider three different kinds of systematics :

a. $\epsilon^{\rm P}_\ell = $ cte, $\epsilon^{\rm T}_\ell = 1$ (Fig. (2.1(a)))

b. $\epsilon^{\rm P}_\ell = \epsilon^{\rm P}(\ell)$, $\epsilon^{\rm T}_\ell = 1$ (Fig. (2.1(b)))

c. $\epsilon^{\rm P}_\ell = 1$, $\epsilon^{\rm T}_\ell = \epsilon^{\rm T}(\ell)$ (Fig. (2.1(c)))

For illustration purpose we choose a transfer function such as

$$\epsilon(\ell) = \begin{cases} \epsilon_{\rm min} & \text{if } \ell < \ell_{\rm min} \\ \epsilon_{\rm min} + \Delta\epsilon \cdot \sin^2\left(\frac{\pi}{2}\frac{\ell - \ell_{\rm min}}{\Delta\ell}\right) & \text{if } \ell_{\rm min} \leq \ell \leq \ell_{\rm max} \\ \epsilon_{\rm max} & \text{if } \ell > \ell_{\rm max} \end{cases} \tag{2.2}$$

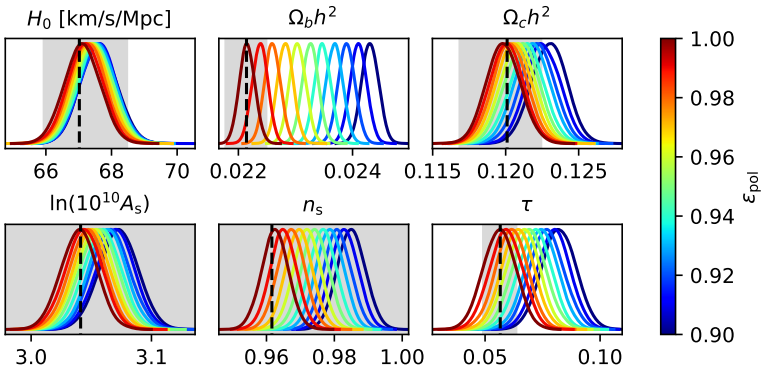

(a) Polarisation efficiency

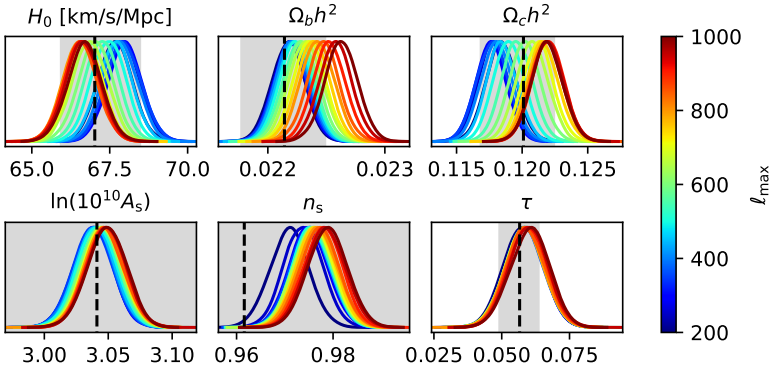

(b) Polarisation transfer function

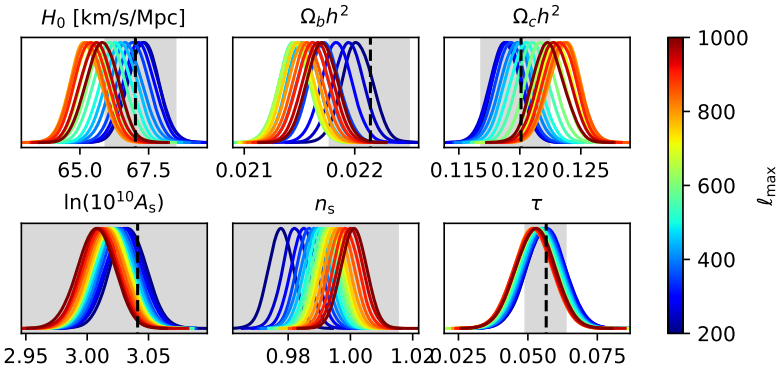

(c) Temperature transfer function

Figure 2.1: 1D posterior distributions of the six ΛCDM parameters using a simulated dataset (TT, TE, EE) biased with a constant polarisation efficiency (a), with a polarisation transfer function (b) and with a temperature transfer function (c). The transfer function model is described in Eq. (2.2). We vary the $\ell_{\rm max}$ parameter from 200 to 1000. The dashed black lines correspond to the fiducial model. Gray bands correspond to $\pm 1\sigma$ $\mathcal{R}_\ell^{\rm TE}$ constraints.

where $\Delta\epsilon = \epsilon_{\rm max} - \epsilon_{\rm min}$ and $\Delta\ell = \ell_{\rm max} - \ell_{\rm min}$ with $\ell_{\rm min} = 100$. The transfer function will smoothly increase from $\epsilon_{\rm min} = 0.95$ to $\epsilon_{\rm max} = 1$ between $\ell_{\rm min}$ and $\ell_{\rm max}$.

Adding an inconsistency between temperature and polarisation leads to significant shifts for all the cosmological parameters for the three different models used in this analysis. The effect is clearly noticeable for baryon density and particularly for the polarisation efficiency case (see Fig. (2.1(a))). Using the biased simulations, we obtain constraints on $\Omega_b h^2$ that are more than 3σ discrepant with the unbiased C_ℓs-derived constraint for $\epsilon_{\rm P} \leq 0.97$. H_0 is particularly affected by a temperature transfer function : the H_0 constraint is shifted towards lower values (see Fig. (2.1(c))). The $\mathcal{R}_\ell^{TE}$ correlation coefficient could therefore be an interesting consistency test, it could help avoiding large bias in our cosmological parameter measurements arising from multiplicative systematic effects.

2.2. The Pearson's correlation coefficient of T and E modes

Measurements of CMB anisotropies may be affected by a wide range of instrumental effects. The measured power spectra that are used to constrain cosmology would therefore be biased leading to a misestimation of the cosmological parameters as shown in Section (2.1.2). Common instrumental effects are multiplicative in harmonic space and may be written as

$$a_{\ell m}^{T,\rm obs} = cF_\ell^T b_\ell^T a_{\ell m}^T \quad \text{and} \quad a_{\ell m}^{E,\rm obs} = c\epsilon F_\ell^E b_\ell^E a_{\ell m}^E, \tag{2.3}$$

where c is an overall calibration amplitude, ϵ accounts for the polarisation efficiency, F_ℓ^X are transfer functions affecting either temperature or polarisation and b_ℓ^X are the temperature/polarisation beams that account for the finite angular resolution of the instrument. Some of these effects are particularly important for ground-based telescopes that apply filters to the maps to remove unwanted signals such as ground pick-up (i.e. reflection of light on nearby objects that create stripy structures in the maps). In principle, we are able to measure and model these effects (e.g. by measuring the beam with planet maps). However, to get rid of residual effects arising from an unprecise modelling of the instrument, one can define the T-E correlation coefficient in harmonic space defined as

$$\mathcal{R}_\ell^{TE} = \frac{\langle a_{\ell m}^T a_{\ell m}^{E*} \rangle}{\sqrt{\langle a_{\ell m}^T a_{\ell m}^{T*} \rangle \langle a_{\ell m}^E a_{\ell m}^{E*} \rangle}}, \tag{2.4}$$

such that $\mathcal{R}_\ell^{TE,\rm obs} = \mathcal{R}_\ell^{TE}$ when considering only multiplicative effects. The correlation coefficient is therefore a powerful consistency test for the presence of multiplicative systematic effects in a dataset. One should note that additive effects such as T-to-E leakage will affect the correlation coefficient that is not designed to handle it. This quantity has already been computed for Planck data in Ref. [101] in which the authors give a geometrical interpretation of the correlation coefficient as a T-E decorrelation angle. Such correlation coefficients have also been used in large-scale structures analyses to estimate the strength of the correlation between the galaxy distribution and the lensing convergence field estimated from the CMB [103]. A more detailed analysis about $\mathcal{R}_\ell^{TE}$ and its statistical properties has been done in Ref. [104]. An estimator

for the correlation coefficient can be obtained using the estimated TT, TE and EE power spectra $\hat{\mathcal{R}}_\ell^{TE} = \hat{C}_\ell^{TE}/\sqrt{\hat{C}_\ell^{TT}\hat{C}_\ell^{EE}}$. Assuming that the measured power spectra is modeled as $\hat{C}_\ell^{XY} = C_\ell^{XY} + \Delta C_\ell^{XY}$, we can write the $\mathcal{R}_\ell^{TE}$ estimator as

$$\hat{\mathcal{R}}_\ell^{TE} = \mathcal{R}_\ell^{TE} \frac{1 + \Delta C_\ell^{TE}/C_\ell^{TE}}{\sqrt{\left(1 + \Delta C_\ell^{TT}/C_\ell^{TT}\right)\left(1 + \Delta C_\ell^{EE}/C_\ell^{EE}\right)}}. \tag{2.5}$$

This estimator is affected by a subdominant bias such that $\langle \hat{\mathcal{R}}_\ell^{TE} \rangle = \mathcal{R}_\ell^{TE}(1 + \alpha_\ell)$. It can be analytically computed at first order by developing Eq. (2.5)

$$\begin{aligned}\alpha_\ell = &\frac{3}{8}\left(\frac{\mathrm{cov}(C_\ell^{\mathrm{TT}}, C_\ell^{\mathrm{TT}})}{{C_\ell^{\mathrm{TT}}}^2} + \frac{\mathrm{cov}(C_\ell^{\mathrm{EE}}, C_\ell^{\mathrm{EE}})}{{C_\ell^{\mathrm{EE}}}^2}\right) \\ &- \frac{1}{2}\left(\frac{\mathrm{cov}(C_\ell^{\mathrm{TT}}, C_\ell^{\mathrm{TE}})}{C_\ell^{\mathrm{TT}} C_\ell^{\mathrm{TE}}} \frac{\mathrm{cov}(C_\ell^{\mathrm{EE}}, C_\ell^{\mathrm{TE}})}{C_\ell^{\mathrm{EE}} C_\ell^{\mathrm{TE}}}\right) \\ &+ \frac{1}{4}\frac{\mathrm{cov}(C_\ell^{\mathrm{TT}}, C_\ell^{\mathrm{EE}})}{C_\ell^{\mathrm{TT}} C_\ell^{\mathrm{EE}}}.\end{aligned} \tag{2.6}$$

We can build an unbiased estimator from the correlation coefficient with $\hat{\mathcal{R}}_\ell^{TE,\mathrm{unbiased}} = (1 - \alpha_\ell)\hat{\mathcal{R}}_\ell^{TE}$. Analogously, we can get an analytical expression for the covariance matrix of the $\mathcal{R}_\ell^{TE}$ estimator from Eq. (2.5). This was derived in Ref. [104] and the generalisation of the expression to a multi-frequency case is given by

$$\begin{aligned}\mathbf{\Gamma}(\mathcal{R}_\ell^{TE}, \mathcal{R}_{\ell'}^{TE}) = &\mathbf{\Gamma}(C_\ell^{TE}, C_{\ell'}^{TE}) \\ &+ \frac{1}{4}\left[\mathbf{\Gamma}(C_\ell^{TT}, C_{\ell'}^{TT}) + \mathbf{\Gamma}(C_\ell^{EE}, C_{\ell'}^{EE})\right] \\ &- \frac{1}{2}\left[\mathbf{\Gamma}(C_\ell^{TE}, C_{\ell'}^{TT}) + \mathbf{\Gamma}(C_\ell^{TT}, C_{\ell'}^{TE})\right. \\ &\left. + \mathbf{\Gamma}(C_\ell^{TE}, C_{\ell'}^{EE}) + \mathbf{\Gamma}(C_\ell^{EE}, C_{\ell'}^{TE})\right] \\ &+ \frac{1}{4}\left[\mathbf{\Gamma}(C_\ell^{TT}, C_{\ell'}^{EE}) + \mathbf{\Gamma}(C_\ell^{EE}, C_{\ell'}^{TT})\right]\end{aligned} \tag{2.7}$$

where $\mathbf{\Gamma}(\mathrm{X}, \mathrm{Y}) = \mathrm{cov}(\mathrm{X}^{\nu_1\times\nu_2}, \mathrm{Y}^{\nu_3\times\nu_4})/(\mathrm{X}^{\nu_1\times\nu_2} \cdot \mathrm{Y}^{\nu_3\times\nu_4})$. Derivation of Eq. (2.7) is developed in appendix (2.A). It is interesting to note that both the bias and covariance of the correlation coefficient do not need any extra computation with respect to a power spectrum analysis. These analytical estimates have been shown to match the bias and covariance estimated from a set of simulations in Fig. 3 of Ref. [104].

2.3. A likelihood for the Pearson's correlation coefficient of T and E modes

Ref. [104] has demonstrated that the correlation coefficient computed from Planck (PR3) data agree with the best-fit cosmology inferred from the power spectra based likelihood. The next step is to directly constrain cosmology from $\mathcal{R}_\ell^{TE}$. Fig. (2.2) shows the variation of the T-E correlation coefficient corresponding to a $\pm 20\%$ variation of the six main ΛCDM parameters with

respect to the latest Planck best-fit [8]. The T-E correlation coefficient is mainly sensitive to the density parameters $\Omega_b h^2$ and $\Omega_c h^2$ and H_0 (or θ_* that is not displayed) that will impact the relative peak amplitudes or the position of the peaks. By definition, $\mathcal{R}_\ell^{TE}$ will be poorly sensitive to parameters that change the overall amplitude of the spectra such as the combination $A_s e^{-2\tau_{\rm reio}}$. We still see a dependence in A_s due to the fact that Fig. (2.2) displays the lensed correlation coefficient and that the smoothing of the peaks induced by the lensing of CMB photons depends on A_s. There is also a dependence in $\tau_{\rm reio}$ through the reionisation bump at low ℓ.

In the following we propose and validate a multi-frequency likelihood for estimating cosmological parameters based on the correlation coefficients. We adapt the HiLLiPoP C_ℓ-based likelihood introduced in section (2.1.1) in order to fit cosmological parameters from the correlations coefficient. We use the multi-frequency covariance matrix given in Eq. (2.7) and assume that the correlation coefficients follow a multivariate Gaussian distribution. The likelihood is defined as follows :

$$\ln\mathcal{L} \simeq -\frac{1}{2}\left(\Delta\mathcal{R}^{\rm vec}\right)^{\rm T}\mathbf{\Xi}^{-1}\left(\Delta\mathcal{R}^{\rm vec}\right) \tag{2.8}$$

where $\mathbf{\Xi}$ is the $\mathcal{R}_\ell^{TE}$ multi-frequency covariance matrix and $\Delta\mathcal{R}^{\rm vec} = \mathcal{R}^{\rm vec,data} - \mathcal{R}^{\rm vec,th}$ is the residual correlation coefficient vector including the 6 cross-frequency spectra. The $\mathcal{R}_\ell^{\rm TE}$ covariance matrix is computed from the Planck PR4 power spectra covariance matrices using Eq. (2.7).

The data vector is computed from the C_ℓs data vector using the unbiased estimator $\hat{\mathcal{R}}_\ell^{\rm TE,unbiased}$. The model for the correlation coefficient is constructed using theoretical and foregrounds TT, EE, and TE power spectra. For a cross frequency $\nu_1 \times \nu_2$, we model the XY power spectra as

$$\begin{aligned} C_\ell^{XY,{\rm th},\nu_1\times\nu_2} = A_{\rm Pl} A^{XY,\nu_1\times\nu_2}[&C_\ell^{XY,{\rm CMB}}(\theta) \\ &+ C_\ell^{XY,{\rm fg},\nu_1\times\nu_2}(\theta_{\rm fg})] \end{aligned} \tag{2.9}$$

where $(X,Y) \in \{T,E\}^2$, $A^{XY,\nu_1\times\nu_2}$ depends on the map calibration parameters and $A_{\rm Pl}$ is a global calibration parameter. $\theta_{\rm fg}$ is the set of parameters describing the foregrounds power spectra amplitudes and θ are the ΛCDM parameters. We give more details about Eq. (2.9) in appendix (2.B).

While the approximation of Gaussianity is excellent for CMB power spectra at multipoles $\ell \geq 30$, it is not straightforward that it holds for a non linear combination of power spectra. However, the Gaussianity of the correlation coefficient has been shown to be a good assumption in the high EE signal-to-noise regime [104]. We check the robustness of this approximation running MCMC chains for the set of simulations described in section (2.1). Figure (2.3) displays the distributions and the mean posterior for each ΛCDM parameters for $N_{\rm sim} = 100$ simulations. Recovered posterior distributions are statistically consistent with expectations. The use of a τ-prior $\tau_{\rm reio} = 0.054 \pm 0.007$ explains the small dispersion of the posterior distributions for this parameter.

2.4. Application to Planck data

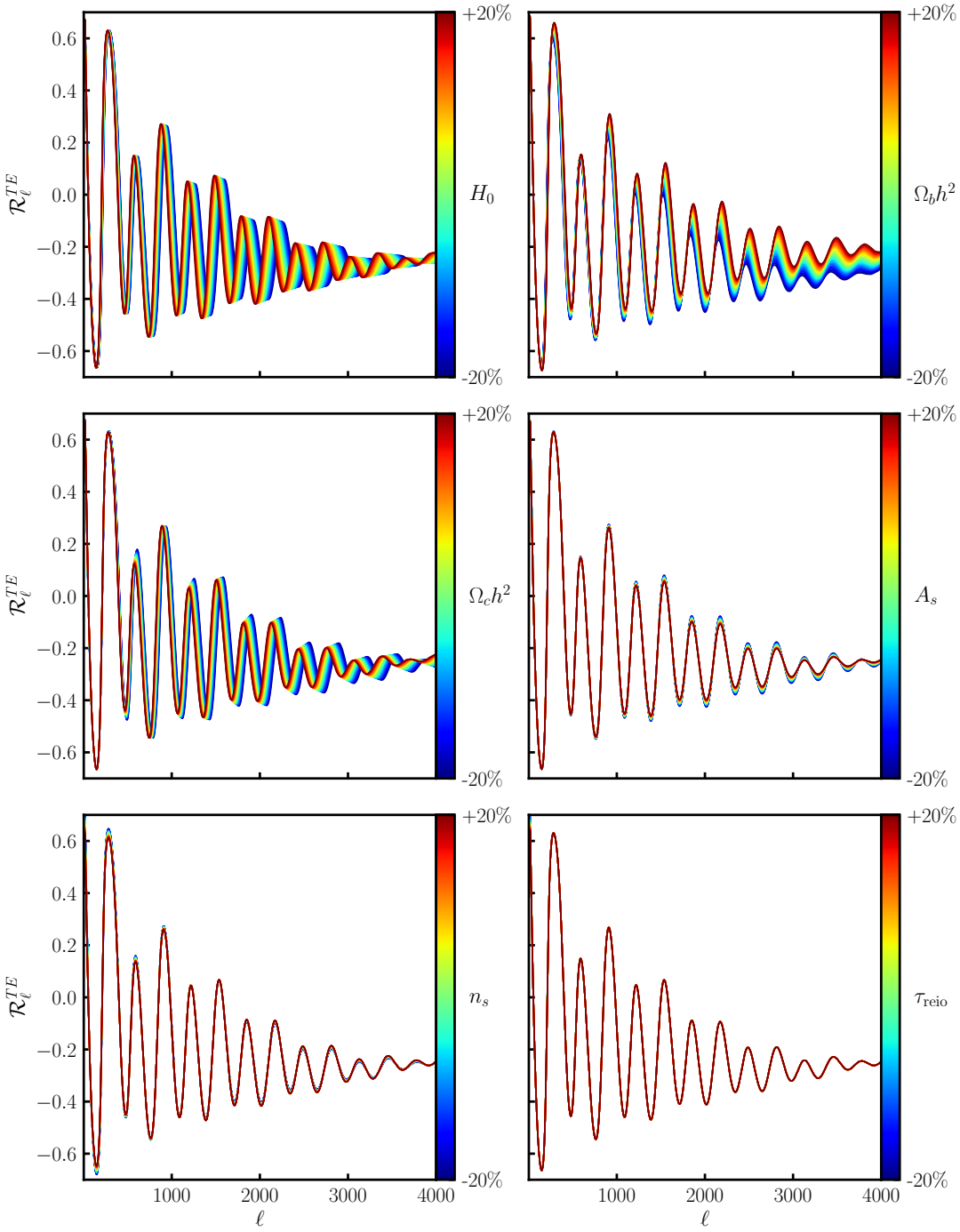

Figure 2.2: Response of the correlation coefficient $\mathcal{R}_\ell^{TE}$ to a 20% variation of the six main ΛCDM parameters with respect to a fiducial cosmology from Planck 2018 constraints [8].

In this section, we estimate cosmological parameters using the $\mathcal{R}_\ell^{\rm TE}$-likelihood on Planck PR4 data. We also compute a CMB-only correlation coefficient, by marginalising over the foreground parameters.

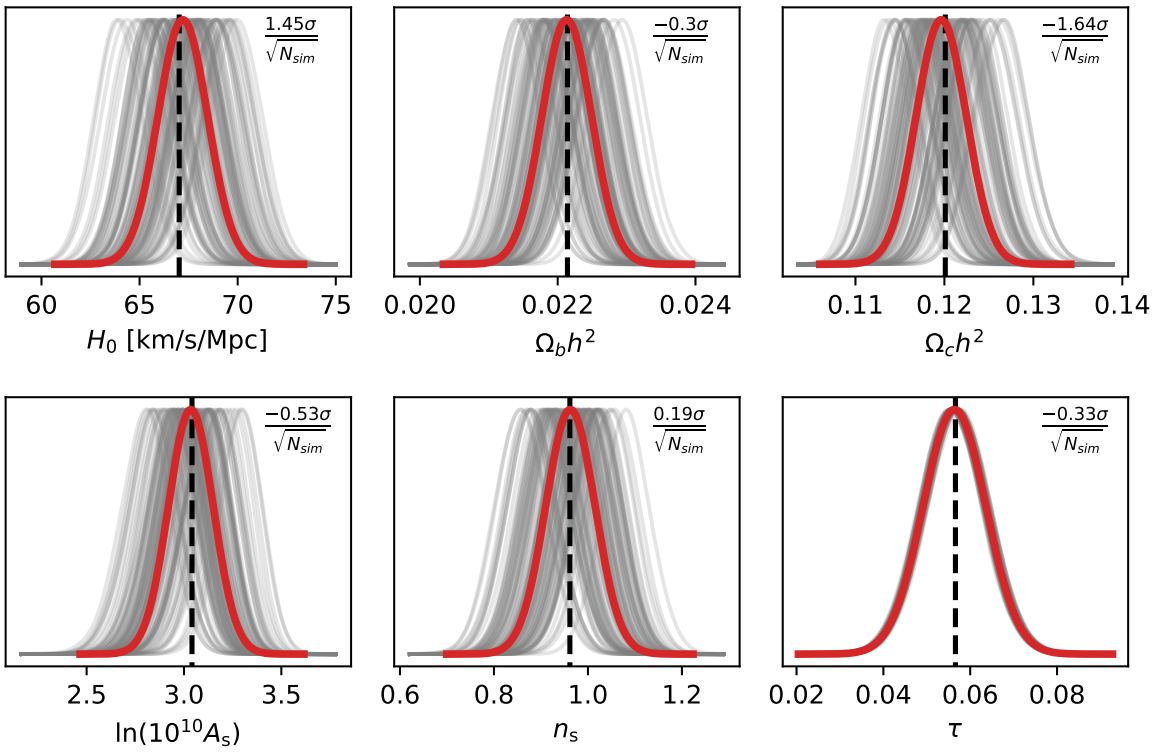

Figure 2.3: ΛCDM parameters constraints for a set of $N_{\rm sim} = 100$ simulations (gray). The average posterior distribution is shown in red. The distance from the average to the input value (in sigma units) is displayed in the top right corner of each panel. Mean posterior distributions are consistent with input values of the simulations

	$C_\ell^{\rm TT}$		$C_\ell^{\rm EE}$		$C_\ell^{\rm TE}$		$\mathcal{R}_\ell^{\rm TE}$	
Frequencies (GHz)	$\ell_{\rm min}$	$\ell_{\rm max}$	$\ell_{\rm min}$	$\ell_{\rm max}$	$\ell_{\rm min}$	$\ell_{\rm max}$	$\ell_{\rm min}$	$\ell_{\rm max}$
100×100	30	1200	30	1000	30	1200	50	1000
100×143	30	1500	30	1250	30	1500	50	1250
100×217	100	1500	400	1250	300	1500	400	1250
143×143	30	2000	30	1750	30	1750	50	1500
143×217	100	2500	400	1750	300	1750	400	1500
217×217	100	2500	400	2000	300	2000	400	1500

Table 2.1: Multipole ranges used for each power spectrum and for the $\mathcal{R}_\ell^{\rm TE}$ correlation coefficient.

2.4.1. Cosmological results

We use COBAYA to sample the likelihoods and derive the posterior of the cosmological and foregrounds parameters. We run MCMC chains on Planck PR4 data using the C_ℓ-likelihood and the $\mathcal{R}_\ell^{\rm TE}$-likelihood. We use wide flat priors for cosmological parameters, and a Gaussian prior on the optical depth of reionisation $\tau = 0.054 \pm 0.007$ [8]. The derivation of the statistical properties of the correlation coefficient (cf. appendix (2.A)) relies on a second order development, which is valid only on scales with a high EE signal-to-noise ratio. We apply cuts in multipole to avoid the

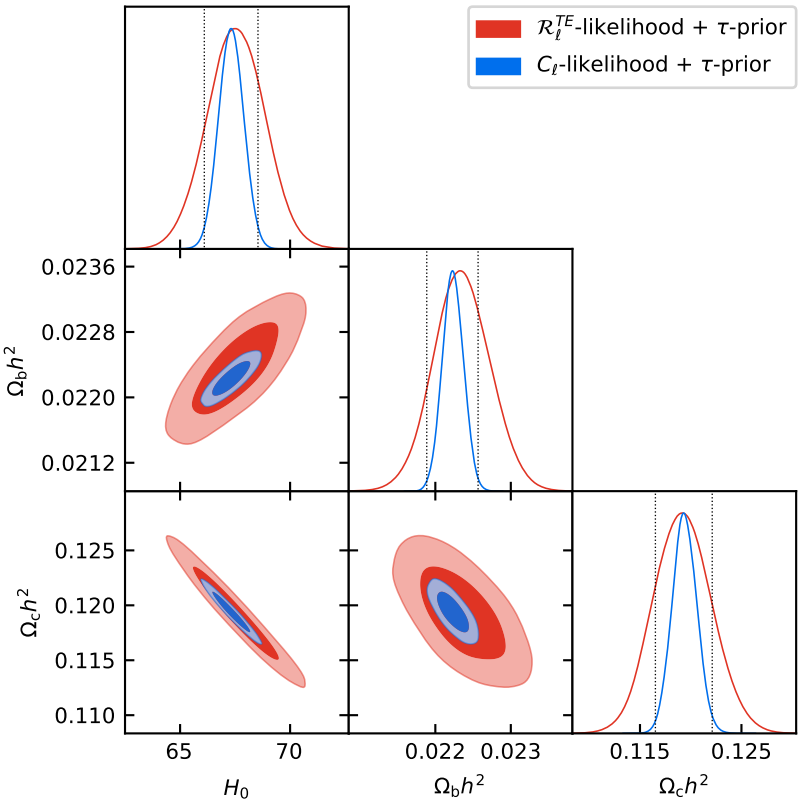

Figure 2.4: 2D posterior distributions for H_0, $\Omega_b h^2$ and $\Omega_c h^2$ constrained using C_ℓ-based likelihood (blue) or the $\mathcal{R}_\ell^{TE}$-based likelihood (red). The expected 1σ scatter between parameters estimated from the two different likelihoods is displayed with gray dotted lines.

foreground-dominated scales (low-ℓ) and noise dominated scales (high-ℓ). The multipole ranges used in the two likelihoods for the different cross-frequency spectra are displayed in table (2.1).

The posterior distributions for H_0, and the density parameters $\Omega_b h^2$ and $\Omega_c h^2$ are shown in Fig. (2.4). We display the expected 1 σ fluctuations between C_ℓ-derived parameters and $\mathcal{R}_\ell^{TE}$-derived ones in gray. This was derived from the set of simulations introduced in section (2.1). Cosmological parameters estimated from the correlation coefficient $\mathcal{R}_\ell^{TE}$ are consistent with the one estimated from power spectra. We do not detect the effect of any multiplicative systematic in the data.

Table (2.2) presents mean values and 1σ errors for the cosmological parameters discussed in this paper. As expected, using $\mathcal{R}_\ell^{\rm TE}$ worsens the constraints on cosmological parameters with respect to the C_ℓ-based likelihood. The $\mathcal{R}_\ell^{\rm TE}$-derived errors on H_0 and $\Omega_b h^2$ are 2.6 times wider than the C_ℓ-derived ones and the error on $\Omega_c h^2$ is 2.3 times larger. The correlation coefficient is poorly sensitive to the parameters describing the shape of the initial matter power spectrum, A_s and n_s. Interestingly, while the amplitude parameter A_s appears to cancel in the ratio of power spectra, it can be measured through the effect of lensing on the power spectra [19]. The posterior

Parameter	$C_\ell^{\rm TT}$, $C_\ell^{\rm TE}$, $C_\ell^{\rm EE}$	$\mathcal{R}_\ell^{\rm TE}$
H_0 [km/s/Mpc]	67.3 ± 0.5	67.5 ± 1.3
$\Omega_b h^2$	0.02233 ± 0.00014	0.02235 ± 0.00037
$\Omega_c h^2$	0.1194 ± 0.0012	0.1192 ± 0.0028
$\ln(10^{10} A_s)$	3.040 ± 0.015	3.098 ± 0.152

Table 2.2: Cosmological parameter constraints (mean values and 1σ errors) derived from the C_ℓ-likelihood and the $\mathcal{R}_\ell^{\rm TE}$-likelihood.

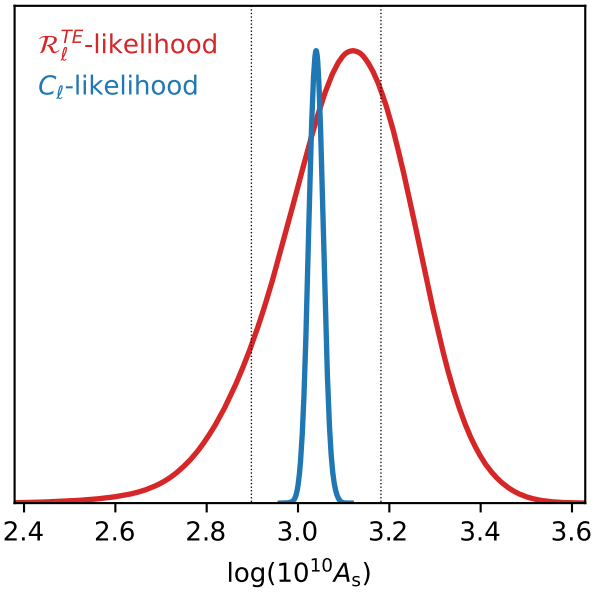

Figure 2.5: 1D posterior distribution for $\log(10^{10} A_s)$ using the C_ℓ-based likelihood (blue) or the $\mathcal{R}_\ell^{\rm TE}$-based likelihood (red). The correlation coefficient constraint is sensitive to A_s only through the effect of lensing on the power spectra.

distribution of $\log(10^{10} A_s)$ is displayed in Fig. (2.5). The $\mathcal{R}_\ell^{\rm TE}$-derived error on $\ln(10^{10} A_s)$ is 10 times larger than the C_ℓ-derived one.

We note that our value of the Hubble parameter $H_0 = 67.5 \pm 1.3$ km/s/Mpc, derived from the correlation coefficient is consistent with other CMB based measurements of H_0. The Hubble parameter we obtain using $\mathcal{R}_\ell^{\rm TE}$ is still 3.1σ and 3.3σ discrepant with the latest measurements from Cepheids-calibrated cosmic distance ladder from Refs. [77], [78] respectively.

2.4.2. CMB-only $\mathcal{R}_\ell^{TE}$

We produce CMB-only power spectra, marginalising over foreground parameters. We follow the method used in [105]. The multi-frequency vector is modelled as

$$C_{\rm b}^{\rm model} = \mathbf{A} \cdot C_{\rm b}^{\rm CMB} + C_{\rm b}^{\rm fg}(\theta_{\rm fg}) \tag{2.10}$$

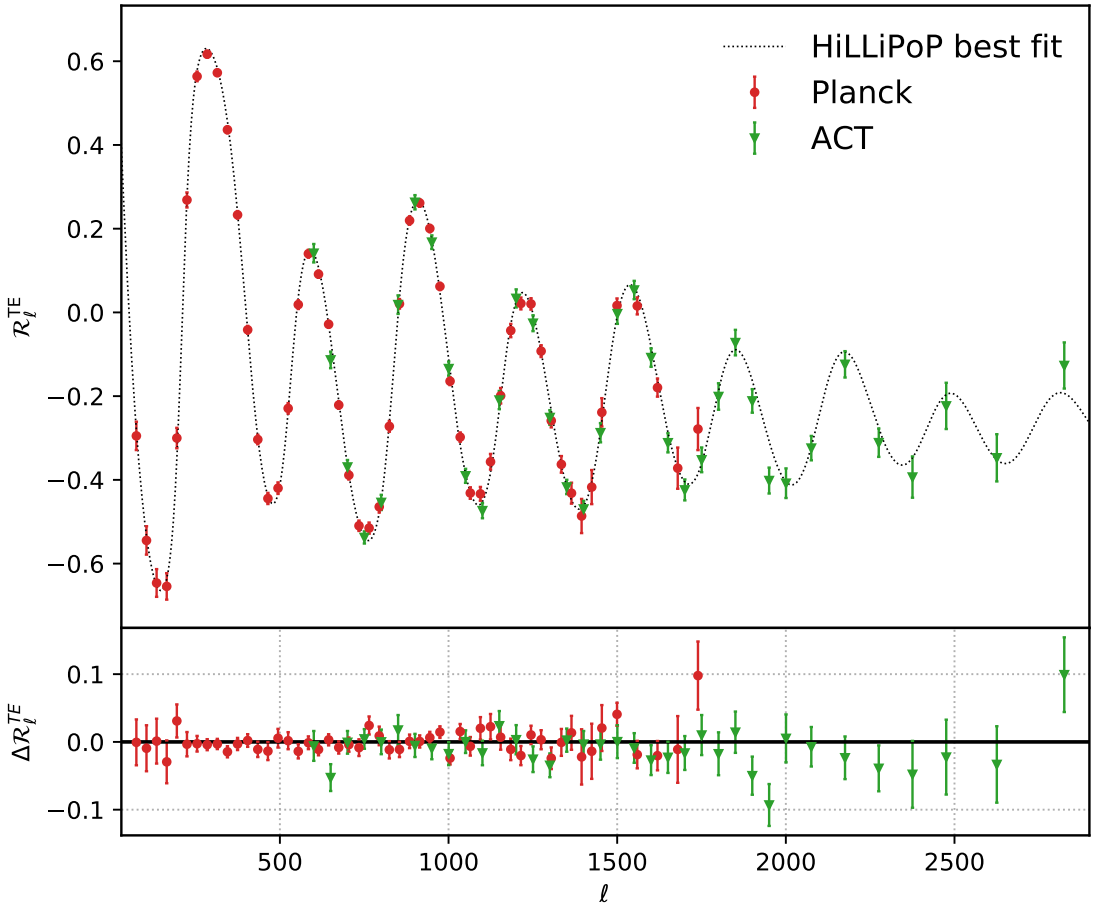

Figure 2.6: (Top) : CMB-only $\mathcal{R}_\ell^{\rm TE}$ correlation coefficient for Planck PR4 data (red) and ACT data (green) after foreground marginalisation. The best-fit correlation coefficient (gray dashed line) is computed with CAMB from the HiLLiPoP C_ℓ-likelihood best fit cosmology — (Bottom) : Residual plot with respect to the binned correlation coefficient best-fit.

with $\mathbf{A}$ a matrix that projects the CMB bandpowers to their corresponding elements in each cross-frequency spectrum, and $C_{\rm b}^{\rm fg}(\theta_{\rm fg})$ the foregrounds power spectra corresponding to a set of foreground parameters $\theta_{\rm fg}$.

Instead of sampling simultaneously CMB bandpowers and nuisance parameters, we split the joint probability distribution $p(C_{\rm b}^{\rm CMB}, \theta_{\rm fg}|\text{data})$ into two conditional probability densities $p(C_{\rm b}^{\rm CMB}|\theta_{\rm fg}, \text{data})$ and $p(\theta_{\rm fg}|C_{\rm b}^{\rm CMB}, \text{data})$. The main advantage here is that the CMB bandpowers sampling is simple because $C_{\rm b}^{\rm CMB}$ follows a multivariate normal distribution with mean $\hat{C}_{\rm b}$ and covariance $\mathbf{Q}$ given by

$$\hat{C}_{\rm b} = [\mathbf{A}^{\rm T}\mathbf{\Sigma}^{-1}\mathbf{A}]^{-1}[\mathbf{A}^{\rm T}\mathbf{\Sigma}^{-1}(C_{\rm b}^{\rm data} - C_{\rm b}^{\rm fg}(\theta_{\rm fg}))] \tag{2.11}$$

$$\mathbf{Q}^{-1} = \mathbf{A}^{\rm T}\mathbf{\Sigma}^{-1}\mathbf{A} \tag{2.12}$$

with $\mathbf{\Sigma}$ the C_ℓs multifrequency covariance matrix. We alternate CMB bandpowers sampling (using the known probability distribution described in Eqs. [(2.11),(2.12)]) and Metropolis-Hastings sampling for the nuisance parameters using a Gaussian likelihood. We then compute the correlation coefficient and its covariance matrix using the CMB-only power spectra and the $\mathbf{Q}$ covariance matrix.

In Fig. (2.6), we compare the CMB-only $\mathcal{R}_\ell^{\rm TE}$ with the best-fit model obtained using the C_ℓ-based likelihood. The correlation coefficient is compatible with the model with $\chi^2/{\rm dof} = 52.2/52$ (PTE = 0.47).

Higher resolution experiments such as Atacama Cosmology Telescope (ACT) bring more information about the correlation coefficient at small scales. We display on Fig (2.6) the ACT CMB-only $\mathcal{R}_\ell^{\rm TE}$, computed from the power spectra provided by the ACT collaboration [106] and publicly available.[2] Before computing the correlation coefficient, we remove points for which the EE SNR is lower than 3. We find that the ACT correlation coefficient is in good agreement with the Planck PR4 best-fit, with $\chi^2/{\rm dof} = 39.0/36$ (PTE = 0.33).

2.5. Conclusion

Given the current context of tensions between early and late Universe measurements, it is important to assess the robustness of the cosmological parameter constraints. In this work, we have studied the impact of remaining multiplicative systematic effects that would have been neglected in the data treatment, resulting in a bias at the power spectra level. We have shown that this kind of bias can significantly shift the cosmological parameter constraints determined from the combination of $C_\ell^{\rm TT}$, $C_\ell^{\rm TE}$ and $C_\ell^{\rm EE}$.

To prevent the cosmological parameter measurements from being biased, we have proposed to use a likelihood based on the Pearson's correlation coefficient $\mathcal{R}_\ell^{\rm TE}$, an observable that is insensitive to multiplicative biases. We have obtained the first constraints on cosmology only from the correlation between T and E modes. We have shown that it gives cosmological parameters that are consistent with other CMB-based measurements. Using $\mathcal{R}_\ell^{\rm TE}$ increases the error on the cosmological parameters with respect to the errors derived from the combination of TT, TE, and EE power spectra. However, we have measured the Hubble parameter $H_0 = 67.5 \pm 1.3$ km/s/Mpc with an associated error which is similar to the error obtained by ground-based CMB experiments such as ACTPol [37]. The correlation coefficient provides a good consistency check on Planck data. We have not observed the effect of any multiplicative bias in Planck PR4 data and we have obtained a value for the Hubble parameter which is still discrepant with late time measurements.

Next generation of ground based CMB experiments such as Simons Observatory [14] or CMB-S4 [15] will produce data with a high EE signal-to-noise ratio for a wide range of multipoles.

[2] https://github.com/ACTCollaboration/

This will allow the computation of $\mathcal{R}_\ell^{\rm TE}$ up to smaller scales, increasing its constraining power and relevance. Ground-based experiments are also typically more affected by transfer functions due to atmospheric and ground pick up filtering. We expect that observables such as $\mathcal{R}_\ell^{\rm TE}$ will provide a strong consistency check on these data.

2.A. Statistical properties of $\mathcal{R}_\ell^{\rm TE}$ estimator

In the high signal-to-noise regime, the correlation coefficient estimator can be developed as :

$$\begin{aligned}\hat{\mathcal{R}}_b^{\rm TE} &= \mathcal{R}_b^{\rm TE}\frac{1+\frac{\Delta C_b^{\rm TE}}{C_b^{\rm TE}}}{\sqrt{\left(1+\frac{\Delta C_b^{\rm TT}}{C_b^{\rm TT}}\right)\left(1+\frac{\Delta C_b^{\rm EE}}{C_b^{\rm EE}}\right)}}\\ &= \mathcal{R}_b^{\rm TE}\left(1+\frac{\Delta C_b^{\rm TE}}{C_b^{\rm TE}}\right)\times\left(1-\frac{1}{2}\frac{\Delta C_b^{\rm TT}}{C_b^{\rm TT}}+\frac{3}{8}\left(\frac{\Delta C_b^{\rm TT}}{C_b^{\rm TT}}\right)^2\right)\\ &\quad\times\left(1-\frac{1}{2}\frac{\Delta C_b^{\rm EE}}{C_b^{\rm EE}}+\frac{3}{8}\left(\frac{\Delta C_b^{\rm EE}}{C_b^{\rm EE}}\right)^2\right)\end{aligned} \tag{2.13}$$

where $\mathcal{R}_b^{\rm TE}$, $C_b^{\rm TT}$, $C_b^{\rm EE}$ and $C_b^{\rm TE}$ are the spectra we want to estimate.

Such an estimator is not an unbiased estimator (i.e. $\langle\hat{\mathcal{R}}_b^{\rm TE}\rangle \neq \mathcal{R}_b^{\rm TE}$), but is affected by a bias term such that : $\langle\hat{\mathcal{R}}_b^{\rm TE}\rangle = \mathcal{R}_b^{\rm TE}(1+\alpha_b)$. The bias term α_b can be easily computed taking the mean value of Eq. (2.13)

$$\begin{aligned}\alpha_b &= \frac{3}{8}\left(\frac{\mathrm{cov}(C_b^{\rm TT},C_b^{\rm TT})}{{C_b^{\rm TT}}^2}+\frac{\mathrm{cov}(C_b^{\rm EE},C_b^{\rm EE})}{{C_b^{\rm EE}}^2}\right)\\ &\quad-\frac{1}{2}\left(\frac{\mathrm{cov}(C_b^{\rm TT},C_b^{\rm TE})}{C_b^{\rm TT}C_b^{\rm TE}}+\frac{\mathrm{cov}(C_b^{\rm EE},C_b^{\rm TE})}{C_b^{\rm EE}C_b^{\rm TE}}\right)\\ &\quad+\frac{1}{4}\frac{\mathrm{cov}(C_b^{\rm TT},C_b^{\rm EE})}{C_b^{\rm TT}C_b^{\rm EE}}.\end{aligned} \tag{2.14}$$

From Eq. (2.13) we can compute the $\mathcal{R}_\ell^{TE}$ covariance matrices defined by

$$\mathrm{cov}(\mathcal{R}_b^{{\rm TE},\nu_1\times\nu_2},\mathcal{R}_{b'}^{{\rm TE},\nu_3\times\nu_4}) = \langle\Delta\mathcal{R}_b^{{\rm TE},\nu_1\times\nu_2}\Delta\mathcal{R}_b^{{\rm TE},\nu_3\times\nu_4}\rangle, \tag{2.15}$$

with $\nu_1\times\nu_2$ and $\nu_3\times\nu_4$ two cross frequencies and $\Delta\mathcal{R}_b^{\rm TE} = \hat{\mathcal{R}}_b^{\rm TE} - \mathcal{R}_b^{\rm TE}$ the deviation to the mean value. $\Delta\mathcal{R}_b^{\rm TE}$ can be expressed analytically (at second order) using Eq. (2.13)

2.B. HiLLiPoP power spectra model

In section (2.1.1) we present the HiLLiPoP C_ℓ-based likelihood. In section (2.3), we construct a $\mathcal{R}_\ell^{\rm TE}$-based likelihood. In this appendix, we explain how the model in Eq. (2.9) is computed.

We work with three frequencies : 100, 143 and 217 GHz (indexed by ν_i, ν_j for $(i,j)\in\{0,1,2\}^2$) and two split maps (indexed by R, S with $(R,S)\in\{A,B\}^2$. We also define X and Y such as $(X,Y)\in\{T,E\}^2$. For two frequencies (ν_i, ν_j) with $j\geq i$ and two maps (R, S), we model the power spectra as

$$C_\ell^{XY,{\rm th},\nu_i^R\times\nu_j^S} = A_{\rm Pl}c^{\nu_i^R}c^{\nu_j^S}\left[C_\ell^{XY,{\rm CMB}}+C_\ell^{XY,{\rm fg},\nu_i\times\nu_j}\right], \tag{2.16}$$

where $A_{\rm Pl}$ is a global amplitude calibration parameter and $c^{\nu_i^R}$, $c^{\nu_j^S}$ are calibration parameters at map level. This set of parameter is sampled in the likelihood as nuisance parameters.

We take the weighted average of cross-map power spectra to compute the cross-frequency power spectra, ignoring the auto power spectra.

$$C_\ell^{XY,{\rm th},\nu_i\times\nu_j} = A_{\rm Pl}\left[\sum_{\substack{(R,S)\in\\ \{A,B\}^2}} w_\ell^{XY,\nu_i^R\times\nu_j^S} c^{\nu_i^R} c^{\nu_j^S}\left(C_\ell^{XY,{\rm CMB}} + C_\ell^{XY,{\rm fg},\nu_i\times\nu_j}\right)(1-\delta_{ij}(1-\delta_{RA}\delta_{SB}))\right], \tag{2.17}$$

where $w_\ell^{XY,\nu_i^R\times\nu_j^S}$ are the weights associated to the $\nu_i^R\times\nu_j^S$ XY power spectrum and δ is the Kronecker delta. We can express Eq. (2.17) as Eq. (2.9) using the following definition

$$A^{XY,\nu_i\times\nu_j} = \sum_{\substack{(R,S)\in\\ \{A,B\}^2}} w_\ell^{XY,\nu_i^R\times\nu_j^S} c^{\nu_i^R} c^{\nu_j^S}\left(1-\delta_{ij}(1-\delta_{RA}\delta_{SB})\right). \tag{2.18}$$

We obtain the equation describing the model used to compute the power spectra in the likelihood

$$C_\ell^{XY,{\rm th},\nu_i\times\nu_j} = A_{\rm Pl} A^{XY,\nu_i\times\nu_j}\left[C_\ell^{XY,{\rm CMB}} + C_\ell^{XY,{\rm fg},\nu_i\times\nu_j}\right]. \tag{2.19}$$

CHAPTER 3

Assessing consistency between CMB temperature and polarisation measurements, with application to Planck, ACT and SPT

Summary

In the continuity of Chapter 2, this chapter will address the issue of instrumental systematic effects in CMB datasets. We present a method to look for systematics by allowing for a deviation with respect to ΛCDM that we can parametrise. In this way we are able to look for specific effects in CMB data while marginalising over cosmological and foreground parameters. This chapter is adapted from *La Posta et al. Phys. Rev. D 107, 023510 (2023)* [2].

3.1. Introduction

Since density perturbations in the primordial plasma have sourced both CMB temperature and polarisation anisotropies, there is a tight relation between these two fields. Increasingly precise polarisation measurements from ground-based CMB experiments will allow for powerful consistency tests with respect to temperature anisotropies to track down deviations from our expectations within the ΛCDM framework. As discussed in Chapter 2, a precise polarisation measurement will allow for a computation of the correlation coefficient $\mathcal{R}_\ell^{TE}$ which constitutes a good probe of multiplicative systematics. Another method that was first explored in Ref. [34] proposes to use conditional probabilities. Given a measurement of the temperature (resp. polarisation) power spectrum, one can analytically compute the probability density associated with the polarisation (resp. temperature) power spectrum. The analyses performed in Refs. [34], [107] have demonstrated a good agreement between the Planck polarisation and temperature power spectra. In the continuity, this chapter proposes another method to catch T-E inconsistencies that can be due to either ΛCDM deviations or instrumental systematics and apply it on Planck, ACT and SPT data.

3.2. Data, Likelihoods and basic cosmological model

The method presented here can be generally applied to any CMB dataset covering Gaussianly-distributed anisotropies, i.e., following the *Planck* terminology the 'high$-\ell$' scales. In this chapter we consider the three CMB experiments that today set the most stringent limits on cosmological parameters, *Planck*, *ACT* and *SPT*.

- ***Planck***
  Our baseline for *Planck* includes the temperature, temperature cross E modes and E-modes power spectra, TT, TE, and EE, and covariances from the *Planck* 2018 legacy release (PR3) [107]. We use the PLIK_LITE CMB-only high-ℓ likelihood, implemented in COBAYA [102], to analyse these data. The spectra entering in the computation of this likelihood have been marginalised over foreground and instrumental systematic uncertainties (see [101], [107]), and include TT measurements in the range $30 < \ell < 2500$ and TE, EE measurements at $30 < \ell < 2000$.

- ***ACT***
  We use the latest *ACT* data including temperature and polarisation from the forth data release, *ACT* DR4 [106]. Also in this case, the TT, TE and EE power spectra have been marginalised over foregrounds and systematic uncertainties (see [106]) and are contained in the publicly available PYACTLIKE likelihood. The TE and EE power spectra cover multipoles $326 < \ell < 4325$, while the TT power spectrum spans $576 < \ell < 4325$.

- ***SPT***
  For *SPT* we use the most recent power spectra from the 2020 SPT-3G data release [108] which included only TE and EE spanning multipoles $300 < \ell < 3000$. We do not include the temperature measurement that was recently released in Ref. [39]. The *SPT* data were released with a fortran likelihood characterising the spectra; we present here and use throughout a python version of this likelihood[1]. We verify that our python implementation leads to the same results as the official *SPT* constraints published in Ref. [108] in Appendix (3.A). These *SPT* power spectra have not been marginalised over foregrounds and therefore this likelihood includes the modelling of polarised Galactic dust both for EE and TE and Poisson-distributed point sources in EE for the three frequency channels 95, 150 and 220 GHz presented in Ref. [108].

- ***Low-ℓ***
  Although not examined and not scrutinised with the methods presented in this paper, we add low-ℓ temperature and polarisation information in our cosmological fits. When *Planck* is included in the analysis, we also use the *Planck* COMMANDER likelihood which models the non-Gaussian range between $2 < \ell < 30$. To incorporate the low-ℓ polarisation information in all data combinations (i.e., even when *Planck* is not included) we use a Gaussian prior for the reionisation optical depth, $\tau = 0.054 \pm 0.007$ [8]. This is a proxy that allows us to treat *Planck*, *ACT* and *SPT* consistently.

In all cases we work within the ΛCDM model which is described by: the angular scale at recombination $\theta_{\rm MC}$ (or alternatively the Hubble constant, H_0), the amplitude and the scalar spectral index of primordial perturbations A_s and n_s, the baryon and cold dark matter densities

[1] Made available at https://github.com/xgarrido/spt_likelihoods

$\Omega_b h^2$ and $\Omega_c h^2$, and τ. We also carry forward in the fits the additional parameters needed in the *Planck*, *ACT* and *SPT* likelihoods. These include a global calibration amplitude for *Planck*, $A_{\rm Planck}$, and an overall polarisation efficiency, y_p, for *ACT*. The *SPT* likelihood contains 6 foreground parameters modelling point sources for each cross-frequency spectrum $\nu_1 \times \nu_2$ ($D^{{\rm ps},\nu_1\times\nu_2}$) and 4 parameters describing polarised galactic dust emissions in EE ($A^{EE}_{\rm d}$, $\alpha^{EE}_{\rm d}$) and TE ($A^{TE}_{\rm d}$, $\alpha^{TE}_{\rm d}$) and 7 nuisance parameters including a temperature/polarisation map calibration parameter for each frequency band ($T^{\nu}_{\rm cal}$, $E^{\nu}_{\rm cal}$), and the mean lensing convergence κ modelling super-sample lensing.

3.3. Modelling residual transfer functions in CMB polarisation

As long as a model of their effects is available, instrumental systematics (such as polarisation efficiency, T-to-E leakage, etc.) can be handled during data processing or in the likelihood functions used to put constraints on cosmology. However, even after modelling and marginalising over these effects, some unresolved and/or unknown systematics can still be present and have an impact. In this section we discuss a method to constrain deviations from ΛCDM expectation marginalising over cosmological and foreground parameters. Implementing a model for the $T-E$ inconsistency with this method can help characterise the type and nature of the inconsistency preferred by the data. We will focus on four different models, either inspired by physically motivated systematic effects or by assuming more arbitrary parametrisations. Since these are potentially multipole-dependent deviations from our data model, we consider them as an additional 'transfer function', introducing an inconsistency between the CMB temperature and polarisation measurements. Here, we use a set of extra parameters to constrain the multipole dependence of the deviations and we obtain a joint posterior distribution for them and ΛCDM parameters. This method should be able to catch either deviations from the ΛCDM model or unmodelled systematic effects.

3.3.1. Transfer function models

We introduce four different parametrisations – a to d below – to quantify the consistency of temperature and polarisation measurements assuming the ΛCDM model. The first two models explore a polarisation transfer function and T-to-E leakage and are inspired by common CMB systematic effects. The other two models look at possible effects that would alter the EE or TE power spectra separately. In all cases we leave the temperature measurements unaffected by these transfer functions, such that the model for the TT power spectrum corresponds to the actual TT theory power spectrum: $\tilde{C}^{TT}_\ell = C^{TT}_\ell$. In this way the TT data will help to break the degeneracies between the cosmological parameters and the extra transfer function parameters.

(a) **Polarisation transfer function**
We include a transfer function in the polarisation E modes (F_ℓ) such that our model for the observed temperature and polarisation modes are $\tilde{a}^T_{\ell m} = a^T_{\ell m}$ and $\tilde{a}^E_{\ell m} = F_\ell a^E_{\ell m}$ respectively. The model for the measured TE and EE power spectra can be expressed as

$$\begin{aligned}\tilde{C}^{TE}_\ell &= F_\ell C^{TE}_\ell,\\ \tilde{C}^{EE}_\ell &= F^2_\ell C^{EE}_\ell.\end{aligned} \tag{3.1}$$

(b) **T-to-E leakage**
In the case of power leakage between T and E a transfer function, β_ℓ, alters the modes such that $\tilde{a}^T_{\ell m} = a^T_{\ell m}$ and $\tilde{a}^E_{\ell m} = a^E_{\ell m} + \beta_\ell a^T_{\ell m}$. The measured power spectra are then affected as follows

$$\begin{aligned}\tilde{C}^{TE}_\ell &= C^{TE}_\ell + \beta_\ell C^{TT}_\ell, \\ \tilde{C}^{EE}_\ell &= C^{EE}_\ell + 2\beta_\ell C^{TE}_\ell + \beta^2_\ell C^{TT}_\ell. \end{aligned} \tag{3.2}$$

(c) **Independent EE bias**
In the case of a transfer function affecting only the EE power spectrum, α_ℓ, the spectra become

$$\begin{aligned}\tilde{C}^{TE}_\ell &= C^{TE}_\ell, \\ \tilde{C}^{EE}_\ell &= \alpha_\ell C^{EE}_\ell. \end{aligned} \tag{3.3}$$

(d) **Independent TE bias**
Finally, a transfer function affecting only the TE power spectrum, δ_ℓ, leads to

$$\begin{aligned}\tilde{C}^{TE}_\ell &= \delta_\ell C^{TE}_\ell, \\ \tilde{C}^{EE}_\ell &= C^{EE}_\ell. \end{aligned} \tag{3.4}$$

With these parametrisations we have four functions to constrain: F_ℓ, β_ℓ, α_ℓ and δ_ℓ – always considered separately. To study in a model independent way the multipole dependence of potential deviations from theory that they encode, we use step functions for them with a given number of extra parameters related to the number of available bandpowers in different experiments. We use $n_b = 10$ extra parameters for ACT and $n_b = 11$ for SPT; with $N_{\rm bins} = 40$ for ACT power spectra and $N_{\rm bins} = 44$ for the SPT ones, each extra parameter in our model acts on four consecutive CMB bandpowers in the same way. Apart from spotting residual power, this methodology will also capture T-E inconsistencies that are localised in a specific multipole range.

3.3.2. Results

We first constrain the self consistency between temperature and polarisation measurements within *Planck*, ACT and SPT latest data. In order to assess the consistency between the *Planck* temperature measurements and the polarisation measurements from ground-based experiments, we then also consider some combinations between the TT power spectrum from *Planck* and the TE+EE power spectra from ACT or SPT. Therefore, below we work with the following data combinations

- *Planck* TT+TE+EE,
- ACT TT+TE+EE,
- SPT TE+EE,
- *Planck* TT + ACT TE+EE,
- *Planck* TT + SPT TE+EE.

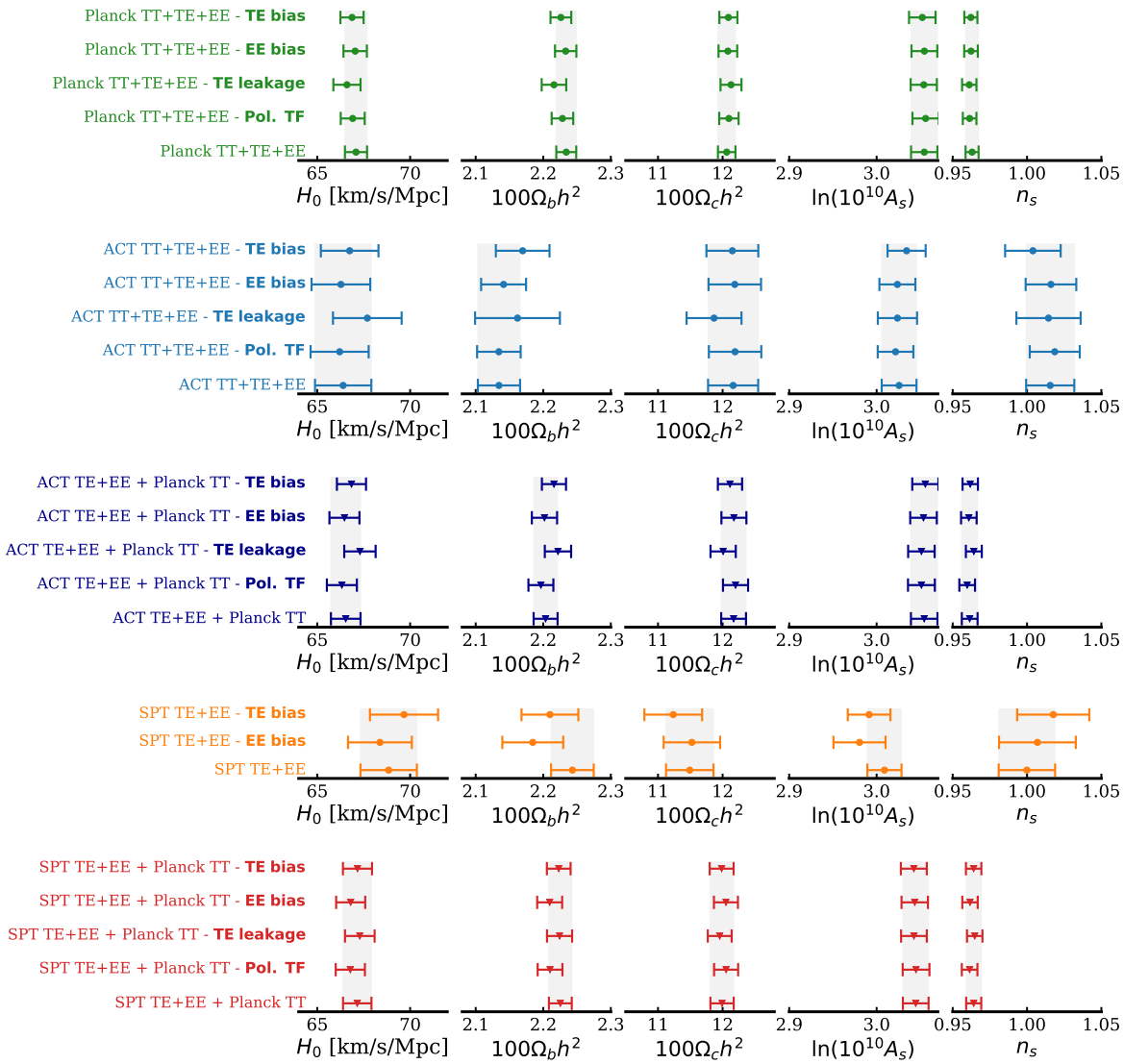

Figure 3.1: Marginalised constraints on ΛCDM parameters derived from the different datasets described in Sec. (3.3.2): *Planck TT+TE+EE* (green), *ACT TT+TE+EE* (lightblue), *SPT TE+EE* (orange), *ACT TE+EE + Planck TT* (blue) and *SPT TE+EE + Planck TT* (red). We display the $\pm 1\sigma$ (68%C.L.) constraints on ΛCDM parameters obtained while also fitting for the transfer function models detailed in Sec. (3.3.1). Standard ΛCDM constraints – without any additional transfer function – are displayed at the bottom of each panel and with a vertical grey band.

Since there is no available measurement of *SPT* temperature, we are limited on the number of tests that we can perform with this dataset. In particular, we cannot study here the case of a polarisation transfer function (a) and $T-E$ leakage (b) for *SPT* data alone.

As mentioned above, in order to constrain the n_b extra parameters modelling the $T-E$ inconsistencies, we explore the joint posterior distributions of the n_b extra-parameters, the 6 ΛCDM parameters and the foreground and nuisance parameters described in Sec. (3.2) depend-

Dataset	χ^2/d.o.f (PTE) Pol. TF	T-to-E leakage	EE bias	TE bias
Planck TT+TE+EE	6.74/10 (0.75)	14.2/10 (0.16)	8.07/10 (0.62)	12.6/10 (0.25)
ACT TT+TE+EE	8.91/10 (0.54)	4.76/10 (0.91)	10.52/10 (0.40)	6.61/10 (0.76)
Planck TT + *ACT* TE+EE	11.29/10 (0.34)	15.30/10 (0.12)	11.35/10 (0.33)	17.82/10 (0.06)
SPT TE+EE	—	—	14.38/11 (0.21)	11.69/11 (0.39)
Planck TT + *SPT* TE+EE	18.26/11 (0.08)	8.89/11 (0.63)	16.53/11 (0.12)	10.32/11 (0.50)

Table 3.1: Goodness of the fit, in terms of χ^2 and probability to exceed (PTE), for all for the different datasets and transfer function models considered in this analysis.

ing on the specific dataset. Parameters are sampled using the MCMC algorithm implemented in Cobaya and marginalised constraints are obtained using GetDist [109]. Apart from τ, we use flat priors on cosmological and n_b extra parameters. For *SPT* foreground parameters we use the priors described in Ref. [108]. Since we are explicitly modelling and fitting for functions that could capture the effect of some systematics that are already accounted for in the likelihoods, to avoid large degeneracy between parameters in some cases we need to change the treatment of the nuisance parameters of the likelihoods. More specifically, we have to fix the polarisation efficiencies/calibrations for both *ACT* and *SPT* likelihoods in order to remove some degeneracies between these and the n_b parameters. We use the Bobyqa likelihood maximiser [110], [111] implemented in Cobaya to obtain (within ΛCDM) the best-fit values: $y_p = 1.00047$ for the *ACT* overall polarisation efficiency and $E_{\rm cal}^{\rm 90GHz} = 0.99517$, $E_{\rm cal}^{\rm 150GHz} = 0.99519$ and $E_{\rm cal}^{\rm 220GHz} = 1.00073$ for the *SPT* polarisation calibrations. We then fix these parameters to their best fits.

We display the 1σ constraints on the ΛCDM parameters derived from *Planck*, *ACT* and *SPT* latest results while fitting at the same time for each of the transfer function models in Fig. (3.1). We do not see any significant cosmological parameter deviation with respect to the standard analysis (without additional transfer function) also shown in the figure as reference. The ΛCDM parameters determination is not strongly dependent on the extra parameters describing the $T - E$ inconsistencies (apart from when we lack temperature data as shown later for *SPT*). For all studied cases we observe a preference for high values of the scalar index measured from ground-based experiments, and we recover a preference for lower values of n_s when combining with *Planck* temperature data.

In order to quantify the deviation with respect to theory expectations, we compare the n_b constraints to the expected value for the studied bias (i.e., 0 for T-to-E leakage and 1 otherwise). We then compute a χ^2 for each dataset and bias model using the parameter covariance matrix obtained from the MCMC chains. The results are displayed in Table (3.1). Figures (3.2(a)),

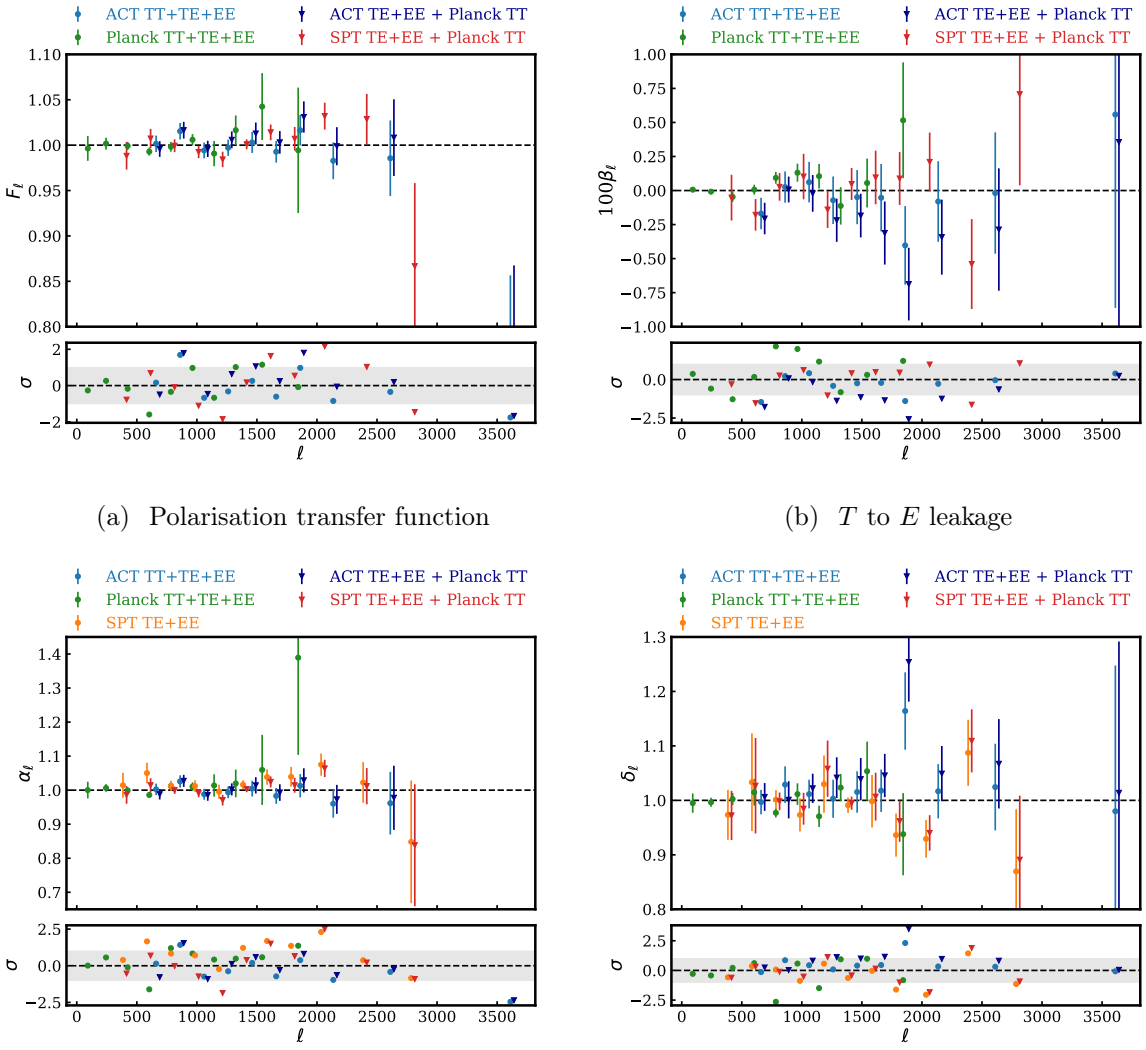

(a) Polarisation transfer function

(b) T to E leakage

(c) EE bias

(d) TE bias

Figure 3.2: Transfer function bandpowers with $\pm 1\sigma$ errors for the four different models studied: the F_ℓ polarisation transfer function (a), the β_ℓ T-to-E leakage (b), the α_ℓ EE bias (c) and the δ_ℓ TE bias (d). On each panel we display the results for different datasets: Planck 2018 TT+TE+EE (green), *ACT* TT+TE+EE (lightblue), *SPT* TE+EE (orange), *Planck* TT + *ACT* TE+EE (blue) and *Planck* TT + *SPT* TE+EE (red). The lower panels of each sub-figure show the comparison with, or potential deviation from, the expected value in units of σ. The gray band corresponds to the $\pm 1\sigma$ limits. No statistically-significant deviation is observed.

(3.2(b)), (3.2(c)) and (3.2(d)) display the 1σ constraints on the transfer function bandpowers and compares them with the expectation in the case of consistency. We find no evidence for a polarisation transfer function in both *Planck* and *ACT* data (Fig. (3.2(a))), with PTE=75%, 54% respectively. We observe a small feature around $\ell \simeq 900$ in the T-to-E leakage transfer function estimated from *Planck* data, but this deviation is not statistically significant with a PTE=16% (Fig. (3.2(b))). The EE/TE transfer functions derived from *Planck*, *ACT* and *SPT*

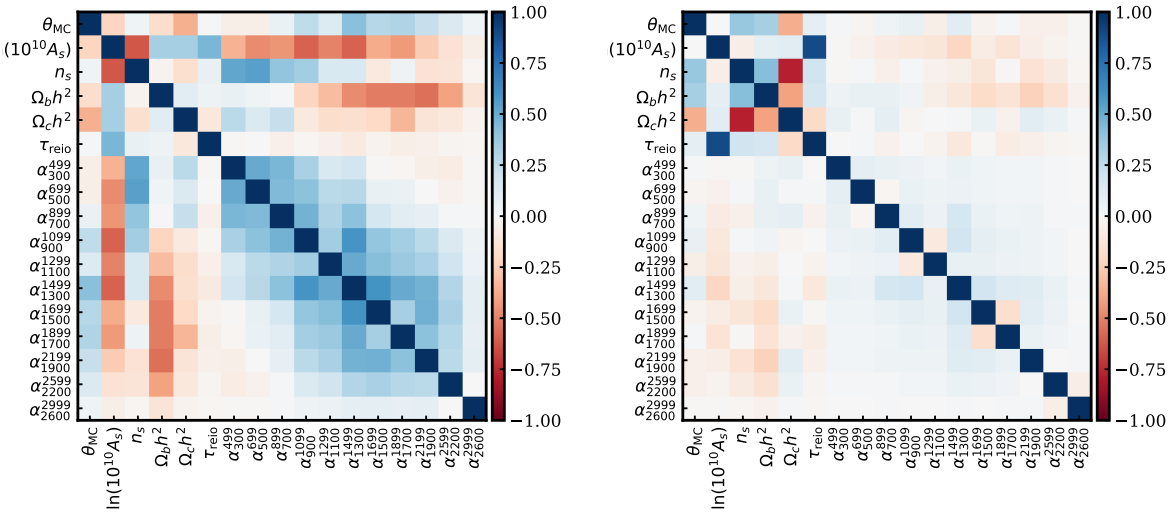

(a) *SPT TE+EE* (b) *SPT TE+EE + Planck TT*

Figure 3.3: Correlation matrices of cosmological parameters and transfer function bandpowers obtained using a EE transfer function. We display on the left the correlation matrix derived from *SPT* (TE+EE) data [(a)] and on the right the correlation matrix derived from a combination of *SPT* (TE+EE) and *Planck* 2018 TT data [(b)].

data are also in good agreement with expectations with PTE=62%, 40% and 21% (EE transfer function) and PTE=25%, 76% and 39% (TE transfer function).

When we quantify the $T-E$ inconsistencies between polarisation measurements from ground-based experiments (*ACT*, *SPT*) and temperature measurements from *Planck*, we observe a slight degradation in χ^2 with respect to the values obtained considering *Planck*, *ACT* and *SPT* individually (except for the TE transfer function constrained from *SPT* data) but still no significant deviation from consistency. We note one case in particular. For the combination of *Planck* TT and *ACT* TE+EE, we recover a slight preference for higher values of the TE power spectrum with respect to what the ΛCDM model predicts, with a PTE=6%, and mostly driven by the large value of the transfer function in the bin centered on $\ell = 1875.5$. As mentioned above, this effect was noticed in Ref. [37] where an artificial 5% effect in the TE calibration was explored and discussed. We run additional tests here to quantify this feature in more detail. We define and constrain three independent calibration amplitudes A_{TT}, A_{EE} and A_{TE} for *ACT* DR4 (C_ℓ^{TT}, C_ℓ^{EE}, C_ℓ^{TE}) and including also the large scale temperature measurements from *Planck* (C_ℓ^{TT} at $\ell < 650$). While for TT and EE we find no particular preference away from unity, for TE we obtain a marginalised constraint $A_{TE} = 1.037 \pm 0.015$ at 68% confidence which is 2.5σ away from the standard, no-inconsistency, value of 1. Even if visible in our results, we note that this is a small deviation with respect to ΛCDM. Overall, we find no statistically significant evidence for transfer functions.

Finally we highlight the importance of temperature data for fitting these systematic models. We show the correlation matrices between ΛCDM and the parameters describing the shape of the EE transfer function for *SPT* TE+EE alone (Fig. (3.3(a))) or for a combination of *SPT* data with *Planck* TT data (Fig. (3.3(b))). In the first case, we do not have any measurement of the temperature power spectrum and we observe non-zero correlations between the extra parameters and cosmological parameters even if the TE power spectrum is unchanged when we constrain the EE transfer function. These correlations are much smaller when we include temperature data from *Planck*.

3.4. Conclusion

In this chapter we have presented a method to quantify the consistency between CMB temperature and polarisation measurements and applied them to the most recent data from *Planck* and *ACT* and the polarisation data from *SPT*. We have studied potential $T - E$ inconsistencies directly modelling and fitting for transfer functions in Sec. (3.3). We constrained the extra parameters introduced to model the transfer functions together with cosmological parameters. We found no evidence for an inconsistency within *ACT*, *SPT*, and *Planck* or between the ground-based polarisation data and the *Planck* temperature measurements. A short term follow-up study could be to include the most recent SPT-3G temperature power spectra from Ref. [39]. While we found no significant evidence for deviations from the ΛCDM predictions, the accuracy of the future small-scale polarisation data from *ACT* (see chapter 5) and *SPT* and the Simons Observatory will allow to apply this method in a much more stringent way and potentially identify and study inconsistencies between CMB temperature and polarisation with high significance.

3.A. SPT-3G python likelihood

In this section we validate the results of our SPT-3G python likelihood with respect to the results published in Ref. [108]. Since our SPT-3G likelihood is compatible with Cobaya, we obtain the posterior distributions displayed in Fig. 3.4 using Cobaya, computing the theory power spectra with Camb (with the default accuracy settings and `lens_potential_accuracy=1.0`). For the MCMC analysis, we set flat priors on cosmological parameters except for the reionisation optical depth τ for which we use $\tau = 0.0544 \pm 0.0073$. We use the Gaussian priors from Ref. [108] for the point sources parameters ($D^{\mathrm{ps},\nu_1\times\nu_2}$), the parameters describing the polarised galactic dust emissions in EE and TE (A_{d}^{EE}, α_{d}^{EE}, A_{d}^{TE}, α_{d}^{TE}) and the mean lensing convergence κ. We impose flat priors on the temperature and polarisation map calibration parameters $(T_{\mathrm{cal}}^{\nu}, E_{\mathrm{cal}}^{\nu}) \in [0.85, 1.15]^2$. The 68% constraints obtained with our likelihood are displayed in Table 3.2. We recover well the published constraints on cosmology. We compute a χ^2 using cosmological parameters from Table 3.2, and obtained $\chi^2 = 513.5$ for 528 bandpowers ($\chi 2 = 513.0/528$ in Ref. [108])

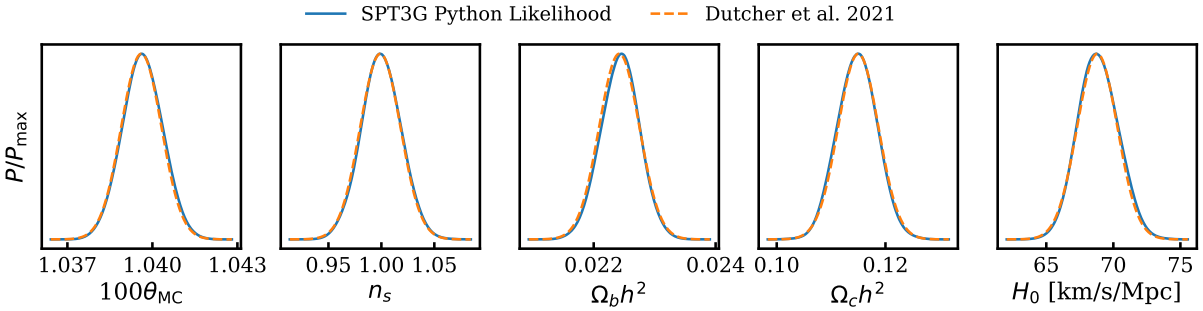

Figure 3.4: ΛCDM parameters posterior distributions derived using the python implementation of the SPT-3G likelihood (solid blue) compared to the official SPT-3G collaboration constraints from Ref. [108] (dashed orange).

	SPT-3G (this work)	SPT-3G [108]
$100\theta_{\mathrm{MC}}$	1.03965 ± 0.00072	1.03961 ± 0.00071
$\Omega_b h^2$	0.02243 ± 0.00032	0.02242 ± 0.00033
$\Omega_c h^2$	0.1148 ± 0.0037	0.1150 ± 0.0037
n_s	1.000 ± 0.019	0.999 ± 0.019
H_0 [km/s/Mpc]	68.9 ± 1.5	68.8 ± 1.5

Table 3.2: Constraints and 68% errors on ΛCDM parameters from SPT-3G using our python likelihood compared with the constraints from Ref. [108]

CHAPTER 4

Search for new physics with ground-base CMB experiments : the example of Early Dark Energy

Summary

This chapter is focused on a particular extension to the ΛCDM model designed to alleviate the Hubble tension by reducing the size of the sound horizon at recombination. This model proposes to introduce a new species in the early Universe that will cause a phase of accelerated expansion prior to recombination. This chapter is adapted from *Hill et al. Phys. Rev. D 105, 123536 (2022)* [112] and *La Posta et al. Phys. Rev. D 105, 083519 (2022)* [3].

4.1. Introduction

As discussed in Section (1.4.3), there seems to be a tension between early and late-time measurements of the Hubble constant. In the previous chapters, we have explored the possibility that the CMB is affected by systematics that are responsible for the low value of H_0 inferred from the cosmic microwave background anisotropies. The two studies conducted in Chapter 2 and Chapter 3 did not reveal any potential instrumental systematics in the studied CMB datasets. Furthermore, independent measurements of the Hubble constant from the CMB are consistent as shown in Section (1.4.3). It is unlikely that instrumental systematic effects in CMB datasets can explain the Hubble tension. This chapter will explore the possibility that both measurements of the expansion rate are correct and that this difference can be explained by introducing physics beyond the standard model. To reconcile the two measurements we can either develop a model that will lower the value of H_0 derived from the cosmic distance ladder or develop a model that will shift the expansion rate derived from CMB anisotropies towards higher values. Due to the broad range of low-redshift observations, it is more difficult to build late-time modifications to ΛCDM that matches with observations. In particular, the low value of H_0 inferred from inverse distance ladder (BAO+BBN) is challenging for this class of models. In the following, we will focus on early-time modifications to ΛCDM that change the size of the sound horizon at recombination. Reviews on the possible solutions to the so-called Hubble tension can be found in

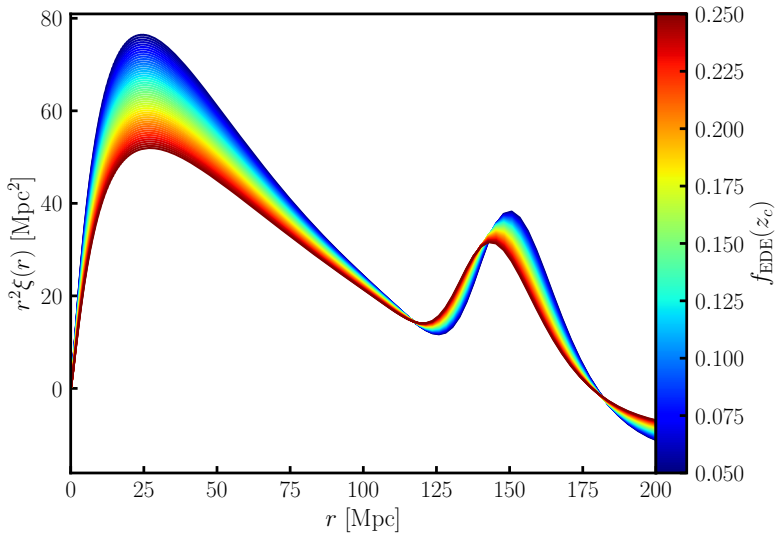

Figure 4.1: Two-point correlation function of the matter density field for different values of the fractional contribution of early dark energy at redshift z_c. The critical redshift is fixed to $z_c = 4000$ and we vary only $f_{\rm EDE}$. The main effect of this dark energy injection in the early Universe is to reduce the comoving size of the sound horizon.

Refs. [92], [93].

CMB anisotropies have tightly constrained the angular size of the sound horizon $\theta_* = r_s^*/d_A^*$. Lowering the size of the sound horizon implies that d_A^* has to be reduced to keep being consistent with CMB observations. This results in a higher value of the expansion rate H_0. Since r_s^* is inversely proportional to the expansion rate in the early Universe (see Eq. (1.61)), an efficient way of lowering the size of the sound horizon at recombination is to add a phase of accelerated expansion before recombination similar to what is happening at late times with dark energy, such that

$$H^2_{\rm early}(z) = \frac{8\pi G}{3}\left[\rho_r^0(1+z)^4 + \rho_m^0(1+z)^3 + \rho_{\rm EDE}(z)\right]. \tag{4.1}$$

This phase of accelerated expansion lower the conformal time at decoupling and reduce the distance travelled by sound waves in the primordial plasma. This phenomenon is illustrated in Fig. (4.1) which displays the correlation function of the matter density field as a function of the contribution of the ***early dark energy*** component to the total energy budget of the Universe. Such a solution has been first proposed in Ref. [113] based on a description of the dark energy as a scalar field arising from string theory axions [114]. The current description of the Early Dark Energy (EDE) was developed in Refs. [95], [96]. The EDE component is described as a scalar field ϕ evolving in the potential

$$V_n(\phi) = m_\phi^2 f_\phi^2 \left[1 - \cos(\phi/f_\phi)\right]^n, \tag{4.2}$$

where m_ϕ and f_ϕ are the mass and decay constant of the scalar field respectively. n is a parameter that rules the dilution rate of the EDE component when the field starts to oscillate. The evolution

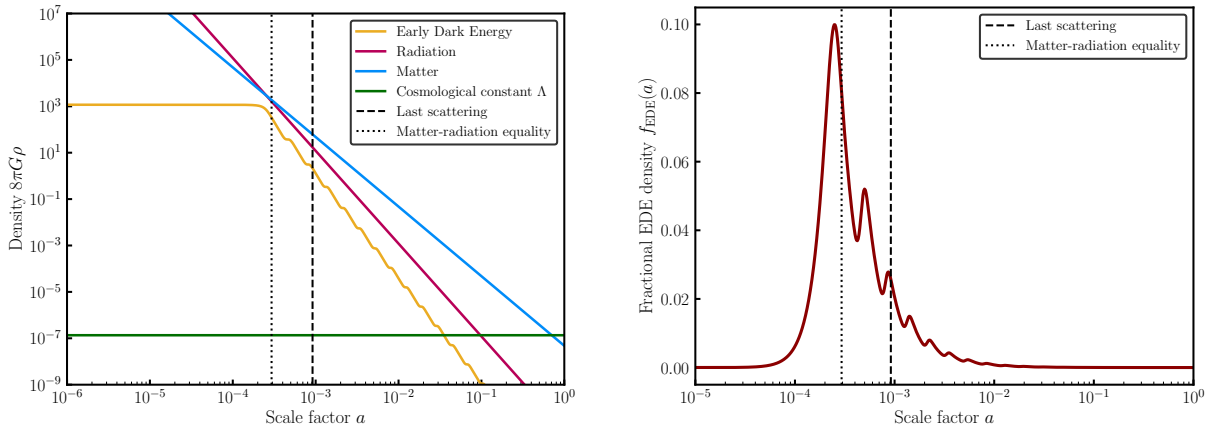

(a) (b)

Figure 4.2: (a) Energy densities as a function of the scale factor a. The early dark energy density (yellow) is constant and starts to dilute close to matter radiation equality. — (b) Fractional early dark energy density as a function of the scale factor a.

equation for the scalar field, at the background level is the Klein-Gordon equation in an expanding Universe

$$\ddot{\phi} + 3H\dot{\phi} + \frac{dV_n}{d\phi} = 0. \tag{4.3}$$

The second term acts as a friction term that dominates in the very early Universe implying that the field has a negligible kinetic energy. Recalling that the energy density of a scalar field is $\rho_\phi = \dot{\phi}^2/2 + V_n$ and the pressure is $P_\phi = \dot{\phi}^2/2 - V_n$, the equation of state $w = P_\phi/\rho_\phi$ is close to $w = -1$ when the field is slowly rolling. This behavior is illustrated in Fig. (4.2(a)) : the energy density ρ_ϕ is constant at early times and starts to dilute around a critical redshift z_c when the fields oscillates in its potential. As depicted in Fig. (4.2(b)), the EDE field is designed to reach its maximum contribution just prior to recombination such that the late-time Universe physics is unaffected. The dilution rate of the energy density depends on n such that $w_n = (n-1)/(n+1)$ where $n \geq 2$ to ensure that the EDE component will dilute faster than radiation. The field is *a priori* described from the field initial displacement ϕ_i, its mass m_ϕ and its decay constant f_ϕ. Observationally, a variation in these parameters induces a change in the critical redshift z_c at which the field energy density starts to dilute and in the fractional energy contribution of the field at z_c $f_{\rm EDE}(z_c) = \rho_\phi(z_c)/\rho_{\rm tot}(z_c)$. We define the unitless initial field displacement $\theta_i = \phi_i/f$ such that for each θ_i, one can find the unique couple $(f_{\rm EDE}, z_c)$ corresponding to the field parameters (m_ϕ, f_ϕ) [96]. In this chapter, we will discuss constraints on the EDE parameters $f_{\rm EDE}$, z_c and Θ_i, following what was previously done in the litterature.

Previous studies have already demonstrated that EDE is a viable candidate to solve the Hubble tension [95], [96]. The inclusion of the EDE component significantly reduces the χ^2 in the joint-fit of Planck data along with BOSS DR12 BAO measurements, the Pantheon supernovae sample and the SH0ES measurement of H_0 ($\Delta\chi^2 = -14.5$ with respect to ΛCDM) [95]. This improvement comes with a higher value of the expansion rate inferred from this dataset : $H_0 =$

68.18 ± 0.54 km/s/Mpc for ΛCDM and $H_0 = 70.6 \pm 1.3$ km/s/Mpc assuming the EDE ($n = 3$) model with a peak contribution of EDE around 10%. Note that the broadening of the 1σ error on H_0 has a significant contribution to the resolution of the tension. Refs. [115]–[117] have shown that Planck data alone does not show a preference in favor of the Early Dark Energy model resulting in a marginalised 95% upper limit of $f_{\rm EDE} \leq 0.087$.

4.2. Constraints from ACT DR4 data

While the Planck data alone do not favor large values of $f_{\rm EDE}$, the EDE scenario has been constrained from other CMB datasets such as ACT DR4 and SPT-3G polarisation. This section will briefly summarise the results obtained in Ref. [112] (that have also been discussed in Refs. [118], [119]), starting with a description of the data used in this analysis.

ACT data

Ref. [112] makes use of the latest ACT data, which includes multi-frequency temperature and polarisation measurements from the fourth data release, ACT DR4 [37], [106]. The TT, TE, and EE power spectra have been marginalised over foregrounds and systematic uncertainties and are contained in the publicly available PYACTLIKE likelihood,[1] which also uses data from the ACT MBAC DR2 data set [120]. The TE and EE power spectra cover multipoles $326 < \ell < 4325$, while the TT power spectrum spans $576 < \ell < 4325$ [37]. The likelihood depends on only the cosmological parameters (6 for ΛCDM + 3 more for EDE) and one nuisance parameter, the overall polarisation efficiency. Note that due to atmospheric noise, the Atacama Cosmology Telescope does not probe the largest angular scale and therefore needs to use a prior on the reionisation optical depth $\tau_{\rm reio}$ to break degeneracies with the amplitude of the primordial power spectrum A_s. The τ-prior used in this analysis is a Gaussian prior $\tau_{\rm reio} = 0.065 \pm 0.015$. [37]

High-ℓ Planck data

As a baseline for Planck we use the multifrequency TT, TE, and EE power spectra and covariances from the Planck 2018 legacy release (PR3) [107] included in the publicly available PLIK high-ℓ likelihood. We also use the low-ℓ TT likelihood, but we do not include low-ℓ EE data from Planck, and instead use the Gaussian prior on the optical depth metionned above. When combining Planck with ACT, we impose a multipole cut $\ell_{\rm min}^{\rm ACT} = 1800$ in temperature to ensure that ACT and Planck are quasi-independent measurements. For some runs, we have also included the Planck reconstructed lensing power spectrum as a probe of the large-scale structures [48] including multipoles from $L = 8$ to $L = 400$.

Low-ℓ Planck data

To complement the ACT power spectra with the largest scales, we have extracted a subset of Planck data consisting only of the TT power spectrum up to a multipole of $\ell < 650$. This data subset can also be seen as an emulation of the WMAP measurements, which was shown to agree very precisely with Planck on these angular scales (see Fig. 48 of Ref. [101]). For simplicity purposes, we will refer to this Planck data subset as "PlanckTT650".

[1] https://github.com/ACTCollaboration/pyactlike

Large-scale structure probes

In addition to the results using only primary CMB data, some of the constraints presented in this chapter also include large-scale structure probes, in particular BAO data. BAO data probe the expansion history of the Universe and allows to break some degeneracies that is often necessary in ΛCDM extensions with a larger parameter space. We use data from the SDSS BOSS DR12 LOWZ and CMASS galaxy samples at $z = 0.38$, 0.51, and 0.61 [121], from the 6dF galaxy redshift survey at $z = 0.106$ [122], and from the SDSS DR7 main galaxy sample at $z = 0.15$ [123].

Parameter constraints have been obtained by sampling the parameter space using MCMC techniques implemented in the public software Cobaya [102]. The Gelman-Rubin criterion that have been used to assess the convergence of the chains was $R - 1 \leq 0.03$. We use the Bobyqa minimiser [110], [111] to get the maximum likelihood point of the parameter space. Posterior distributions have been obtained using GetDist [109] and the power spectra model used are provided by a modified version of the CLASS Boltzmann solver [12], the CLASS_EDE software.[2] For the ACT DR4 analysis, we set flat priors on the EDE parameters such that $f_{\rm EDE} \in [0.001, 0.5]$, $\log(z_c) \in [3, 4.3]$ and $\theta_i \in [0.1, 3.1]$. A quantitative model comparison is performed by computing the $\Delta\chi^2$ with respect to the ΛCDM best-fit. This quantity follows a χ^2 distribution with $n = 3$ degrees of freedom (corresponding to the number of parameter necessary to describe the EDE scenario.

ACT DR4 constraints on the EDE model are shown in Fig. (4.3) for different dataset combinations. To ease the comparison, the marginalised posterior distributions are also shown considering only Planck primary CMB data. As displayed in Fig. (4.3), ACT DR4 data show a small preference in favor of non-zero $f_{\rm EDE}$ with $f_{\rm EDE} = 0.142^{+0.039}_{-0.072}$ with a $\Delta\chi^2 = -8.7$ improvement in the best-fit χ^2 with respect to ΛCDM. The derived constraint on the expansion rate is $H_0 = 74.5^{+2.5}_{-4.4}$ km/s/Mpc, consistent with the local measurement of H_0 from the SH0ES team. Joint constraints from ACT DR4 data and the large scale temperature from Planck (PlanckTT650) yield a tighter constraint $f_{\rm EDE} = 0.129^{+0.028}_{-0.055}$ as well as a greater improvement in the best-fit χ^2 with $\Delta\chi^2 = -15.4$ — which can be translated in a 3.2σ preference for EDE. The associated constraint on H_0 still have significantly large errors with $H_0 = 74.4^{+2.2}_{-3.0}$ km/s/Mpc. Combining the previous dataset with large-scale structure probes such as BAO and CMB lensing leads to smaller $f_{\rm EDE}$ and H_0 but still consistent with the local measurement from Cepheids-calibrated type IA supernovae $H_0 = 70.9^{+1.0}_{-2.0}$ km/s/Mpc. As displayed in Fig. (4.3), although ACT DR4 data seem to have a mild preference in favor of the EDE model, the Planck TT+TE+EE dataset have enough statistical power to drive the combined constraint to the Planck TT+TE+EE results. The ACT DR4 + Planck TT+TE+EE combination yield to a 95% upper limit $f_{\rm EDE} \leq 0.124$ with small marginalised constraint differences with respect to Planck TT+TE+EE posteriors. Another study performed on ACT DR4 data in Ref. [119] has also led to the same conclusion [118], [119] : ACT DR4 data seems to have a preference for a non negligible dark energy component at early times.

4.3. Constraints from SPT-3G polarisation data

[2] publicly available at https://github.com/mwt5345/class_ede

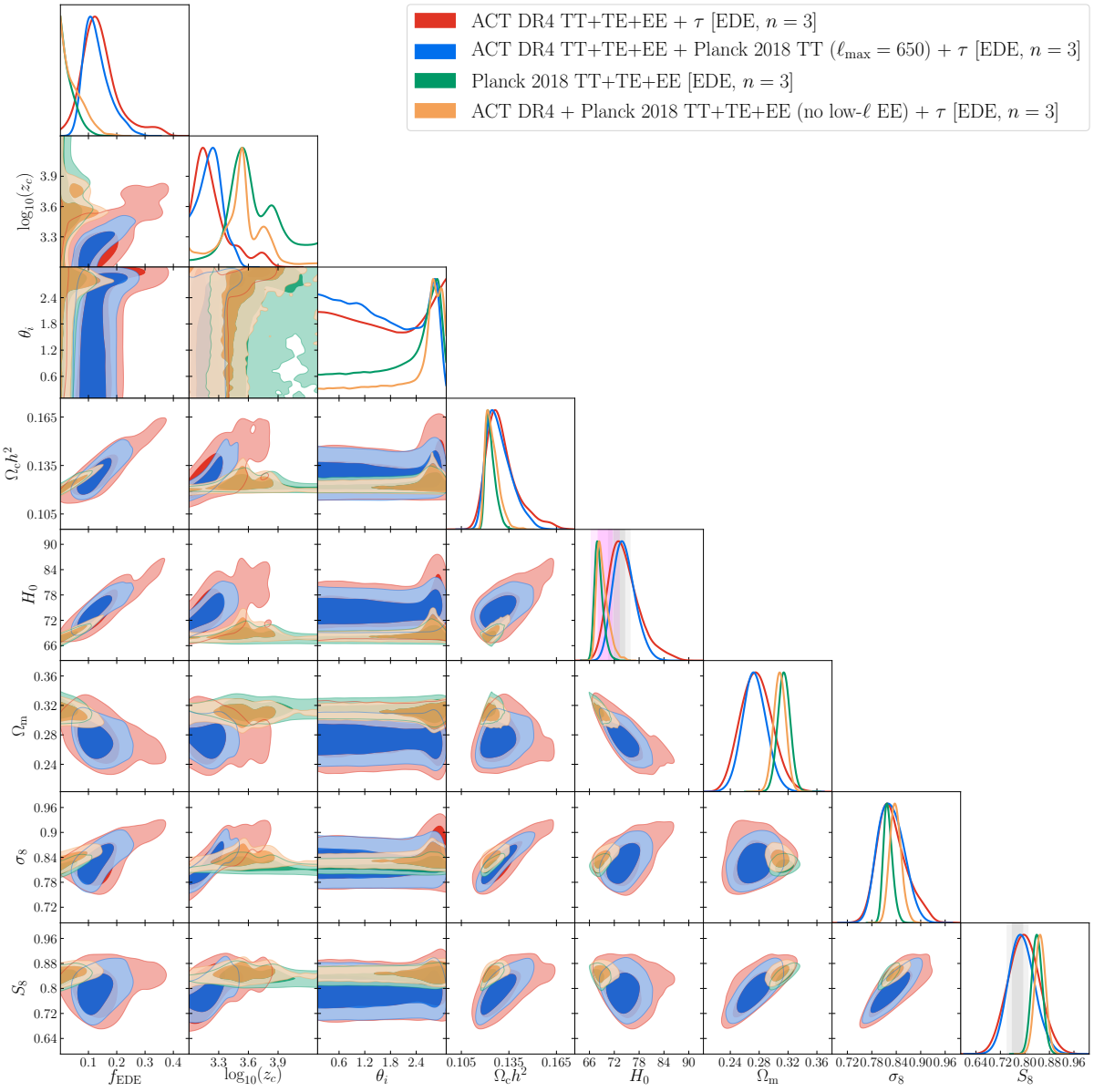

Figure 4.3: Marginalised posterior distributions for the EDE parameters and a subset of other parameters of interest. We display constraints obtained from ACT DR4 TT+TE+EE (red), ACT DR4 TT+TE+EE combined with the large-scale ($\ell < 650$) temperature power spectrum from Planck (blue), Planck 2018 TT+TE+EE using the Plik likelihood (green) and the full Planck TT+TE+EE dataset combined with ACT DR4 TT+TE+EE (yellow). All analyses, apart from Planck alone, include a Gaussian prior on the reionisation optical depth $\tau_{\rm reio} = 0.065 \pm 0.015$. The gray and magenta bands in the H_0 panel show constraints from SH0ES [77] and TRGB [79] respectively. The gray bands in the S_8 panel show constraints from DES-Y3 [64]

In the previous section we discussed the constraints on the early dark energy model obtained from ACT DR4 data. Planck and ACT data do not tell the same story about the EDE scenario even if it has been shown that parameters derived from both datasets are in good agreement

($\sim 2.4\sigma$) when considering the ΛCDM model [37]. The apparent disagreement between the two datasets motivate to pay a particular attention to the presence of systematic effects in ACT DR4 data that explains this difference. We already discussed ways of looking for systematics in CMB datasets in Chapters 2 and 3. In this section we constrain the EDE model using the latest data from another ground-based high resolution instrument, the South Pole Telescope, and in particular the SPT-3G [108] polarisation data. Our goal is to provide an independent test of the hints in favor of EDE seen in the ACT DR4 data.

In addition to the previously described data, we have used the SPT-3G polarisation power spectra from the 2020 data release [108] which includes only TE and EE spanning multipoles $300 < \ell < 3000$. The data have been collected during just half of a typical season of observation (4 months) and with only part of the focal place operational. The SPT-3G data release includes a FORTRAN likelihood characterising these spectra. In this analysis, we use a PYTHON version of the likelihood[3]. We have verified that our PYTHON implementation leads to the same results as the official SPT-3G constraints published in Ref. [108] in Appendix (3.A). For ΛCDM, the recovered parameter posteriors agree to better than 0.1σ. The likelihood includes a modelling of polarised Galactic dust both for TE and EE and Poisson-distributed point source in EE for the three frequency channels centered on 95, 150 and 220 GHz. The SPT-3G collaboration has recently released their temperature power spectrum in Ref. [39] which significantly improve the cosmological parameter constraints. One should note that the results presented here use only polarisation data from SPT-3G.

In the following, we will discuss constraints obtained on the EDE model using the MCMC method as described above for the ACT DR4 data. We use the same convergence criterion $R - 1 \leq 0.03$. The theory power spectra are computed using CAMB [10], [11] for which the EDE model is implemented as a new dark energy model named `EarlyQuintessence`. The CAMB `EarlyQuintessence` module solves both the background evolution of the field and the evolution of perturbations as described in Ref. [96]. In Appendix (4.A), we show that we are able to reproduce the results for the ACT DR4 + PlanckTT650 dataset from Ref. [112], which were computed using a modified version of the CLASS Boltzmann solver. We use the CAMB default precision settings for our MCMC runs, and we increase the accuracy settings following the prescription described in Ref. [112] for obtaining the best-fit values using the BOBYQA minimiser (see also Ref. [124] for further discussion related to Boltzmann accuracy settings). In order to quantify the preference in favor of the EDE model with respect to ΛCDM, we quote a level of preference in units of "sigmas" with the associated probability, computed from the fact that the $\Delta\chi^2$ for EDE compared to ΛCDM follows a χ^2 distribution with $\Delta N_{\rm p} = 3$ degrees of freedom.

In this work, we thus explore a parameter space defined by the three extra parameters introduced in the EDE scenario ($\{f_{\rm EDE}$, $\log_{10}(z_c)$, $\theta_i\}$ and by the ΛCDM parameters ($\{\theta_{\rm MC}$, $\Omega_b h^2$, $\Omega_c h^2$, $\ln(10^{10} A_s)$, n_s, $\tau_{\rm reio}\}$). We choose to use wide uninformative priors on the cosmological parameters, except for the reionisation optical depth, for which we impose a Gaussian prior instead of using large-scale polarisation data from Planck. We also use wide flat priors on the EDE parameters, allowing for higher values of the critical redshift z_c with respect to what was assumed in Refs. [96], [112], [115], [116]. We discuss the effect of this prior in detail at the end

[3]Made available at https://github.com/xgarrido/spt_likelihoods

of Section (4.3.1). The exact priors used in this analysis are shown in Table (4.1).

Parameters	Prior
$f_{\rm EDE}$	$[0.001, 0.5]$
$\log_{10} z_c$	$[3, 5]$
θ_i	$[0.1, 3.1]$
$100\theta_{\rm MC}$	$[1.03, 1.05]$
$\log(10^{10} A_{\rm s})$	$[1.6, 3.9]$
$n_{\rm s}$	$[0.8, 1.2]$
$\Omega_{\rm b} h^2$	$[0.01, 0.03]$
$\Omega_{\rm c} h^2$	$[0.05, 0.3]$
$\tau_{\rm reio}$	$\mathcal{N}(0.065, 0.015)$

Table 4.1: Prior distributions for the EDE and ΛCDM parameters. The reionisation optical depth prior is a Gaussian probability density centered at 0.065 with a 0.015 standard deviation.

4.3.1. Constraining EDE from SPT-3G data

First, we constrain the EDE model using the three most constraining CMB datasets today: Planck 2018, ACT DR4, and SPT-3G. Posterior distributions for the EDE and ΛCDM parameters are shown in Fig. (4.4) and marginalised constraints are available in the associated table. As found in previous studies, Planck data alone do not favor a large fraction of EDE, $f_{\rm EDE} < 0.095$ (95% C.L.), while ACT data display a slight preference for non-zero EDE, $f_{\rm EDE} = 0.148^{+0.045}_{-0.086}$. These marginalised constraints are consistent with what can be found in Refs. [112], [115], [119]. Our new result for SPT-3G, $f_{\rm EDE} = 0.163^{+0.045}_{-0.160}$, is consistent with these two measurements, but can not yet be used to discriminate between them.

Interestingly, the posterior distribution of z_c, the redshift for which the fractional contribution of the EDE to the total energy content of the Universe is maximal, follows a similar distribution for SPT-3G and Planck, peaking near matter-radiation equality, while we find a slight preference for lower redshift for the ACT data, consistent with previous work [112], with a peak closer to decoupling. We observe with the SPT-3G data the now-familiar $f_{\rm EDE} - H_0$ degeneracy that serves to increase the value of H_0 (and its uncertainties), and reconcile the value of H_0 inferred from CMB experiments with the ones inferred from local observation of Cepheid-calibrated SNIa. The $\Delta\chi^2$ of the EDE scenario with respect to ΛCDM is of order -4.1, which corresponds to a 74.9% C.L. (1.1σ) preference over ΛCDM. This does not indicate a significant improvement coming from this scenario given the extra degrees of freedom introduced.

We now consider the following combinations using SPT-3G data:

- SPT-3G (TE+EE) + Planck 2018 (TT, $\ell < 650$)
- SPT-3G (TE+EE) + Planck 2018 (TT, $\ell < 650$) + BAO [6dF,SDSS DR7/DR12] + Planck 2018 CMB lensing

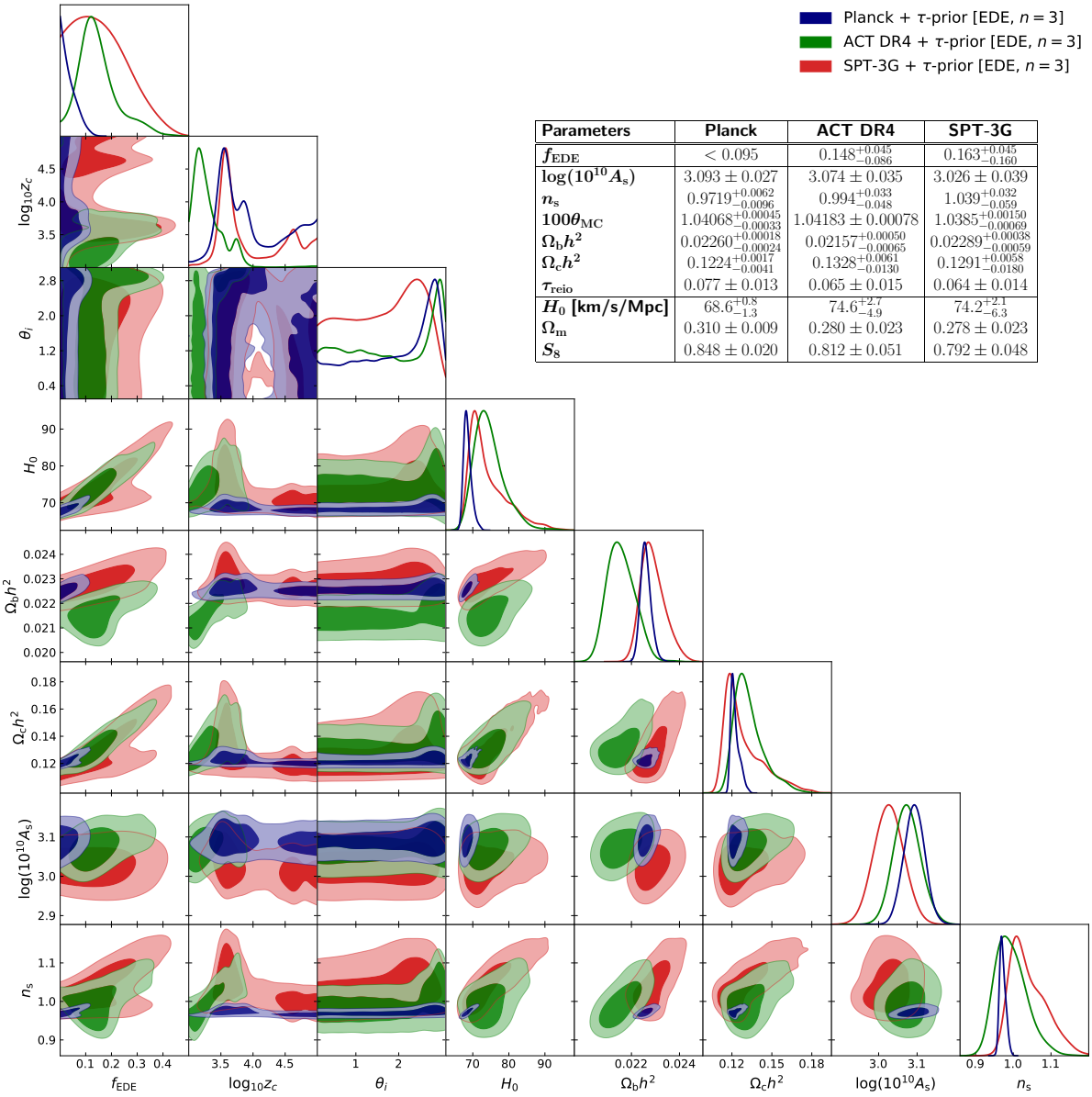

Parameters	Planck	ACT DR4	SPT-3G
$f_{\rm EDE}$	< 0.095	$0.148^{+0.045}_{-0.086}$	$0.163^{+0.045}_{-0.160}$
$\log(10^{10}A_{\rm s})$	3.093 ± 0.027	3.074 ± 0.035	3.026 ± 0.039
$n_{\rm s}$	$0.9719^{+0.0062}_{-0.0096}$	$0.994^{+0.033}_{-0.048}$	$1.039^{+0.032}_{-0.059}$
$100\theta_{\rm MC}$	$1.04068^{+0.00045}_{-0.00033}$	1.04183 ± 0.00078	$1.0385^{+0.00150}_{-0.00069}$
$\Omega_{\rm b}h^2$	$0.02260^{+0.00018}_{-0.00024}$	$0.02157^{+0.00050}_{-0.00065}$	$0.02289^{+0.00038}_{-0.00059}$
$\Omega_{\rm c}h^2$	$0.1224^{+0.0017}_{-0.0041}$	$0.1328^{+0.0061}_{-0.0130}$	$0.1291^{+0.0058}_{-0.0180}$
$\tau_{\rm reio}$	0.077 ± 0.013	0.065 ± 0.015	0.064 ± 0.014
H_0 [km/s/Mpc]	$68.6^{+0.8}_{-1.3}$	$74.6^{+2.7}_{-4.9}$	$74.2^{+2.1}_{-6.3}$
$\Omega_{\rm m}$	0.310 ± 0.009	0.280 ± 0.023	0.278 ± 0.023
S_8	0.848 ± 0.020	0.812 ± 0.051	0.792 ± 0.048

Figure 4.4: Marginalised posterior distributions of EDE ($n = 3$) and ΛCDM parameters derived from Planck 2018 (TT+TE+EE) high-ℓ + Planck 2018 low-ℓ (TT) data (dark blue); ACT DR4 (TT+TE+EE) data [37], [106] (green); and SPT-3G (TE+EE) latest polarisation measurements [108] (red). We impose the same Gaussian prior on the reionisation optical depth τ for all the analyses. We display the 68% marginalised constraints and the upper/lower limits (95% C.L.) for the EDE and ΛCDM in the table associated with the figure.

Posterior distributions and marginalised constraints for these two datasets are shown in Fig. (4.5). A summary of the best-fit χ^2 values for the studied datasets can be found in Table (4.2). Adding the large-scale TT power spectrum from Planck to SPT-3G data tightens the constraints on cosmology (it is particularly noticeable for the scalar index $n_{\rm s}$). Large-scale temperature data from Planck also shift the EDE posterior distribution peak towards lower val-

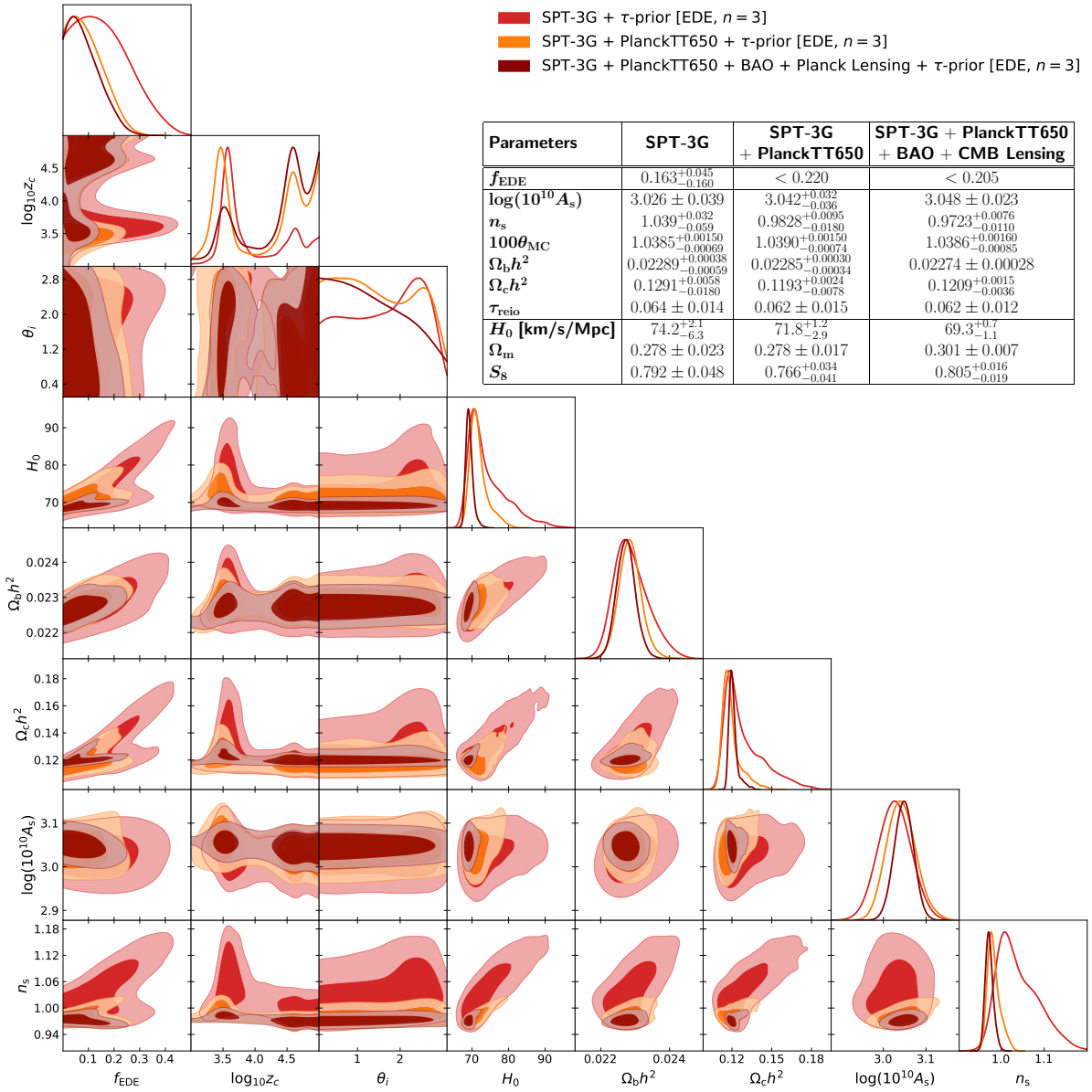

Parameters	SPT-3G	SPT-3G + PlanckTT650	SPT-3G + PlanckTT650 + BAO + CMB Lensing
$f_{\rm EDE}$	$0.163^{+0.045}_{-0.160}$	< 0.220	< 0.205
$\log(10^{10}A_{\rm s})$	3.026 ± 0.039	$3.042^{+0.032}_{-0.036}$	3.048 ± 0.023
$n_{\rm s}$	$1.039^{+0.032}_{-0.059}$	$0.9828^{+0.0095}_{-0.0180}$	$0.9723^{+0.0076}_{-0.0110}$
$100\theta_{\rm MC}$	$1.0385^{+0.00150}_{-0.00069}$	$1.0390^{+0.00150}_{-0.00074}$	$1.0386^{+0.00160}_{-0.00085}$
$\Omega_{\rm b}h^2$	$0.02289^{+0.00038}_{-0.00059}$	$0.02285^{+0.00030}_{-0.00034}$	0.02274 ± 0.00028
$\Omega_{\rm c}h^2$	$0.1291^{+0.0058}_{-0.0180}$	$0.1193^{+0.0024}_{-0.0078}$	$0.1209^{+0.0015}_{-0.0036}$
$\tau_{\rm reio}$	0.064 ± 0.014	0.062 ± 0.015	0.062 ± 0.012
H_0 [km/s/Mpc]	$74.2^{+2.1}_{-6.3}$	$71.8^{+1.2}_{-2.9}$	$69.3^{+0.7}_{-1.1}$
$\Omega_{\rm m}$	0.278 ± 0.023	0.278 ± 0.017	0.301 ± 0.007
S_8	0.792 ± 0.048	$0.766^{+0.034}_{-0.041}$	$0.805^{+0.016}_{-0.019}$

Figure 4.5: Marginalised posterior distributions of EDE ($n = 3$) and ΛCDM parameters derived from SPT-3G (TE+EE) latest data [108] alone (red); in combination with Planck 2018 TT ($\ell < 650$) (orange); and combined with Planck 2018 TT ($\ell < 650$), Planck CMB lensing and BAO data (6dF [122], SDSS DR7/DR12 [121], [123]) (darker red). We impose the same Gaussian prior on the reionisation optical depth τ for all the analyses. We display the 68% marginalised constraints and the upper/lower limits (95% C.L.) for the EDE and ΛCDM in the table associated with the figure.

ues: we find $f_{\rm EDE} < 0.220$ (95% C.L.) with SPT-3G combined with Planck TT ($\ell < 650$), with $\Delta\chi^2 = -4.4$ (1.2σ) with respect to ΛCDM. We obtain slightly better constraints on cosmology by adding CMB lensing and BAO measurements, and in particular for the EDE density, we obtain $f_{\rm EDE} < 0.205$. Due to the wide prior imposed on z_c in this analysis, we allow for high

values of the critical redshift z_c, for which the EDE field has a very small impact on the CMB observables. Indeed, we observe a tail out to high redshift in the $\log_{10}(z_c)$ posterior distribution displayed in Fig. (4.5), particularly when SPT-3G data are combined with PlanckTT650 and large-scale structure probes. For this dataset, we compute a $\Delta\chi^2$ of -3.7 (1.0σ) with respect to ΛCDM.

We study the impact of a high value of z_c on the measurements of other cosmological parameters by re-weighting the samples to favor the higher (lower) $\log_{10}(z_c)$ values using Gaussian weights centered on $\mu_{\rm high} = 4.5$ ($\mu_{\rm low} = 3.5$). As shown in Fig. (4.6), if the EDE field reaches its maximum energy contribution at very early times ($\log_{10}(z_c) \simeq 4.5$), $f_{\rm EDE}$ will have a much smaller impact on the sound horizon, and hence the inferred Hubble expansion rate H_0, than if it had peaked near the time of recombination. We see this effect on the 2D posterior distributions in the $H_0 - f_{\rm EDE}$ plane shown in the first column of Fig. (4.6): the correlation between H_0 and $f_{\rm EDE}$ tends to disappear when we favor higher z_c values.

We observe this behavior when we use CMB lensing and BAO data combined with SPT-3G due to the preference for high z_c values. There are two different degeneracy directions in the 2D posterior distribution of $f_{\rm EDE}$ and H_0, and the direction with the lowest correlation between these two parameters is favored by this dataset. This leads to low-value of the Hubble parameter $H_0 = 69.3^{+0.7}_{-1.1}$ km/s/Mpc, 3σ away from the latest local measurement of $H_0 = 73.04 \pm 1.04$ km/s/Mpc from Ref. [78]. An important takeaway is that the 1D marginalised posterior on $f_{\rm EDE}$ can be quite sensitive to the assumed prior range for z_c, and thus assessing evidence for the EDE model based solely on the posterior for this parameter may not always be robust.

4.3.2. Combining with other small-scale CMB data

We have shown in Section (4.3.1) that the constraints on the EDE model from Planck 2018, ACT DR4, and SPT-3G data are consistent, but SPT-3G data are not constraining enough to reach a firm conclusion on the existence of an EDE component in the Universe.

In this section, we focus on the following combined constraints on the EDE model using the Planck, ACT, and SPT data:

- SPT-3G (TE+EE) + Planck 2018 (TT+TE+EE)
- SPT-3G (TE+EE) + Planck 2018 (TT, $\ell < 650$) + ACT DR4 (TT+TE+EE)
- SPT-3G (TE+EE) + Planck 2018 (TT+TE+EE) + ACT DR4 (TT+TE+EE, $\ell^{TT}_{\rm min} = 1800$)

Posterior distributions of EDE and ΛCDM parameters are shown in Fig. (4.7), and marginalised constraints are displayed in the associated table. To quantify the preference in favor of the EDE model over ΛCDM, we show the best-fit χ^2 values for these dataset combinations in Table (4.2). We do not see any hint in favor of the EDE model in SPT-3G + Planck 2018 data with $f_{\rm EDE} < 0.088$ (95% C.L.). We compute $\Delta\chi^2 = -5.7$, corresponding to an insignificant 1.5σ preference in favor of the EDE model. However, SPT-3G data combined with ACT DR4 and Planck 2018 TT ($\ell < 650$) show a hint for non-zero $f_{\rm EDE}$ with $f_{\rm EDE} = 0.121^{+0.040}_{-0.064}$ (formally 1.9σ away from zero). This comes with a higher χ^2 difference between EDE and ΛCDM:

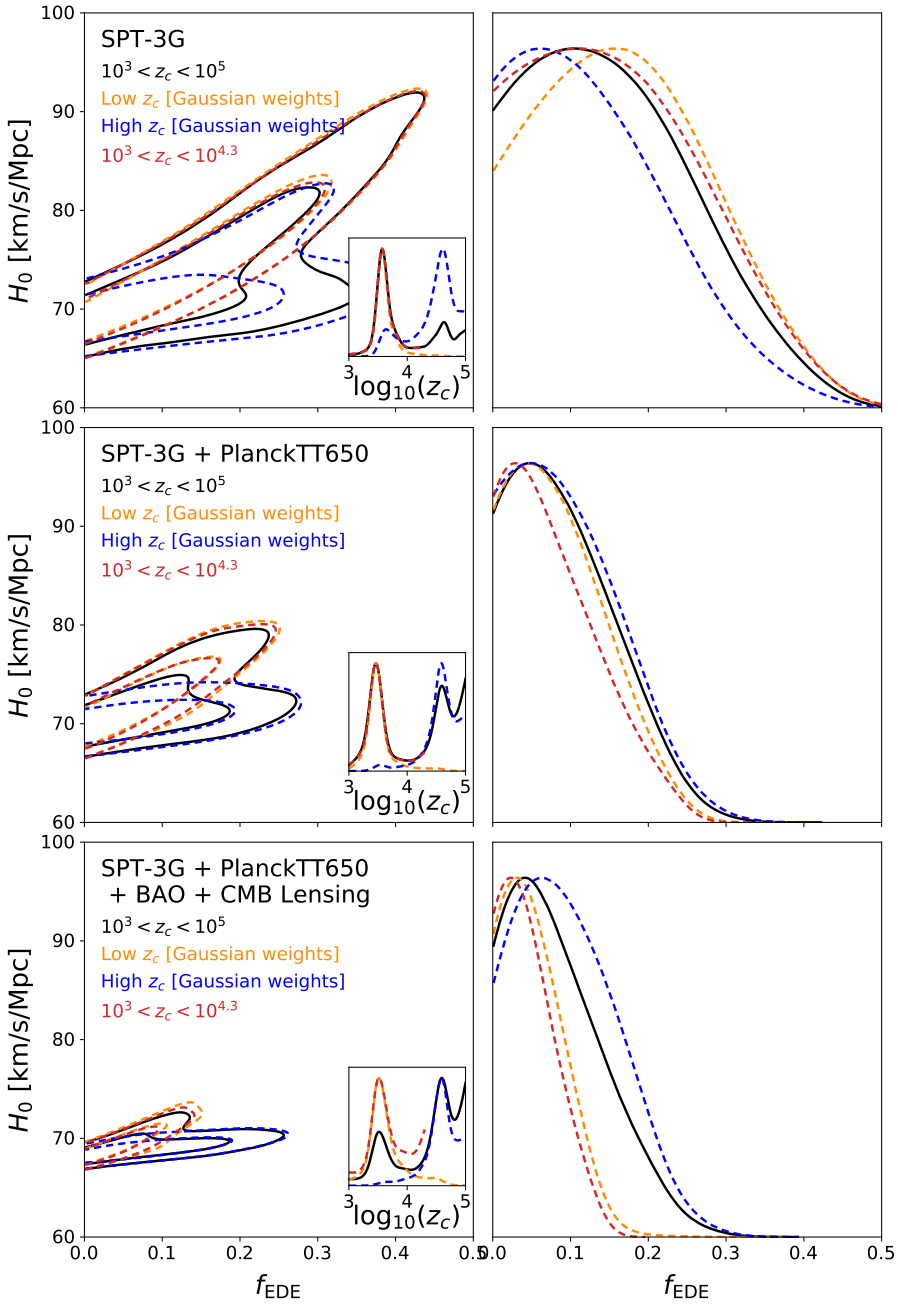

Figure 4.6: 2D contours at 68% and 95% C.L. in the reduced parameter space $f_{\rm EDE} - H_0$ and $f_{\rm EDE}$ 1D posterior distributions derived from the three datasets displayed in Fig. (4.5): SPT-3G [top panels], SPT-3G + PlanckTT650 [middle panel], and SPT-3G + PlanckTT650 + BAO + Planck Lensing [bottom panel]. We display the 2D posterior distribution using the z_c prior described in Table (4.1) as a black solid line. We apply a re-weighting of the samples according to z_c using Gaussian weights with mean $\mu_{\rm low} = 3.5$ and standard deviation $\sigma = 0.4$ to focus on the samples associated with a small value of z_c (orange). We use Gaussian weights with mean $\mu_{\rm high} = 4.5$ and standard deviation σ to focus on the high z_c samples (blue). We also display the posterior distributions derived from filtered samples using a narrower flat prior on $\log_{10}(z_c)$ (red), which matches the prior range used in [96], [112], [115], [116].

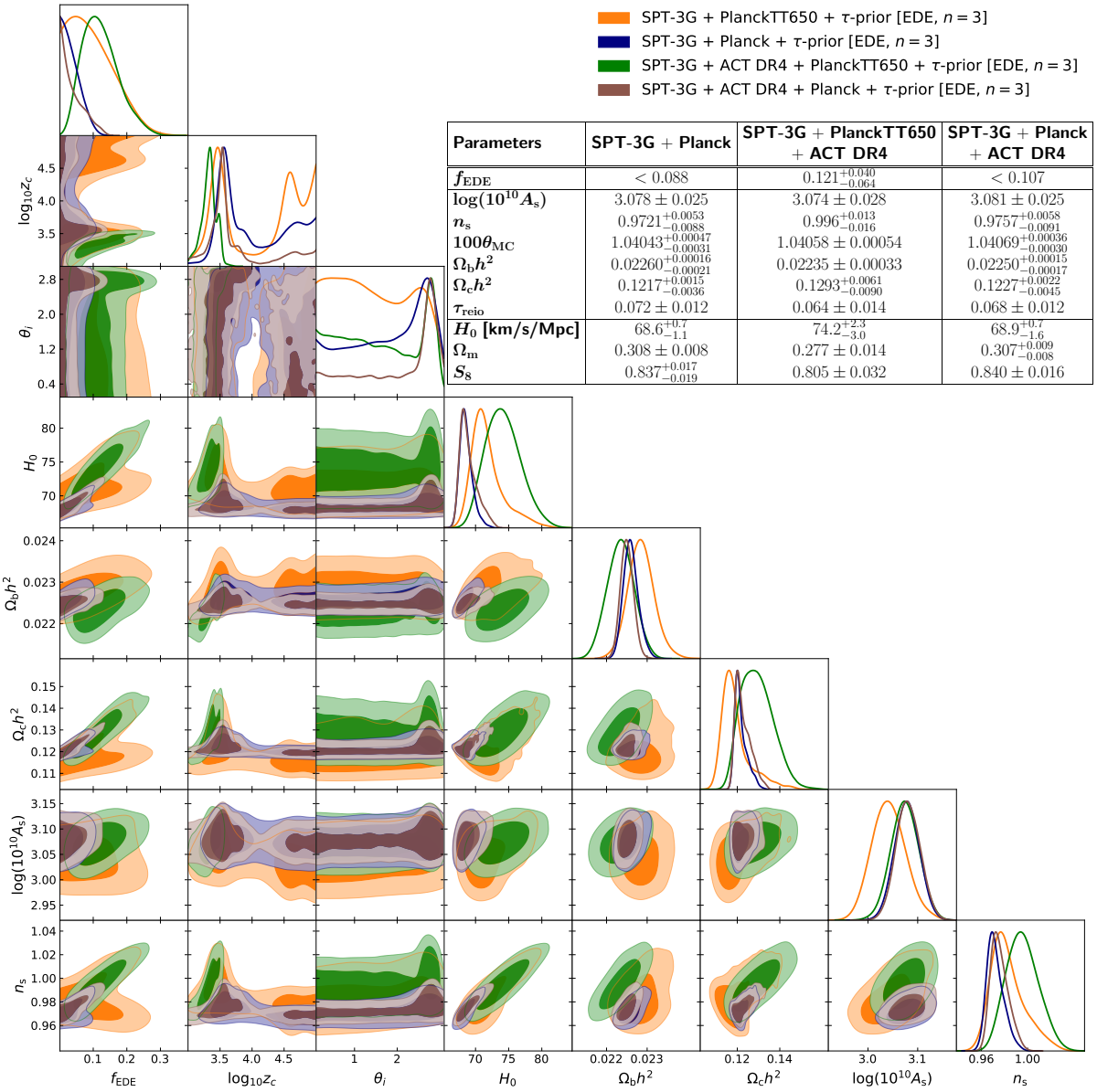

Parameters	SPT-3G + Planck	SPT-3G + PlanckTT650 + ACT DR4	SPT-3G + Planck + ACT DR4
$f_{\rm EDE}$	< 0.088	$0.121^{+0.040}_{-0.064}$	< 0.107
$\log(10^{10}A_{\rm s})$	3.078 ± 0.025	3.074 ± 0.028	3.081 ± 0.025
$n_{\rm s}$	$0.9721^{+0.0053}_{-0.0088}$	$0.996^{+0.013}_{-0.016}$	$0.9757^{+0.0058}_{-0.0091}$
$100\theta_{\rm MC}$	$1.04043^{+0.00047}_{-0.00031}$	1.04058 ± 0.00054	$1.04069^{+0.00036}_{-0.00030}$
$\Omega_{\rm b}h^2$	$0.02260^{+0.00016}_{-0.00021}$	0.02235 ± 0.00033	$0.02250^{+0.00015}_{-0.00017}$
$\Omega_{\rm c}h^2$	$0.1217^{+0.0015}_{-0.0036}$	$0.1293^{+0.0061}_{-0.0090}$	$0.1227^{+0.0022}_{-0.0045}$
$\tau_{\rm reio}$	0.072 ± 0.012	0.064 ± 0.014	0.068 ± 0.012
H_0 [km/s/Mpc]	$68.6^{+0.7}_{-1.1}$	$74.2^{+2.3}_{-3.0}$	$68.9^{+0.7}_{-1.6}$
$\Omega_{\rm m}$	0.308 ± 0.008	0.277 ± 0.014	$0.307^{+0.009}_{-0.008}$
S_8	$0.837^{+0.017}_{-0.019}$	0.805 ± 0.032	0.840 ± 0.016

Figure 4.7: Marginalised posterior distributions of EDE ($n = 3$) and ΛCDM parameters derived from SPT-3G (TE+EE) latest data [108] combined with Planck 2018 TT ($\ell < 650$) (orange); SPT-3G (TE+EE) combined with the full Planck 2018 dataset (TT+TE+EE) (dark blue); SPT-3G (TE+EE) combined with ACT DR4 (TT+TE+EE) [37], [106] and Planck 2018 TT ($\ell < 650$) (green); and SPT-3G (TE+EE) combined with ACT DR4 (TT+TE+EE) and the full Planck 2018 dataset (TT+TE+EE) (brown). We impose the same Gaussian prior on the reionisation optical depth τ for all the analyses. We display the 68% marginalised constraints and the upper/lower limits (95% C.L.) for the EDE and ΛCDM in the table associated with the figure.

$\Delta\chi^2$ of -11.4, which corresponds to a 99.0% C.L. (2.6σ) preference for EDE over the ΛCDM model. We note that the $\Delta\chi^2$ improvement is mainly driven by ACT DR4 data, for which we

Dataset		ΛCDM	EDE
SPT-3G	SPT-3G (TE+EE)	**513.7**	**509.6**
$\mathbf{\Delta\chi^2}$	.....	—	**−4.1**
	SPT-3G (TE+EE)	516.3	513.1
SPT-3G + PlanckTT650	Planck 2018 high-ℓ TT [$\ell < 650$]	250.6	250.1
	Planck 2018 low-ℓ TT	20.8	20.1
		787.7	**783.3**
$\mathbf{\Delta\chi^2}$	.....	—	**−4.4**
	SPT-3G (TE+EE)	516.8	513.8
	Planck 2018 high-ℓ TT [$\ell < 650$]	251.1	249.4
SPT-3G + PlanckTT650	Planck 2018 low-ℓ TT	21.7	22.6
+ BAO + Planck Lensing	BAO [6dF, SDSS DR7/DR12]	7.8	8.0
	Planck 2018 Lensing	8.7	8.6
		806.1	**802.4**
$\mathbf{\Delta\chi^2}$	.....	—	**−3.7**
	SPT-3G (TE+EE)	519.2	520.7
SPT-3G + PlanckTT650	Planck 2018 high-ℓ TT [$\ell < 650$]	251.3	249.2
+ACT DR4	Planck 2018 low-ℓ TT	21.1	20.6
	ACT DR4 (TT+TE+EE)	295.3	285.0
		1086.9	**1075.5**
$\mathbf{\Delta\chi^2}$	.....	—	**−11.4**
	SPT-3G (TE+EE)	520.4	519.0
SPT-3G + Planck	Planck 2018 high-ℓ (TT+TE+EE)	2343.3	2340.5
	Planck 2018 low-ℓ TT	23.0	21.5
		2886.7	**2881.0**
$\mathbf{\Delta\chi^2}$	.....	—	**−5.7**
	SPT-3G (TE+EE)	521.1	520.2
SPT-3G + Planck	Planck 2018 high-ℓ (TT+TE+EE)	2344.0	2340.9
+ ACT DR4	Planck 2018 low-ℓ TT	22.5	21.4
	ACT DR4 (TT+TE+EE)	244.4	242.2
		3132.0	**3124.7**
$\mathbf{\Delta\chi^2}$	.....	—	**−7.3**

Table 4.2: Best-fit χ^2 values computed for ΛCDM and EDE models and the different dataset combinations. We also display the value of $\Delta\chi^2$ with respect to ΛCDM in order to quantify the preference for the EDE model.

compute $\Delta\chi^2 = -10.3$. We also observe that including ACT DR4 data in the analysis provides a strong constraint on $\log_{10}(z_c)$, with a preference for lower values of z_c compared to SPT-3G

Parameter	PLIK (PR3)	CAMSPEC (PR3)
H_0 [km/s/Mpc]	$68.55^{+0.75}_{-1.3}$ (69.88)	$68.10^{+0.60}_{-0.94}$ (68.67)
$\Omega_b h^2$	$0.02260^{+0.00018}_{-0.00024}$ (0.02279)	$0.02239^{+0.00016}_{-0.00019}$ (0.02241)
$\Omega_c h^2$	$0.1224^{+0.0017}_{-0.0041}$ (0.1259)	$0.1213^{+0.0013}_{-0.0027}$ (0.1226)
$10^9 A_s$	2.204 ± 0.059 (2.245)	2.188 ± 0.061 (2.189)
n_s	$0.9719^{+0.0062}_{-0.0096}$ (0.9857)	$0.9687^{+0.0053}_{-0.0072}$ (0.9726)
$f_{\rm EDE}$	< 0.0947 (0.0730)	< 0.0788 (0.0349)
Parameter	CAMSPEC (PR4)	HILLIPOP (PR4)
H_0 [km/s/Mpc]	$68.00^{+0.50}_{-0.98}$ (68.60)	$67.51^{+0.57}_{-1.1}$ (68.15)
$\Omega_b h^2$	$0.02231^{+0.00015}_{-0.00018}$ (0.02233)	$0.02231^{+0.00016}_{-0.00020}$ (0.02245)
$\Omega_c h^2$	$0.1212^{+0.0011}_{-0.0027}$ (0.1232)	$0.1228^{+0.0013}_{-0.0032}$ (0.1251)
$10^9 A_s$	2.165 ± 0.059 (2.137)	2.137 ± 0.058 (2.135)
n_s	$0.9664^{+0.0047}_{-0.0076}$ (0.9728)	$0.9645^{+0.0054}_{0.0088}$ (0.9722)
$f_{\rm EDE}$	< 0.0776 (0.0425)	< 0.0766 (0.0474)

Table 4.3: Cosmological parameters 68% marginalised constraints and 95% upper limits derived from different Planck likelihoods and datasets using the EDE model.

+ PlanckTT650, resulting in a stronger correlation between $f_{\rm EDE}$ and H_0. Again, the hint for non-zero $f_{\rm EDE}$ and the preference in favor of EDE disappears when the full Planck 2018 data are included along with ACT DR4 and SPT-3G data. We find a 95% C.L. upper limit $f_{\rm EDE} < 0.107$.

4.4. Additional constraints from Planck

Previous EDE studies [3], [95], [96], [112], [115], [119] have used the Planck 2018 (PR3) PLIK likelihood. However, we know that the PLIK likelihood analysis contains some issues such as the $A_{\rm lens} \neq 1$ anomaly. Studying the EDE scenario using different likelihoods may be of interest to get a clear view of EDE constraints from CMB data. This section discuss the constraints obtained from other likelihoods : the HILLIPOP likelihood [100] that has already been introduced in Chapter 2, and the CAMSPEC likelihood [125], [126]. To be consistent with the previous section, we use the priors defined in Table (4.1) to derive the posterior distributions.

Figure (4.8) shows the marginalised posterior distributions derived from the PLIK likelihood for Planck PR3 data, the CAMSPEC likelihood for both PR3 and PR4 data and the HILLIPOP likelihood for PR4 data. Parameter marginalised constraints and best-fit values can be found in Table (4.3). The overall conclusion does not change when we use a different likelihood. However, we notice that the PLIK likelihood is the one that imposes the weakest constraint on the early dark energy density. While this analysis has yielded $f_{\rm EDE} < 0.0947$ (95%C.L.) using the PLIK PR3 likelihood, the other constraints are tighter with $f_{\rm EDE} < 0.0788$ (95%C.L.), $f_{\rm EDE} < 0.0776$ (95%C.L.) and $f_{\rm EDE} < 0.0766$ (95%C.L.) for CAMSPEC (PR3), CAMSPEC (PR4) and HILLIPOP (PR4) respectively. The maximum likelihood $f_{\rm EDE} = 0.0730$ derived from the PLIK likelihood is also higher than the best-fit derived from the CAMSPEC (PR3) likelihood

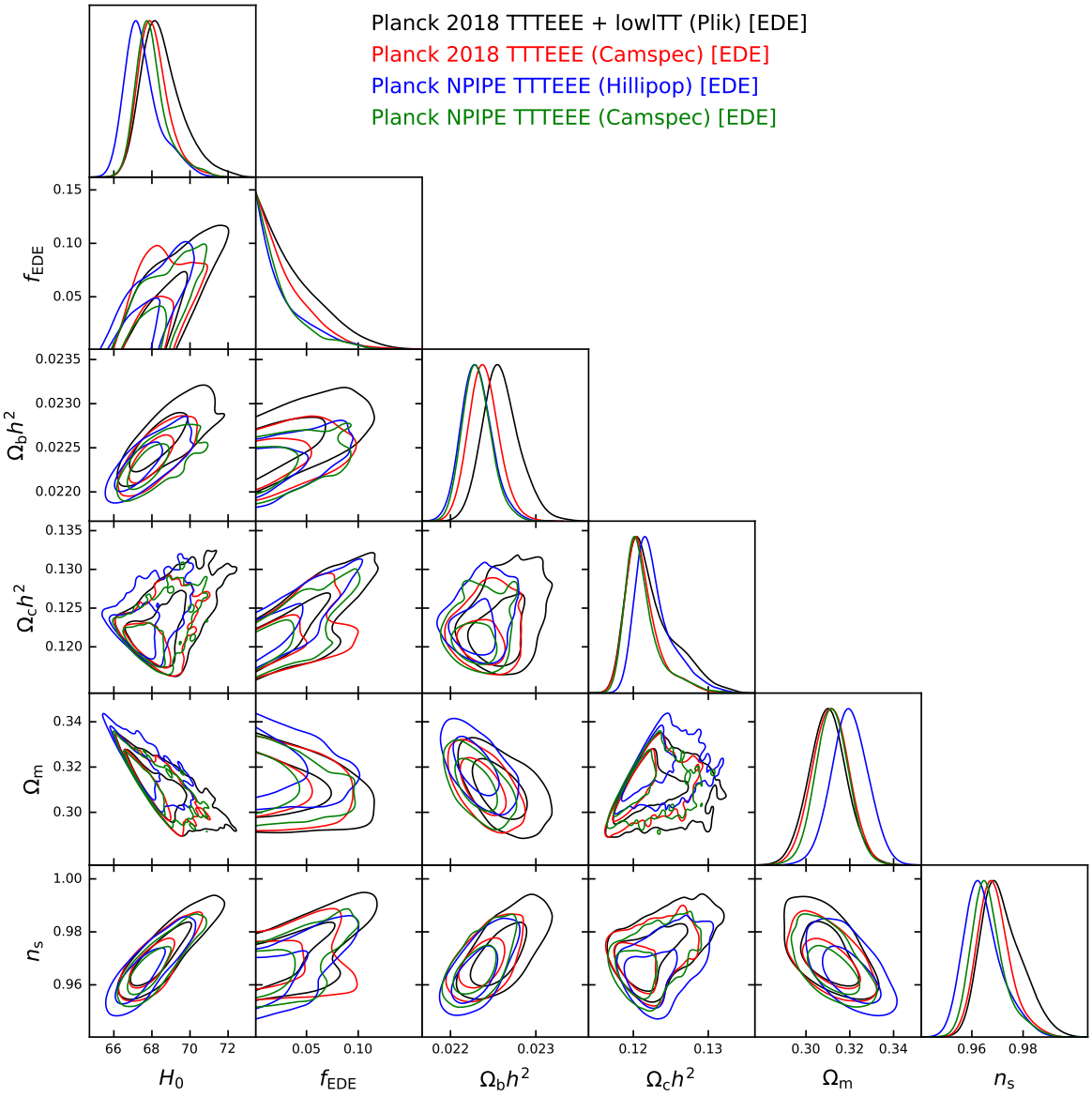

Figure 4.8: Marginalised posterior distributions for a set of cosmological parameters including the fractional early dark energy density derived from different Planck data and from different likelihoods. The black contours show the constraints from the PLIK likelihood with Planck PR3 data. An analysis using the same dataset with the CamSpec likelihood is displayed in red. We also show constraints from the Planck NPIPE dataset using the HiLLiPoP likelihood (blue) and the CamSpec likelihood (green).

$f_{\rm EDE} = 0.0349$.

4.5. Conclusion

The early dark energy scenario is a popular theoretical solution to the Hubble tension. In this chapter we have presented constraints on this ΛCDM extension from the most constraining data available to date. Although the EDE scenario seems to be disfavored by Planck data, ACT DR4 temperature and polarisation data shows a slight preference in favor of non-zero early dark energy in the primordial Universe. It was demonstrated in Ref. [112] that the EDE model is also a better fit of the ACT DR4 data than ΛCDM (with a small statistical significance). The third section is focused on the EDE constraints derived from the latest SPT-3G polarisation data. We have shown that this dataset is not sensitive enough to reject or favor the presence of a $\sim 10\%$ contribution of EDE to the total energy budget of the Universe near recombination. Finally, we have studied the constraints on EDE from Planck data using different likelihoods (HiLLiPoP and CamSpec) which also disfavor large fractions of early dark energy and impose smaller upper limits on $f_{\rm EDE}$. We expect that forthcoming data releases from ACT and SPT along with the next generation of CMB experiments (Simons Observatory [14] and CMB-S4 [15], [16]) should be able to discriminate between such a scenario and ΛCDM with a high statistical significance [96]. In particular, the next chapter will present the status of the sixth data release from the Atacama Cosmology Telescope that will provide a highly constraining dataset (similar to Planck for ΛCDM) significantly improving the current small scale measurements both in temperature and polarisation.

4.A. Early dark energy model in CAMB

Previous studies of the EDE model using Planck and ACT DR4 data have been performed with modified versions of CLASS [95], [96], [112], [115], [119]. In the analysis here, we use CMB power spectra computed with the CAMB Boltzmann solver, with an implementation of the EDE model based on Ref. [96].

We reproduce the results of Ref. [112] using the EDE implementation in CAMB. We use ACT DR4 (TT+TE+EE) in combination with the lowest multipoles of the Planck 2018 TT power spectrum ($\ell < 650$). The posterior distributions of EDE and ΛCDM parameters are displayed in Fig. 4.9.

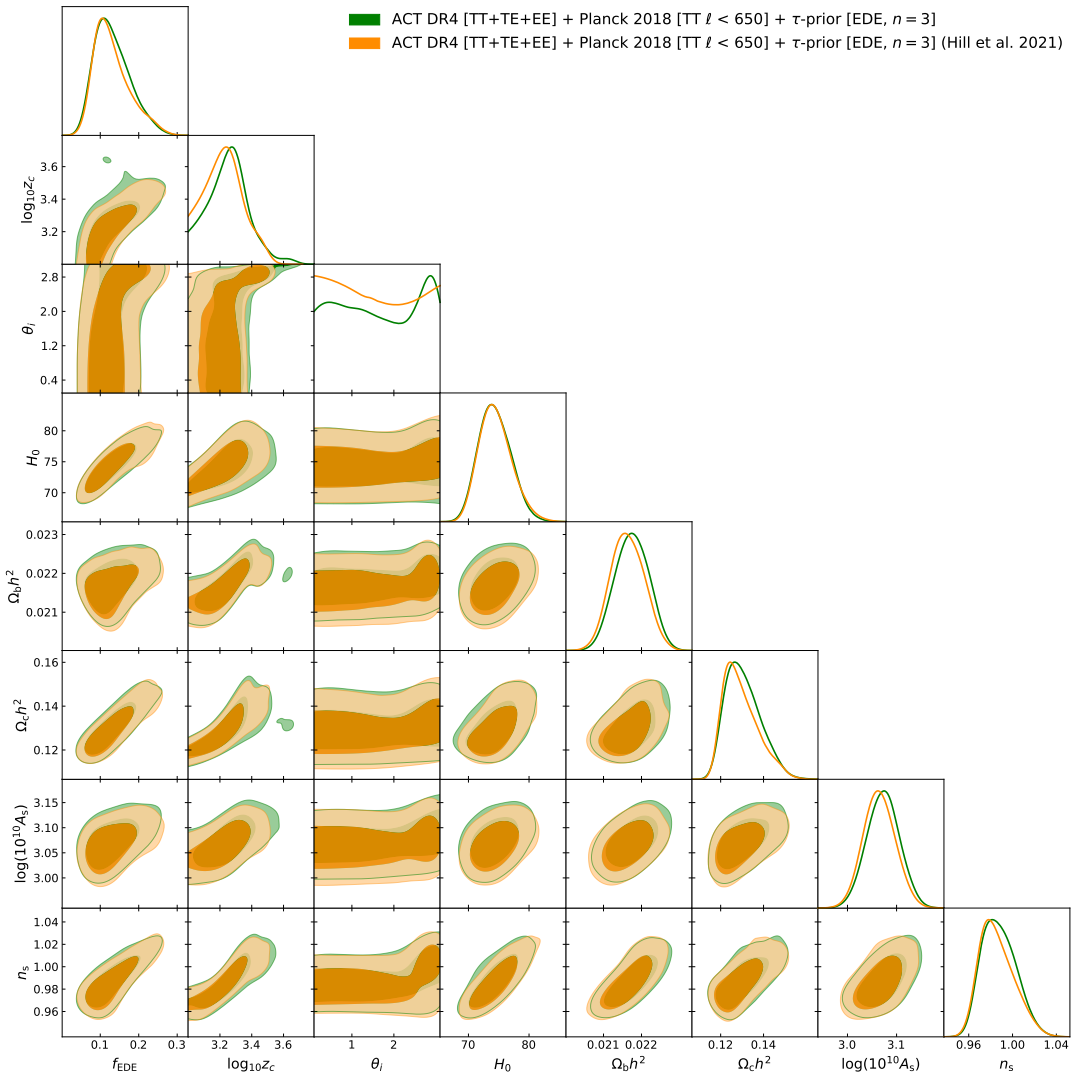

Figure 4.9: Marginalised posterior distributions of EDE ($n = 3$) and ΛCDM parameters derived from ACT DR4 (TT+TE+EE) and Planck 2018 TT ($\ell < 650$) using the CAMB Boltzmann solver (green) compared to the results obtained using CLASS_EDE [115] in Ref. [112] (orange). In both cases, we impose the same Gaussian prior on the reionisation optical depth τ.

We find that the posterior distributions of both EDE and ΛCDM parameters are in excellent agreement between the two implementations of the EDE scalar field model, and we recover a $f_{\rm EDE}$ posterior distribution that peaks 2.4σ away from zero in ACT DR4 + PlanckTT650 data with $f_{\rm EDE} = 0.132^{+0.034}_{-0.056}$. We observe an improvement in the χ^2 with respect to ΛCDM with $\Delta\chi^2 = -16.1$, corresponding to a 99.9% C.L. (3.3σ) preference in favor of the EDE model over ΛCDM mainly driven by the ACT DR4 data. This has already been observed in Ref. [112], with $\Delta\chi^2 = -15.4$ (99.8% C.L. or 3.2σ using the same datasets.

CHAPTER 5

CMB data analysis from high-resolution polarisation data with the Atacama Cosmology Telescope sixth data release

Summary

Previous chapters have highligted the importance of having indepdendent measurements of CMB anisotropies whether for the purpose of identifying potential systematics or for constraining models beyond ΛCDM. This chapter presents the status of the power spectrum data analysis for the sixth data release of the Atacama Cosmology Telescope. We introduce the PSpipe data analysis pipeline designed for the power spectra estimation from ACT DR6 and Simons Observatory large aperture telescope data. We then discuss preliminary results about the characterisation of the ACT DR6 maps that have been obtained using data collected from 2017 to 2022.

5.1. The Atacama Cosmology Telescope

The Atacama Cosmology Telescope was a 6 meter telescope located in the Atacama desert in Chile which measured the CMB anisotropies at arcminute resolution from 2008 to 2022 at an altitude of $\sim$ 5200 meters. The telescope was equipped with different receivers. The first was the Millimeter Bolometric Array Camera (MBAC), sensitive to temperature anisotropies only and which measured the CMB sky at 148, 218 and 277 GHz (see Ref. [127]). MBAC data were used in the first two ACT cosmological analyses (e.g. see Refs. [35], [128] for cosmological parameter constraints) which yielded to the cosmological constraints shown in Fig. (1.10). The receiver was first upgraded to ACTPol [129] that uses polarisation sensitive detector with transition-edge sensor (TES) bolometers cooled to 100 mK. The ACTPol receiver uses three polarisation detector arrays (PA) : PA1 & PA2, operating at 148 GHz and PA3, a dichroic detector array operating at 97 and 148 GHz [130]. Cosmological constraints derived from ACTPol data were presented in Refs. [36], [37], [106], [131]. The last upgrade of the ACT receiver known as Advanced ACT (AdvACT) has proposed to install 4 new detector arrays observing from 30 to 220 GHz : PA4 (150 & 220 GHz), PA5 (90 & 150 GHz), PA6 (90 & 150 GHz), and PA7 (30 & 40 GHz). The AdvACT upgrade started in 2016 and the telescope was operating until 2022.

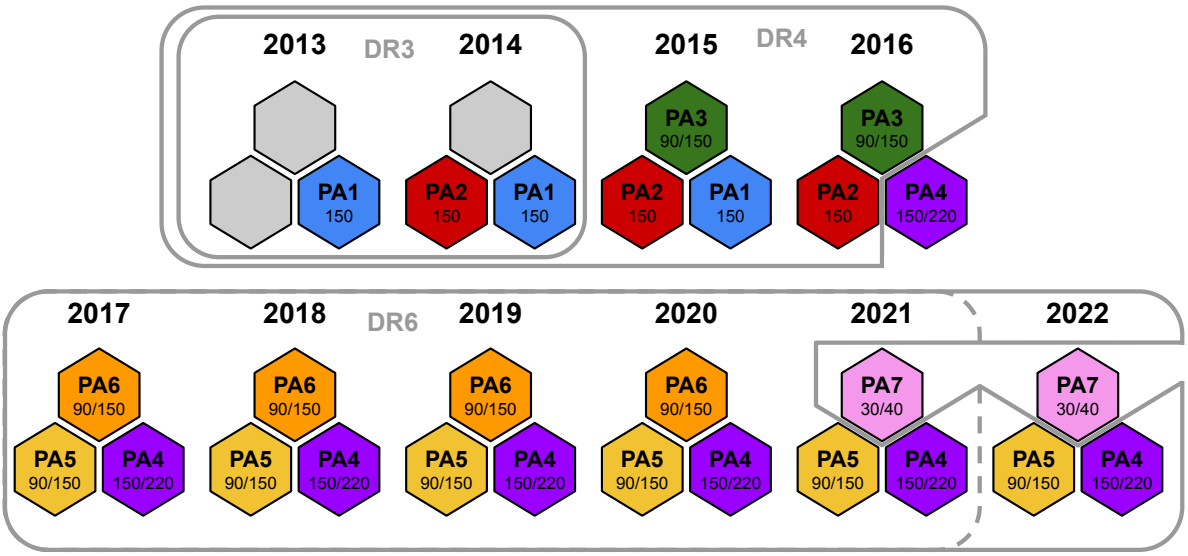

Figure 5.1: Diagram showing the polarisation arrays that were in use for ACTPol and AdvACT. The DR6.01 data release compiles data from 2017 to 2021 and the latest DR6 data also include data from 2022. Credit to *E. Storer*.

In addition to astrophysical foreground signals described in Section (1.3.6), ground-based CMB measurements are contaminated by the atmosphere. At millimeter wavelengths, atmospheric emissions are dominated by molecular oxygen lines around 60 GHz and at 119 GHz as well as by the water vapor emission lines at 22, 183, 325 and 380 GHz [132]. Atmospheric contamination may be mitigated by observing at frequencies lying between molecular emission lines (e.g. 30, 40, 90, 150, 220 GHz for AdvACT detector arrays). Observing at high altitude also helps to reduce the atmospheric contamination by lowering the Precipitable Water Vapor (PWV) value. Atmospheric emission increases the effective photon noise and induces correlated noise between different detectors. However, the atmosphere is only weakly polarised [133] and affects mainly the largest scales (at low multipole ℓ) allowing to measure accurately the polarisation anisotropies at small scales.

This chapter presents the analysis status of the most recent data from AdvACT collected from 2017 to 2022 focusing on the mid-frequency arrays PA4, PA5 and PA6. Part of these data have been used in the most recent ACT CMB lensing analysis which uses data acquired from 2017 to 2021 and are presented in Refs. [4], [5]. The night-time CMB power spectra analysis is still ongoing and Section (5.3) will discuss preliminary results on data products characterisation and consistency tests.

5.2. Description of the PSpipe data analysis pipeline

PSpipe is a public[1] CMB data analysis pipeline which estimates temperature and polarisation power spectra and their associated covariances from a set of maps and additional metadata such as beams and passbands. This pipeline heavily uses the python module pspy[2] which provides tools for CMB analysis in harmonic space following the MASTER algorithm [134]. This data analysis pipeline will be used to analyse the sixth data release of the Atacama Cosmology Telescope as well as the data from Simons Observatory Large Aperture Telescope. This section summarises the different steps of the data analysis pipeline.

5.2.1. Observation of a masked sky

Ground-based instruments only have access to a fraction of the celestial sphere. This leads to an incomplete measurement of the temperature anisotropies $\tilde{T}(\hat{n}) = W(\hat{n})T(\hat{n})$ where the window W encodes the accessible area. Space telescopes such as Planck are able to measure the CMB anisotropies on the full sky, but still require to mask some part of the sky to get rid of foreground contamination such as galactic dust emission and radio point sources. This masking operation comes at a cost : the estimated power spectra will suffer from mode mixing. Let's assume that the underlying signal observed at a frequency ν is $T^{\nu}(\hat{n})$ and that we observe this signal inside a window $W^{\nu}(\hat{n})$. The spherical harmonics coefficients of the masked temperature field are given by

$$\begin{aligned}
\tilde{a}^{T\nu}_{\ell m} &= \int d\hat{n} W^{\nu}(\hat{n}) T^{\nu}(\hat{n}) Y^{*}_{\ell m}(\hat{n}) \\
&= \sum_{\ell' m'} \left[\int d\hat{n} Y_{\ell' m'}(\hat{n}) W^{\nu}(\hat{n}) Y^{*}_{\ell m}(\hat{n}) \right] a^{T\nu}_{\ell' m'} \\
&= \sum_{\ell' m'} K_{\ell m \ell' m'} a_{\ell' m'}. \qquad (5.1)
\end{aligned}$$

Then, the cross power spectrum of the observed temperature fields $\tilde{T}^{\nu_1}(\hat{n})$ and $\tilde{T}^{\nu_2}(\hat{n})$ estimated from the standard pseudo-C_ℓ estimator $\hat{C}^{TT,\nu_1\times\nu_2}_{\ell} = \frac{1}{2\ell+1}\sum_m \tilde{a}^{T\nu_1}_{\ell m}\tilde{a}^{T\nu_2}_{\ell m}$ has the following mean value

$$\begin{aligned}
\langle \hat{C}^{TT,\nu_1\times\nu_2}_{\ell} \rangle &= \sum_{m,\ell_1,m_1} K^{\nu_1}_{\ell m \ell_1 m_1} K^{\nu_2 *}_{\ell m \ell_1 m_1} C^{TT,\nu_1\times\nu_2}_{\ell_1} \\
&= \sum_{\ell_1} M^{\nu_1\times\nu_2}_{\ell\ell_1} C^{TT,\nu_1\times\nu_2}_{\ell_1}. \qquad (5.2)
\end{aligned}$$

We can get an unbiased estimator by computing and deconvolving the mode coupling matrix. This process also applies to polarisation E and B modes such that

$$\begin{pmatrix} \langle \hat{C}^{EE,\nu_1\times\nu_2}_{\ell} \rangle \\ \langle \hat{C}^{EB,\nu_1\times\nu_2}_{\ell} \rangle \\ \langle \hat{C}^{BE,\nu_1\times\nu_2}_{\ell} \rangle \\ \langle \hat{C}^{BB,\nu_1\times\nu_2}_{\ell} \rangle \end{pmatrix} = \sum_{\ell_1} \begin{pmatrix} M^{++,\nu_1\nu_2}_{\ell\ell_1} & 0 & 0 & M^{--,\nu_1\nu_2}_{\ell\ell_1} \\ 0 & M^{++,\nu_1\nu_2}_{\ell\ell_1} & -M^{--,\nu_1\nu_2}_{\ell\ell_1} & 0 \\ 0 & -M^{--,\nu_1\nu_2}_{\ell\ell_1} & M^{++,\nu_1\nu_2}_{\ell\ell_1} & 0 \\ M^{--,\nu_1\nu_2}_{\ell\ell_1} & 0 & 0 & M^{++,\nu_1\nu_2}_{\ell\ell_1} \end{pmatrix} \begin{pmatrix} C^{EE,\nu_1\times\nu_2}_{\ell_1} \\ C^{EB,\nu_1\times\nu_2}_{\ell_1} \\ C^{BE,\nu_1\times\nu_2}_{\ell_1} \\ C^{BB,\nu_1\times\nu_2}_{\ell_1} \end{pmatrix}, \qquad (5.3)$$

[1] made available at https://github.com/simonsobs/PSpipe

[2] https://github.com/simonsobs/pspy

and

$$\begin{pmatrix} \langle \hat{C}_\ell^{TE,\nu_1\times\nu_2} \rangle \\ \langle \hat{C}_\ell^{TB,\nu_1\times\nu_2} \rangle \\ \langle \hat{C}_\ell^{ET,\nu_1\times\nu_2} \rangle \\ \langle \hat{C}_\ell^{BT,\nu_1\times\nu_2} \rangle \end{pmatrix} = \sum_{\ell_1} \begin{pmatrix} M_{\ell\ell_1}^{02,\nu_1\nu_2} & 0 & 0 & 0 \\ 0 & M_{\ell\ell_1}^{02,\nu_1\nu_2} & 0 & 0 \\ 0 & 0 & M_{\ell\ell_1}^{02,\nu_1\nu_2} & 0 \\ 0 & 0 & 0 & M_{\ell\ell_1}^{02,\nu_1\nu_2} \end{pmatrix} \begin{pmatrix} C_{\ell_1}^{TE,\nu_1\times\nu_2} \\ C_{\ell_1}^{TB,\nu_1\times\nu_2} \\ C_{\ell_1}^{ET,\nu_1\times\nu_2} \\ C_{\ell_1}^{BT,\nu_1\times\nu_2} \end{pmatrix}, \tag{5.4}$$

where $M_{\ell\ell_1}^{02,\nu_1\nu_2}$ and $M_{\ell\ell_1}^{++/--,\nu_1\nu_2}$ are the mode coupling matrices computed from the spin-2 spherical harmonic decomposition of the polarisation field. If we combine Eqs. (5.2), (5.3) and (5.4), we get the linear relation $\langle \hat{\mathbf{C}}_\ell^{\nu_1\times\nu_2} \rangle = \sum_{\ell_1} \mathcal{M}_{\ell\ell_1}^{\nu_1\times\nu_2} \mathbf{C}_{\ell_1}^{\nu_1\times\nu_2}$ from which we build an unbiased pseudo-C_ℓ estimator

$$\tilde{\mathbf{C}}_\ell^{\nu_1\times\nu_2} = \sum_{\ell_1} \left[\mathcal{M}^{\nu_1\times\nu_2 -1} \right]_{\ell\ell_1} \hat{\mathbf{C}}_{\ell_1}^{\nu_1\times\nu_2}. \tag{5.5}$$

The mode coupling at the power spectrum level also affects the covariance of the unbiased pseudo-C_ℓ estimator

$$\begin{aligned} \Xi_{\ell\ell'}^{\nu_1\times\nu_2,\nu_3\times\nu_4} &= \langle \left(\tilde{\mathbf{C}}_\ell^{\nu_1\times\nu_2} - \mathbf{C}_\ell^{\nu_1\times\nu_2} \right) \left(\tilde{\mathbf{C}}_{\ell'}^{\nu_3\times\nu_4} - \mathbf{C}_{\ell'}^{\nu_3\times\nu_4} \right) \rangle \\ &= \sum_{\ell_1\ell_2} \left[\mathcal{M}^{\nu_1\times\nu_2 -1} \right]_{\ell\ell_1} \mathrm{cov} \left(\hat{\mathbf{C}}_{\ell_1}^{\nu_1\times\nu_2}, \hat{\mathbf{C}}_{\ell_2}^{\nu_3\times\nu_4} \right) \left[\mathcal{M}^{\nu_3\times\nu_4 -1} \right]_{\ell'\ell_2}. \end{aligned} \tag{5.6}$$

5.2.2. Power spectrum estimation and covariance

The signal $X \in \{T, E, B\}$ observed with an experiment α at the frequency ν can be modeled as

$$X_{i,\ell m}^{\alpha\nu} = b_\ell^{\alpha\nu} X_{\ell m}^{\nu} + n_{i,\ell m}^{X,\alpha\nu}, \tag{5.7}$$

where $b_\ell^{\alpha\nu}$ accounts for the finite angular resolution of the instrument (the maps are convolved with the beam) and $n_{i,\ell m}^{\alpha\nu}$ accounts for the noise in the i-th split map. By definition, the difference between split maps is due to the fact that each split map contains an independent realisation of the noise. Considering two experiments α and β that have provided maps at frequencies ν_1 and ν_2 respectively, we build a power spectrum estimator such as

$$\hat{C}_\ell^{XY,\alpha\nu_1\times\beta\nu_2} = \frac{1}{N_{\alpha\beta}} \frac{1}{2\ell+1} \sum_{i=1}^{n_s^\alpha} \sum_{j=1}^{n_s^\beta} \frac{1}{b_\ell^{\alpha\nu_1} b_\ell^{\beta\nu_2}} \sum_m X_{i,\ell m}^{\alpha\nu_1} Y_{j,\ell m}^{\beta\nu_2 *} (1 - \delta_{ij}\delta_{\alpha\beta}). \tag{5.8}$$

where $N_{\alpha\beta} = n_s^\beta (n_s^\alpha - \delta_{\alpha\beta})$ is the number of possible split combination. This estimator uses only the cross power spectra between splits since different splits do not contain the same noise realisation and are considered independent such that $\langle n_{i,\ell m}^{\alpha\nu_1} n_{j,\ell m}^{\beta\nu_2 *} \rangle = \delta_{ij}\delta_{\alpha\beta} N_\ell^{XY,\alpha,\nu_1\times\nu_2}$. The noise power spectrum is also estimated from the data from the difference between the mean auto-spectra and the mean cross-spectra for given combination of arrays and frequencies. Assuming that we have a full-sky measurement of CMB anisotropies, the covariance of this estimator may be computed analytically, accounting for the noise and the combinatorics [135]

$$\Xi^{\alpha\nu_1\times\beta\nu_2,\gamma\nu_3\times\eta\nu_4}_{RSXY,\ell} = \frac{1}{2\ell+1}\left[C_\ell^{RX,\alpha\nu_1\times\gamma\nu_3}C_\ell^{SY,\beta\nu_2\times\eta\nu_4} + C_\ell^{RY,\alpha\nu_1\times\eta\nu_4}C_\ell^{SX,\beta\nu_2\times\gamma\nu_3}\right] \tag{5.9}$$

$$+ \frac{1}{2\ell+1}\left[C_\ell^{RX,\alpha\nu_1\times\gamma\nu_3}\tilde{N}_\ell^{SY,\beta\nu_2\times\eta\nu_4}f^{\alpha\gamma}_{\beta\eta} + C_\ell^{SY,\beta\nu_2\times\eta\nu_4}\tilde{N}_\ell^{RX,\alpha\nu_1\times\gamma\nu_3}f^{\beta\eta}_{\alpha\gamma}\right] \tag{5.10}$$

$$+ \frac{1}{2\ell+1}\left[C_\ell^{RY,\alpha\nu_1\times\eta\nu_4}\tilde{N}_\ell^{SX,\beta\nu_2\times\gamma\nu_3}f^{\alpha\eta}_{\beta\gamma} + C_\ell^{SX,\beta\nu_2\times\gamma\nu_3}\tilde{N}_\ell^{RY,\alpha\nu_1\times\eta\nu_4}f^{\beta\gamma}_{\alpha\eta}\right] \tag{5.11}$$

$$+ \frac{1}{2\ell+1}\left[\tilde{N}_\ell^{RX,\alpha\nu_1\times\gamma\nu_3}\tilde{N}_\ell^{SY,\beta\nu_2\times\eta\nu_4}g_{\alpha\gamma,\beta\eta} + \tilde{N}_\ell^{RY,\alpha\nu_1\times\eta\nu_4}\tilde{N}_\ell^{SX,\beta\nu_2\times\gamma\nu_3}g_{\alpha\eta,\beta\gamma}\right], \tag{5.12}$$

where $g_{\alpha\gamma,\beta\eta}$ and $f^{\beta\eta}_{\alpha\gamma}$ are determined from the combinatorics of the survey (i.e. the number of splits ...) such that

$$g_{\alpha\gamma,\beta\eta} = \frac{n_s^\alpha(n_s^\beta\delta_{\alpha\gamma}\delta_{\beta\eta} - \delta_{\alpha\beta\gamma\eta})}{n_s^\beta n_s^\eta(n_s^\alpha - \delta_{\alpha\beta})(n_s^\gamma - \delta_{\gamma\eta})}, \tag{5.13}$$

$$f^{\beta\eta}_{\alpha\gamma} = \frac{n_s^\alpha\left(n_s^\beta n_s^\eta\delta_{\alpha\gamma} - n_s^\beta\delta_{\alpha\gamma\eta} - n_s^\eta\delta_{\alpha\gamma\beta} + \delta_{\alpha\gamma\beta\eta}\right)}{n_s^\beta n_s^\eta(n_s^\alpha - \delta_{\alpha\beta})(n_s^\gamma - \delta_{\gamma\eta})}. \tag{5.14}$$

$\tilde{N}_\ell^{XY,\alpha\nu_1\times\beta\nu_2} = N_\ell^{XY,\alpha\nu_1\times\beta\nu_2}/(b_\ell^{\alpha\nu_1}b_\ell^{\beta\nu_2})$ is the noise power spectrum normalised by the beam arising from the fact that we deconvolve the beam in the power spectrum estimator. (Eq. (5.8))

5.2.3. Foreground modelling at the power spectra level

To get an analytical estimate of the covariance matrices, one needs to have an estimate of the underlying signal $C_\ell^{XY,\nu_1\times\nu_2}$ where $(X,Y)\in\{T,E,B\}^2$. As discussed in Section (1.3.6), the observed signal is a sum of the CMB signal and astrophysical foreground contributions. This section will describe the models used to parametrise the different foreground components. We model the foregrounds at the power spectrum level by taking the sum of the different contributions to the observed sky such that

$$\begin{aligned} D_\ell^{XY,\nu_1\times\nu_2} = {} & D_\ell^{XY,\mathrm{CMB}} + D_\ell^{XY,\mathrm{dust},\nu_1\times\nu_2} + D_\ell^{XY,\mathrm{radio},\nu_1\times\nu_2} + D_\ell^{XY,\mathrm{CIB},\nu_1\times\nu_2} \\ & + D_\ell^{XY,\mathrm{tSZ},\nu_1\times\nu_2} + D_\ell^{XY,\mathrm{tSZ}\times\mathrm{CIB},\nu_1\times\nu_2} + D_\ell^{XY,\mathrm{kSZ}}. \end{aligned} \tag{5.15}$$

The following paragraphs describe the foreground modelling used in the PSpipe and implemented in the public software fgspectra[3] as described in Ref. [105].

Galactic dust

The diffuse dust emission contributes to both temperature and polarisation. We model it by rescaling a power law template $\ell^{\alpha^{XY}_{\mathrm{dust}}}$ with a modified black body spectrum also known as a gray body model.

$$D_\ell^{XY,\mathrm{dust},\nu_1\times\nu_2} = A^{XY}_{\mathrm{dust}}\left(\frac{\ell}{\ell_0}\right)^{\alpha^{XY}_{\mathrm{dust}}}\left(\frac{\mu(\nu_1,\beta_{\mathrm{dust}})\mu(\nu_2,\beta_{\mathrm{dust}})}{\mu^2(\nu_0,\beta_{\mathrm{dust}})}\right), \tag{5.16}$$

[3] available at https://github.com/simonsobs/fgspectra

where $\mu(\nu, \beta_{\rm dust}) = \nu^{\beta_{\rm dust}} B_\nu(T_{\rm dust}) g(\nu)$ with $g^{-1}(\nu) = (\partial B_\nu/\partial T)|_{T_{\rm CMB}}$, the conversion factor from thermodyamic units to flux. Following measurements of Refs. [107], [136], we set $\alpha^{TT}_{\rm dust} = -0.6$ and $\alpha^{EE/BB/TE/TB}_{\rm dust} = -0.4$. The spectral index is fixed to $\beta_{\rm dust} = 2.5$ and we assume a temperature of $T_{\rm dust} = 19.6$ K for the dust grains. The galactic dust power spectrum defined this way is normalised to $A^{XY}_{\rm dust}$ μK^2 at $\ell_0 = 3000$ and at a frequency $\nu_0 = 150$ GHz.

Radio sources Radio sources also contributes significantly to the foreground contamination both in temperature and polarisation at small scales. We rescale a power-law template describing the scale dependence with a power-law SED $\nu^{\alpha^{XY}_{\rm radio}}$.

$$D_\ell^{XY,{\rm radio},\nu_1\times\nu_2} = A^{XY}_{\rm radio} \left(\frac{\ell(\ell+1)}{\ell_0(\ell_0+1)}\right) \left(\frac{\nu_1\nu_2}{\nu_0^2}\right)^{\alpha^{XY}_{\rm radio}} \left(\frac{g(\nu_1)g(\nu_2)}{g^2(\nu_0)}\right), \tag{5.17}$$

where we set $\alpha^{XY}_{\rm radio} = -2.5$ for $XY \in \{TT, EE, BB, TE, TB\}$. The only remaining degrees of freedom are the 150 GHz amplitudes at $\ell = 3000$ $A^{XY}_{\rm radio}$.

Cosmic Infrared Background

The CIB emission is described by the sum of two components : a clustered part (CIBc) and a Poisson distributed part (CIBp). The CIBc contribution is modeled from an hybrid template based on Planck measurements [34] below $\ell = 3000$ and a power-law template $\ell^{0.8}$ for $\ell \geq 3000$ as described in Ref. [106]. This template is then multiplied with a gray body SED. The CIBp contribution is modeled as the product of a power-law template $\ell(\ell+1)$ with a gray body SED.

$$D_\ell^{TT,{\rm CIBc},\nu_1\times\nu_2} = A_c D^{\rm CIBc}_{\ell,0} \left(\frac{\mu(\nu_1,\beta_c)\mu(\nu_2,\beta_c)}{\mu^2(\nu_0,\beta_c)}\right) \tag{5.18}$$

$$D_\ell^{TT,{\rm CIBp},\nu_1\times\nu_2} = A_p \left(\frac{\ell(\ell+1)}{\ell_0(\ell_0+1)}\right) \left(\frac{\mu(\nu_1,\beta_p)\mu(\nu_2,\beta_p)}{\mu^2(\nu_0,\beta_p)}\right). \tag{5.19}$$

The temperature of the gray body is set to $T_d = 19.6$ K as it was done for the galactic dust emission. β_c and β_p are the spectra indices of the clustered and Poisson distributed contributions respectively.

Thermal and kinetic Sunyaev Zel'dovich effects

The contributions of tSZ and kSZ are modeled using templates from Ref. [137] and Ref. [138] respectively. The templates have been normalised to $A_{\rm tSZ}$ and $A_{\rm kSZ}$ in μK^2 at $\ell = 3000$ and the tSZ and kSZ power spectra are given by

$$D_\ell^{TT,{\rm tSZ},\nu_1\times\nu_2} = A_{\rm tSZ} \frac{f(\nu_1)f(\nu_2)}{f^2(\nu_0)} D^{\rm tSZ}_{\ell,0} \tag{5.20}$$

$$D_\ell^{TT,{\rm kSZ},\nu_1\times\nu_2} = A_{\rm kSZ} D^{\rm kSZ}_{\ell,0}, \tag{5.21}$$

where $f(\nu) = x{\rm coth}(x/2) - 4$ with $x = h\nu/k_B T_{\rm CMB}$ encodes the frequency dependence of the tSZ emission [139], [140].

tSZ-CIB correlations

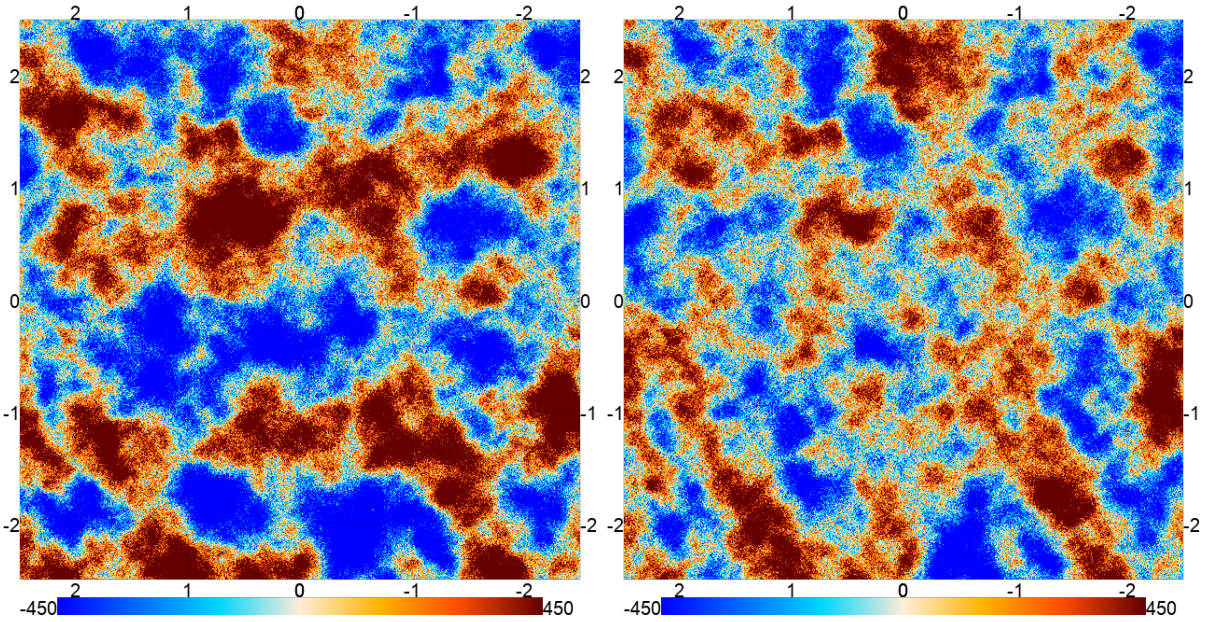

(a) (b)

Figure 5.2: Coadded 220 GHz ACT DR6 maps with no filtering (a) and after applying a filter in Fourier space. The unfiltered map shows horizontal features that are handled by the filter which removes modes with $|\ell_x| < \ell_x^{\rm cut}$ and $|\ell_y| < \ell_y^{\rm cut}$.

We expect a non-negligible correlation between the tSZ effect and the IR emission from clustered dusty galaxies. We use a template $D_{\ell,0}^{\rm tSZ\times CIB}$ from Ref. [141] and rescale it with a joint tSZ-CIB SED such that

$$D_\ell^{TT,\rm tSZ\times CIB} = -\xi\sqrt{A_c A_{\rm tSZ}}\left(\frac{f(\nu_1)\mu(\nu_2,\beta_c)+f(\nu_2)\mu(\nu_1,\beta_c)}{f(\nu_0)\mu(\nu_0,\beta_c)}\right) D_{\ell,0}^{\rm tSZ\times CIB}. \tag{5.22}$$

ξ encodes the correlation between tSZ and CIB emissions at $\ell = 3000$ and $\nu = 150$ GHz. As pointed out in Ref. [105], this contribution is correlated with the kSZ contribution and therefore should be included to provide reliable constraints.

Bandpass integration

In practice, detectors do not have a perfect frequency resolution and are therefore sensitive to a range of frequencies. A sky signal $T(\hat{n},\nu)$ will be weighted by the transmission function (or bandpass) of the detector wafer α such that we measure the following signal

$$T^\alpha(\hat{n}) = \int d\nu B^\alpha(\nu) T(\hat{n},\nu). \tag{5.23}$$

In is common to work in CMB units — in which the CMB signal does not depend on the frequency. The signal measured by the wafer α in CMB units is computed from

$$T^\alpha\ [\mathrm{K_{CMB}}] = \int d\nu \left(\frac{B^\alpha(\nu) g(\nu)}{\int d\nu' B^\alpha(\nu') g(\nu')}\right) T(\nu)\ [\mathrm{K_{CMB}}], \tag{5.24}$$

as implemented in FGSPECTRA, where $g(\nu)$ is the conversion factor from flux to thermodynamic units defined above.

5.2.4. Filtering ground contamination

The signal measured from ground-based telescopes such as ACT may have a stripy structure. These features arise from ground pickup or other scan synchronous effects. To prevent our measurement from being affected by this nuisance, PSPIPE allows to apply a filtering in Fourier space to remove horizontal and vertical features in the maps. The idea is to Fourier transform the map and to apply two cuts in Fourier space $|\ell_x| \leq \ell_x^{\rm cut}$ and $|\ell_y| \leq \ell_y^{\rm cut}$. Such filtering operation also removes part of the signal and therefore we need to estimate the filter-induced transfer function. One can derive easily an analytical expression for such a filter. The total number of modes in the bin $[\ell, \ell + d\ell]$ is given by $dN_{\rm modes} = 2\pi\ell d\ell$. The filtering operation removes part of the modes such that $dN_{\rm modes}^{\rm filtered} = \left(2\pi\ell - 4\ell_x^{\rm cut} - 4\ell_y^{\rm cut}\right) d\ell$. This back of the enveloppe calculation leads to an estimate of the k-space filter transfer function

$$F(\vec{\ell}) = \frac{dN_{\rm modes}^{\rm filtered}}{dN_{\rm modes}} = 1 - 2\frac{\ell_x^{\rm cut} + \ell_y^{\rm cut}}{\pi|\vec{\ell}|}. \tag{5.25}$$

The effect of the filter is illustrated on the second panel of Fig. (5.2) which shows the filtered version of the left panel. Filtering in Fourier space may also induce a mixing between E and B modes as discussed in Ref. [106]. In practice, PSPIPE provides tools to get a high precision numerical estimate of the transfer matrix that quantify the impact of the filter on T,E and B modes.

5.3. Power spectrum analysis of the ACT sixth data release

This section summarises the status of the ACT DR6 data power spectrum analysis as of Spring 2023. ACT DR6 will provide maps at different frequency bands centered on 97, 149 and 225 GHz, covering $19,000$ deg^2 before applying a galactic cut. A first cosmological analysis on CMB lensing [4], [5] has been performed with preliminary DR6 science ready data products refered as DR6.01. This intermediate release compiles data from 2017 to 2021 for the three dichroic detector arrays PA4, PA5 and PA6 as depicted in Fig. (5.1). In the following we will also discuss preliminary results based on the latest version of DR6 maps (hereafter called v4) that includes data from the 2022 season.

5.3.1. Summary of the map-making process

Raw data are collected as a set of samples measured at different times. These data are split into small data streams called time ordered data (TOD). The TODs are stored in a data vector $\vec{d}$, and one needs to solve the following linear system to estimate the sky signal $\vec{m}$,

$$\vec{d} = P\vec{m} + \vec{n}. \tag{5.26}$$

Here $\vec{n}$ encodes the noise, assumed to be normally distributed with a covariance $\langle \vec{n}\vec{n}^\top \rangle = N$, and P is the pointing matrix that map the pixel into the TOD space. In principle this can be solved exactly using a maximum likelihood approach such that

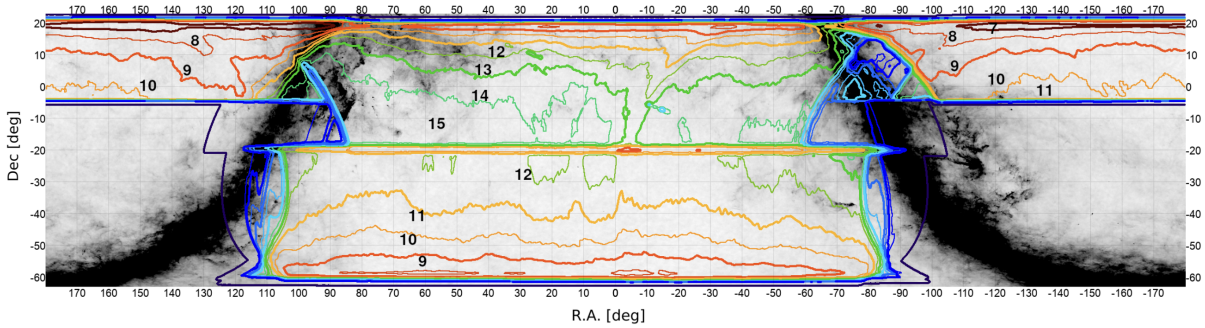

Figure 5.3: Sky coverage and depth of ACT DR6 night time observations in right ascension (R.A.) - declination (Dec.) equatorial coordinates. The background map is the Planck 353 GHz temperature map. The contours are corresponding to different noise levels in μK − arcmin. Taken from Ref. [4].

$$\vec{m} = \left(P^\top N^{-1} P\right)^{-1} P^\top N^{-1} \vec{d}. \tag{5.27}$$

In practice, the matrix $P^\top N^{-1} P$ is very large (corresponding to the number of pixels) and cannot be loaded into memory. Therefore, iterative methods such as conjugate gradient algorithms are used to solve this linear system without ever representing the entire matrix. Since the noise is estimated from the TODs themselves, the conjugate gradient steps are also repeated to get a better estimate of the noise at each iteration. To get rid of the noise bias in the power spectrum estimation, the samples are splitted into subsets with similar properties. A more detailed description of the map-making process is available in Ref. [142] and the upcoming ACT DR6 map-making paper.

DR6.01 maps have a 0.5 arcmin resolution and consists in 8 splits per array and frequency resulting in 48 maps of the signal as well as inverse variance maps to quantify the depth of each maps and cross-linking maps that measure the amount of cross-linking in the maps. There is no pickup filtering at the TOD level and these nuisances are handled with the filter in Fourier space described in Section (5.2.4). Figure (5.3) shows the sky coverage and depth of the ACT DR6 maps from night time observations from which we will estimate the CMB power spectra and discuss their consistency in the following subsections.

Although maximum likelihood estimators are by definition unbiased if we have a correct model for the data, Ref. [143] have identified two sources that can lead to a significant bias in the reconstructed signal at large scales. The first source of bias is called sub-pixel errors. It is due to the fact that we discretise the sky into 0.5 arcmin pixels while the underlying signal have a smooth evolution (infinite resolution). The second, and more important source of bias that have been identified is the miscalibration of individual detector gains. Both effects lead to a large-scale power deficit that has been identified in DR6 data and will be discussed in Section (5.3.6). A re-calibration of detector gains has been performed resulting in a new set of DR6 maps called DR6v4. The other changes compared to the DR6.01 are the use of a bilinear interpolation instead of a nearest neighbors interpolation and the number of splits (4 splits for

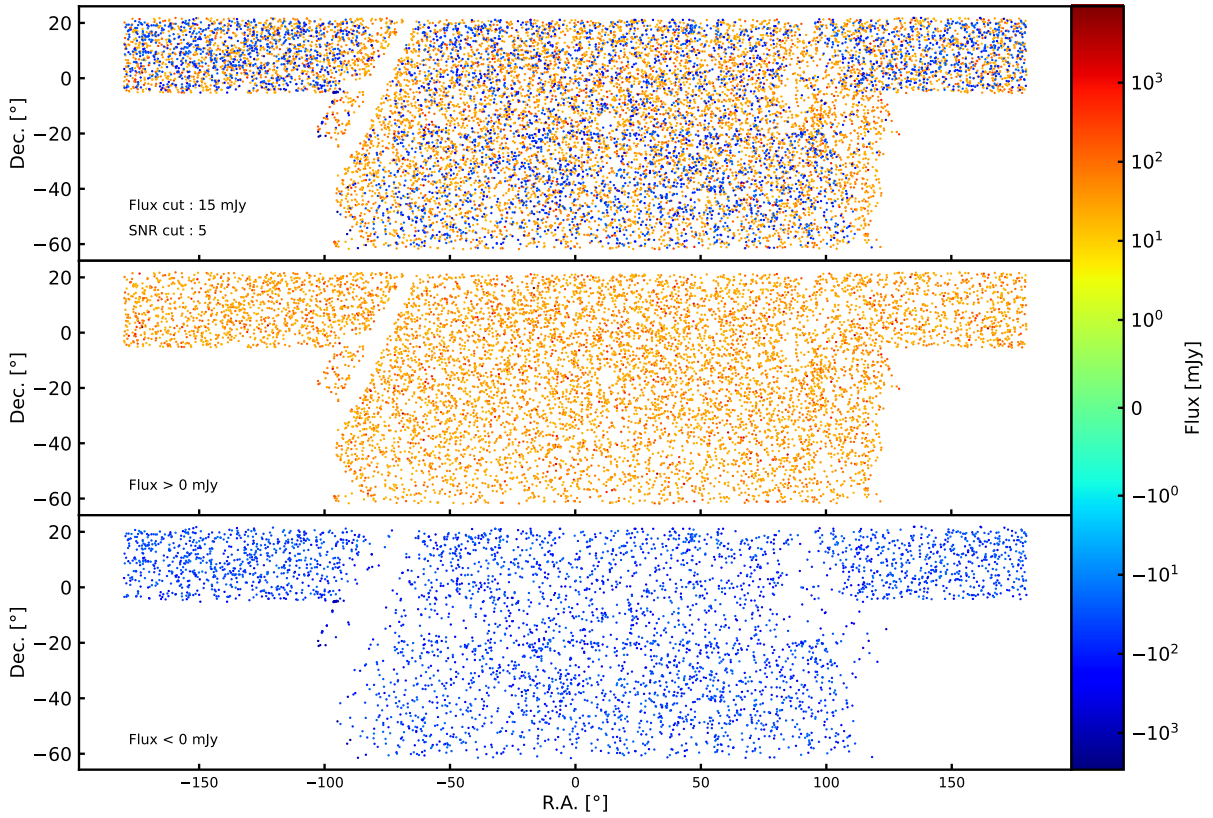

Figure 5.4: Visualisation of the source catalog used to build a point source mask for the DR6 analysis. Sources are displayed in the right ascension (R.A.) - declination (Dec.) coordinate system. The colorscale corresponds to their flux in mJy at 150 GHz. The top panel displays all the sources and the two last panels show the sources with a positive flux (middle) and negative flux (bottom) that correspond to galaxy clusters.

the DR6v4 compared to DR6.01). It has been shown that the large-scale power loss identified in DR6.01 maps has a negligible impact on the DR6 CMB lensing analysis in Refs. [4], [5].

5.3.2. Estimation of the beam

The beam is a way of quantifying the instrument angular resolution. Since it appears in the power spectrum estimator Eq. (5.8), it needs to be measured precisely to prevent the power spectra from being biased. It can be measured from observation of sources. The main beam is computed from Uranus observations by measuring its radial intensity profile for each observation season. Then, a weighted average of the per-season beams is performed to get a set of per-split beams (8 for DR6.01 and 4 for DR6v4). As described in Ref. [144], additional corrections (jitter corrections) are included to account for the broadening of the effective beams due to the fact that the final maps contain multiple observations at different times. Additionally, since Uranus is expected to be weakly polarised, the polarisation signal observed from Uranus observation provides a direct measurement of temperature-to-polarisation leakage. Further observations of Saturn are used to constrain the polarisation sidelobes that are removed during the map making process.

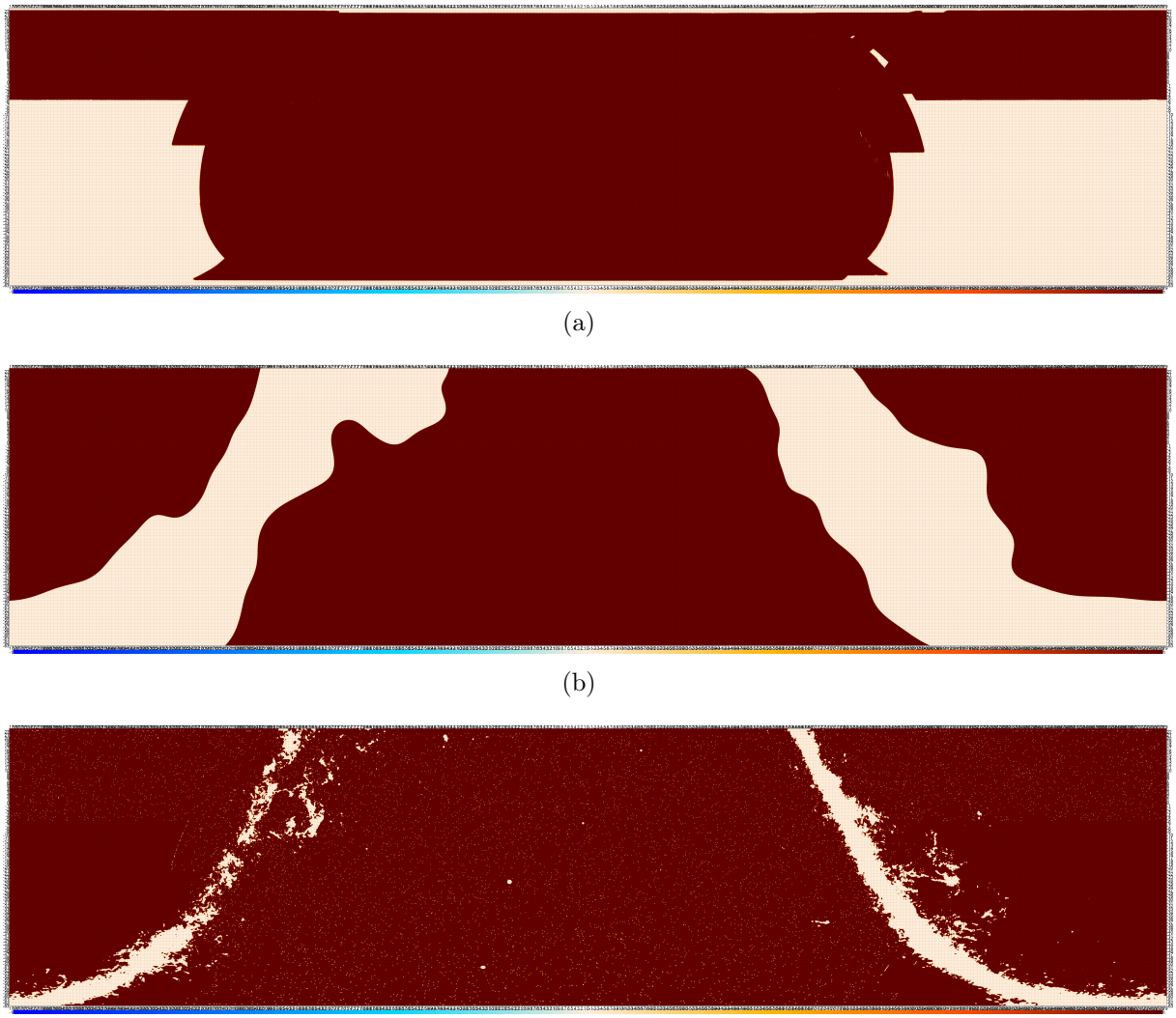

(a)

(b)

(c)

Figure 5.5: Masks used to build the ACT DR6 window function. (a) Survey mask (b) Galactic mask (c) Point sources mask

5.3.3. Building a mask

Before computing the spectra, we need to define window functions for each of the maps. The first contribution to the window function is the survey mask, setting the observed pixels to 1 and the pixels that cannot be observed from the Atacama desert to 0. Then we also have to mask the brightest part of the galaxy to minimise large-scale foreground contamination. This mask is obtained by re-projecting a Planck galactic mask into the CAR pixellisation used in the ACT data analysis. The galactic mask used in the power spectrum analysis cover 30% of the sky. At small scales, the tail of the power spectrum is dominated by radio sources. We mask the brightest sources using a catalog built from a coadded version of ACT and Planck data [142]. The sources in the catalog are displayed in Fig. (5.4). In order to build the mask, we select the sources detected with a signal-to-noise ratio higher than 5σ and with a flux at 150 GHz higher

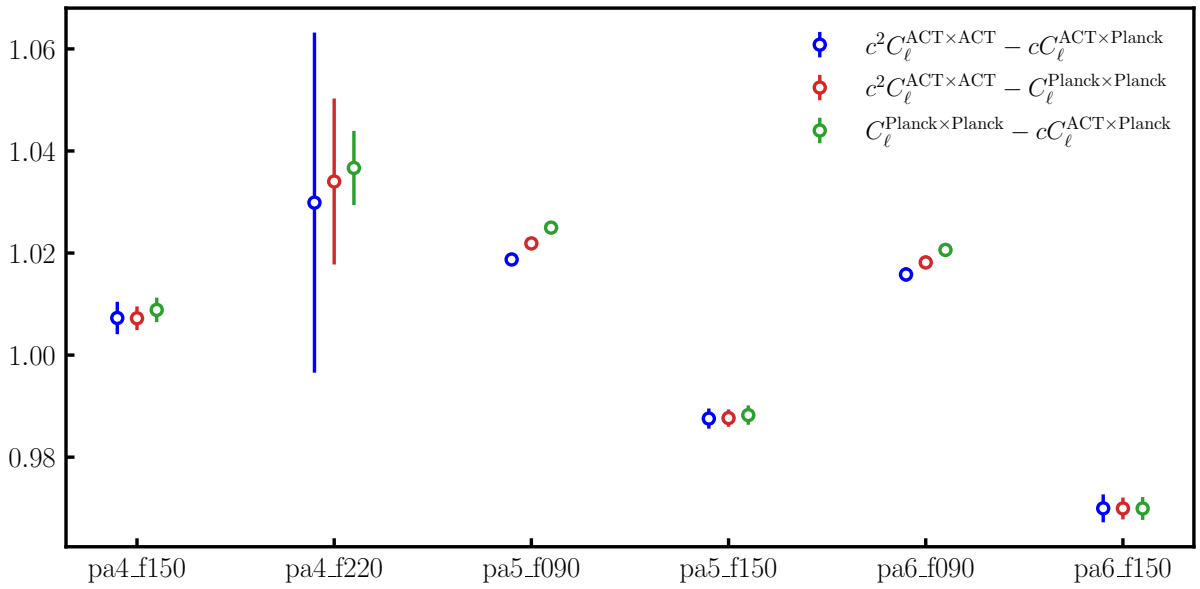

Figure 5.6: Calibration amplitudes obtained for DR6v4 data using different power spectra combination.

than 15 mJy. As in Ref. [106], clusters are not masked in the analysis.

Figure (5.5) shows the different masks mentioned above : the survey mask (Fig. (5.5(a))), the galactic mask from Planck 353 GHz map (Fig. (5.5(b))) and the point source mask (Fig. (5.5(c))). The point source mask also contains resolved sources and remove some dust sources. It is built from the source catalog by including a 5 arcmin-radius hole centered at the position of each sources that are above the 150 GHz flux cut. Before applying the galactic mask, ACT data cover roughly 47% of the sky. When applying the galactic mask, the remaining observed sky fraction is 37%. This sky fraction does not significantly change when applying the point source mask.

5.3.4. External calibration of the maps

ACT DR6 array	Frequency	Reference map	Multipole range
PA4	f150	Planck_f143	$1250 \leq \ell \leq 1800$
	f220	Planck_f217	$1500 \leq \ell \leq 2000$
PA5	f090	Planck_f100	$800 \leq \ell \leq 1100$
	f150	Planck_f143	$1250 \leq \ell \leq 1800$
PA6	f090	Planck_f100	$800 \leq \ell \leq 1100$
	f150	Planck_f143	$1250 \leq \ell \leq 1800$

Table 5.1: Table summarising the reference arrays and multipole ranges that have been used to perform the external calibration of ACT DR6 data with Planck NPIPE maps.

We perform an external calibration against Planck maps by computing power spectra differences that are sensitive to the calibration amplitude. We first compute the cross power spectra between ACT DR6 arrays and Planck NPIPE frequency maps in order to build the following data vector.

$$\mathbf{D}_\ell^{\mathrm{DR6}\alpha,\nu\times\mathrm{Planck},\nu_{\mathrm{ref}}} = \begin{pmatrix} D_\ell^{\mathrm{DR6}\alpha,\nu\times\mathrm{DR6}\alpha,\nu} \\ D_\ell^{\mathrm{DR6}\alpha,\nu\times\mathrm{Planck},\nu_{\mathrm{ref}}} \\ D_\ell^{\mathrm{Planck},\nu_{\mathrm{ref}}\times\mathrm{Planck},\nu_{\mathrm{ref}}} \end{pmatrix} \tag{5.28}$$

Then, we define a projector $\mathbf{P}(c_{\mathrm{DR6}}^{\alpha,\nu})$ which depends on the calibration amplitude of the corresponding ACT DR6 detector array such that

$$\mathbf{P}(c_{\mathrm{DR6}}^{\alpha,\nu}) = \begin{pmatrix} {c_{\mathrm{DR6}}^{\alpha,\nu}}^2 & 0 & 0 \\ 0 & c_{\mathrm{DR6}}^{\alpha,\nu} & 0 \\ 0 & 0 & 1 \end{pmatrix} \times \mathbf{P}, \tag{5.29}$$

where $\mathbf{P}$ determine which power spectra difference will be used. The calibration amplitude $c_{\mathrm{DR6}}^{\alpha,\nu}$ is then defined as the multiplicative factor to apply to the DR6 map to match the reference map. Hereafter we define three different projectors : $\mathbf{P}^{(1)} = (1, -1, 0)$, $\mathbf{P}^{(2)} = (0, -1, 1)$ and $\mathbf{P}^{(3)} = (1, 0, -1)$ from which we compute power spectra residuals as

$$\Delta D_\ell^{(i)} = \left[\mathbf{P}^{(i)}(c_{\mathrm{DR6}}^{\alpha,\nu})\right]^\top \mathbf{D}_\ell^{\mathrm{DR6}\alpha,\nu\times\mathrm{Planck},\nu_{\mathrm{ref}}}. \tag{5.30}$$

In order to get the calibration amplitude, we minimise this residual power spectrum using the Gaussian likelihood

$$\log\mathcal{L}^{(i)}(c_{\mathrm{DR6}}^{\alpha,\nu}) = -\frac{1}{2}\sum_{\ell\ell'} \Delta D_\ell^{(i)} [\Sigma_{(i)}^{-1}]_{\ell\ell'} \Delta D_{\ell'}^{(i)}, \tag{5.31}$$

with $\Sigma_{(i)}$ is the residual covariance matrix for the projector i given by

$$\Sigma_{(i),\ell\ell'} = \left[\mathbf{P}^{(i)}\right]^\top \mathrm{cov}\left(\mathbf{D}_\ell^{\mathrm{DR6}\alpha,\nu\times\mathrm{Planck},\nu_{\mathrm{ref}}}, \mathbf{D}_{\ell'}^{\mathrm{DR6}\alpha,\nu\times\mathrm{Planck},\nu_{\mathrm{ref}}}\right) \mathbf{P}^{(i)}. \tag{5.32}$$

To estimate the calibration amplitude as well as its associated error we use the MCMC sampling algorithm implemented in Cobaya with the likelihood defined in Eq. (5.31).

This method has been implemented in the python module PSpipe_utils [4] in which we have developed a series of tutorials and validated this calibration procedure on simulations in which the array we want to calibrate and the reference array have different beams and noise levels.

ACT DR6 maps are calibrated using NPIPE [99] maps as a reference. We use conservative multipole ranges as shown in Table. (5.1) to avoid the largest scales not well measured by ACT and for which we have identified a scale-dependent power loss with respect to Planck (discussed in Section. (5.3.6)). At these scales, we expect the power spectra to be dominated by primary CMB signal such that the calibration will be weakly sensitive to foreground contamination. Note that we increase the size of the point source holes from 5 arcmin to 12 arcmin when computing

[4] available at https://github.com/simonsobs/pspipe_utils

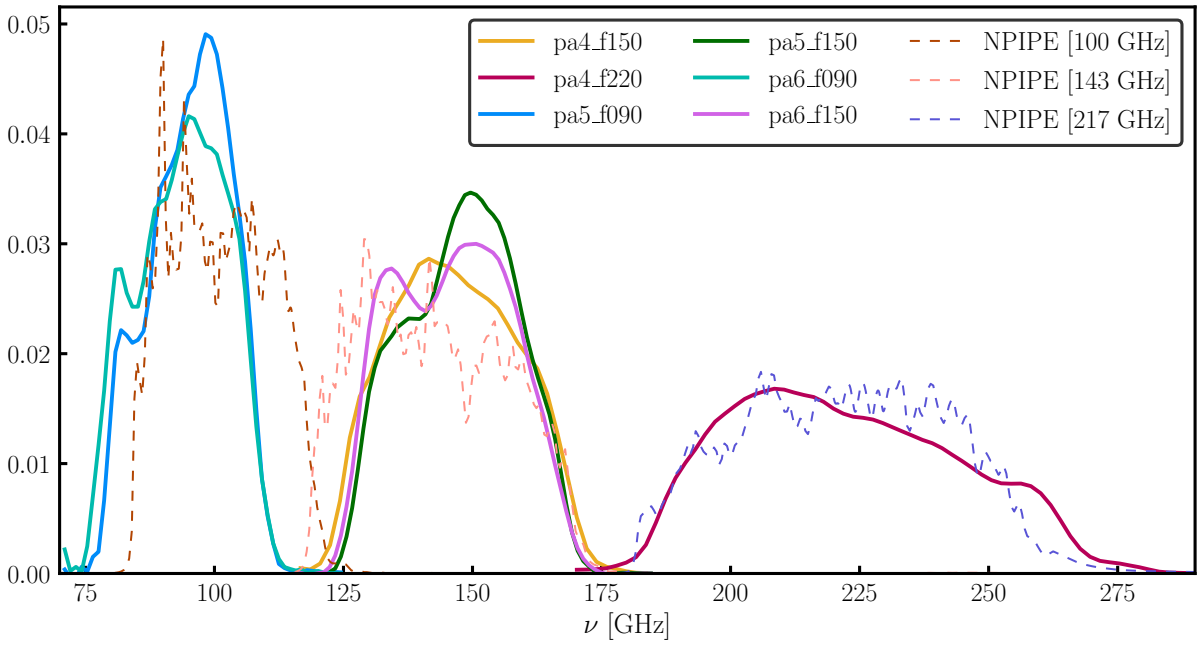

Figure 5.7: Passbands for ACT DR6 detector arrays (solid) and for NPIPE frequency maps (dashed). The passbands have been normalised such that the area under the curve is 1.

jointly the ACT and Planck power spectra in order to account for the lower resolution of Planck.

Calibration amplitudes for the different arrays are given in Fig. (5.6). The different power spectra combination used to derive the calibration agree quite well at 150 GHz and 220 GHz, while we notice a difference at 90 GHz corresponding to a cross power spectrum (ACT $\times$ *Planck*) lower than the auto power spectra. The fact that this difference does not show up at 150 and 220 GHz may be compatible with source variability and need to be investigated further.

During the calibration process, we have assumed that the signal in Planck NPIPE maps should match the signal in ACT DR6 maps. Due to foreground residuals contamination, we expect a small difference at intermediate scales between ACT and Planck temperature power spectra. We assess the impact of this assumption by computing a bandpass integrated best-fit foreground power spectra from Ref. [105] using the passbands displayed in Fig. (5.7). We achieve a $\sim 0.2\%$ determination of the calibration amplitudes at 90 and 150 GHz, and $\sim 1.6\%$ at 220 GHz. The fractional differences between the CMB+foregrounds power spectra at intermediate scales are much smaller than the 1σ errors on the calibration amplitudes. As a result, we can neglect the effect of bandpass integration on the calibration amplitudes.

5.3.5. Estimation of the polarisation efficiencies

The blinding policy of the ACT DR6 analysis prevents us for comparing DR6 polarisation with Planck polarisation. Therefore we cannot perform an external measurement of polarisation efficiency. However as described in Ref. [4], the lensing estimator requires to use fiducial power spectra. A polarisation efficiency different from unity could lead to biases in the lensing quadratic estimator. Therefore we use a simple polarisation efficiency measurement with respect to the

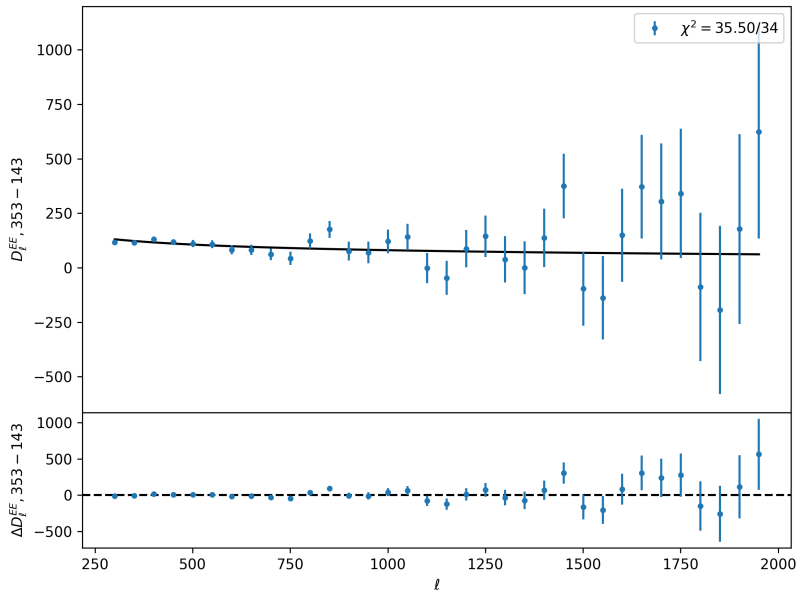

Figure 5.8: EE power spectrum of the Planck NPIPE 353 GHz-143 GHz map difference computed using ACT window functions. The bottom panel shows the residual with respect to the best-fit foreground model.

fiducial ΛCDM power spectrum used in Ref. [4]. We minimise the following residual power spectrum

$$\Delta D_\ell^{EE,\alpha,\nu}(\epsilon_{\rm pol}^{\alpha,\nu}) = D_\ell^{EE,{\rm DR6}\alpha,\nu\times{\rm DR6}\alpha,\nu} - \left(\epsilon_{\rm pol}^{\alpha,\nu}\right)^2 \left(D_\ell^{EE,{\rm CMB}} + D_\ell^{EE,{\rm fg},\nu}\right) \tag{5.33}$$

to find an estimate of the polarisation efficiency $\epsilon_{\rm pol}^{\alpha,\nu}$. $D_\ell^{EE,{\rm CMB}}$ is a fiducial EE power spectrum. Before constraining the polarisation efficiency, we first need to estimate the foreground power spectrum in polarisation $D_\ell^{EE,{\rm fg},\nu}$.

In the ACT patch, the polarisation foreground signal is dominated by dust emission. We use the Planck NPIPE 143 and 353 GHz to get a prior on the polarised galactic dust. We get rid of the dependence on cosmological parameters by computing the power spectrum of the map difference

$$D_\ell^{EE,353-143} = D_\ell^{EE,353\times353} + D_\ell^{EE,143\times143} - 2D_\ell^{EE,143\times343}, \tag{5.34}$$

which depends only on the foreground signals. The EE dust power spectra are modeled as described in Eq. (5.16). We constrain the amplitude of the polarised galactic dust to $A_{\rm dust}^{EE} = 0.271 \pm 0.012$, providing a good model for the map difference power spectrum displayed in Fig. (5.8) with $\chi^2/{\rm d.o.f.} = 35.5/34$ (PTE = 0.40). The relative polarisation efficiencies obtained from this method on ACT DR6.01 maps have been used in the lensing analysis [4], [5].

5.3.6. Quantifying the large-scale power loss

As mentioned earlier, ACT DR6 maps are affected by a lack of power at large scale due to model errors in the map-making process (see Section (5.3.1)). A direct consequence is that we

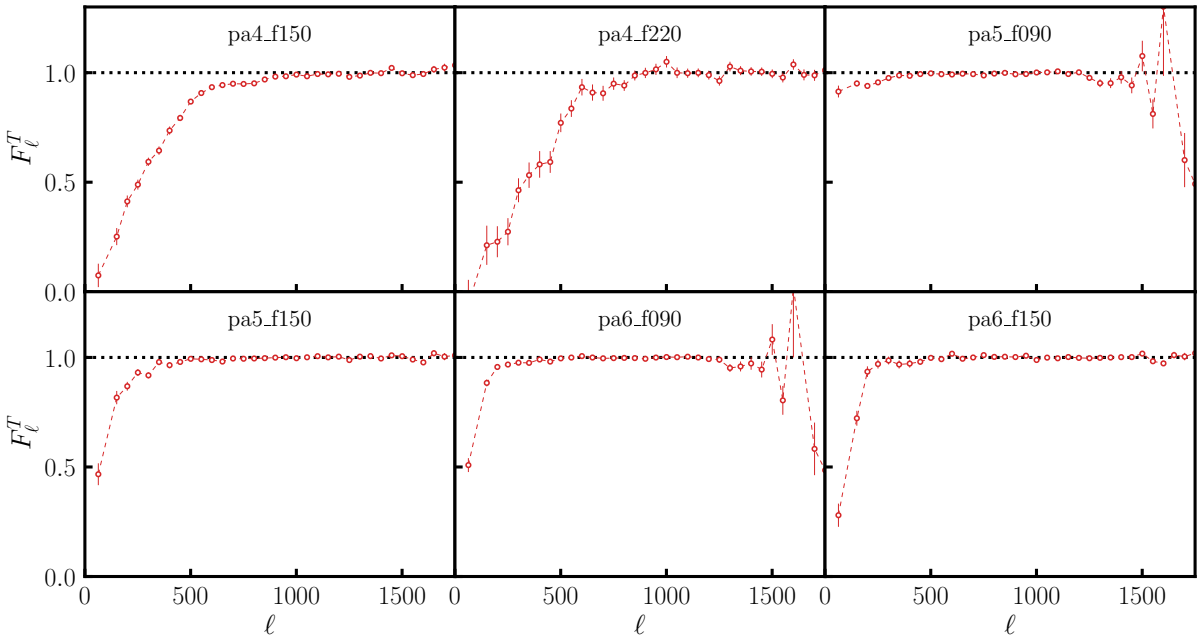

Figure 5.9: Estimation of the transfer function characterising the large-scale lack of power in the temperature power spectra for the DR6 detector arrays computed from the estimator described in Eq. (5.35).

need to quantify this effect to select multipole ranges on which the power spectra are reliable. As done in Section (5.3.4), we can use the Planck power spectra as a reference to estimate the transfer function induced by model errors. From the ACT-Planck cross power spectra, one can build an estimator for the transfer function

$$\hat{F}_\ell^{\alpha,\nu} = \frac{\hat{D}_\ell^{\mathrm{DR6}\alpha,\nu\times\mathrm{Planck},\nu_{\mathrm{ref}}}}{\hat{D}_\ell^{\mathrm{Planck},\nu_{\mathrm{ref}}\times\mathrm{Planck},\nu_{\mathrm{ref}}}}. \tag{5.35}$$

The ratio of two random variables estimated from a particular realisation of these two variables will be affected by a subdominant bias. In order to get an estimate of the bias, we write a generic estimator of the ratio between two power spectra as $\hat{F}_\ell^{WX,YZ} = \hat{D}_\ell^{WX}/\hat{D}_\ell^{YZ}$ where W,X,Y and Z correspond to different maps. Assuming that $\hat{D}_\ell^{WX} = D_\ell^{WX} + \Delta D_\ell^{WX}$, we can expand the ratio estimator at second order as

$$\begin{aligned}\hat{F}_\ell^{WX,YZ} &= F_\ell^{WX,YZ}\frac{1+\Delta D_\ell^{WX}/D_\ell^{WX}}{1+\Delta D_\ell^{YZ}/D_\ell^{YZ}} \\ &= F_\ell^{WX,YZ}\left(1+\frac{\Delta D_\ell^{WX}}{D_\ell^{WX}}\right)\left(1-\frac{\Delta D_\ell^{YZ}}{D_\ell^{YZ}}+\left(\frac{\Delta D_\ell^{YZ}}{D_\ell^{YZ}}\right)^2\right).\end{aligned} \tag{5.36}$$

This estimator is biased such that

$$\langle \hat{F}_\ell^{WX,YZ} \rangle = F_\ell^{WX,YZ} \left(1 + \frac{\mathrm{cov}(D_\ell^{YZ}, D_\ell^{YZ})}{{D_\ell^{YZ}}^2} - \frac{\mathrm{cov}(D_\ell^{WX}, D_\ell^{YZ})}{D_\ell^{WX} D_\ell^{YZ}} \right)$$
$$= F_\ell^{WX,YZ} \left(1 + \alpha_\ell^{WX,YZ} \right). \tag{5.37}$$

The bias may be used to build an unbiased estimator $\hat{F}_\ell^{WX,YZ,\mathrm{corr}} = \hat{F}_\ell^{WX,YZ} \left(1 - \alpha_\ell^{WX,YZ} \right)$. The main interest of this second order development is to get an analytical expression for the covariance. We define the covariance as

$$\mathrm{cov} \left(\hat{F}_\ell^{WX,YZ,\mathrm{corr}}, \hat{F}_{\ell'}^{WX,YZ,\mathrm{corr}} \right) = \langle (\hat{F}_\ell^{WX,YZ,\mathrm{corr}} - F_\ell^{WX,YZ})(\hat{F}_{\ell'}^{WX,YZ,\mathrm{corr}} - F_{\ell'}^{WX,YZ})^\top \rangle, \tag{5.38}$$

such that the second order development leads to

$$\mathrm{cov} \left(\hat{F}_\ell^{WX,YZ,\mathrm{corr}}, \hat{F}_{\ell'}^{WX,YZ,\mathrm{corr}} \right) = -\alpha_\ell \alpha_{\ell'} + \frac{\mathrm{cov} \left(D_\ell^{WX}, D_{\ell'}^{WX} \right)}{D_\ell^{WX} D_{\ell'}^{WX}}$$
$$+ \frac{\mathrm{cov} \left(D_\ell^{YZ}, D_{\ell'}^{YZ} \right)}{D_\ell^{YZ} D_{\ell'}^{YZ}} - 2 \frac{\mathrm{cov} \left(D_\ell^{WX}, D_{\ell'}^{YZ} \right)}{D_\ell^{WX} D_{\ell'}^{YZ}}. \tag{5.39}$$

Note that the second order development is valid only in the high signal-to-noise regime. We estimate the transfer function at multipoles for which we have a signal to noise higher than 3. The analytical expression of the power spectra ratio covariance has been verified against simulations as shown in the top panel of Fig. (5.10).

We estimate the transfer function from the estimator defined in Eq. (5.35) and the results are displayed in Fig. (5.9) for the six DR6 detector arrays. The large scale power loss increases with frequency such that we are able to recover unbiased spectra from $\ell = 600$ at 90 and 150 GHz (except for PA4_F150 which is strongly impacted by the transfer function) and from $\ell = 1000$ at 220 GHz. We do not deconvolve the transfer functions in the analysis, but we use them to select a reliable multipole range for the calibration procedure (see Table (5.1)). Additionally, we performed anisotropy tests by computing the power spectra in disjoint patches and estimating the large scale power loss from them. We found that the one dimensional transfer functions are consistent from patch to patch. Although the large-scale power deficit is well described with the transfer functions shown in Fig. (5.9), a next step would be to look at its effect on the two dimensional power spectra.

5.4. Assessing the consistency of ACT DR6 data with null tests

The ACT sixth data release compiles data acquired from 3 dichroic detector arrays resulting in 6 array-frequency pairs from which we can compute 171 cross power spectra (21 for TT,EE and BB, and 36 for TE, TB and EB). Some of these spectra were used in Section (5.3) to get calibration amplitudes and relative polarisation efficiencies. This section describes and discusses various consistency tests performed on ACT DR6 data.

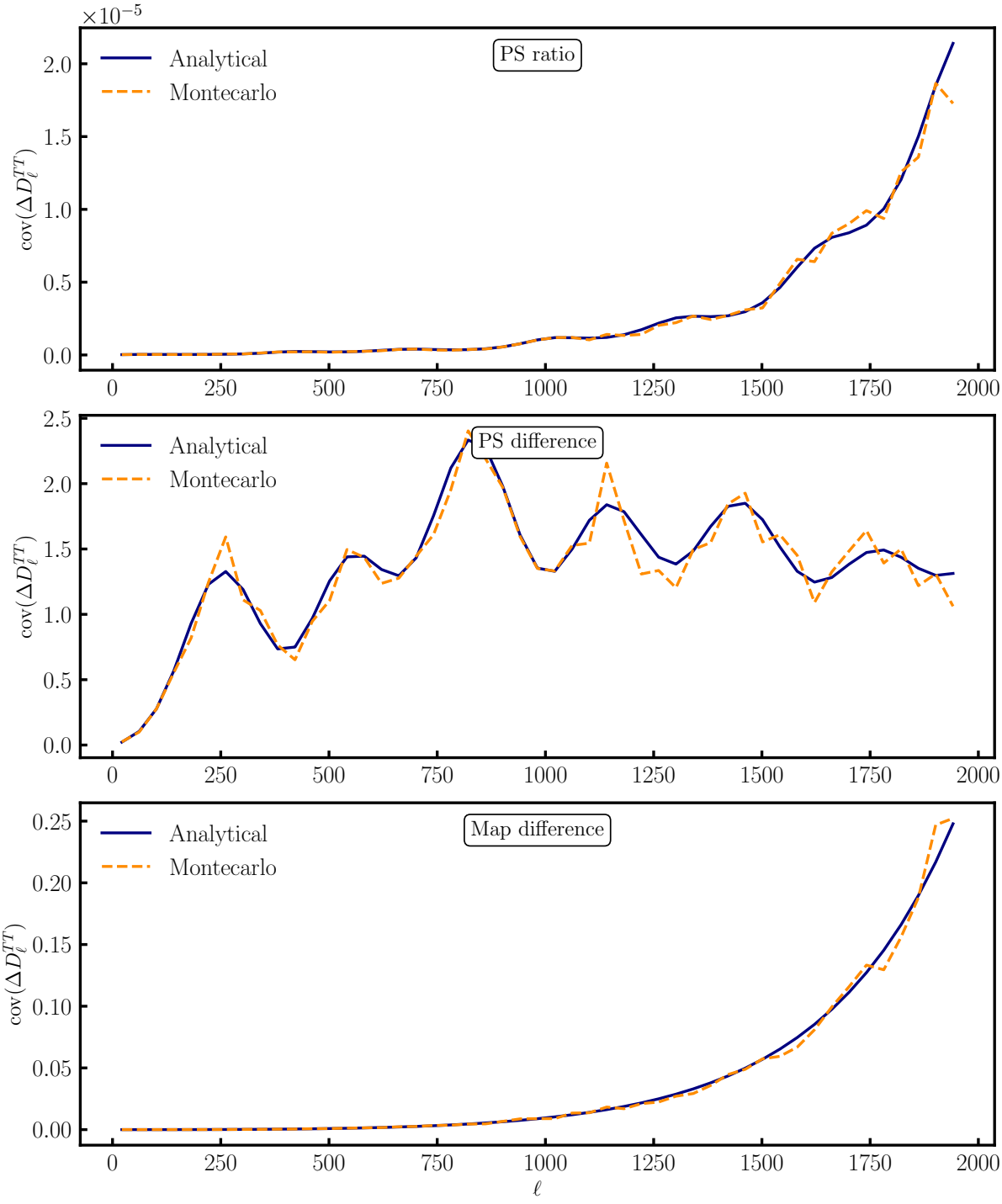

Figure 5.10: Comparison of analytical covariances to montecarlo estimated covariances for a ratio between two power spectra (top panel), for a difference (middle panel) and for the power spectrum of the difference between two maps (bottom panel). The montecarlo covariances were estimated on a set of $N_{\mathrm{sim}} = 300$ simulations.

ACT DR6 array	Multipole range	χ^2 [AA-PP]	χ^2 [AA-AP]	χ^2 [PP-AP]
PA4_f150	$1250 \leq \ell \leq 2500$	26.4/20	21.0/20	38.2/20
PA4_f220	$1000 \leq \ell \leq 2500$	22.6/25	24.7/25	23.7/25
PA5_f090	$800 \leq \ell \leq 1200$	8.7/8	15.8/8	12.0/8
PA5_f150	$800 \leq \ell \leq 2500$	27.7/29	32.4/29	29.1/29
PA6_f090	$600 \leq \ell \leq 1200$	13.7/12	28.1/12	12.0/12
PA6_f150	$600 \leq \ell \leq 2500$	33.7/33	32.9/33	35.3/33

Table 5.2: ACT DR6 consistency test results at intermediate scales with respect to Planck NPIPE temperature data. Note that the χ^2 and PTE presented in this table are preliminary and are computed using a analytical covariance matrices that need to be corrected with simulations as shown in Ref. [145].

5.4.1. Assessing the consistency with respect to Planck

First, we run some consistency tests by comparing the ACT DR6 temperature power spectra with the NPIPE ones. Since Planck NPIPE was used as a reference for calibration, these power spectra should be in close agreement. We chose to quantify the consistency with a χ^2 computed on a selected multipole range on which the spectra are not strongly affected by the transfer function discussed in Section (5.3.6). We report the χ^2 with their associated multipole range in Table (5.2). PA4, PA5 and PA6 show a good consistency with respect to Planck NPIPE data at 150 GHz with a caveat on the high signal to noise combination PP-AP for PA4 with a low PTE value (0.008). 220 GHz is also consistent with NPIPE 217 GHz data regardless of the power spectra residual used. At 90 GHz the situation is less clear. Since we calibrate the DR6 maps using only the auto spectra, the residual AA-PP yields to acceptable PTE values of 0.37 and 0.32 for PA5 and PA6 respectively. The other power spectra combinations yield to lower PTE, the worst being for PA6 and the combination AA-AP (PTE = 0.005). The χ^2 and PTE are preliminary and should be treated with caution since we do not use montecarlo corrected covariances to perform this null test. Indeed, the analyic covariances computation describes accurately the data covariance assuming homogeneous noise, but accounting for spatial variation of the noise properties should lead to a $\sim 10\%$ increase of the errors with respect to the analytical expression. [145]

5.4.2. Assessing the consistency of the different arrays

Since we have different arrays observing at 90 GHz and 150 GHz, we are able to perform internal consistency tests between the signal measured from different detector arrays both in temperature and polarisation. These null tests are currently under investigation and the combinatorics is quite large, therefore we will not discuss them individually in this section. Instead, we will focus on some examples which allowed us to identify potential systematics in the DR6v4 dataset.

In addition to the fact that PA4 is strongly affected by the transfer function at large scales, we have noticed that this array also shows an unexpected excess of power at small scales with respect to PA5 and PA6 at 150 GHz as shown in Fig.(5.11) which shows the ratio between the

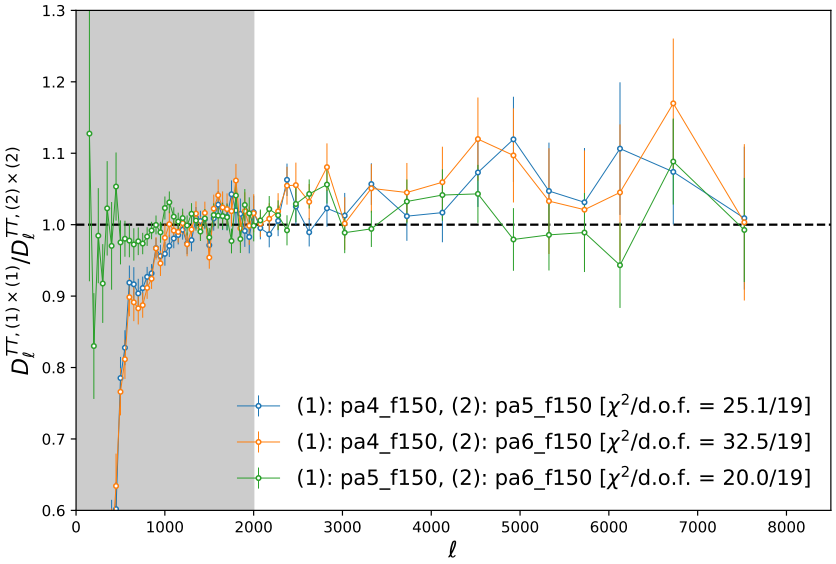

Figure 5.11: Power spectra ratios computed from the AdvACT 150 GHz polarisation arrays. This figure highlights a small scale excess of power in PA4. Data points that are in the shaded area ($\ell \leq 2000$) are not considered to compute the χ^2.

150 GHz power spectra. We observe that the ratio between PA4 and any of PA5 and PA6 are consistently above 1 at $\ell \geq 2000$, while PA5 and PA6 show a good consistency at 150 GHz. We have explored several hypothesis to explain this difference such as a shift in the passband central frequency but this is still under investigation.

Then the polarisation consistency tests between arrays highlight the presence of temperature-to-polarisation (T-to-P) leakage in the data at 150 GHz for PA4 and at 90 GHz for both PA5 and PA6. We can use the TE power spectrum using temperature measurements from the same array to quantify the leakage without being affected by the large-scale transfer function. Figure (5.12) shows the TE power spectra residuals which highlight the polarisation differences for PA4 and PA6 at 150 GHz (see Fig. (5.12(a))) and between PA5 and PA6 at 90 GHz (see Fig. (5.12(b))). We see a significant evidence for array-dependent T-to-P leakage in the data at 150 GHz (χ^2/d.o.f. = 189.9/47) and at 90 GHz (χ^2/d.o.f. = 107.8/47). This differences may be explained by beam leakage differences between the detector arrays. As shown in the two panels, quantifying the consistency with respect to the T-to-E leakage model derived from planet observations yields to significantly better χ^2 with χ^2/d.o.f = 49/47 (PTE = 39.4%) at 150 GHz and χ^2/d.o.f. = 52.8/d.o.f. (PTE = 26%) at 90 GHz. One should note that we do not account for uncertainties on the measured leakage beams and that we use analytical power spectra covariances that should be corrected with simulations.

5.4.3. Assessing the consistency between splits

As explained in Section (5.3.1), the map-making process provide a set of maps for each detector arrays made up of different splits. In practice, these splits should have similar properties and therefore their power spectra should all be consistent. To check if these splits are consistent for a pair of detector array α observing at a fixed frequency ν, we compute the following residual

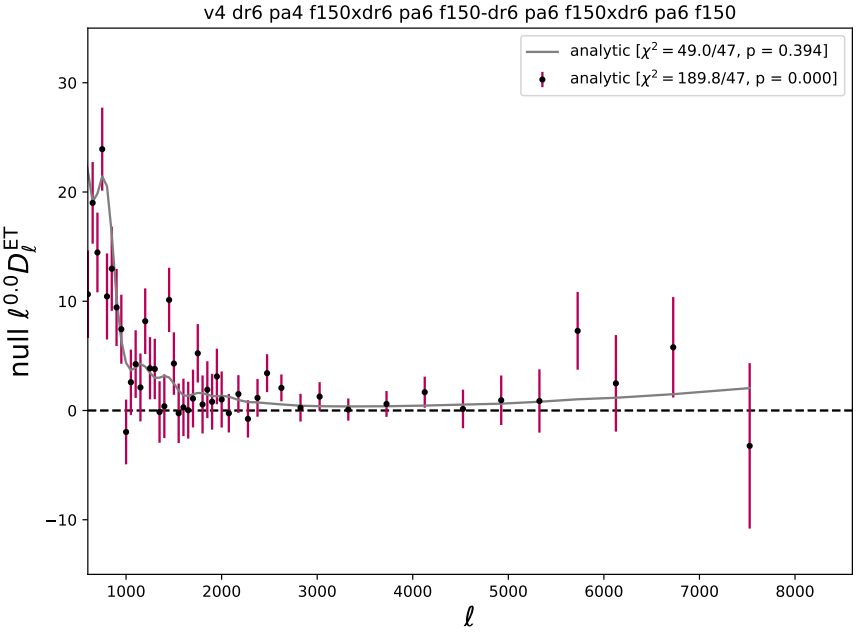

(a)

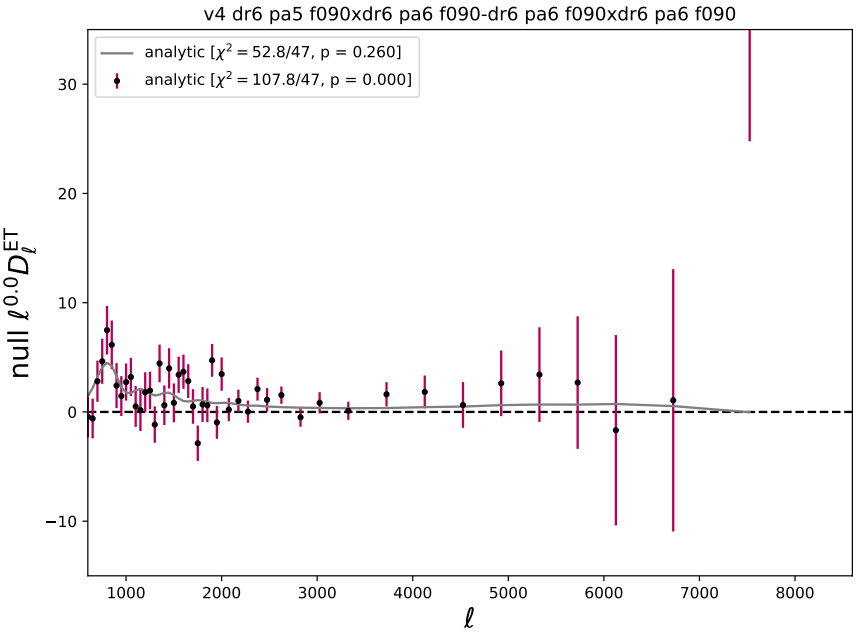

(b)

Figure 5.12: Polarisation consistency test : (a) 150 GHz residual ET power spectrum between PA4 and PA6 — (b) 90 GHz power spectrum between PA5 and PA6. The gray line shows the expected residual computed from a T-to-P leakage measurement on planet observations. The χ^2 were computed using analytic covariance and accounting for the expected leakage significantly improve the PTE of these array consistency tests.

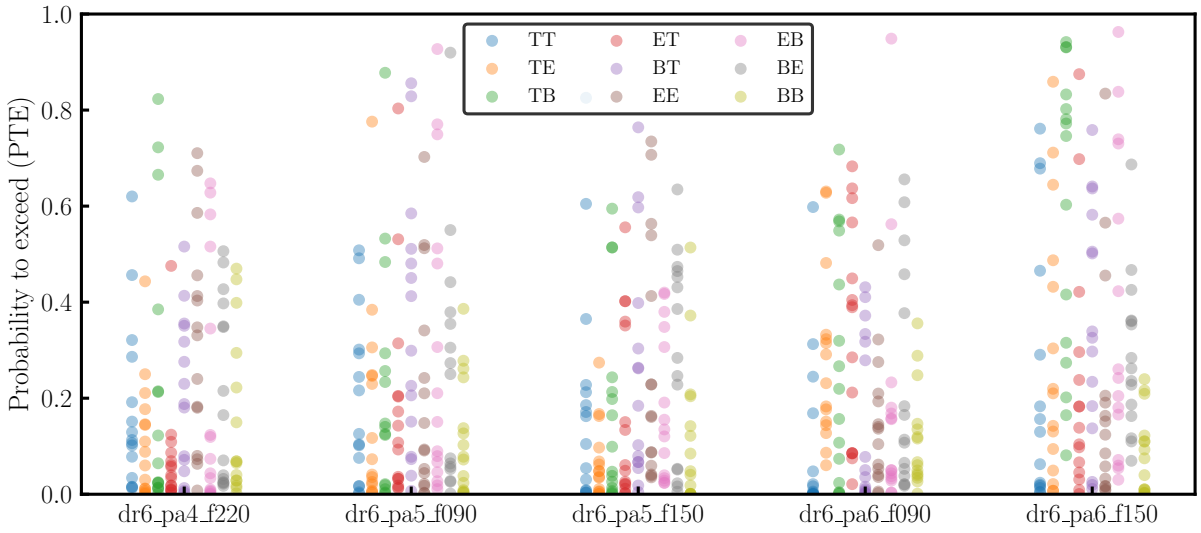

(a)

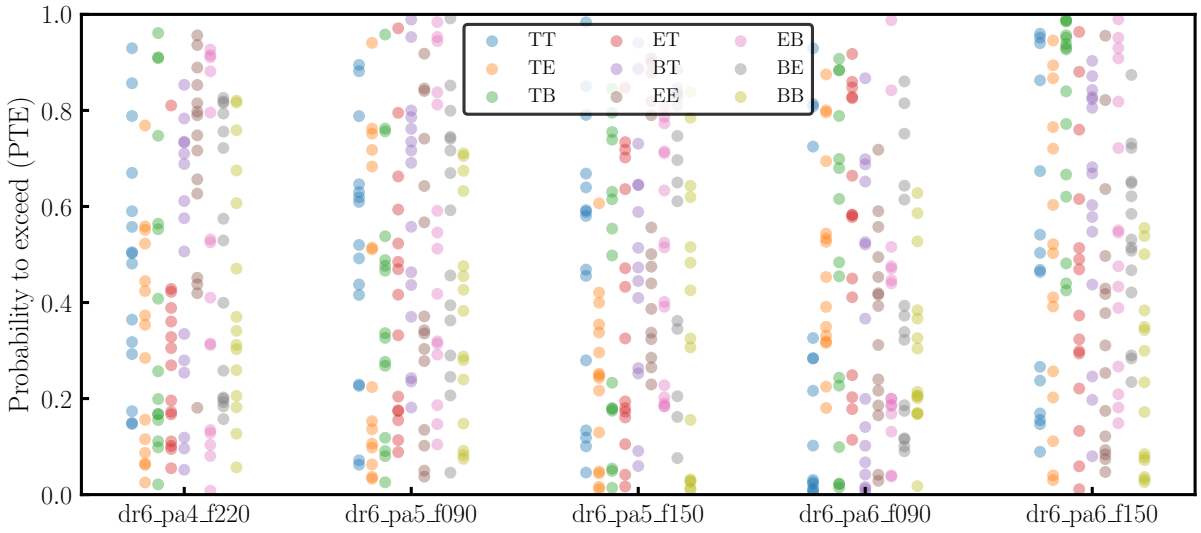

(b)

Figure 5.13: We perform split null tests by computing the difference between cross split power spectra as described in Eq. (5.40). We compute the probability-to-exceed (PTE) for each residual using analytical covariances (a) and montecarlo corrected covariances using a set of 256 simulations (b).

power spectra

$$\Delta D_\ell^{XY,\alpha,\nu} = D_\ell^{XY,\alpha,\nu,i\times j} - D_\ell^{XY,\alpha,\nu,k\times l}, \tag{5.40}$$

where $(X,Y) \in \{T,E\}^2$ and i,j,k and l are the split indices. In order to make sure that the estimated power spectra are independent of the noise, we impose $i \neq j$ and $k \neq l$. From $n_{\rm splits} = 4$ maps, we can build $N_{\rm cross} = n_{\rm splits}(n_{\rm splits}-1)/2 = 6$ cross power spectra. The number

of possible split power spectrum differences is then $N_{\text{split nulls}} = N_{\text{cross}}(N_{\text{cross}}-1)/2 = 15$ for each array and for the 9 power spectra using T, E and B modes. The total number of possible split null tests is too large to report on them individually. Figure (5.13) compiles the probability-to-exceed of each individual split power spectrum difference for the different modes and detector arrays. The top panel displays the PTE values computed from analytical covariances. The PTE should be uniformly distributed between 0 and 1. Figure (5.13(a)) highlights the fact that we have underestimated the power spectra errors since the PTE distributions are consistently biased towards low-values. Indeed in Ref. [145], we have shown that assuming uniform noise properties in the analytical covariance leads to an underestimation of order 20% of the diagonal covariances. Using the MNMS noise simulation code [5], we are able to draw realistic simulations of the ACT DR6 noise which capture the inhomogeneous properties of the noise (either due to the atmosphere or the scanning strategy). We draw a set of 256 simulations including CMB, foregrounds as described in Section (5.2.3), and noise realisations generated using MNMS. We then numerically estimate the covariance matrix from simulations and apply a diagonal correction to the analytical covariance matrices. The PTE values computed after applying the corrections are displayed in Fig. (5.13(b)). The PTE distribution will be further improved by using the per-split beams instead of the coadded beam that is currently used in the pipeline.

5.5. Constraining power of ACT DR6 data

The current status of the analysis does not allow to show cosmological constraints from ACT DR6 power spectra. However, in this section we will give a brief overview of the constraining power of DR6 data.

Figure (5.14) shows the 150 GHz coadded DR6 power spectra using data from PA5 and PA6. The ACT DR6 data points are centered on the Planck 2018 best-fit power spectra and the errors are estimated analytically as described in Section (5.2). We compare them to the Planck 2018 legacy TE and EE power spectra at 143 GHz. We do not show the smallest scales ($\ell \geq 3500$) at which the power spectra are dominated with foreground contamination such as polarised point sources.

The likelihood that will be used to perform the cosmological analysis from DR6 power spectra is MFLIKE[6], a public likelihood code developed for Simons Observatory large aperture telescope cosmological analysis. It includes a modelling of the foreground (as described in Section (5.2.3)) at the power spectrum level as well as a modelling of standard systematic effects such as the miscalibration of polarisation angles, bandpass shifts and calibration amplitudes. This likelihood has been tested extensively against SO LAT and ACT DR6 simulated data. Figure (5.16) displays the 1D marginalised posterior distributions for the 6 standard ΛCDM parameters for a set of $N_{\text{sim}} = 49$ DR6 simulations (gray) as well as the mean posterior distribution (black). We found that the likelihood yields unbiased constraints on cosmology. One should note that the small dispersion observed for the reionisation optical depth τ_{reio} is due to the use of a τ-prior $\tau_{\text{reio}} = 0.0544 \pm 0.0073$. Figure (5.15) displays the expected constraints on cosmology derived

[5] made available at https://github.com/simonsobs/mnms

[6] https://github.com/simonsobs/LAT_MFLike

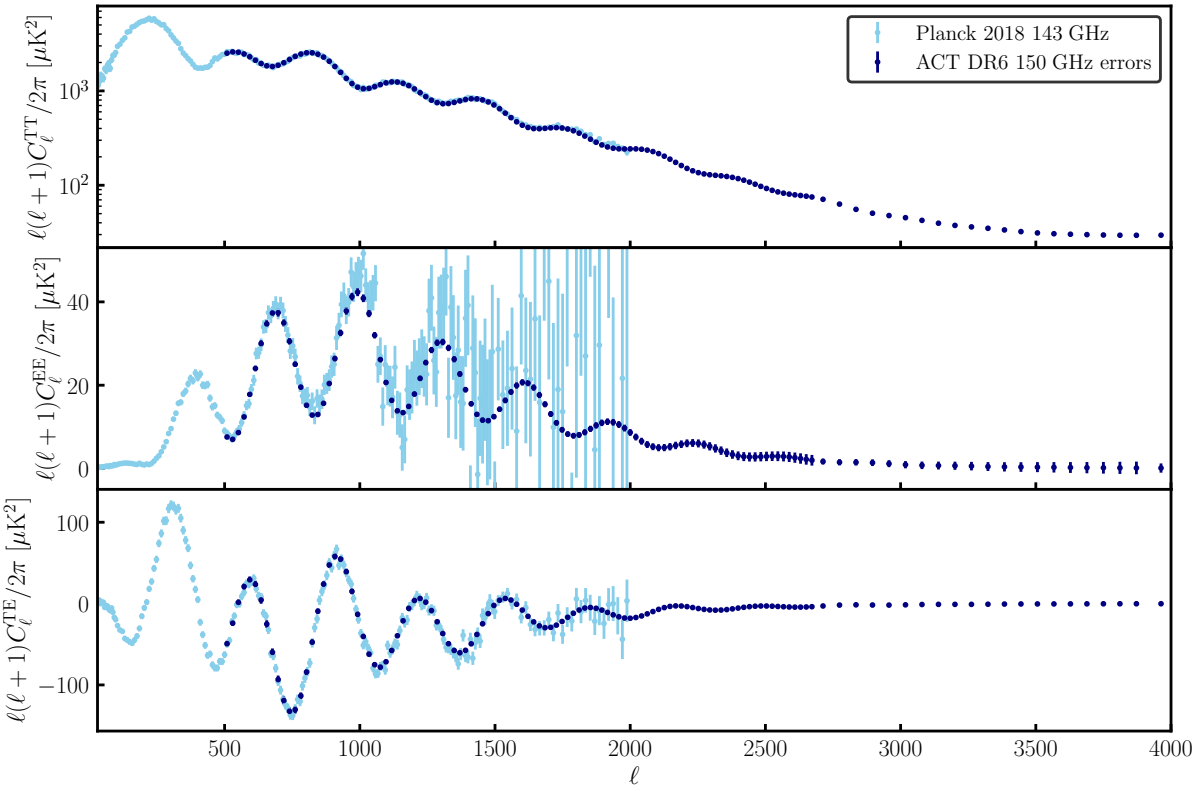

Figure 5.14: Preliminary errors on the ACT DR6 temperature and polarisation power spectra compared to Planck legacy measurements at 143 GHz. This figure does not show actual ACT DR6 data : ACT data points are centered on the Planck 2018 best-fit power spectra with errors computed from the data.

using the DR6 data covariance matrix compared to Planck 2018 and ACT DR4 constraints. ACT DR6 will provide independent cosmological parameter constraints with a precision similar to the Planck latest data release. Note that Figure (5.15) does not show the combination of ACT data with WMAP large scale temperature measurements which will further improve the constraints and allow to get a constraint on the Hubble expansion rate H_0 tighter than Planck's one. The combination between these two datasets (including the correlations) will provide the best cosmological constraints to date by benefiting from the wide range of scales probed by the two telescopes.

5.6. Conclusion and next steps

This section discussed the ACT DR6 data analysis pipeline. First we described the external calibration procedure using cross-correlations with the Planck NPIPE maps. These cross correlations were also useful to highlight and quantify the large-scale power deficit in ACT DR6 maps. Once unblinded, these cross correlations will provide highly informative consistency tests in polarisation between ACT and Planck at intermediate scales since ACT polarisation signal seems to be weakly affected by the large-scale lack of power discussed in Section (5.3.6). We then

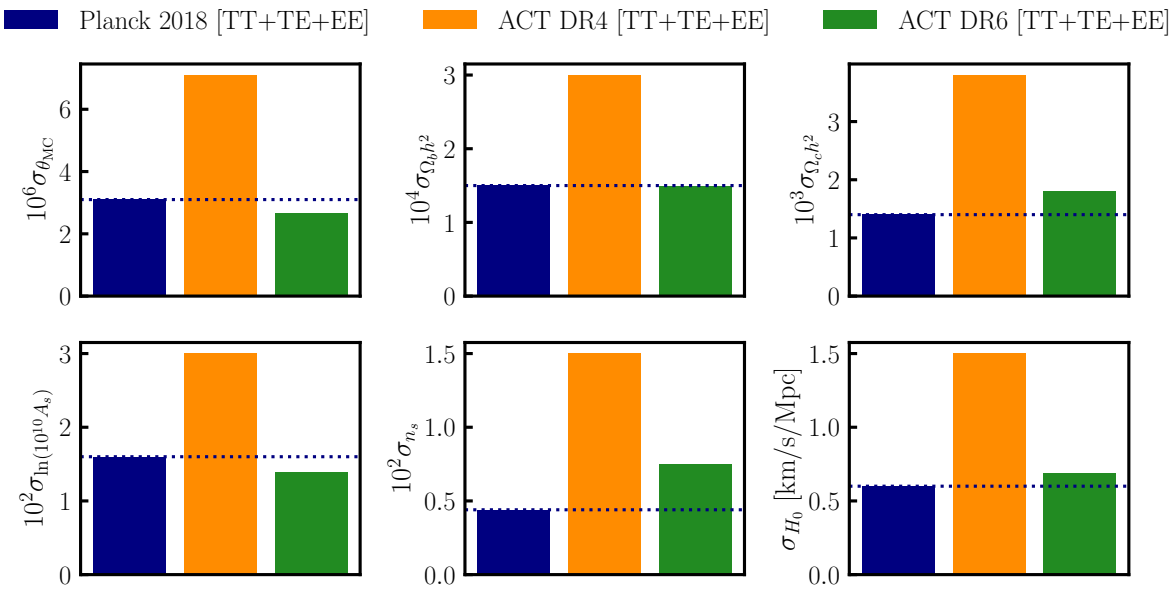

Figure 5.15: Cosmological parameter 68% marginalised errors derived from the temperature and polarisation power spectra (TT,TE,EE) for Planck 2018 [8], ACT DR4 [37] and the expected constraint from ACT DR6 data. The reionisation optical depth τ is not displayed due to the use of a Gaussian prior to derive the ACT constraints.

discussed different consistency tests performed on the data. We were able to compute consistency tests with respect to Planck NPIPE in temperature to validate the calibration procedure and to identify a multipole range on which the DR6 power spectra are reliable. In order to compare the DR6 polarisation measurements with Planck polarisation, we need to pass a set of internal consistency tests. Two of them that do not require additional data products have been introduced in this section : the array and split null tests. We have identified some issues among these consistency tests such as T-to-P leakage but we have shown that our leakage measurement from planet observations correctly describes the leakage observed in the data and drastically improves the χ^2. We have found an acceptable overall consistency between the different splits once the covariance matrices has been corrected to account for the inhomogeneous noise properties. The next step in the analysis of these null tests will be to propagate uncertainties from beam or leakage measurement to refine our estimation of covariance matrices.

Then, we also need to pass more specific null tests before unblinding : elevation, precipitable water vapor and detector null tests. In particular, elevation null tests will allow to look for residual ground pick-up that are not handled by the filter in Fourier space (since we expect the ground pick-up level to vary with elevation).

Finally, the covariance matrices estimation requires a high-level of scrutiny. We have observed that the analytic covariance estimation, that describes precisely the power spectra covariance with homogeneous noise is not able to describe the particular features observed in the ACT DR6 noise. A highly important remaining step would be to implement a better analytical estimate to

account for anisotropic noise since correcting the covariance matrices requires a large number of computationally expansive simulations.

Lastly, ACT DR6 data will be able to provide cosmological constraints that are independent from Planck constraints with a similar precision. The ACT sixth data release will be a valuable dataset to look for deviations to ΛCDM either by constraining new models or by using methods similar to what was presented in Chapter 2 and Chapter 3. This data release also provide an interesting test case for the PSpipe data analysis pipeline — that was already validated by reproducing Planck results.

5.A. Validation of the MFLike likelihood on simulations

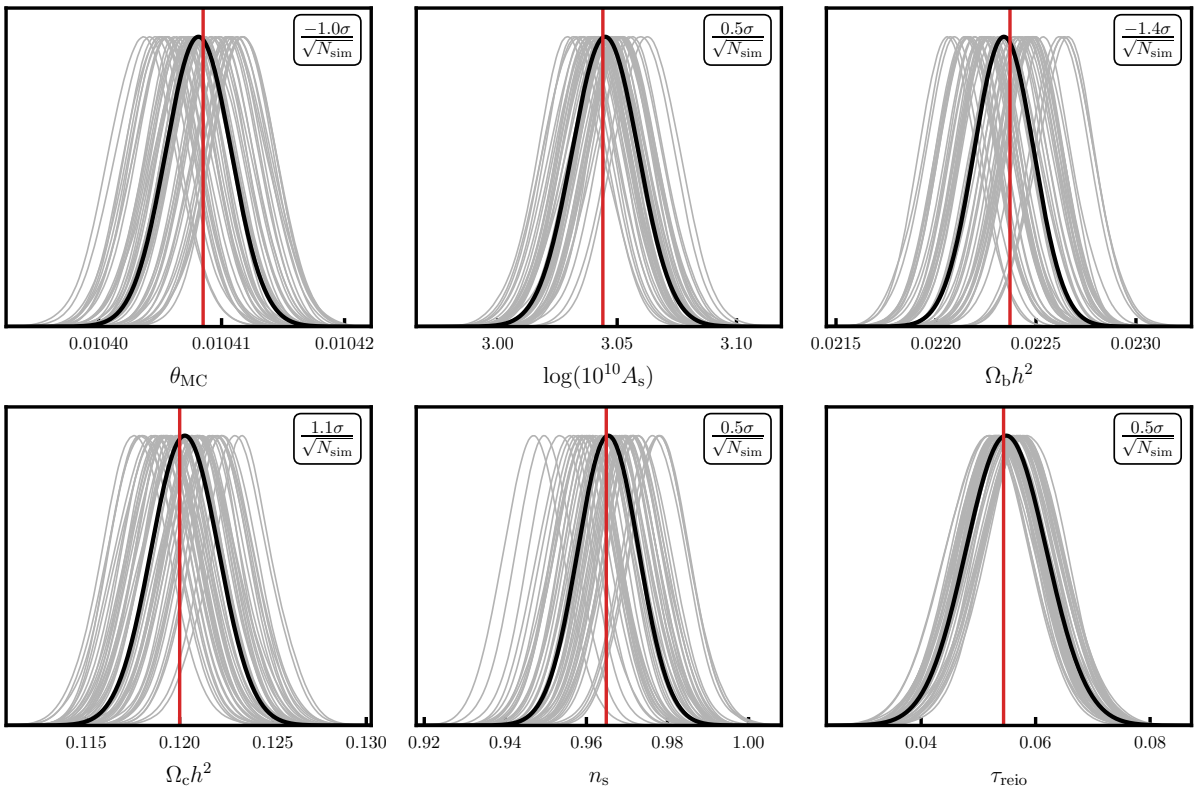

Figure 5.16: Validation of the MFLike likelihood on a set of $N_{\rm sims} = 49$ simulations of ACT DR6 data. We show the posterior distribution derived from each simulation in gray and the mean posterior distributions in black.

CHAPTER 6

Conclusion and perspectives

The measurement of cosmic microwave background (CMB) anisotropies yields valuable insights into the early universe and also allows us to study the distribution of matter through the lensing of CMB photons by large-scale structures. In this manuscript, we first introduced the commonly used paradigm for describing the universe, known as the ΛCDM model, and provided a mathematical description of CMB anisotropies in Chapter 1. The measurement of CMB anisotropies provides the most precise constraints on the standard set of cosmological parameters. Notably, it provides tight constraints on the current expansion rate of the universe H_0, which is also constrained by local probes with 1% precision. Over the past decade, increasingly precise measurements have revealed the existence of the "Hubble tension." The various analyses presented in this manuscript aim to resolve this tension by examining systematic effects in CMB datasets or by incorporating physics beyond the standard model.

In Chapter 2, we present a new quantity called the correlation coefficient between CMB temperature and polarisation E-modes. This observable is specifically designed to be unaffected by multiplicative instrumental effects. It provides a means to detect unmodelled residual instrumental effects that may have been missed during data processing. We have constructed a likelihood function based on this correlation coefficient and used it to constrain cosmological parameters using the Planck T-E correlation coefficient. Our results demonstrate a strong agreement with the constraints obtained from the standard analysis conducted by Planck. In particular, the value of the Hubble constant aligns with other CMB measurements while being still discrepant with local measurements from Cepheids-calibrated type IA supernovae.

Chapter 3 introduces an alternative approach for evaluating the consistency between temperature and polarisation E-modes measurements. To achieve this, we have modified publicly available likelihoods by incorporating additional parameters that capture potential scale-dependent inconsistencies between temperature and polarisation. We then performed a joint-fit analysis of this set of extra-parameters with cosmological parameters to get a measurement of the

marginalised T-E inconsistency. We found an overall good agreement between the datasets studied in this analysis. Importantly, these two studies did not reveal any indications of unmodeled systematic effects within the CMB datasets that could be responsible for the Hubble tension.

A potential approach to solve the Hubble tension is to seek an extension to the ΛCDM model that leads to a higher inferred value of H_0 derived from CMB observations. In Chapter 4, we introduced an extension known as the Early Dark Energy (EDE) scenario, which is a promising solution to address the Hubble tension. We showed that while the EDE scenario is not favored by the Planck data, the fourth data release from ACT demonstrated a slight preference in favor of this model with respect to ΛCDM. We also discussed the constraints obtained from the SPT-3G polarisation data which are not constraining enough on the EDE parameters to conclude for a preference in favor of EDE. We finally discussed alternative Planck constraints on the EDE model using different datasets and likelihoods and concluded that Planck data do not favor high $f_{\rm EDE}$ values regardless of the likelihood and dataset.

Finally, in Chapter 5, we provided an update on the Advanced Atacama Cosmology Telescope sixth data release. This data release will provide measurements of the power spectra with an exquisite precision — particularly in polarisation — which requires a high level of scrutiny of potential instrumental systematic effects. Following a brief overview of the pipeline employed for power spectra estimation and covariance calculations, we presented preliminary results regarding calibration and the primary identified systematic effect: a deficit in large-scale power attributed to model errors in the map-making process. We also reported on the consistency tests conducted up until Spring 2023. The ACT DR6 dataset is anticipated to offer cosmological constraints at the same level of precision as Planck, enabling stringent consistency assessments between these datasets. Moreover, ACT DR6 serves as a valuable test case for the data analysis pipeline PSpipe, that will be used to analyse Simons Observatory Large Aperture Telescope (SO LAT) data, excepted to start acquiring data during 2024. The tools and methodologies developed during the ACT DR6 data analysis will prove very useful with SO LAT data, which will measure the CMB anisotropies with a even higher sensitivity than AdvACT and for which instrumental systematics will need to be quantified with high precision.

Synthèse en français

Introduction

Pour décrire l'Univers dans sa globalité et son évolution, le modèle standard de la cosmologie se base sur la théorie de la Relativité Générale. Le principe cosmologique, selon lequel l'Univers est considéré homogène et isotrope à grande échelle, autorise l'utilisation de la métrique FLRW (Friedmann-Lemaître-Robertson-Walker) pour décrire l'espace-temps

$$ds^2 = -dt^2 + a^2(t)\left[\frac{dr^2}{1-Kr^2} + r^2 d\Omega^2\right]. \tag{6.1}$$

L'expansion de l'Univers est encodée dans une fonction nommée facteur d'échelle $a(t)$ et sa géométrie est régie par la constante K. En utilisant cette métrique dans les équations d'Einstein, il est possible d'établir une relation entre l'évolution du facteur d'échelle et le contenu en énergie de l'Univers, aussi appelée équation de Friedmann

$$H^2(a) = \left(\frac{\dot{a}}{a}\right)^2 = \frac{8\pi G}{3}\left[\rho_b a^{-3} + \rho_c a^{-3} + \rho_r a^{-4} + \rho_\Lambda\right]. \tag{6.2}$$

Le modèle standard de la cosmologie, ou modèle ΛCDM, fournit une description d'un Univers en expansion, homogène, isotrope et de courbure nulle ($K = 0$) dont le contenu en énergie est décrit par de la matière baryonique (ρ_b), du rayonnement (ρ_r), de la matière noire (ρ_c) et de l'énergie noire (ρ_Λ). L'énergie noire est nécessaire pour rendre compte de l'expansion accélérée de l'Univers mise en évidence pour la première fois en 1998 via des mesures de distance de supernovae [67]. La matière noire est également nécessaire pour expliquer (dans le cadre de la Relativité Générale) les courbes de rotation des galaxies observées [146], [147], la distribution de matière observée dans l'amas de Coma [148], [149], ainsi que la structure des pics observés dans les spectres en puissance des anisotropies du fond diffus cosmologique (CMB). Le fond diffus cosmologique, qui est l'objet d'étude de cette thèse, est un rayonnement émis environ 400 000 ans après le Big Bang lors de la recombinaison des protons et électrons dans le plasma primordial. Le satellite COBE a mesuré le spectre d'émission du CMB qui se trouve être extrêmement bien décrit par un spectre de corps noir d'une température de $T_{\mathrm{CMB}} = 2.725$ K. [9] Cependant, le modèle ΛCDM va au-delà de la cosmologie homogène en décrivant également l'évolution de faibles perturbations générées

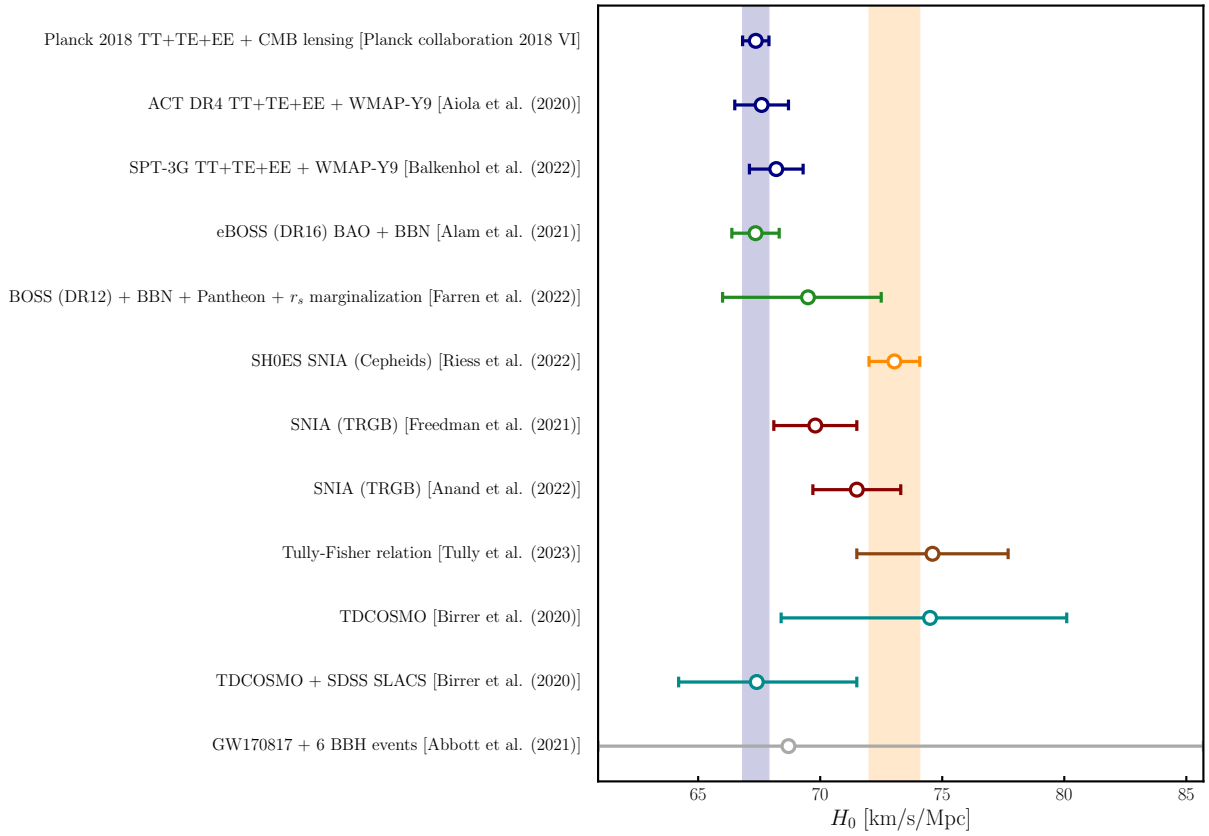

Figure 6.1: Mesures de la constante de Hubble H_0 issues de différentes sondes cosmologiques. Les mesures présentées ici ne sont pas tous indépendentes. La bande bleue correspond à l'erreur à 1σ sur la mesure de H_0 à partir des données du satellite Planck (2018) [8]. La bande orange correspond à l'erreur à 1σ sur la mesure de H_0 effectuée par la collaboration SH0ES [77].

lors d'une phase d'inflation (expansion accélérée) de l'Univers. Ces perturbations initiales sont décrites par un spectre en puissance, paramétrisé par une amplitude A_s et un indice spectral n_s et sont à l'origine des anisotropies observées dans le fond diffus cosmologique. L'analyse des propriétés statistiques des anisotropies du CMB permet d'apporter des contraintes fortes sur les paramètres cosmologiques (densités et spectre en puissance des fluctuations primordiales), ainsi que sur le taux d'expansion de l'Univers aujourd'hui $H_0 = H(t = t_0)$ aussi appelée constante de Hubble.

La figure (6.1) présente une compilation non-exhaustive de différentes mesures de la constante de Hubble à partir de différentes sondes cosmologiques. Deux mesures en particulier vont attirer notre intérêt dans le cadre de ce résumé : la mesure effectuée à partir des anisotropies du CMB par le satellite Planck $H_0 = 67.36 \pm 0.54$ km/s/Mpc et la mesure effectuée en construisant une échelle de distance à partir des supernovae de type IA $H_0 = 73.04 \pm 1.04$ km/s/Mpc. Le désaccord entre ces deux mesures est significatif (de l'ordre de 5σ). Au cours de mes trois années de doctorat, j'ai exploré différentes hypothèses pour tenter d'expliquer ce désaccord qui pourrait être causé soit par des effets systématiques instrumentaux soit par la présence de physique au-delà du modèle ΛCDM.

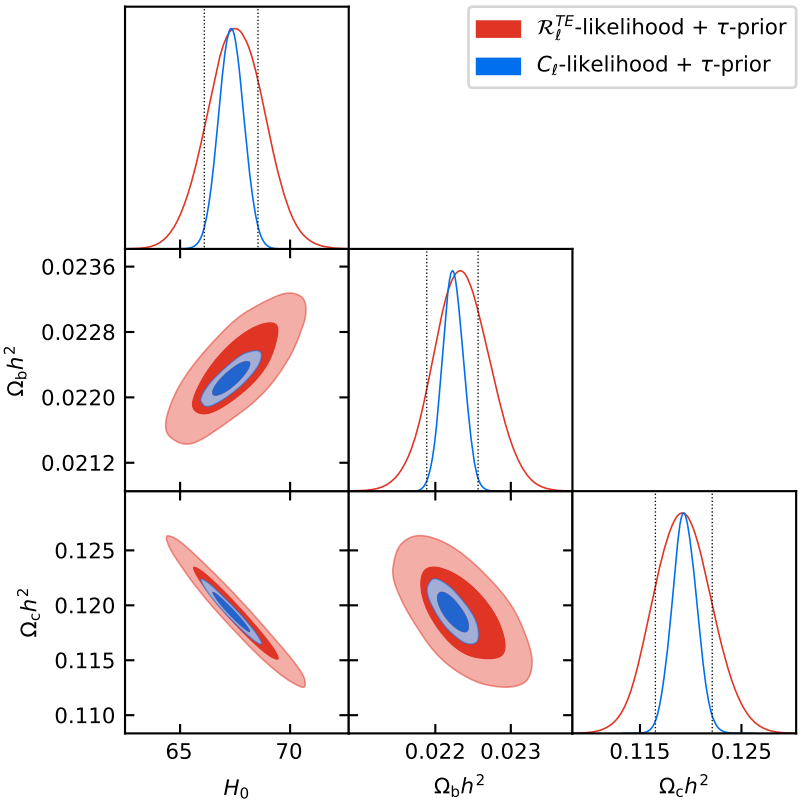

Figure 6.2: Distributions postérieures marginalisées des paramètres H_0, $\Omega_b h^2$ et $\Omega_c h^2$ obtenues à partir des spectres en puissance (bleu) et à partir du coefficient de corrélation (rouge).

Corrélation température-polarisation[1]

Les propriétés statistiques des anisotropies en température T et polarisation E du fond diffus cosmologique sont encodées dans les spectres en puissance C_ℓ^{TT}, C_ℓ^{EE} et C_ℓ^{TE} qui permettent de contraindre les paramètres cosmologiques. Cependant, il est nécessaire de quantifier suffisamment précisément les effets instrumentaux (e.g. calibrations, fonctions de transfert) afin d'obtenir des contraintes non biaisées sur les paramètres du modèle standard (en particulier sur la constante de Hubble H_0). Une façon de résoudre ce problème est d'utiliser des observables qui sont plus robustes vis-à-vis du modèle instrumental.

Le coefficient de corrélation $\mathcal{R}_\ell^{TE} = C_\ell^{TE}/\sqrt{C_\ell^{TT} C_\ell^{EE}}$ est par construction insensible aux effets instrumentaux multiplicatifs en espace harmonique. En utilisant les données les plus récentes du satellite Planck [99] (NPIPE), j'ai implémenté un estimateur pour le coefficient de corrélation $\mathcal{R}_\ell^{TE}$ directement calculé à partir des spectres en puissance et de leur covariance. J'ai ensuite obtenu des contraintes sur les paramètres cosmologiques en développant un code de fonction de vraisemblance Gaussienne pour $\mathcal{R}_\ell^{TE}$ et en utilisant un algorithme MCMC (Monte Carlo Markov Chain) pour l'exploration des paramètres. L'utilisation d'une fonction de vraisem-

[1] Adapté du Chapitre 2

blance Gaussienne pour $\mathcal{R}_\ell^{TE}$ a été validée sur un jeu de 100 simulations (cf. figure (2.3)). La figure (6.2) montre les distribution postérieures marginalisées pour H_0, la densité de baryon $\Omega_b h^2$ et la densité de matière noire $\Omega_c h^2$ obtenues via les spectres en puissance (bleu) et via le coefficient de corrélation (rouge). Les deux méthodes produisent des résultats en très bon accord. En particulier, le coefficient de corrélation permet de contraindre le taux d'expansion de l'Univers $H_0 = 67.5 \pm 1.3$ km/s/Mpc. Cette contrainte, bien que moins précise que celle dérivée de l'analyse standard des anisotropies du CMB mesurées par le satellite Planck [8], est indépendante des effets systématiques multiplicatifs et toujours en tension avec la mesure locale de H_0 obtenu par la collaboration SH0ES [77].

En conclusion, cette ré-analyse des données Planck NPIPE à partir du coefficient de corrélation a conduit à des résultats compatibles avec l'analyse standard et n'a pas permis de mettre en évidence un biais dû à de potentiels effets systématiques multiplicatifs.

Étude de la conformité température-polarisation[2]

Le modèle ΛCDM impose une relation forte entre les anisotropies de températures et les anisotropies de polarisation, sourcées par les mêmes fluctuations de densité dans le plasma primordial. Dès lors, il est possible d'identifier de potentielles déviations au modèle standard en étudiant la compatibilité entre les anisotropies de température et de polarisation par rapport aux prédictions du modèle. Une incohérence entre les mesures de température et de polarisation pourrait être le signe de nouvelle physique ou bien d'une erreur dans le modèle instrumental. Dans cette étude j'ai tiré avantage des mesures précises des anisotropies de température et des modes E de polarisation obtenues par le satellite Planck [107], par le South Pole Telescope [108] (SPT) et par le télescope cosmologique d'Atacama [106] (ACT). Avoir différentes mesures indépendantes permet de discriminer entre un effet instrumental — qui ne sera visible que pour un jeu de données — et une déviation au modèle standard.

Afin d'étudier l'adéquation des mesures de température et de polarisation, j'ai introduit de nouveaux degrés de liberté dans les fonctions de vraisemblance décrites dans les refs. [8], [106], [108] pour Planck, ACT et SPT respectivement, tel que

$$\tilde{T}_{\ell m} = T_{\ell m} \qquad \tilde{E}_{\ell m} \neq E_{\ell m}, \tag{6.3}$$

où les quantités $\tilde{T}$ et $\tilde{E}$ représentent les mesures de température et de polarisation après introduction des paramètres libres supplémentaires. Selon cette modélisation, le spectre en puissance de température C_ℓ^{TT} sera inchangé et servira à réduire la dégénérescence entre les paramètres cosmologiques et les nouveaux degrés de liberté introduits.

J'ai étudié plusieurs modèle d'incohérence T-E : un modèle de *leakage* (fuite de la température dans la polarisation) $\tilde{E}_{\ell m} = E_{\ell m} + \beta_\ell T_{\ell m}$, un modèle d'efficacité de polarisation $\tilde{E}_{\ell m} = F_\ell E_{\ell m}$ et deux modèles qui introduisent des degrés de liberté supplémentaires au niveau des spectres en puissance tel que $\tilde{C}_\ell^{TE} = \delta_\ell C_\ell^{TE}$ et $\tilde{C}_\ell^{EE} = \alpha_\ell C_\ell^{EE}$. Selon ce modèle, la déviation peut dépendre de l'échelle considérée. Afin de contraindre ces paramètres supplémentaires, j'ai utilisé un algorithme MCMC afin d'obtenir les distributions postérieures jointes des paramètres

[2] Adapté du Chapitre 3

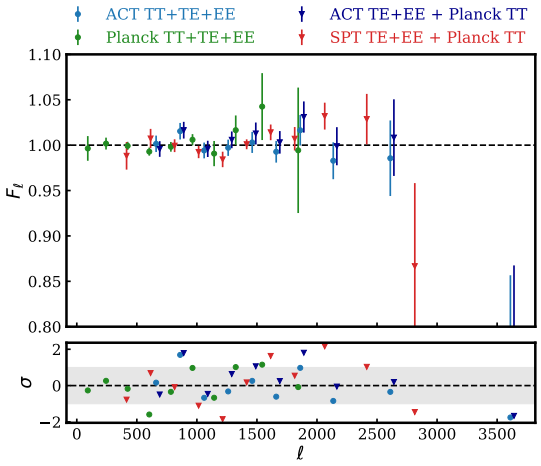

(a) Fonction de transfert en polarisation

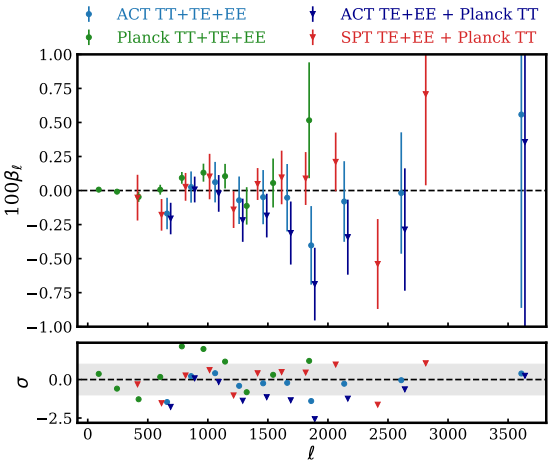

(b) T-E leakage

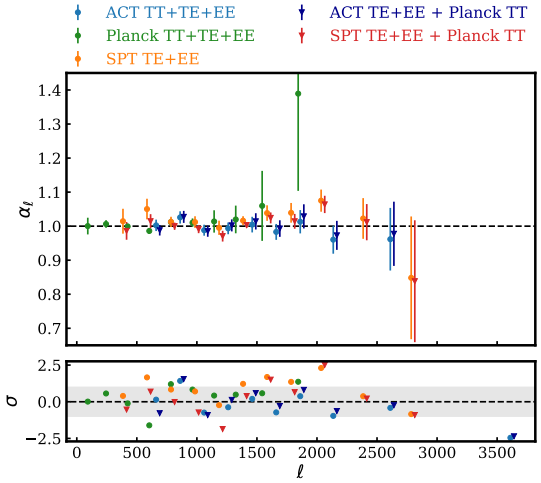

(c) Biais dans EE

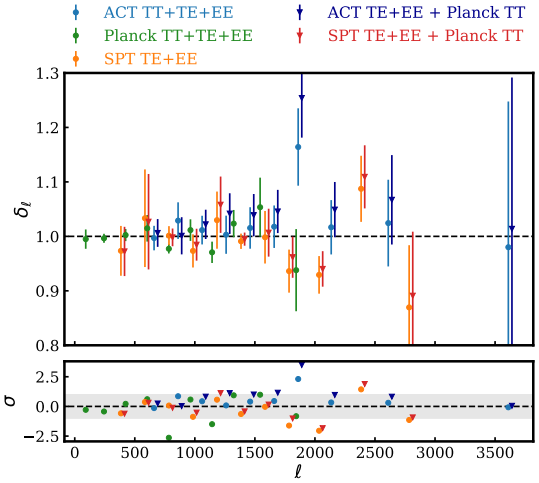

(d) Biais dans TE

Figure 6.3: Contraintes marginalisées à $\pm 1\sigma$ sur les paramètres de nuisance pour les 4 modèles étudiés : la fonction de transfert en polarisation F_ℓ (a), le leakage de T dans E β_ℓ (b), le biais dans le spectre en puissance EE α_ℓ (c) ainsi que le biais dans le spectre en puissance TE δ_ℓ (d). Chaque sous-figure contient des cotraintes obtenues à partir de différents jeux de donnée : Planck 2018 TT+TE+EE (vert), *ACT* TT+TE+EE (bleu clair), *SPT* TE+EE (orange), *Planck* TT + *ACT* TE+EE (bleu) and *Planck* TT + *SPT* TE+EE (rouge). La partie inférieure de chaque sous-figure montre la déviation par rapport à la valeur attendue en unité de σ avec une bande grise correspondant aux limites à $\pm 1\sigma$.

cosmologiques et des paramètres de nuisance. Les résultats sont présentés dans la figure (6.6). Aucune déviation statistiquement significative n'a été observée dans les jeux de données étudiés et pour chacun de modèle de nuisance. Une table présentée dans le chapitre 3 quantifie la signification statistique de chaque cas étudié (cf. table (3.1)). De plus l'introduction de ces paramètres supplémentaires a un impact négligeable sur les contraintes cosmologiques et en particulier sur

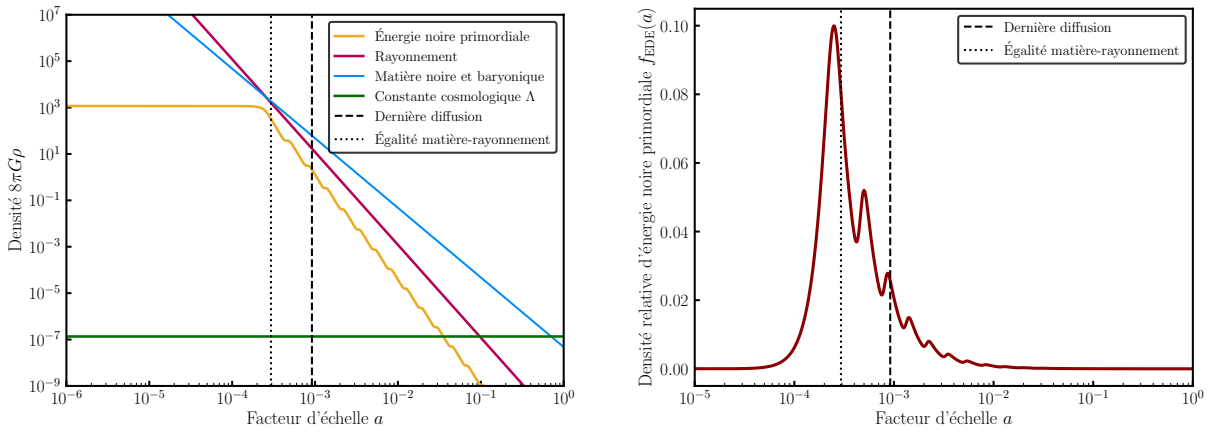

(a) (b)

Figure 6.4: (a) Densité d'énergies en fonction du facteur d'échelle a. La densité d'énergie noire primordiale (jaune) est constante et commence à se diluer à un temps proche de l'égalité matière-rayonnement. — (b) Densité relative d'énergie noire primordiale en fonction du facteur d'échelle a.

la constante de Hubble H_0.

Cosmologie au-delà du modèle standard : modèle d'énergie noire primordiale[3]

La tension entre les mesures locales de la constante de Hubble, en particulier la mesure de la collaboration SH0ES [77], et les mesures dérivées du fond diffus cosmologique [8], [106], [108] pourrait être un indice en faveur de physique au-delà du modèle standard. Parmi les modèles proposés comme solution à la tension de Hubble, une approche consistant à réduire la taille comobile de l'horizon sonore à recombinaison $r_s^* = \int_z^\infty d\tilde{z} c_s(\tilde{z})/H(\tilde{z})$ est particulièrement prometteuse [93], [94].

Dans ce chapitre, j'ai centré cette analyse sur un modèle en particulier, formulé dans les refs. [95], [96] : l'énergie noire primordiale (ou Early Dark Energy abrégé en EDE). Afin de réduire la taille de l'horizon sonore, on ajoute une composante d'énergie noire primordiale à la densité totale d'énergie dans l'Univers tel que

$$H^2(z) = \frac{8\pi G}{3}\left[(\rho_b + \rho_c)(1+z)^3 + \rho_r(1+z)^4 + \rho_\Lambda + \rho_{\rm EDE}(z)\right]. \tag{6.4}$$

Ce nouveau composant est modélisé par un champ scalaire ϕ, évoluant dans un potentiel $V(\phi) = m_\phi^2 f_\phi^2 \left[1 - \cos(\phi/f_\phi)\right]^3$, avec m_ϕ et f_ϕ la masse et la constante de désintégration du champ scalaire ϕ. Le champ évolue selon l'équation de Klein-Gordon dans un Univers en expansion

$$\ddot{\phi} + 3H\dot{\phi} + \frac{dV}{d\phi} = 0. \tag{6.5}$$

[3] Adapté du Chapitre 4

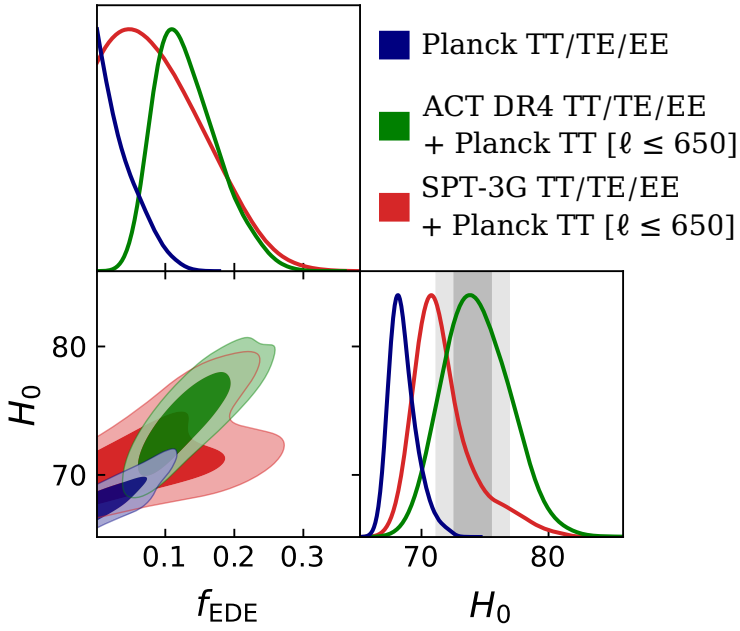

Figure 6.5: Distributions postérieures marginalisées de la densité relative d'énergie noire primordiale $f_{\rm EDE}$ au redshift $z = z_c$ et de la constante de Hubble H_0. Les bandes grises correspondent aux contraintes à $\pm 1\sigma$ et $\pm 2\sigma$ obtenue par la collaboration SH0ES [77].

Comme illustré sur la figure (6.4(a)), le champ est initialement gelé sur son potentiel (il n'évolue pas et a une densité d'énergie constante). Il en résulte une phase d'expansion accélérée avant la recombinaison. Le champ évolue ensuite sur son potentiel en oscillant et sa densité d'énergie se dilue proportionnellement à $a^{-9/2}$ (i.e. plus rapidement que le rayonnement). L'énergie noire primordiale atteint sa contribution maximale à la densité totale d'énergie dans l'Univers à un redshift critique $z = z_c$, proche de l'égalité matière-rayonnement (voir figure (6.4(b))). Cette extension au modèle ΛCDM ajoute trois paramètres supplémentaires : le redshift critique z_c, la densité relative d'énergie noire primordiale au redshift critique $f_{\rm EDE}$ et la valeur initiale du champ scalaire $\Theta_i = \phi_i / f_\phi$.

La figure (6.5) résume les contraintes obtenues sur la densité maximale d'énergie noise primordiale et sur H_0 en utilisant les données issues de Planck, ACT et SPT. Dans un article portant sur les contraintes apportées par les données Planck PR3 [8] sur le modèle EDE, les auteurs ont montré qu'une large fraction d'énergie noire primordiale n'était pas favorisée par les données avec une limite supérieure $f_{\rm EDE} < 0.087$ (95%) [115]. Les télescopes au sol que sont ACT et SPT ont fourni des mesures à haute résolution des anisotropies de température et de polarisation. Ceci permet d'apporter des contraintes sur les paramètres cosmologiques provenant des petites échelles angulaires, complémentaires aux contraintes apportées par les grandes échelles angulaires, mesurées par le satellite Planck.

Au sein de la collaboration ACT, nous avons contraint le modèle EDE à partir du jeu de données ACT DR4 [37], [106] comprenant une mesure du spectre en puissance C_ℓ^{TT} pour

$576 < \ell < 4325$ et une mesure des spectres en puissance C_ℓ^{TE} et C_ℓ^{EE} pour $325 < \ell < 4325$. Le jeu de données ACT DR4 (TT+TE+EE) montre une faible préférence en faveur d'une densité relative d'énergie noire primordiale non nulle $f_{\rm EDE} = 0.142^{+0.039}_{-0.072}$ [112] ainsi qu'une valeur de la constante de Hubble $H_0 = 74.5^{+2.5}_{-4.4}$ km/s/Mpc en accord avec les mesures locales. Lorsque l'on inclut les mesures d'anisotropies de température aux grandes échelles angulaires du satellite Planck (C_ℓ^{TT} avec $\ell < 650$) en plus des mesures des spectres en puissance de ACT DR4, la contrainte sur l'énergie noire primordiale est renforcée $f_{\rm EDE} = 0.129^{+0.028}_{-0.055}$ avec $H_0 = 74.4^{+2.2}_{-3.0}$ km/s/Mpc. De plus, la préférence en faveur du modèle EDE par rapport au modèle ΛCDM atteint une significativité statistique de 3.2σ (voir la figure (6.5) pour les distributions postérieures dans le plan ($f_{\rm EDE}$, H_0).

Ces résultats obtenus à partir des données Planck PR3 et ACT DR4 ont motivé mon analyse des contraintes sur le modèle EDE apportées par le jeu de données SPT-3G [108] contenant des mesures des spectres en puissance C_ℓ^{TE} et C_ℓ^{EE} à 95, 150 et 220 GHz pour $300 < \ell < 3000$. Les données SPT-3G seules apportent de nouvelles contraintes sur le modèle EDE, en particulier $f_{\rm EDE} = 0.163^{+0.045}_{-0.160}$, en accord avec les contraintes précédentes. L'ajout d'information sur les grandes échelles via les données Planck PR3 renforce la contrainte sur $f_{\rm EDE}$ et permet d'obtenir une limite supérieure $f_{\rm EDE} < 0.220$ (95%) toujours en bon accord avec les contraintes précédentes (voir la figure (6.5)). Ces nouveaux résultats mettent en évidence la nécessité d'obtenir de meilleures données afin de contraindre fortement les déviations au modèle ΛCDM.

Analyse des spectres en puissance du télescope cosmologique d'Atacama ACT[4]

Les sections précédentes ont mis en évidence l'importance d'avoir des mesures indépendantes des anisotropies du fond diffus cosmologique, que ce soit pour identifier de potentiels effets systématiques instrumentaux ou bien pour mettre en évidence de la physique au-delà du modèle standard. Cette section résume le travail que j'ai effectué dans le cadre de l'analyse des données récoltées de 2017 à 2022 par le télescope cosmologique d'Atacama ACT.

ACT est un télescope avec un miroir primaire d'une taille de 6 mètres situé dans le désert d'Atacama au Chili à environ 5200 mètres d'altitude. La mise à niveau la plus récente du télescope a eu lieu à partir de 2016 avec l'installation de différents tableaux de détecteurs observant le ciel à 30, 40, 90, 150 et 220 GHz. J'ai participé activement au développement des codes d'analyse de spectre en puissance à partir de cartes des anisotropies de température et de polarisation PSpipe. Le code est basé sur l'algorithme MASTER [134] pour l'estimation des spectres et des matrices de covariances associées. J'ai développé des outils afin de pouvoir effectuer des tests de consistance sur les spectres en puissance. Tout d'abord j'ai pu calibrer les tableaux de détecteurs de ACT à partir des spectres en puissance croisés entre ACT et Planck. Ces derniers nous ont permis d'identifier un effet systématique majeur dans les données ACT : une perte de puissance aux grandes échelles illustrée sur la figure (6.6). J'ai implémenté un estimateur non biaisé pour la fonction de transfert affectant les grandes échelles des cartes ACT à partir du ratio $C_\ell^{\rm ACT\times Planck}/C_\ell^{\rm Planck\times Planck}$. La mesure des fonctions de transfert nous a permis de sélectionner un intervalle de multipole ℓ robuste pour effectuer l'analyse cosmologique.

[4] Adapté du Chapitre 5

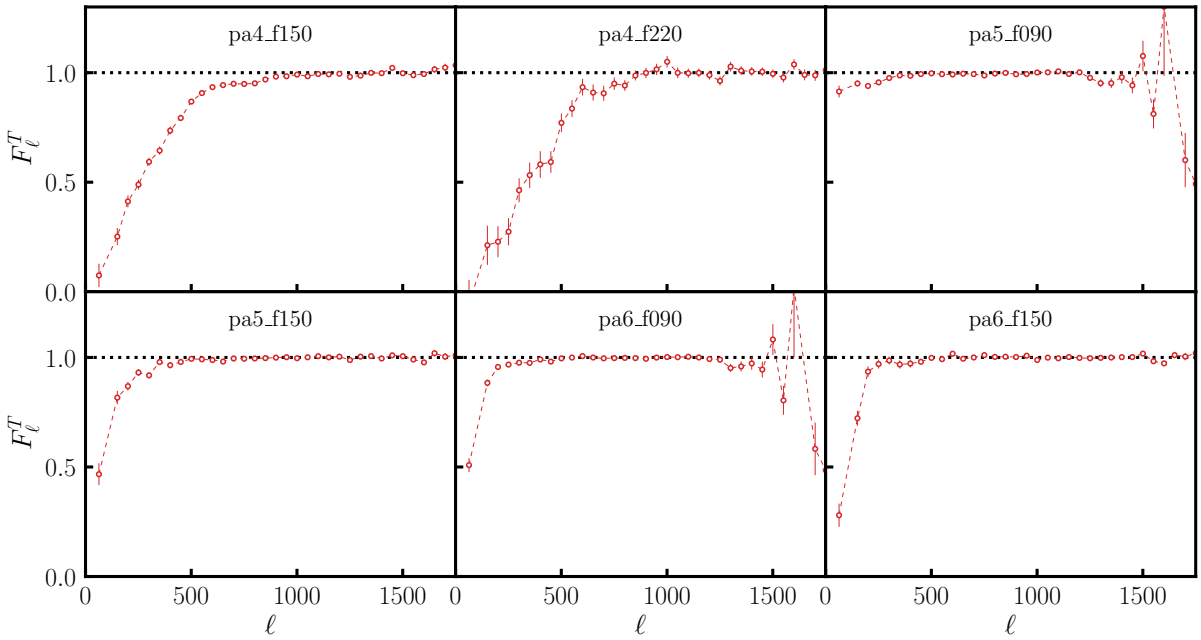

Figure 6.6: Estimation de la fonction de transfert caractérisant la perte de puissance aux grandes échelles pour les différents tableaux de détecteurs (PA ou Polarized Arrays) à différentes fréquences.

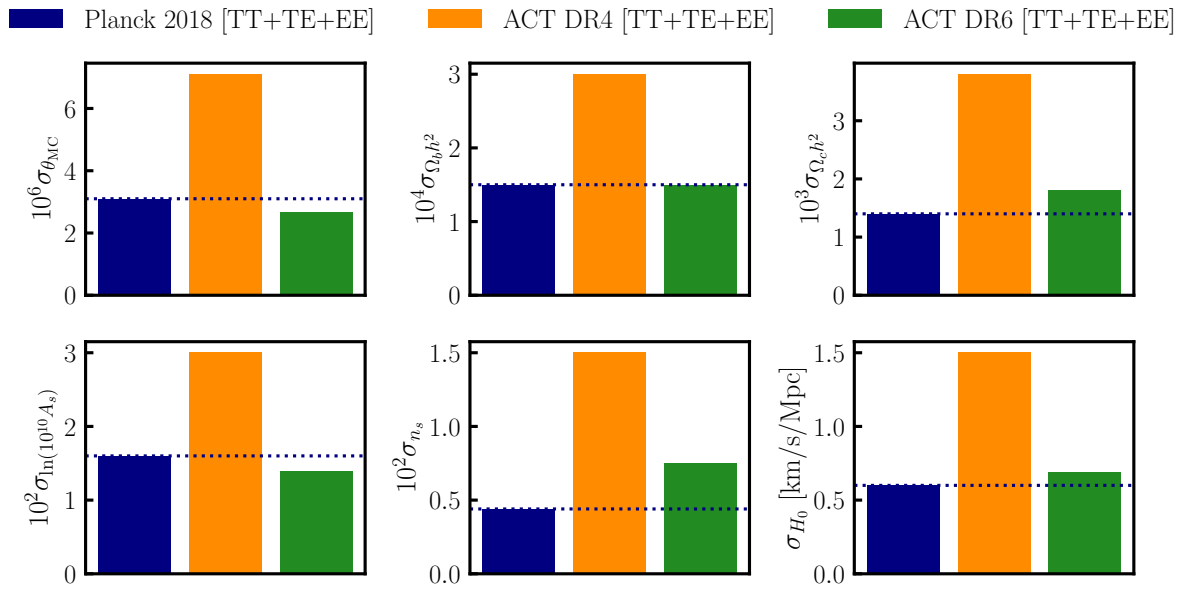

Figure 6.7: Erreurs marginales à 1σ sur les paramètres cosmologiques du modèle ΛCDM dérivées des spectres en puissance TT, TE et EE pour Planck PR3 [8], ACT DR4 [37], [106] ainsi qu'une prévision pour ACT DR6.

Sur l'intervalle de multipole choisi (voir la table (5.1)) et après la calibration des spectres en

puissance de ACT, j'ai effectué des tests de consistance par rapport aux données Planck PR4 (NPIPE) et validé la consistance des mesures des anisotropies de température par Planck et ACT. Les tests de consistance internes entre tableaux de détecteurs nous ont permis de mettre en évidence un leakage de T dans E, que l'on peut modéliser précisément via des observations de planètes et prendre en compte dans l'analyse. L'analyse est encore en cours et nous prévoyons d'étudier la consistance interne des données en fonction de l'élévation du télescope, de la quantité de vapeur d'eau dans l'atmosphère ou bien de la position des détecteurs au sein des différents tableaux de détecteurs.

La figure (6.7) montre des prévisions sur les barres d'erreur des paramètres cosmologiques du modèle ΛCDM pour le jeu de donnée ACT DR6 (2017-2022) ainsi qu'une comparaison avec les contraintes cosmologiques provenant du jeu de donnée Planck PR3 [8] et de la précédente diffusion de données de ACT (ACT DR4) [37], [106]. Ces prévisions ont été dérivées à partir de la matrice de covariance estimée sur les données par le code PSpipe, et sont compétitives par rapport aux résultats du satellite Planck tout en utilisant des échelles complémentaires.

Conclusion

Le modèle ΛCDM offre une description remarquablement précise d'observables cosmologiques telles que les propriétés statistiques du fond diffus cosmologique ou de la distribution des galaxies. La tension entre les mesures locales de la constante de Hubble H_0 et les mesures basées sur le fond diffus cosmologique vient noircir ce tableau. Dans cette thèse j'ai présenté plusieurs de mes travaux ayant pour but d'explorer de potentielles solutions à cette tension.

J'ai tout d'abord utilisé la corrélation entre les mesures des anisotropies de température et de polarisation pour apporter une contrainte sur les paramètres cosmologiques à partir des données du satellite Planck, indépendante de tout biais multiplicatif.

J'ai également effectué une étude de la cohérence entre les mesures de température et de polarisation en utilisant les meilleurs jeux de données CMB disponibles à ce jour. En utilisant cette méthode, je n'ai observé aucune déviation statistiquement significative par rapport aux prévisions du modèle ΛCDM.

Je me suis ensuite intéressé à un exemple particulier de modèle proposé comme solution à la tension de Hubble : l'énergie noire primordiale. Cette composante semble être légèrement favorisée par les données ACT DR4. J'ai mené une analyse cosmologique sur les données SPT-3G afin de contraindre les paramètres de l'énergie noire primordiale de façon indépendante, en utilisant des mesures à haute résolution de la polarisation.

Enfin, j'ai tenté de résumer ma participation à l'analyse des données récoltées par le télescope cosmologique d'Atacama de 2017 à 2022. J'ai contribué à l'élaboration des codes d'analyse des spectres en puissance, en particulier en produisant des outils qui ont pour but de caractériser les données provenant des différents tableaux de détecteurs (calibrations, efficacité de polarisation). J'ai également contribué à l'élaboration de tests de cohérence externes (comparaison avec Planck) ou internes (comparaisons entre tableaux de détecteurs) qui ont permis de mettre en évidence des effets instrumentaux qui ont ensuite pu être pris en compte dans l'analyse.

Bibliography

[1] A. La Posta, T. Louis, X. Garrido, et al. "Cosmology with the Planck $T - E$ correlation coefficient". In: *Phys. Rev. D* 104 (2 July 2021), p. 023527. DOI: 10.1103/PhysRevD.104.023527. URL: https://link.aps.org/doi/10.1103/PhysRevD.104.023527.

[2] Adrien La Posta, Umberto Natale, Erminia Calabrese, et al. "Assessing the consistency between CMB temperature and polarization measurements with application to Planck, ACT, and SPT data". In: *Phys. Rev. D* 107 (2 Jan. 2023), p. 023510. DOI: 10.1103/PhysRevD.107.023510. URL: https://link.aps.org/doi/10.1103/PhysRevD.107.023510.

[3] Adrien La Posta, Thibaut Louis, Xavier Garrido, et al. "Constraints on prerecombination early dark energy from SPT-3G public data". In: *Phys. Rev. D* 105 (8 Apr. 2022), p. 083519. DOI: 10.1103/PhysRevD.105.083519. URL: https://link.aps.org/doi/10.1103/PhysRevD.105.083519.

[4] Frank J. Qu, Blake D. Sherwin, Mathew S. Madhavacheril, et al. *The Atacama Cosmology Telescope: A Measurement of the DR6 CMB Lensing Power Spectrum and its Implications for Structure Growth*. 2023. arXiv: 2304.05202 [astro-ph.CO].

[5] Mathew S. Madhavacheril, Frank J. Qu, Blake D. Sherwin, et al. *The Atacama Cosmology Telescope: DR6 Gravitational Lensing Map and Cosmological Parameters*. 2023. arXiv: 2304.05203 [astro-ph.CO].

[6] Scott Dodelson and Fabian Schmidt. *Modern Cosmology*. Elsevier, 2021.

[7] Oliver Piattella. *Lecture Notes in Cosmology*. Springer International Publishing, 2018. DOI: 10.1007/978-3-319-95570-4. URL: https://doi.org/10.1007/978-3-319-95570-4.

[8] Planck Collaboration VI. "Planck 2018 results - VI. Cosmological parameters". In: *A&A* 641 (2020), A6. DOI: 10.1051/0004-6361/201833910. URL: https://doi.org/10.1051/0004-6361/201833910.

[9] D. J. Fixsen, E. S. Cheng, J. M. Gales, et al. "The Cosmic Microwave Background Spectrum from the Full COBE* FIRAS Data Set". In: *The Astrophysical Journal* 473.2 (Dec. 1996), p. 576. DOI: 10.1086/178173. URL: https://dx.doi.org/10.1086/178173.

[10] Antony Lewis, Anthony Challinor, and Anthony Lasenby. "Efficient Computation of Cosmic Microwave Background Anisotropies in Closed Friedmann-Robertson-Walker Models". In: *The Astrophysical Journal* 538.2 (Aug. 2000), pp. 473–476. DOI: 10.1086/309179. URL: https://doi.org/10.1086/309179.

[11] Cullan Howlett, Antony Lewis, Alex Hall, et al. "CMB power spectrum parameter degeneracies in the era of precision cosmology". In: *Journal of Cosmology and Astroparticle Physics* 2012.04 (Apr. 2012), pp. 027–027. DOI: 10.1088/1475-7516/2012/04/027. URL: https://doi.org/10.1088/1475-7516/2012/04/027.

[12] Diego Blas, Julien Lesgourgues, and Thomas Tram. "The Cosmic Linear Anisotropy Solving System (CLASS). Part II: Approximation schemes". In: *JCAP* 2011.7, 034 (July 2011), p. 034. DOI: 10.1088/1475-7516/2011/07/034. arXiv: 1104.2933 [astro-ph.CO].

[13] J. R. Bond and G. Efstathiou. "Cosmic background radiation anisotropies in universes dominated by nonbaryonic dark matter". In: *The Astrophysical Journal* 285 (Oct. 1984), pp. L45–L48. DOI: 10.1086/184362.

[14] Peter Ade, James Aguirre, Zeeshan Ahmed, et al. "The Simons Observatory: science goals and forecasts". In: *Journal of Cosmology and Astroparticle Physics* 2019.02 (Feb. 2019), pp. 056–056. DOI: 10.1088/1475-7516/2019/02/056. URL: https://doi.org/10.1088/1475-7516/2019/02/056.

[15] Kevork N. Abazajian, Peter Adshead, Zeeshan Ahmed, et al. *CMB-S4 Science Book, First Edition*. 2016. DOI: 10.48550/ARXIV.1610.02743. URL: https://arxiv.org/abs/1610.02743.

[16] Kevork Abazajian, Graeme Addison, Peter Adshead, et al. "CMB-S4 Science Case, Reference Design, and Project Plan". In: *arXiv e-prints*, arXiv:1907.04473 (July 2019), arXiv:1907.04473. arXiv: 1907.04473 [astro-ph.IM].

[17] LiteBIRD Collaboration, E Allys, K Arnold, et al. "Probing cosmic inflation with the LiteBIRD cosmic microwave background polarization survey". In: *Progress of Theoretical and Experimental Physics* 2023.4 (Nov. 2022). 042F01. ISSN: 2050-3911. DOI: 10.1093/ptep/ptac150. eprint: https://academic.oup.com/ptep/article-pdf/2023/4/042F01/50578404/ptac150.pdf. URL: https://doi.org/10.1093/ptep/ptac150.

[18] Wayne Hu. "Weak lensing of the CMB: A harmonic approach". In: *Phys. Rev. D* 62 (4 July 2000), p. 043007. DOI: 10.1103/PhysRevD.62.043007. URL: https://link.aps.org/doi/10.1103/PhysRevD.62.043007.

[19] Antony Lewis and Anthony Challinor. "Weak gravitational lensing of the CMB". In: *Physics Reports* 429.1 (2006), pp. 1–65. ISSN: 0370-1573. DOI: https://doi.org/10.1016/j.physrep.2006.03.002. URL: https://www.sciencedirect.com/science/article/pii/S0370157306000810.

[20] R. A. Sunyaev and Ya. B. Zeldovich. "The Observations of Relic Radiation as a Test of the Nature of X-Ray Radiation from the Clusters of Galaxies". In: *Comments on Astrophysics and Space Physics* 4 (Nov. 1972), p. 173.

[21] J. L. Puget, A. Abergel, J. P. Bernard, et al. "Tentative detection of a cosmic far-infrared background with COBE." In: *A&A* 308 (Apr. 1996), p. L5.

[22] M. G. Hauser, R. G. Arendt, T. Kelsall, et al. "The COBE Diffuse Infrared Background Experiment Search for the Cosmic Infrared Background. I. Limits and Detections". In: *The Astrophysical Journal* 508.1 (Nov. 1998), pp. 25–43. DOI: 10.1086/306379. arXiv: astro-ph/9806167 [astro-ph].

[23] Planck Collaboration, Ade, P. A. R., Aghanim, N., et al. "Planck 2015 results - XXV. Diffuse low-frequency Galactic foregrounds". In: *A&A* 594 (2016), A25. DOI: 10.1051/0004-6361/201526803. URL: https://doi.org/10.1051/0004-6361/201526803.

[24] Planck Collaboration, Aghanim, N., Akrami, Y., et al. "Planck 2018 results - XII. Galactic astrophysics using polarized dust emission". In: *A&A* 641 (2020), A12. DOI: 10.1051/0004-6361/201833885. URL: https://doi.org/10.1051/0004-6361/201833885.

[25] Planck Collaboration, Akrami, Y., Ashdown, M., et al. "Planck 2018 results - IV. Diffuse component separation". In: *A&A* 641 (2020), A4. DOI: 10.1051/0004-6361/201833881. URL: https://doi.org/10.1051/0004-6361/201833881.

[26] C. Dickinson, R. D. Davies, and R. J. Davis. "Towards a free–free template for CMB foregrounds". In: *Monthly Notices of the Royal Astronomical Society* 341.2 (May 2003), pp. 369–384. ISSN: 0035-8711. DOI: 10.1046/j.1365-8711.2003.06439.x. eprint: https://academic.oup.com/mnras/article-pdf/341/2/369/3851468/341-2-369.pdf. URL: https://doi.org/10.1046/j.1365-8711.2003.06439.x.

[27] Planck Collaboration, Ade, P. A. R., Aghanim, N., et al. "Planck 2013 results. XIII. Galactic CO emission". In: *A&A* 571 (2014), A13. DOI: 10.1051/0004-6361/201321553. URL: https://doi.org/10.1051/0004-6361/201321553.

[28] D. N. Spergel, L. Verde, H. V. Peiris, et al. "First-Year Wilkinson Microwave Anisotropy Probe (WMAP)* Observations: Determination of Cosmological Parameters". In: *The Astrophysical Journal Supplement Series* 148.1 (Sept. 2003), p. 175. DOI: 10.1086/377226. URL: https://dx.doi.org/10.1086/377226.

[29] D. N. Spergel, R. Bean, O. Doré, et al. "Three-Year Wilkinson Microwave Anisotropy Probe (WMAP) Observations: Implications for Cosmology". In: *The Astrophysical Journal Supplement Series* 170.2 (June 2007), pp. 377–408. DOI: 10.1086/513700. arXiv: astro-ph/0603449 [astro-ph].

[30] E. Komatsu, J. Dunkley, M. R. Nolta, et al. "Five-year Wilkinson Microwave Anisotropy Probe (WMAP) observations: cosmological interpretation". In: *The Astrophysical Journal Supplement Series* 180.2 (Feb. 2009), p. 330. DOI: 10.1088/0067-0049/180/2/330. URL: https://dx.doi.org/10.1088/0067-0049/180/2/330.

[31] E. Komatsu, K. M. Smith, J. Dunkley, et al. "Seven-year Wilkinson Microwave Anisotropy Probe (WMAP) observations: cosmological interpretation". In: *The Astrophysical Journal Supplement Series* 192.2 (Jan. 2011), p. 18. DOI: 10.1088/0067-0049/192/2/18. URL: https://dx.doi.org/10.1088/0067-0049/192/2/18.

[32] G. Hinshaw, D. Larson, E. Komatsu, et al. "Nine-year Wilkinson Microwave Anisotropy Probe (WMAP) observations: cosmological parameter results". In: *The Astrophysical Journal Supplement Series* 208.2 (Sept. 2013), p. 19. DOI: 10.1088/0067-0049/208/2/19. URL: https://dx.doi.org/10.1088/0067-0049/208/2/19.

[33] Planck Collaboration, Ade, P. A. R., Aghanim, N., et al. "Planck 2013 results. XVI. Cosmological parameters". In: *A&A* 571 (2014), A16. DOI: 10.1051/0004-6361/201321591. URL: https://doi.org/10.1051/0004-6361/201321591.

[34] Planck Collaboration, Ade, P. A. R., Aghanim, N., et al. "Planck 2015 results - XIII. Cosmological parameters". In: *A&A* 594 (2016), A13. DOI: 10.1051/0004-6361/201525830. URL: https://doi.org/10.1051/0004-6361/201525830.

[35] J. Dunkley, R. Hlozek, J. Sievers, et al. "The Atacama Cosmology Telescope: Cosmological parameters from the 2008 power spectrum". In: *The Astrophysical Journal* 739.1 (Sept. 2011), p. 52. DOI: 10.1088/0004-637X/739/1/52. URL: https://dx.doi.org/10.1088/0004-637X/739/1/52.

[36] Sigurd Naess, Matthew Hasselfield, Jeff McMahon, et al. "The Atacama Cosmology Telescope: CMB polarization at 200<ell<9000". In: *Journal of Cosmology and Astroparticle Physics* 2014.10 (Oct. 2014), p. 007. DOI: 10.1088/1475-7516/2014/10/007. URL: https://dx.doi.org/10.1088/1475-7516/2014/10/007.

[37] Simone Aiola, Erminia Calabrese, Loïc Maurin, et al. "The Atacama Cosmology Telescope: DR4 maps and cosmological parameters". In: *Journal of Cosmology and Astroparticle Physics* 2020.12 (Dec. 2020), pp. 047–047. DOI: 10.1088/1475-7516/2020/12/047. URL: https://doi.org/10.1088/1475-7516/2020/12/047.

[38] J. W. Henning, J. T. Sayre, C. L. Reichardt, et al. "Measurements of the Temperature and E-mode Polarization of the CMB from 500 Square Degrees of SPTpol Data". In: *The Astrophysical Journal* 852.2 (Jan. 2018), p. 97. DOI: 10.3847/1538-4357/aa9ff4. URL: https://dx.doi.org/10.3847/1538-4357/aa9ff4.

[39] L. Balkenhol, D. Dutcher, A. Spurio Mancini, et al. *A Measurement of the CMB Temperature Power Spectrum and Constraints on Cosmology from the SPT-3G 2018 TT/TE/EE Data Set*. 2022. arXiv: 2212.05642 [astro-ph.CO].

[40] A. Kogut, D. N. Spergel, C. Barnes, et al. "First-Year Wilkinson Microwave Anisotropy Probe (WMAP)* Observations: Temperature-Polarization Correlation". In: *The Astrophysical Journal Supplement Series* 148.1 (Sept. 2003), p. 161. DOI: 10.1086/377219. URL: https://dx.doi.org/10.1086/377219.

[41] Planck Collaboration, Ade, P. A. R., Aghanim, N., et al. "Planck 2013 results. XII. Diffuse component separation". In: *A&A* 571 (2014), A12. DOI: 10.1051/0004-6361/201321580. URL: https://doi.org/10.1051/0004-6361/201321580.

[42] Planck Collaboration, Adam, R., Ade, P. A. R., et al. "Planck 2015 results - IX. Diffuse component separation: CMB maps". In: *A&A* 594 (2016), A9. DOI: 10.1051/0004-6361/201525936. URL: https://doi.org/10.1051/0004-6361/201525936.

[43] Planck Collaboration, Adam, R., Ade, P. A. R., et al. "Planck 2015 results - X. Diffuse component separation: Foreground maps". In: *A&A* 594 (2016), A10. DOI: 10.1051/0004-6361/201525967. URL: https://doi.org/10.1051/0004-6361/201525967.

[44] Planck Collaboration, Aghanim, N., Akrami, Y., et al. "Planck 2018 results - I. Overview and the cosmological legacy of Planck". In: *A&A* 641 (2020), A1. DOI: 10.1051/0004-6361/201833880. URL: https://doi.org/10.1051/0004-6361/201833880.

[45] M. Tristram, A. J. Banday, K. M. Górski, et al. "Improved limits on the tensor-to-scalar ratio using BICEP and Planck data". In: *Phys. Rev. D* 105 (8 Apr. 2022), p. 083524. DOI: 10.1103/PhysRevD.105.083524. URL: https://link.aps.org/doi/10.1103/PhysRevD.105.083524.

[46] Planck Collaboration, Ade, P. A. R., Aghanim, N., et al. "Planck 2013 results. XVII. Gravitational lensing by large-scale structure". In: *A&A* 571 (2014), A17. DOI: 10.1051/0004-6361/201321543. URL: https://doi.org/10.1051/0004-6361/201321543.

[47] Planck Collaboration, Ade, P. A. R., Aghanim, N., et al. "Planck 2015 results - XV. Gravitational lensing". In: *A&A* 594 (2016), A15. DOI: 10.1051/0004-6361/201525941. URL: https://doi.org/10.1051/0004-6361/201525941.

[48] Planck Collaboration, N. Aghanim, Y. Akrami, et al. "Planck 2018 results. VIII. Gravitational lensing". In: *A&A* 641, A8 (Sept. 2020), A8. DOI: 10.1051/0004-6361/201833886. arXiv: 1807.06210 [astro-ph.CO].

[49] Sudeep Das, Blake D. Sherwin, Paula Aguirre, et al. "Detection of the Power Spectrum of Cosmic Microwave Background Lensing by the Atacama Cosmology Telescope". In: *Phys. Rev. Lett.* 107 (2 July 2011), p. 021301. DOI: 10.1103/PhysRevLett.107.021301. URL: https://link.aps.org/doi/10.1103/PhysRevLett.107.021301.

[50] Nick Kaiser. "Clustering in real space and in redshift space". In: *Monthly Notices of the Royal Astronomical Society* 227.1 (July 1987), pp. 1–21. ISSN: 0035-8711. DOI: 10.1093/mnras/227.1.1. eprint: https://academic.oup.com/mnras/article-pdf/227/1/1/18522208/mnras227-0001.pdf. URL: https://doi.org/10.1093/mnras/227.1.1.

[51] Kyle S. Dawson, David J. Schlegel, Christopher P. Ahn, et al. "The Baryon Oscillation Spectroscopic Survey of SDSS-III". In: *The Astronomical Journal* 145.1 (Dec. 2012), p. 10. DOI: 10.1088/0004-6256/145/1/10. URL: https://dx.doi.org/10.1088/0004-6256/145/1/10.

[52] Kyle S. Dawson, Jean-Paul Kneib, Will J. Percival, et al. "THE SDSS-IV EXTENDED BARYON OSCILLATION SPECTROSCOPIC SURVEY: OVERVIEW AND EARLY DATA". In: *The Astronomical Journal* 151.2 (Feb. 2016), p. 44. DOI: 10.3847/0004-6256/151/2/44. URL: https://dx.doi.org/10.3847/0004-6256/151/2/44.

[53] Shadab Alam, Marie Aubert, Santiago Avila, et al. "Completed SDSS-IV extended Baryon Oscillation Spectroscopic Survey: Cosmological implications from two decades of spectroscopic surveys at the Apache Point Observatory". In: *Phys. Rev. D* 103 (8 Apr. 2021), p. 083533. DOI: 10.1103/PhysRevD.103.083533. URL: https://link.aps.org/doi/10.1103/PhysRevD.103.083533.

[54] DESI Collaboration, Amir Aghamousa, Jessica Aguilar, et al. *The DESI Experiment Part I: Science,Targeting, and Survey Design*. 2016. arXiv: 1611.00036 [astro-ph.IM].

[55] Hélion du Mas des Bourboux, James Rich, Andreu Font-Ribera, et al. "The Completed SDSS-IV Extended Baryon Oscillation Spectroscopic Survey: Baryon Acoustic Oscillations with Ly-α Forests". In: *The Astrophysical Journal* 901.2 (Oct. 2020), p. 153. DOI: 10.3847/1538-4357/abb085. URL: https://dx.doi.org/10.3847/1538-4357/abb085.

[56] Solène Chabanier, Nathalie Palanque-Delabrouille, Christophe Yèche, et al. "The one-dimensional power spectrum from the SDSS DR14 Lyα forests". In: *Journal of Cosmology and Astroparticle Physics* 2019.07 (July 2019), p. 017. DOI: 10.1088/1475-7516/2019/07/017. URL: https://dx.doi.org/10.1088/1475-7516/2019/07/017.

[57] Corentin Ravoux, Marie Lynn Abdul Karim, Eric Armengaud, et al. *The Dark Energy Spectroscopic Instrument: One-dimensional power spectrum from first Lyman-α forest samples with Fast Fourier Transform*. 2023. arXiv: 2306.06311 [astro-ph.CO].

[58] C. Ravoux, E. Armengaud, M. Walther, et al. "A tomographic map of the large-scale matter distribution using the eBOSS—Stripe 82 Ly-α forest". In: *Journal of Cosmology and Astroparticle Physics* 2020.07 (July 2020), p. 010. DOI: 10.1088/1475-7516/2020/07/010. URL: https://dx.doi.org/10.1088/1475-7516/2020/07/010.

[59] Jelte T. A. de Jong, Gijs A. Verdoes Kleijn, Konrad H. Kuijken, et al. "The Kilo-Degree Survey". In: *Experimental Astronomy* 35.1 (Jan. 2013), pp. 25–44. ISSN: 1572-9508. DOI: 10.1007/s10686-012-9306-1. URL: https://doi.org/10.1007/s10686-012-9306-1.

[60] B. Flaugher, H. T. Diehl, K. Honscheid, et al. "THE DARK ENERGY CAMERA". In: *The Astronomical Journal* 150.5 (Oct. 2015), p. 150. DOI: 10.1088/0004-6256/150/5/150. URL: https://dx.doi.org/10.1088/0004-6256/150/5/150.

[61] Hiroaki Aihara, Nobuo Arimoto, Robert Armstrong, et al. "The Hyper Suprime-Cam SSP Survey: Overview and survey design". In: *Publications of the Astronomical Society of Japan* 70.SP1 (Sept. 2017). S4. ISSN: 0004-6264. DOI: 10.1093/pasj/psx066. eprint: https://academic.oup.com/pasj/article-pdf/70/SP1/S4/23692189/psx066.pdf. URL: https://doi.org/10.1093/pasj/psx066.

[62] Planck Collaboration, Ade, P. A. R., Aghanim, N., et al. "Planck 2013 results. XX. Cosmology from Sunyaev-Zeldovich cluster counts". In: *A&A* 571 (2014), A20. DOI: 10.1051/0004-6361/201321521. URL: https://doi.org/10.1051/0004-6361/201321521.

[63] Heymans, Catherine, Tröster, Tilman, Asgari, Marika, et al. "KiDS-1000 Cosmology: Multi-probe weak gravitational lensing and spectroscopic galaxy clustering constraints". In: *A&A* 646 (2021), A140. DOI: 10.1051/0004-6361/202039063. URL: https://doi.org/10.1051/0004-6361/202039063.

[64] T. M. C. Abbott, M. Aguena, A. Alarcon, et al. "Dark Energy Survey Year 3 results: Cosmological constraints from galaxy clustering and weak lensing". In: *Phys. Rev. D* 105 (2 Jan. 2022), p. 023520. DOI: 10.1103/PhysRevD.105.023520. URL: https://link.aps.org/doi/10.1103/PhysRevD.105.023520.

[65] Hironao Miyatake, Sunao Sugiyama, Masahiro Takada, et al. *Hyper Suprime-Cam Year 3 Results: Cosmology from Galaxy Clustering and Weak Lensing with HSC and SDSS using the Emulator Based Halo Model*. 2023. arXiv: 2304.00704 [astro-ph.CO].

[66] Sunao Sugiyama, Hironao Miyatake, Surhud More, et al. *Hyper Suprime-Cam Year 3 Results: Cosmology from Galaxy Clustering and Weak Lensing with HSC and SDSS using the Minimal Bias Model*. 2023. arXiv: 2304.00705 [astro-ph.CO].

[67] Adam G. Riess, Alexei V. Filippenko, Peter Challis, et al. "Observational Evidence from Supernovae for an Accelerating Universe and a Cosmological Constant". In: *The Astronomical Journal* 116.3 (Sept. 1998), p. 1009. DOI: 10.1086/300499. URL: https://dx.doi.org/10.1086/300499.

[68] D. M. Scolnic, D. O. Jones, A. Rest, et al. "The Complete Light-curve Sample of Spectroscopically Confirmed SNe Ia from Pan-STARRS1 and Cosmological Constraints from the Combined Pantheon Sample". In: *The Astrophysical Journal* 859.2 (May 2018), p. 101. DOI: 10.3847/1538-4357/aab9bb. URL: https://dx.doi.org/10.3847/1538-4357/aab9bb.

[69] Dillon Brout, Dan Scolnic, Brodie Popovic, et al. "The Pantheon+ Analysis: Cosmological Constraints". In: *The Astrophysical Journal* 938.2 (Oct. 2022), p. 110. DOI: 10.3847/1538-4357/ac8e04. URL: https://dx.doi.org/10.3847/1538-4357/ac8e04.

[70] Betoule, M., Kessler, R., Guy, J., et al. "Improved cosmological constraints from a joint analysis of the SDSS-II and SNLS supernova samples". In: *A&A* 568 (2014), A22. DOI: 10.1051/0004-6361/201423413. URL: https://doi.org/10.1051/0004-6361/201423413.

[71] B P Abbott, R Abbott, R Adhikari, et al. "LIGO: the Laser Interferometer Gravitational-Wave Observatory". In: *Reports on Progress in Physics* 72.7 (June 2009), p. 076901. DOI: 10.1088/0034-4885/72/7/076901. URL: https://dx.doi.org/10.1088/0034-4885/72/7/076901.

[72] T Accadia, F Acernese, M Alshourbagy, et al. "Virgo: a laser interferometer to detect gravitational waves". In: *Journal of Instrumentation* 7.03 (Mar. 2012), P03012. DOI: 10.1088/1748-0221/7/03/P03012. URL: https://dx.doi.org/10.1088/1748-0221/7/03/P03012.

[73] Ryan J. Cooke, Max Pettini, and Charles C. Steidel. "One Percent Determination of the Primordial Deuterium Abundance*". In: *The Astrophysical Journal* 855.2 (Mar. 2018), p. 102. DOI: 10.3847/1538-4357/aaab53. URL: https://dx.doi.org/10.3847/1538-4357/aaab53.

[74] Eric J Baxter and Blake D Sherwin. "Determining the Hubble constant without the sound horizon scale: measurements from CMB lensing". In: *Monthly Notices of the Royal Astronomical Society* 501.2 (Dec. 2020), pp. 1823–1835. ISSN: 0035-8711. DOI: 10.1093/mnras/staa3706. eprint: https://academic.oup.com/mnras/article-pdf/501/2/1823/35331993/staa3706.pdf. URL: https://doi.org/10.1093/mnras/staa3706.

[75] Gerrit S. Farren, Oliver H. E. Philcox, and Blake D. Sherwin. "Determining the Hubble constant without the sound horizon: Perspectives with future galaxy surveys". In: *Phys. Rev. D* 105 (6 Mar. 2022), p. 063503. DOI: 10.1103/PhysRevD.105.063503. URL: https://link.aps.org/doi/10.1103/PhysRevD.105.063503.

[76] Oliver H. E. Philcox and Mikhail M. Ivanov. "BOSS DR12 full-shape cosmology: ΛCDM constraints from the large-scale galaxy power spectrum and bispectrum monopole". In: *Phys. Rev. D* 105 (4 Feb. 2022), p. 043517. DOI: 10.1103/PhysRevD.105.043517. URL: https://link.aps.org/doi/10.1103/PhysRevD.105.043517.

[77] Adam G. Riess, Stefano Casertano, Wenlong Yuan, et al. "Cosmic Distances Calibrated to 1% Precision with Gaia EDR3 Parallaxes and Hubble Space Telescope Photometry of 75 Milky Way Cepheids Confirm Tension with LambdaCDM". In: *The Astrophysical Journal* 908.1 (Feb. 2021), p. L6. DOI: 10.3847/2041-8213/abdbaf. URL: https://doi.org/10.3847/2041-8213/abdbaf.

[78] Adam G. Riess, Wenlong Yuan, Lucas M. Macri, et al. "A Comprehensive Measurement of the Local Value of the Hubble Constant with 1 km/s/Mpc Uncertainty from the Hubble Space Telescope and the SH0ES Team". In: *The Astrophysical Journal Letters* 934.1 (July 2022), p. L7. DOI: 10.3847/2041-8213/ac5c5b. URL: https://dx.doi.org/10.3847/2041-8213/ac5c5b.

[79] Wendy L. Freedman, Barry F. Madore, Dylan Hatt, et al. "The Carnegie-Chicago Hubble Program. VIII. An Independent Determination of the Hubble Constant Based on the Tip of the Red Giant Branch". In: *The Astrophysical Journal* 882.1 (Aug. 2019), p. 34. DOI: 10.3847/1538-4357/ab2f73. URL: https://doi.org/10.3847/1538-4357/ab2f73.

[80] Wendy L. Freedman, Barry F. Madore, Taylor Hoyt, et al. "Calibration of the Tip of the Red Giant Branch". In: *The Astrophysical Journal* 891.1 (Mar. 2020), p. 57. DOI: 10.3847/1538-4357/ab7339. URL: https://doi.org/10.3847/1538-4357/ab7339.

[81] Wendy L. Freedman. "Measurements of the Hubble Constant: Tensions in Perspective*". In: *The Astrophysical Journal* 919.1 (Sept. 2021), p. 16. DOI: 10.3847/1538-4357/ac0e95. URL: https://dx.doi.org/10.3847/1538-4357/ac0e95.

[82] Kevin Krisciunas, Carlos Contreras, Christopher R. Burns, et al. "The Carnegie Supernova Project. I. Third Photometry Data Release of Low-redshift Type Ia Supernovae and Other White Dwarf Explosions". In: *The Astronomical Journal* 154.5 (Nov. 2017), p. 211. DOI: 10.3847/1538-3881/aa8df0. URL: https://dx.doi.org/10.3847/1538-3881/aa8df0.

[83] Gagandeep S. Anand, R. Brent Tully, Luca Rizzi, et al. "Comparing Tip of the Red Giant Branch Distance Scales: An Independent Reduction of the Carnegie-Chicago Hubble Program and the Value of the Hubble Constant". In: *The Astrophysical Journal* 932.1 (June 2022), p. 15. DOI: 10.3847/1538-4357/ac68df. URL: https://dx.doi.org/10.3847/1538-4357/ac68df.

[84] R. B. Tully and J. R. Fisher. "A new method of determining distances to galaxies." In: *Astronomy and Astrophysics* 54 (Feb. 1977), pp. 661–673.

[85] R. Brent Tully, Ehsan Kourkchi, Hélène M. Courtois, et al. "Cosmicflows-4". In: *The Astrophysical Journal* 944.1 (Feb. 2023), p. 94. DOI: 10.3847/1538-4357/ac94d8. URL: https://dx.doi.org/10.3847/1538-4357/ac94d8.

[86] S. Birrer, A. J. Shajib, A. Galan, et al. "TDCOSMO. IV. Hierarchical time-delay cosmography - joint inference of the Hubble constant and galaxy density profiles". In: *A&A* 643, A165 (Nov. 2020), A165. DOI: 10.1051/0004-6361/202038861. arXiv: 2007.02941 [astro-ph.CO].

[87] Kenneth C Wong, Sherry H Suyu, Geoff C-F Chen, et al. "H0LiCOW – XIII. A 2.4 per cent measurement of H0 from lensed quasars: 5.3sigma tension between early- and late-Universe probes". In: *Monthly Notices of the Royal Astronomical Society* 498.1 (Sept. 2019), pp. 1420–1439. ISSN: 0035-8711. DOI: 10.1093/mnras/stz3094. eprint: https://academic.oup.com/mnras/article-pdf/498/1/1420/33755111/stz3094.pdf. URL: https://doi.org/10.1093/mnras/stz3094.

[88] B. P. Abbott, R. Abbott, T. D. Abbott, et al. "Observation of Gravitational Waves from a Binary Black Hole Merger". In: *Phys. Rev. Lett.* 116 (6 Feb. 2016), p. 061102. DOI: 10.1103/PhysRevLett.116.061102. URL: https://link.aps.org/doi/10.1103/PhysRevLett.116.061102.

[89] Bernard F. Schutz. "Determining the Hubble constant from gravitational wave observations". In: *Nature* 323.6086 (Sept. 1986), pp. 310–311. ISSN: 1476-4687. DOI: 10.1038/323310a0. URL: https://doi.org/10.1038/323310a0.

[90] Rachel Gray, Ignacio Magaña Hernandez, Hong Qi, et al. "Cosmological inference using gravitational wave standard sirens: A mock data analysis". In: *Phys. Rev. D* 101 (12 June 2020), p. 122001. DOI: 10.1103/PhysRevD.101.122001. URL: https://link.aps.org/doi/10.1103/PhysRevD.101.122001.

[91] B. P. Abbott, R. Abbott, T. D. Abbott, et al. "A Gravitational-wave Measurement of the Hubble Constant Following the Second Observing Run of Advanced LIGO and Virgo". In: *The Astrophysical Journal* 909.2 (Mar. 2021), p. 218. DOI: 10.3847/1538-4357/abdcb7. URL: https://dx.doi.org/10.3847/1538-4357/abdcb7.

[92] Eleonora Di Valentino, Olga Mena, Supriya Pan, et al. "In the realm of the Hubble tension—a review of solutions*". In: *Classical and Quantum Gravity* 38.15 (July 2021), p. 153001. DOI: 10.1088/1361-6382/ac086d. URL: https://dx.doi.org/10.1088/1361-6382/ac086d.

[93] L. Knox and M. Millea. "Hubble constant hunter's guide". In: *Phys. Rev. D* 101 (4 Feb. 2020), p. 043533. DOI: 10.1103/PhysRevD.101.043533. URL: https://link.aps.org/doi/10.1103/PhysRevD.101.043533.

[94] Nils Schöneberg, Guillermo Franco Abellán, Andrea Pérez Sánchez, et al. "The H0 Olympics: A fair ranking of proposed models". In: *Physics Reports* 984 (2022). The H0 Olympics: A fair ranking of proposed models, pp. 1–55. ISSN: 0370-1573. DOI: https://doi.org/10.1016/j.physrep.2022.07.001. URL: https://www.sciencedirect.com/science/article/pii/S0370157322002538.

[95] Vivian Poulin, Tristan L. Smith, Tanvi Karwal, et al. "Early Dark Energy can Resolve the Hubble Tension". In: *Phys. Rev. Lett.* 122 (22 June 2019), p. 221301. DOI: 10.1103/PhysRevLett.122.221301. URL: https://link.aps.org/doi/10.1103/PhysRevLett.122.221301.

[96] Tristan L. Smith, Vivian Poulin, and Mustafa A. Amin. "Oscillating scalar fields and the Hubble tension: A resolution with novel signatures". In: *Phys. Rev. D* 101 (6 Mar. 2020), p. 063523. DOI: 10.1103/PhysRevD.101.063523. URL: https://link.aps.org/doi/10.1103/PhysRevD.101.063523.

[97] Rigault, M., Brinnel, V., Aldering, G., et al. "Strong dependence of Type Ia supernova standardization on the local specific star formation rate". In: *A&A* 644 (2020), A176. DOI: 10.1051/0004-6361/201730404. URL: https://doi.org/10.1051/0004-6361/201730404.

[98] C. Saunders, G. Aldering, P. Antilogus, et al. "SNEMO: Improved Empirical Models for Type Ia Supernovae". In: *The Astrophysical Journal* 869.2 (Dec. 2018), p. 167. DOI: 10.3847/1538-4357/aaec7e. URL: https://doi.org/10.3847/1538-4357/aaec7e.

[99] Planck Collaboration, Akrami, Y., Andersen, K. J., et al. "Planck intermediate results - LVII. Joint Planck LFI and HFI data processing". In: *A&A* 643 (2020), A42. DOI: 10.1051/0004-6361/202038073. URL: https://doi.org/10.1051/0004-6361/202038073.

[100] Couchot, F., Henrot-Versillé, S., Perdereau, O., et al. "Cosmology with the cosmic microwave background temperature-polarization correlation". In: *A&A* 602 (2017), A41. DOI: 10.1051/0004-6361/201629815. URL: https://doi.org/10.1051/0004-6361/201629815.

[101] Planck Collaboration XI. "Planck 2015 results - XI. CMB power spectra, likelihoods, and robustness of parameters". In: *A&A* 594 (2016), A11. DOI: 10.1051/0004-6361/201526926. URL: https://doi.org/10.1051/0004-6361/201526926.

[102] Jesus Torrado and Antony Lewis. *Cobaya: Code for Bayesian Analysis of hierarchical physical models*. May 2020. arXiv: 2005.05290 [astro-ph.IM].

[103] J A Peacock and M Bilicki. "Wide-area tomography of CMB lensing and the growth of cosmological density fluctuations". In: *Monthly Notices of the Royal Astronomical Society* 481.1 (Aug. 2018), pp. 1133–1148. ISSN: 0035-8711. DOI: 10.1093/mnras/sty2314. eprint: https://academic.oup.com/mnras/article-pdf/481/1/1133/25699685/sty2314.pdf. URL: https://doi.org/10.1093/mnras/sty2314.

[104] Thibaut Louis, Zack Li, and Matthieu Tristram. "TE correlation coefficient of Planck legacy data". In: *Phys. Rev. D* 100 (10 Nov. 2019), p. 103534. DOI: 10.1103/PhysRevD.100.103534. URL: https://link.aps.org/doi/10.1103/PhysRevD.100.103534.

[105] J Dunkley, E Calabrese, J Sievers, et al. "The Atacama Cosmology Telescope: likelihood for small-scale CMB data". In: *Journal of Cosmology and Astroparticle Physics* 2013.07 (July 2013), pp. 025–025. DOI: 10.1088/1475-7516/2013/07/025. URL: https://doi.org/10.1088/1475-7516/2013/07/025.

[106] Steve K. Choi, Matthew Hasselfield, Shuay-Pwu Patty Ho, et al. "The Atacama Cosmology Telescope: a measurement of the Cosmic Microwave Background power spectra at 98 and 150 GHz". In: *Journal of Cosmology and Astroparticle Physics* 2020.12 (Dec. 2020), pp. 045–045. DOI: 10.1088/1475-7516/2020/12/045. URL: https://doi.org/10.1088/1475-7516/2020/12/045.

[107] Planck Collaboration, Aghanim, N., Akrami, Y., et al. "Planck 2018 results - V. CMB power spectra and likelihoods". In: *A&A* 641 (2020), A5. DOI: 10.1051/0004-6361/201936386. URL: https://doi.org/10.1051/0004-6361/201936386.

[108] D. Dutcher, L. Balkenhol, P. A. R. Ade, et al. "Measurements of the E-mode polarization and temperature-E-mode correlation of the CMB from SPT-3G 2018 data". In: *Phys. Rev. D* 104 (2 July 2021), p. 022003. DOI: 10.1103/PhysRevD.104.022003. URL: https://link.aps.org/doi/10.1103/PhysRevD.104.022003.

[109] Antony Lewis. "GetDist: a Python package for analysing Monte Carlo samples". In: (2019). arXiv: 1910.13970 [astro-ph.IM]. URL: https://getdist.readthedocs.io.

[110] Coralia Cartis, Jan Fiala, Benjamin Marteau, et al. "Improving the Flexibility and Robustness of Model-Based Derivative-Free Optimization Solvers". In: *arXiv e-prints*, arXiv:1804.00154 (Mar. 2018), arXiv:1804.00154. arXiv: 1804.00154 [math.OC].

[111] Coralia Cartis, Lindon Roberts, and Oliver Sheridan-Methven. "Escaping local minima with derivative-free methods: a numerical investigation". In: *arXiv e-prints*, arXiv:1812.11343 (Dec. 2018), arXiv:1812.11343. arXiv: 1812.11343 [math.OC].

[112] J. Colin Hill, Erminia Calabrese, Simone Aiola, et al. "Atacama Cosmology Telescope: Constraints on prerecombination early dark energy". In: *Phys. Rev. D* 105 (12 June 2022), p. 123536. DOI: 10.1103/PhysRevD.105.123536. URL: https://link.aps.org/doi/10.1103/PhysRevD.105.123536.

[113] Tanvi Karwal and Marc Kamionkowski. "Dark energy at early times, the Hubble parameter, and the string axiverse". In: *Phys. Rev. D* 94 (10 Nov. 2016), p. 103523. DOI: 10.1103/PhysRevD.94.103523. URL: https://link.aps.org/doi/10.1103/PhysRevD.94.103523.

[114] Marc Kamionkowski, Josef Pradler, and Devin G. E. Walker. "Dark Energy from the String Axiverse". In: *Phys. Rev. Lett.* 113 (25 Dec. 2014), p. 251302. DOI: 10.1103/PhysRevLett.113.251302. URL: https://link.aps.org/doi/10.1103/PhysRevLett.113.251302.

[115] J. Colin Hill, Evan McDonough, Michael W. Toomey, et al. "Early dark energy does not restore cosmological concordance". In: *Phys. Rev. D* 102 (4 Aug. 2020), p. 043507. DOI: 10.1103/PhysRevD.102.043507. URL: https://link.aps.org/doi/10.1103/PhysRevD.102.043507.

[116] Mikhail M. Ivanov, Evan McDonough, J. Colin Hill, et al. "Constraining early dark energy with large-scale structure". In: *Phys. Rev. D* 102.10, 103502 (Nov. 2020), p. 103502. DOI: 10.1103/PhysRevD.102.103502. arXiv: 2006.11235 [astro-ph.CO].

[117] Guido D'Amico, Leonardo Senatore, Pierre Zhang, et al. "The Hubble tension in light of the Full-Shape analysis of Large-Scale Structure data". In: *JCAP* 2021.5, 072 (May 2021), p. 072. DOI: 10.1088/1475-7516/2021/05/072. arXiv: 2006.12420 [astro-ph.CO].

[118] Meng-Xiang Lin, Wayne Hu, and Marco Raveri. "Testing H_0 in acoustic dark energy models with P l a n c k and ACT polarization data". In: *Phys. Rev. D* 102.12, 123523 (Dec. 2020), p. 123523. DOI: 10.1103/PhysRevD.102.123523. arXiv: 2009.08974 [astro-ph.CO].

[119] Vivian Poulin, Tristan L. Smith, and Alexa Bartlett. "Dark energy at early times and ACT data: A larger Hubble constant without late-time priors". In: *Phys. Rev. D* 104 (12 Dec. 2021), p. 123550. DOI: 10.1103/PhysRevD.104.123550. URL: https://link.aps.org/doi/10.1103/PhysRevD.104.123550.

[120] Sudeep Das, Thibaut Louis, Michael R. Nolta, et al. "The Atacama Cosmology Telescope: temperature and gravitational lensing power spectrum measurements from three seasons of data". In: *Journal of Cosmology and Astroparticle Physics* 2014.04 (Apr. 2014), p. 014. DOI: 10.1088/1475-7516/2014/04/014. URL: https://dx.doi.org/10.1088/1475-7516/2014/04/014.

[121] Shadab Alam, Metin Ata, Stephen Bailey, et al. "The clustering of galaxies in the completed SDSS-III Baryon Oscillation Spectroscopic Survey: cosmological analysis of the DR12 galaxy sample". In: *Monthly Notices of the Royal Astronomical Society* 470.3 (Sept. 2017), pp. 2617–2652. DOI: 10.1093/mnras/stx721. arXiv: 1607.03155 [astro-ph.CO].

[122] Florian Beutler, Chris Blake, Matthew Colless, et al. "The 6dF Galaxy Survey: baryon acoustic oscillations and the local Hubble constant". In: *Monthly Notices of the Royal Astronomical Society* 416.4 (Sept. 2011), pp. 3017–3032. ISSN: 0035-8711. DOI: 10.1111/j.1365-2966.2011.19250.x. eprint: https://academic.oup.com/mnras/article-pdf/416/4/3017/2985042/mnras0416-3017.pdf. URL: https://doi.org/10.1111/j.1365-2966.2011.19250.x.

[123] Ashley J. Ross, Lado Samushia, Cullan Howlett, et al. "The clustering of the SDSS DR7 main Galaxy sample - I. A 4 per cent distance measure at z = 0.15". In: *Monthly Notices of the Royal Astronomical Society* 449.1 (May 2015), pp. 835–847. DOI: 10.1093/mnras/stv154. arXiv: 1409.3242 [astro-ph.CO].

[124] Fiona McCarthy, J. Colin Hill, and Mathew S. Madhavacheril. "Baryonic feedback biases on fundamental physics from lensed CMB power spectra". In: *Phys. Rev. D* 105 (2 Jan. 2022), p. 023517. DOI: 10.1103/PhysRevD.105.023517. URL: https://link.aps.org/doi/10.1103/PhysRevD.105.023517.

[125] George Efstathiou and Steven Gratton. "A Detailed Description of the CAMSPEC Likelihood Pipeline and a Reanalysis of the Planck High Frequency Maps". In: *The Open Journal of Astrophysics* 4.1 (Aug. 2021). DOI: 10.21105/astro.1910.00483. URL: https://doi.org/10.21105/astro.1910.00483.

[126] Erik Rosenberg, Steven Gratton, and George Efstathiou. "CMB power spectra and cosmological parameters from Planck PR4 with CamSpec". In: *Monthly Notices of the Royal Astronomical Society* 517.3 (Sept. 2022), pp. 4620–4636. ISSN: 0035-8711. DOI: 10.1093/mnras/stac2744. eprint: https://academic.oup.com/mnras/article-pdf/517/3/4620/46782205/stac2744.pdf. URL: https://doi.org/10.1093/mnras/stac2744.

[127] D. S. Swetz, P. A. R. Ade, M. Amiri, et al. "Overview of the Atacama Cosmology Telescope: receiver, instrumentation, and telescope systems". In: *The Astrophysical Journal Supplement Series* 194.2 (June 2011), p. 41. DOI: 10.1088/0067-0049/194/2/41. URL: https://dx.doi.org/10.1088/0067-0049/194/2/41.

[128] Jonathan L. Sievers, Renée A. Hlozek, Michael R. Nolta, et al. "The Atacama Cosmology Telescope: cosmological parameters from three seasons of data". In: *Journal of Cosmology and Astroparticle Physics* 2013.10 (Oct. 2013), p. 060. DOI: 10.1088/1475-7516/2013/10/060. URL: https://dx.doi.org/10.1088/1475-7516/2013/10/060.

[129] M. D. Niemack, P. A. R. Ade, J. Aguirre, et al. "ACTPol: a polarization-sensitive receiver for the Atacama Cosmology Telescope". In: *Millimeter, Submillimeter, and Far-Infrared Detectors and Instrumentation for Astronomy V*. Ed. by Wayne S. Holland and Jonas Zmuidzinas. Vol. 7741. International Society for Optics and Photonics. SPIE, 2010, 77411S. DOI: 10.1117/12.857464. URL: https://doi.org/10.1117/12.857464.

[130] R. J. Thornton, P. A. R. Ade, S. Aiola, et al. "The Atacama Cosmology Telescope: the polarization-sensitive ACTPol instrument". In: *The Astrophysical Journal Supplement Series* 227.2 (Dec. 2016), p. 21. DOI: 10.3847/1538-4365/227/2/21. URL: https://dx.doi.org/10.3847/1538-4365/227/2/21.

[131] Blake D. Sherwin, Alexander van Engelen, Neelima Sehgal, et al. "Two-season Atacama Cosmology Telescope polarimeter lensing power spectrum". In: *Phys. Rev. D* 95 (12 June 2017), p. 123529. DOI: 10.1103/PhysRevD.95.123529. URL: https://link.aps.org/doi/10.1103/PhysRevD.95.123529.

[132] J. Errard, P. A. R. Ade, Y. Akiba, et al. "MODELING ATMOSPHERIC EMISSION FOR CMB GROUND-BASED OBSERVATIONS". In: *The Astrophysical Journal* 809.1 (2015), p. 63. DOI: 10.1088/0004-637X/809/1/63. URL: https://dx.doi.org/10.1088/0004-637X/809/1/63.

[133] Shaul Hanany and Philip Rosenkranz. "Polarization of the atmosphere as a foreground for cosmic microwave background polarization experiments". In: *New Astronomy Reviews* 47.11 (2003). Proceedings of the Workshop on The Cosmic Microwave Background Radiation and its Polarization, pp. 1159–1165. ISSN: 1387-6473. DOI: https://doi.org/10.1016/j.newar.2003.09.017. URL: https://www.sciencedirect.com/science/article/pii/S1387647303002409.

[134] Eric Hivon, Krzysztof M. Górski, C. Barth Netterfield, et al. "MASTER of the Cosmic Microwave Background Anisotropy Power Spectrum: A Fast Method for Statistical Analysis of Large and Complex Cosmic Microwave Background Data Sets". In: *The Astrophysical Journal* 567.1 (Mar. 2002), p. 2. DOI: 10.1086/338126. URL: https://dx.doi.org/10.1086/338126.

[135] Thibaut Louis, Xavier Garrido, Adam Soussana, et al. "Consistency of CMB experiments beyond cosmic variance". In: *Phys. Rev. D* 100 (2 July 2019), p. 023518. DOI: 10.1103/PhysRevD.100.023518. URL: https://link.aps.org/doi/10.1103/PhysRevD.100.023518.

[136] Planck Collaboration, Akrami, Y., Ashdown, M., et al. "Planck 2018 results - XI. Polarized dust foregrounds". In: *A&A* 641 (2020), A11. DOI: 10.1051/0004-6361/201832618. URL: https://doi.org/10.1051/0004-6361/201832618.

[137] N. Battaglia, J. R. Bond, C. Pfrommer, et al. "ON THE CLUSTER PHYSICS OF SUNYAEV–ZEL'DOVICH AND X-RAY SURVEYS. II. DECONSTRUCTING THE THERMAL SZ POWER SPECTRUM". In: *The Astrophysical Journal* 758.2 (Sept. 2012), p. 75. DOI: 10.1088/0004-637X/758/2/75. URL: https://dx.doi.org/10.1088/0004-637X/758/2/75.

[138] N. Battaglia, J. R. Bond, C. Pfrommer, et al. "SIMULATIONS OF THE SUNYAEV–ZEL'DOVICH POWER SPECTRUM WITH ACTIVE GALACTIC NUCLEUS FEEDBACK". In: *The Astrophysical Journal* 725.1 (Nov. 2010), p. 91. DOI: 10.1088/0004-637X/725/1/91. URL: https://dx.doi.org/10.1088/0004-637X/725/1/91.

[139] E. Komatsu and U. Seljak. "The Sunyaev–Zel'dovich angular power spectrum as a probe of cosmological parameters". In: *Monthly Notices of the Royal Astronomical Society* 336.4 (Nov. 2002), pp. 1256–1270. ISSN: 0035-8711. DOI: 10.1046/j.1365-8711.2002.05889.x. eprint: https://academic.oup.com/mnras/article-pdf/336/4/1256/3043671/336-4-1256.pdf. URL: https://doi.org/10.1046/j.1365-8711.2002.05889.x.

[140] George Efstathiou and Marina Migliaccio. "A simple empirically motivated template for the thermal Sunyaev–Zel'dovich effect". In: *Monthly Notices of the Royal Astronomical Society* 423.3 (June 2012), pp. 2492–2497. ISSN: 0035-8711. DOI: 10.1111/j.1365-2966.2012.21059.x. eprint: https://academic.oup.com/mnras/article-pdf/423/3/2492/7994096/mnras0423-2492.pdf. URL: https://doi.org/10.1111/j.1365-2966.2012.21059.x.

[141] G. E. Addison, J. Dunkley, and D. N. Spergel. "Modelling the correlation between the thermal Sunyaev Zel'dovich effect and the cosmic infrared background". In: *Monthly Notices of the Royal Astronomical Society* 427.2 (Dec. 2012), pp. 1741–1754. ISSN: 0035-8711. DOI: 10.1111/j.1365-2966.2012.21664.x. eprint: https://academic.oup.com/mnras/article-pdf/427/2/1741/2998405/427-2-1741.pdf. URL: https://doi.org/10.1111/j.1365-2966.2012.21664.x.

[142] Sigurd Naess, Simone Aiola, Jason E. Austermann, et al. "The Atacama Cosmology Telescope: arcminute-resolution maps of 18 000 square degrees of the microwave sky from ACT 2008–2018 data combined with Planck". In: *Journal of Cosmology and Astroparticle Physics* 2020.12 (Dec. 2020), p. 046. DOI: 10.1088/1475-7516/2020/12/046. URL: https://dx.doi.org/10.1088/1475-7516/2020/12/046.

[143] Sigurd Naess and Thibaut Louis. *Large-scale power loss in ground-based CMB mapmaking*. 2023. arXiv: 2210.02243 [astro-ph.IM].

[144] Marius Lungu, Emilie R. Storer, Matthew Hasselfield, et al. "The Atacama Cosmology Telescope: measurement and analysis of 1D beams for DR4". In: *Journal of Cosmology and Astroparticle Physics* 2022.05 (May 2022), p. 044. DOI: 10.1088/1475-7516/2022/05/044. URL: https://dx.doi.org/10.1088/1475-7516/2022/05/044.

[145] Zachary Atkins, Adriaan J. Duivenvoorden, William R. Coulton, et al. *The Atacama Cosmology Telescope: Map-Based Noise Simulations for DR6*. 2023. arXiv: 2303.04180 [astro-ph.CO].

[146] Vera C. Rubin and Jr. Ford W. Kent. "Rotation of the Andromeda Nebula from a Spectroscopic Survey of Emission Regions". In: *Astrophysical journal* 159 (Feb. 1970), p. 379. DOI: 10.1086/150317.

[147] K. G. Begeman. "HI rotation curves of spiral galaxies. I. NGC 3198." In: *Astronomy and Astrophysics* 223 (Oct. 1989), pp. 47–60.

[148] S. M. Kent and J. E. Gunn. "The dynamics of rich clusters of galaxies. I. The Coma cluster." In: *Astronomical journal* 87 (July 1982), pp. 945–960. DOI: 10.1086/113178.

[149] Ewa L. Łokas and Gary A. Mamon. "Dark matter distribution in the Coma cluster from galaxy kinematics: breaking the mass–anisotropy degeneracy". In: *Monthly Notices of the Royal Astronomical Society* 343.2 (Aug. 2003), pp. 401–412. ISSN: 0035-8711. DOI: 10.1046/j.1365-8711.2003.06684.x. eprint: https://academic.oup.com/mnras/article-pdf/343/2/401/18415870/343-2-401.pdf. URL: https://doi.org/10.1046/j.1365-8711.2003.06684.x.